

NORTHWESTERN UNIVERSITY

Screening of Complex Nanomaterials Through Combinatorial Libraries

A DISSERTATION

SUBMITTED TO THE GRADUATE SCHOOL  
IN PARTIAL FULFILLMENT OF THE REQUIREMENTS

for the degree

DOCTOR OF PHILOSOPHY

Field of Materials Science and Engineering

By

Edward James Kluender

EVANSTON, ILLINOIS

September 2020

© Copyright Edward J Kluender 2020

All Rights Reserved

## ABSTRACT

### Screening of Complex Nanomaterials Through Combinatorial Libraries

As humans have evolved over time, so have the materials that they rely on. From the Stone Age through the Iron Age, entire eras have been defined by specific materials, their corresponding properties, and the applications they have enabled. This is still true to this day, as the Silicon Age has led way to the Nano Age. The discovery of new materials has traditionally been a slow process. For nanoscale materials, this has been especially true due to two significant hurdles: synthetic complexity and a massive parameter space. The synthesis of nanoparticles with precise control over size, composition, and shape is extremely challenging because when working on the nanoscale small variations can produce large differences in material properties. Additionally, when one includes size as a variable, in addition to composition and phase structure, the parameter space that needs to be investigated increases exponentially. In this thesis, these challenges are addressed through a combinatorial nanomaterial synthesis method paired with equally high throughput characterization methods. By using large area nanolithography techniques, millions of nanoparticles were deposited onto a single substrate, with their sizes and compositions spatially encoded. Using these “Megalibraries” of nanomaterials, each nanoparticle’s chemical and physical properties were investigated. Specifically, three properties were explored: catalyzed carbon nanotube growth, heterogeneous catalysis (for both hydrogenation of organic molecules and electrochemical reduction of oxygen), and localized surface plasmon tuning.

Chapter one provides an introduction to complex nanomaterial synthesis and characterization methods, establishing literature precedent for the importance of discovering new multi-component

nanostructures. Included in this literature review, the need for new high throughput synthesis and screening methods is highlighted. While there have been many advances in the field of multicomponent nanomaterial screening, current methods have been limited in throughput and flexibility, preventing full exploration of the massive parameter space.

Chapter two describes a method of synthesizing the nanoparticle Megalibraries. Using polymer pen lithography, attoliter volumes of a block copolymer solution coordinated with metal ions can be deposited onto a single substrate over cm-scale areas. To ensure that the deposition occurred in a uniform manner across the entire substrate, new polymer pen arrays were fabricated to overcome any defects in the pen array that would result in variations in the deposited material. With a reliable deposition method, the composition and quantity of the block copolymer ink on the pen array was systematically varied. Continuous gradients were explored using the overlapping linear regimes of two Gaussian spray systems. These novel spray coating methods produced dual gradients of size and composition allowing for the synthesis of 15,876 unique nanoparticle structures on a single substrate with size and composition spatially encoded. This method shrinks the massive material landscape to a single manageable sample.

Chapter three explores these continuous gradients and each nanoparticle's ability to catalyze the growth of single-walled carbon nanotubes. For screening platforms to be used at their maximum capacity, screening methods with a throughput comparable to the synthesis throughput are required. This was achieved by depositing the nanoparticle Megalibraries on top of thermally isolated micropillars for the laser-induced heating required to characterize their ability to grow single-walled carbon nanotubes in a high throughput manner. Using the particle synthesis methods described in chapter one and these screening methods, the highest resolution screen, with respect

to nanoparticle composition, was performed, resulting in the discovery of Au<sub>3</sub>Cu as a new catalyst composition not previously known for this application.

Chapter four describes the use of customized well plate reactors to isolate sections of the combinatorial gradient for heterogeneous catalysis. By using the proper materials and geometries, these reactors were used to study the catalytic activity of nanoparticles on a surface under extreme reaction conditions. This allowed for the study of hydrogenation, a reaction necessary for producing many pharmaceutical reagents as well as electrochemical oxygen reduction. For electrochemical reactions, a conductive glassy carbon substrate was developed to provide a uniform surface for the nanoparticles to be deposited on and analyzed.

In chapter five, the localized surface plasmons of these multimetallic nanoparticles were studied. Due to the isolated nature of this synthesis technique (nanoparticles are microns away from one another) single particle studies are possible for optical characterization. To create desirable multi-plasmon interactions with isolated particles, a thermally stable nanoparticle on mirror substrate was developed to increase the intensity of the plasmons by an order of magnitude. Using multiple adhesion layers, a gold thin film was fabricated to retain its structure when heated above 500 °C, a temperature that would traditionally dewet the film. Using this nanoparticle on mirror geometry, the first study of a multimetallic nanoparticle on mirror was performed, allowing for the surface enhanced Raman spectroscopy measurement of benzene dithiol using a single gold-silver alloy nanoparticle.

Taken together, this thesis presents methodology that has significantly increased the rate of nanomaterial synthesis and characterization. In addition to the specific applications described above, the work can potentially impact almost every field of science that is dependent on new

materials. While only bimetallic systems were studied for these three applications, up to septenary compositions are possible, and screening methods for other applications are actively being developed. Ultimately, this platform will increase the number of nanomaterials accessible to humankind and lead to the discovery of impactful nanomaterials over an accelerated time-frame.

## ACKNOWLEDGEMENTS

I would like to thank my advisor, Chad Mirkin, for all of his guidance and support over the course of my Ph.D. During orientation week, I vividly remember his presentation on the simplicity of the patterning techniques in the Dip Pen Nanolithography subgroup, allowing for the fabrication of extremely complex nanostructures in an organized manner. I am grateful for the opportunity to grow, both as a scientist and as a communicator. During my time at Northwestern I worked on countless projects spanning biology, catalysis and plasmonics, greatly broadening my scientific knowledge and always fulfilling my ever-growing scientific curiosity. Having the chance to work on multiple grant proposals and reporting also allowed me to develop the ability to frame the work I have accomplished in a meaningful way. I will always remember to use one idea per slide and never a font that isn't Arial.

I also thank my committee members, Professor Vinayak Dravid, Professor Mark Hersam, and Professor Teri Odom. They have provided meaningful feedback that helped shape my Ph.D. work, both through their roles on my committee as well as through the Air Force Center of Excellence.

Throughout my Ph.D. I have been fortunate to work with many talented collaborators. First, I thank Dr. Benji Maruyama and Dr. Rahul Rao, my collaborators at the Air Force Research Lab. The visits I made to Dayton each summer were some of the most productive times in lab. At Northwestern, I thank my mentors in the DPN subgroup, Professor Keith Brown and Dr. James Hedrick, for teaching me all they knew about the techniques that I went on to use for my Ph.D. and develop good research habits. Dr. Peng-Cheng Chen and Jingshan Du for pioneering the SPBCL technique and always being there to help with TEM. I would also like to thank Professor Brian Meckes and Dr. David Walker for all of the meaningful conversations, whether they were

scientific or not. I also thank all of the members of the Mirkin group that I have collaborated with or enjoyed a SBR with, especially everyone who participated in the quarantine happy hours that helped me maintain my sanity during the past few months.

On a more personal note, I thank the broader MSE department for making my time at NU so enjoyable. While I am certainly past my prime athletically, beating the undergrad frats in intramurals has been an enjoyable constant through my time here, winning multiple IM shirts in the process. I will always be grateful for the friends I made at Northwestern, remembering fondly the GoT watch parties and “crashing” chemistry’s PLU events.

Finally, I thank my parents for instilling me with scientific curiosity and teaching me to be a better person. Ever since I was a child, I enjoyed solving puzzles, and they always encouraged me to pursue that drive, even teaching me the scientific method for determining the best rabbit repellent in elementary school. I would not be the person I am today without their encouragement and support. I also thank my brothers Ray and Bill. While neither are STE(M) majors, they both push me through their accomplishments and drove me to achieve my goals. I also would not be where I am today without my person, Dr. Linda Guiney. She has always been there for me, especially over the past few months; I cannot imagine that it was easy dealing with someone writing a thesis during quarantine. I cannot thank Linda enough for the love and support she has given me, and I look forward to everything the future holds for us.



**LIST OF ABBREVIATIONS**

AFM	Atomic Force Microscopy
ARES	Autonomous Research System
CNT	Carbon Nanotube
CVD	Chemical Vapor Deposition
DPN	Dip Pen Nanolithography
FDTD	Finite-Difference Time-Domain
FWHM	Fullwidth Half Max
GC	Glassy Carbon
HFB	Hexafluorobenzene
HMDS	Hexamethyldisilazane
LSP	Localized Surface Plasmon
MHA	6-Mercaptohexanoic Acid
NPoM	Nanoparticle on Mirror
PAD	Polymer Assisted Deposition
PDMS	Poly(dimethylsiloxane)
PECVD	Plasma Enhanced Chemical Vapor Deposition
PEO- <i>b</i> -P2VP	Poly(ethylene oxide)- <i>block</i> -Poly(2-vinylpyridine)
PPL	Polymer Pen Lithography
SEM	Scanning Electron Microscopy
SERS	Surface Enhanced Raman Spectroscopy
SOI	Silicon on Insulator

SPBCL	Scanning Probe Block Copolymer Lithography
SWNT	Single Walled Carbon Nanotube
TEM	Transmission Electron Microscopy

## TABLE OF CONTENTS

<b>ABSTRACT.....</b>	<b>3</b>
<b>ACKNOWLEDGEMENTS .....</b>	<b>7</b>
<b>LIST OF ABBREVIATIONS .....</b>	<b>9</b>
<b>TABLE OF CONTENTS .....</b>	<b>11</b>
<b>LIST OF FIGURES .....</b>	<b>15</b>
<b>LIST OF TABLES .....</b>	<b>31</b>
<b>CHAPTER 1 : INTRODUCTION TO COMPLEX NANOMATERIALS .....</b>	<b>32</b>
1.1 Complex Materials Through History .....	33
1.1.2 Importance of Nanomaterials.....	34
1.2 Synthesis of Complex Nanomaterials.....	37
1.2.1 Top-Down Nanomaterial Synthesis.....	38
1.2.2 Bottom-Up Nanomaterial Synthesis .....	43
1.2.3 Nanoreactor Nanomaterial Synthesis.....	47
1.3 Nanomaterial Screening Platforms .....	51
1.4 Scope of Thesis .....	54
<b>CHAPTER 2 : FABRICATING NANOMATERIAL COMBINATORIAL</b>	
<b>MEGALIBRARIES .....</b>	<b>56</b>
2.1 Background.....	57
2.2 Results and Discussion .....	60

	12
2.2.1	Hard Transparent Arrays for Force Independent Uniform Features..... 60
2.2.2	Blade Coating PDMS Pen Arrays for Large Area Patterning..... 71
2.2.3	Sequential Inking of Multiple Wells on PPL Array..... 77
2.2.4	Spray Coating Pen Arrays for Continuous Composition and Size Gradients..... 84
2.3	Experimental Methods ..... 98
2.3.1	Fabrication PPL Arrays..... 98
2.3.2	Patterning ..... 98
2.3.3	MHA Ink and Substrate Preparation..... 99
2.3.4	SPBCL Ink and Substrate Preparation..... 99
2.3.5	SPBCL Nanoparticle Synthesis ..... 99
2.3.6	Imaging ..... 100
2.3.7	X-Ray Fluorescence..... 100
2.4	Summary ..... 100

**CHAPTER 3 : SCREENING CATALYST COMPOSITION FOR THE CHEMICAL**

**VAPOR DEPOSITION GROWTH OF CARBON NANOTUBES.....103**

3.1	Background..... 104
3.2	Results and Discussion ..... 111
3.2.1	Fabrication of Micropillar Substrates ..... 111
3.2.2	Investigating Effects of Growth Conditions on SPBCL Catalysts ..... 119
3.2.3	Combinatorial Screening of Bimetallic SPBCL Catalysts..... 126
3.3	Experimental Methods ..... 139
3.3.1	Fabrication of Micropillar Substrates ..... 139

3.3.2	Tube Furnace Growth of SWNTs .....	140
3.3.3	ARES Growth of SWNTs .....	141
3.3.4	Imaging and Characterization of Nanoparticles and Resulting SWNTs .....	141
3.3.5	SWNT Catalyst Screening Platform Optimized Workflow .....	142
3.4	Summary .....	143

#### **CHAPTER 4 : COMBINATORIAL SCREENING OF CATALYTIC PROPERTIES .....145**

4.1	Background .....	146
4.2	Results and Discussion .....	149
4.2.1	Universal Well-Plate Reactor for Heterogeneous Catalysis .....	149
4.2.2	Electrochemical screening of AuCu on glassy carbon films .....	154
4.3	Experimental Methods .....	163
4.3.1	Fabrication of PAD GC .....	163
4.3.2	Well-plate Electrochemical Measurements .....	164
4.4	Summary .....	164

#### **CHAPTER 5 : SCREENING OPTICAL PROPERTIES OF MULTIMETALLIC**

#### **NANOPARTICLES ON PLASMONIC MIRRORS .....166**

5.1	Background .....	167
5.2	Results and Discussion .....	169
5.2.1	Fabrication of Thermally Stable Mirror Substrates .....	169
5.2.2	Au nanoparticles on mirror substrates .....	174
5.2.3	Multimetallic Nanoparticles on Mirror Substrates .....	178
5.3	Experimental Methods .....	184

	14
5.3.1 Fabrication of NPoM Samples.....	184
5.3.2 Characterization of NPoM Samples.....	186
5.3.3 Finite Difference Time Domain Calculations.....	186
5.4 Summary.....	188
<b>CHAPTER 6 : FUTURE OUTLOOK.....</b>	<b>190</b>
<b>CURRICULUM VITAE.....</b>	<b>220</b>

## LIST OF FIGURES

- Figure 1.1:** Material complexity over time. As humans have evolved, so have the materials that are used, with the impact of some materials being so great that ages of history have been named after them. Today, extremely complex materials are used in everyday applications, with materials databases containing hundreds of thousands of different materials. While this is a large number, it pales in comparison to the total number of materials with this given complexity. This thesis will describe novel methods that were developed to increase the rate of material discovery in the nano-realm using nanomaterial Megalibraries..... 34
- Figure 1.2:** First recorded uses of nanomaterials show their application centuries ago. With the Lycurgus cup taking advantage of the beautiful optical properties that arose when gold and silver nanoparticles were incorporated. Figure adapted from reference.<sup>11</sup> ..... 35
- Figure 1.3:** Combinatorial fabrication of thin film materials. Xiang et al. developed a method of sequential depositions with physical masks to fabricate libraries of nanomaterials, first with (A) 128 different compositions and then expanded to almost 1,000 compositions on a single substrate. These libraries were used to discover (A) superconducting and (B) photoluminescence. Figure adapted from references (A)<sup>32</sup> and (B).<sup>34</sup> ..... 40
- Figure 1.4:** Fabrication of multimetallic nanoparticles through top-down deposition into ionic liquids. (A) Using alloy targets for deposition, AuAg nanoparticles were fabricated with a composition controlled by the relative composition of the foil target. (B) Pentametallic nanoparticles were fabricated in an ionic liquid and screened for the oxygen reduction reaction, finding a material (Cr-Mn-Fe-Co-Ni) with comparable catalytic activity to Pt, but without any

precious metals. (C) Combinatorial co-deposition of AuCu nanoparticles into ionic liquid containing wells allowed for 19 relative compositions to be synthesized on a single substrate. Figure adapted from references (A),<sup>44</sup> (B),<sup>52</sup> and (C).<sup>50</sup> ..... 42

**Figure 1.5:** The growth of nanoparticles in solution follow the schematic explanation of a LaMer plot. Region I represents the prenucleation stage in which the precursors are being decomposed, either thermally or chemically, until  $C_{crit}$  is reached. Once at  $C_{crit}$ , the critical concentration for nucleation, the growth transitions to region II, where nanoparticles begin to nucleate. Nucleation proceeds until the concentration is lowered below  $C_{crit}$  and can be described in region III, the growth stage. The growth stage consists of heterogeneous nucleation on the formed particles, growing them in size until  $C_{\infty}$  is reached, the equilibrium concentration of solute. Figure adapted from reference.<sup>57</sup> ..... 44

**Figure 1.6:** Carbothermal shock nanoparticle synthesis methods have allowed researchers to overcome large differences in precursor decomposition temperatures to synthesize uniform multimetallic nanoparticles at a high throughput. By heating a carbon fiber substrate containing metal precursors, octonary nanoparticles can be readily synthesized (A). Using ink jet printing, this can be scaled to fabricated combinatorial libraries of 22 different composition nanoparticles containing up to 8 different elements (B). These methods were used to study (A)  $NH_3$  conversion and (B) the oxygen reduction reaction. Figures adapted from references (A)<sup>62</sup> and (B).<sup>63</sup> ..... 46

**Figure 1.7:** Molecular nanoreactors were the first methods used to isolate a small quantity of metal precursors to allow the synthesis of a single nanoparticle. While this was first achieved used



templated proteins, it was expanded through the use of (A) block copolymer micelles and (B) single molecule dendrimers. Figure adapted from references (A)<sup>69</sup> and (B).<sup>75</sup> ..... 48

**Figure 1.8:** Scanning probe block copolymer lithography (SPBCL) uses tip-based lithography techniques to deposit attoliter volumes of a metal ion containing block copolymer solution onto a hydrophobic surface in the form of nanodomains. Through a sequential heat treatment process, the metal ions are aggregated and reduced, forming a single nanoparticle per nanodomain, followed by a high temperature treatment to remove the remaining polymer. The composition of the loaded metal ions can directly control the composition of the resulting nanoparticle. The size of the final nanoparticle can be altered either through the absolute concentration of metal ions or the size of the nanodomain. Figure adapted from references.<sup>84,91</sup> ..... 50

**Figure 1.9:** Polymer pen lithography (PPL) is a tip-based lithography that uses thousands of polymer pyramids to deposit material onto a surface in unison. PPL, combined with SPBCL, allows for large areas of multimetallic nanoparticles to be synthesized on a single substrate. Figure adapted from reference.<sup>95</sup> ..... 51

**Figure 1.10:** Indirect measurements of electrocatalysts have produced some of the highest throughput screens to date. (A) Using quinone as a fluorescent proton detector, any reaction that changes the pH of the solution can be used to screen the activity. In this case, the deposited materials (i) perform a methanol oxidation reaction, using the quinone fluorescence to identify peak activity (ii). (B) Using the bubbles produced during the water splitting reaction can be collected on the micron scale to screen 231 unique compositions in parallel. Figure adapted from references (A)<sup>105</sup> and (B).<sup>107</sup> ..... 53

**Figure 2.1:** Schematic of the fabrication process for hard transparent polymer pen arrays. Figure adapted from reference.<sup>143</sup> ..... 61

**Figure 2.2:** (A) Wrinkle wavelength as a function of silica thickness. (B) Silica thickness as a function of deposition time (slope  $0.55 \pm 0.03$  nm/s). (C) Bright-field image of silica deposited onto a slab of PDMS, 200  $\mu\text{m}$  scale bar. (D) Dark-field image of hard transparent array when it is at the goldilocks thickness of 175 nm, 50  $\mu\text{m}$  scale bar. (E) Shattered hard transparent array pens after patterning when silica thickness is too thin at 83 nm, 50  $\mu\text{m}$  scale bar. (F) Bright-field image of hard transparent array when silica thickness is too large, here 250 nm, buckling goes through the pens, 100  $\mu\text{m}$  scale bar. (G) Optical images of  $\text{SiO}_2$  films deposited on PDMS pen arrays using E-beam deposition. These trends agree with PECVD growth  $\text{SiO}_2$ . Figure adapted from reference.<sup>143</sup> ..... 64

**Figure 2.3:** Patterning MHA using (A) a hard transparent array and (B) a polymer array, both with an extension sweep over 5  $\mu\text{m}$  piezo range with 100  $\mu\text{m/s}$  extension and withdraw speed and 5 second dwell time. Patterning MHA using (C) a hard transparent array and (D) a polymer array, both with an extension sweep covering 5  $\mu\text{m}$  piezo range with 1.5  $\mu\text{m/s}$  extension and withdraw speed and no dwell time at full extension., All scale bars are 2.5  $\mu\text{m}$ . Images were taken using lateral force microscopy using AFM. Figure adapted from reference.<sup>143</sup> ..... 66

**Figure 2.4:** Patterning polymer ink with an (A) extension sweep over 5  $\mu\text{m}$  piezo range with 100  $\mu\text{m/s}$  extension and withdraw speed using hard transparent arrays and a dwell time of 2.5 s at full extension, (B) hard transparent arrays extension sweep over 4.2  $\mu\text{m}$  piezo range with 3  $\mu\text{m}$  extension and withdraw with no dwell time at full extension, and (C) PPL extension sweep over

5  $\mu\text{m}$  piezo range with the left half corresponding to the conditions in (D) and the right half corresponding to (B). Scale bars are 2.5  $\mu\text{m}$ . Images were taken with AFM in tapping mode. Figure adapted from reference.<sup>143</sup> ..... 68

**Figure 2.5:** (A) AFM of a dot array with a 175 nm pitch in a hexagonal pattern array written using hard transparent array, 150 nm scale bar. (B) Single polymer feature with a circle of small droplets from original meniscus, 20 nm scale bar. (C) Dark-field optical microscopy of array with 500 nm pitch written using hard transparent array with PPL with 14,641 features written per pen, 100  $\mu\text{m}$  scale bar, and (D) zoomed in image pattern made from a single pyramidal pen, 25  $\mu\text{m}$  scale bar. Figure adapted from reference.<sup>143</sup> ..... 70

**Figure 2.6:** Schematic of pen array bowing that occurs when large area pens are made of s-PDMS. .... 74

**Figure 2.7:** (A) Schematic of blade coating technique. Scotch tape (50-70  $\mu\text{m}$  thick) was used as guard rails to control layer thickness, and to pin the film at each edge of the wafer. Multiple blade coating and curing steps were sequentially performed to create multilayered pen arrays. (B) Schematic of blade coated arrays. By curing each layer without the glass slide present, the internal stresses were able to relax before the glass slide was attached..... 76

**Figure 2.8:** Profilometry measurements of PDMS pen arrays from the same Si master. The normal array was fabricated in one curing step of s-PDMS. The blade coated array was made in three curing steps out of s-PDMS, h-PDMS, and attached to a glass slide with s-PDMS. .... 77

**Figure 2.9:** Photographs of 3D printed 3x3 wells sealed with PPL array. Clamps were used to compress the wells into the elastomeric PDMS to for a seal between each well. .... 79

**Figure 2.10:** Dark field optical images of (A) inked pen array and (B) the resulting polymer dome patterns on a SiO<sub>2</sub> substrate. The red line indicates the edge of the well wall. .... 79

**Figure 2.11:** (A) Photograph of the spray system set up. The center of the spray profile is aligned with the exposed section of the pen array. (B) Photograph of the masks used to expose selected sections of the pen array. The large mask is covered with an absorbent material to prevent excess ink from contaminating the pen array. Each of the smaller masks are used to expose four different sections depending on their orientation. (C) Photograph of pen array sprayed with 15 different inks (the top right section was left blank as a control). .... 82

**Figure 2.12:** Dark field optical images of polymer dome arrays patterned on HMDS treated conductive Si by a sequentially spray coated pen array. Each image is from a different sprayed section of the pen array. All scale bars are 300  $\mu\text{m}$ . .... 83

**Figure 2.13:** Scalability of spray-coating with different arrays. (A) Diagram of how to position air brushes relative to PPL array based on size, (B) scanned spray used to quantify spray profile, (C) linear full width half max slope showing a linear scaling trend for PPL arrays. Figure adapted from reference.<sup>165</sup> .... 85

**Figure 2.14:** Evaporative self-assembly of diffused ink around pyramidal pens. (A) Proposed mechanism of ink evaporation following spray coating in which evaporation and diffusion leads to homogenous mixing of the inks and preferential deposition of the ink on the pens. Optical image

of a single pen under (B) dark field and (C) fluorescence showing preferential inking at the base of the pen. Figure adapted from reference.<sup>165</sup> ..... 87

**Figure 2.15:** Large scale gradients of patterned nanomaterials. (A) Stitched confocal fluorescence image of a compositional gradient of two different fluorophores in patterned polymeric domes, scale bar is 2 mm, and (B) fluorescence intensity across of each region. (C) A magnified fluorescence image showing a single tile from (A), illustrating the dot arrays pattern, as well as the resolution of (A). (D) Schematic of the airbrush position during spraying. Figure adapted from reference.<sup>165</sup> ..... 89

**Figure 2.16:** PPL array spray-coated with a composition gradient. (A) Photograph and (B) confocal micrograph of the composition gradient spray coated onto the PPL array. Figure adapted from reference.<sup>165</sup> ..... 90

**Figure 2.17:** 14 million bimetallic nanoparticles synthesized in parallel with a compositional gradient. (A) X-ray fluorescence profile of AuPd alloy composition of SPBCL patterned array taken with a 3 mm slit, note that the last point is at the edge of the array. (B) SEM of SPBCL AuPd nanoparticles. Scale bar is 2  $\mu\text{m}$ . Figure adapted from reference.<sup>165</sup> ..... 92

**Figure 2.18:** Au  $L\beta$  and Pd  $K\alpha$  Fluorescence Intensities. The Au  $L\beta$  fluorescence line intensity (A) increases towards the Au-rich side of the sample and decreases towards the Pd-rich side. No signal is observed for the case of a blank substrate (green). The Pd  $K\alpha$  fluorescence line intensity (B) decreases towards the Au-rich side of the sample and increases to a well-defined peak (blue) towards the Pd-rich side of the spectrum. +3 Au refers to a 3 mm offset from the sample center

towards the Au-rich side, and +3 Pd refers to a 3 mm offset from the sample center towards the Pd-rich side. Figure adapted from reference.<sup>165</sup> ..... 93

**Figure 2.19:** Pd K $\alpha$  XRF Intensity from sample patterned on quartz glass substrate. Qualitatively, it is observable that from the Au-rich side of the sample (black) to the Pd-rich side of the sample (blue and pink) that the Pd K $\alpha$  fluorescence intensity increases. This demonstrates that a gradient Au-Pd sample can be patterned independent of substrate. Figure adapted from reference.<sup>165</sup> ..... 94

**Figure 2.20:** PPL array spray-coated with both a size and composition gradient. (A) Photograph and (B) confocal micrograph of the composition and size gradient spray coated onto the PPL array. Figure adapted from reference.<sup>165</sup> ..... 96

**Figure 2.21:** Large scale nanopatterned gradients of composition and size. (A) Stitched confocal fluorescence image of compositional and size gradients of two fluorophores in polymeric domes. Scale bar is 2 mm. (B) Average fluorescence intensity of each fluorophore across the array and (C) average total fluorescence intensity in the vertical axis plotted with the average volume of individual features as measured by AFM. (D) High resolution darkfield micrograph of a region showing the patterns written by four pens, scale bar is 50  $\mu\text{m}$ . (E) Schematic of the airbrush position during spraying. (F) AFM of the largest patterned features ( $1.10 \pm 0.02 \mu\text{m}$ ) at the top of the array, and (G) AFM of the smallest patterned features ( $642 \pm 46 \text{ nm}$ ) at the bottom of the array, scale bars are 3  $\mu\text{m}$ . Figure adapted from reference.<sup>165</sup> ..... 97

**Figure 3.1:** Scheme of micropillar fabrication using SOI Wafer..... 112

**Figure 3.2:** SEM images of micropillars etched into Si wafers. (A) Hard mask undercutting occurs when the SF<sub>6</sub> Si etch is ran continuously for the entire etch process. (B) By using the Bosch process and oscillating between etch and passivation steps, near vertical pillar walls are formed, producing micropillars up to 40 μm tall. (C) Ridging occurs on the walls of the micropillars produced by the Bosch process. Each ridge is created by one etch-deposition cycle. .... 115

**Figure 3.3:** (A) SEM image of SWNTs grown on ARES micropillar using a 0.8 nm Fe film catalyst. (B) G-band peak integration measurements from *in situ* Raman spectra collected during growths at two temperatures. Higher growth temperatures exhibited faster growth kinetics but short lifetimes, while lower temperatures produced slower growth kinetics and longer lifetimes..... 117

**Figure 3.4:** AFM micrographs of the top surfaces of micropillars made using (A) SiO<sub>2</sub> and (B) photoresist as the hard mask during Bosch process etching. (B) Optical image of micropillars fabricated using photoresist as a hard mask performed at (i) 0, (ii) 5, and (iii) 10 °C. Scale bars are 50 μm. .... 119

**Figure 3.5:** AFM micrograph of polymer domes containing Co precursors patterning on ALD Al<sub>2</sub>O<sub>3</sub>, made hydrophobic with HMDS. The polymer domes were spaced by 750 nm and were 275 nm in diameter. .... 122

**Figure 3.6:** SWNTs grown from SPBCL synthesized Co nanoparticle catalysts. (A) SEM micrographs of the SWNTS, inset showing excessive bundling. (B) Raman spectrum of SWNTs, sharp G peaks indicate low defect SWNTS. Presence of radial breathing modes (RBMs) confirms

SWNT growth, and fourth from bottom (grey trace) exhibit more than one RBM confirming bundling seen in SEM. .... 123

**Figure 3.7:** Patterning SPBCL nanoparticles onto ARES micropillars. (A) Image of the pen arrays aligned with the ARES micropillars, scale bar is 50  $\mu\text{m}$ . (B) Dark field optical image, scale bar is 50  $\mu\text{m}$ , with expanded inset of four pillars of the nano-dome polymer features in a square array on top of the micropillars. Figure adapted from reference.<sup>165</sup> ..... 125

**Figure 3.8:** Characterization of AuCu alloy catalysts used in compositional screen. (A) AFM of AuCu particles in catalytically active size regime prior to calcination. AFM of AuCu particles on top of ARES micropillar with heights of  $\sim 2.5$  nm. This AFM was performed prior to calcination with residual carbon from the patterned polymer nanoreactor still present surrounding each nanoparticle (B) Scanning transmission electron microscopy of Au-Cu alloy nanoparticles in catalytically active size regime. The particles were synthesized on an electron-transparent silicon nitride thin film but have similar sizes as the ones on ARES micropillars and show a homogenous alloy structure. From left to right: high-angle annular dark field (HAADF) images, annular bright field (ABF) images, energy-dispersive X-ray spectroscopy (EDS) elemental mapping results for Au L and Cu K lines. All images share the same scale bar of 2 nm. HAADF and ADF images were denoised using the block-matching and 3D filtering (BM3D) method. Figure adapted from reference.<sup>165</sup> ..... 128

**Figure 3.9:**  $\text{Au}_x\text{Cu}_{1-x}$  Composition gradient. (A) Photograph of air brushes spraying Au and Cu PEO-*b*-P2VP inks onto a pen array. (B) Optical scan of spray profiles for Au and Cu sources. (C)



Spray profile intensity across the center of both spray profiles, fit to a double Gaussian curve. This fit was used to calculate the composition as a function of position across the pen array. .... 129

**Figure 3.10:** Compositional breakdown of the 75% composition gradient across three 5 mm substrates. Figure adapted from reference.<sup>165</sup> ..... 131

**Figure 3.11:** Compositional breakdown of catalytic activity. (A) Integrated intensity of the SWNT Raman G band as a function of catalyst composition for growths performed between 700 °C and 800 °C. Error bars represent SEM. (B) Growths performed between 800 °C and 900 °C. The  $G_{\max}$  peaks at  $X = 0.75$  suggests  $Au_3Cu$  is the composition that exhibits the highest catalytic activity for SWNT growth. (C) Representative Raman spectra from growths on ARES micropillars at five compositions normalized to the Si peak. Figure adapted from reference.<sup>165</sup> ..... 133

**Figure 3.12:** Average SWNT diameter as a function of Au content. RBMs were collected across the compositional array. The diameter of a SWNT is inversely proportional to the RBM ( $d=248/RBM$ ). Figure adapted from reference.<sup>165</sup> ..... 134

**Figure 3.13:** Raman spectra of SWNTs grown from dip coated catalyst. Raman spectra exhibit similar trends to those seen in SPBCL ARES spectra, with an increased catalytic activity at  $\sim Au_3Cu$ . Figure adapted from reference.<sup>165</sup> ..... 135

**Figure 3.14:** G-band intensity, normalized to the Si Raman peak, as a function of Cu-Ni composition. (A) 200 growths performed in ARES, resulting in a catalyst hit at  $CuNi_3$ . (B) The same catalyst peak was found using traditional tube furnace growth, *ex situ* Raman spectra was

used to collect a representative spectrum from the center pillar of each patch (Patch 210, on this gradient, correlates with the composition  $\text{CuNi}_3$ )..... 137

**Figure 3.15:** G-band intensity as a function composition of Au-Ni nanoparticles. SWNT growth was performed in a tube furnace with analysis completed with *ex situ* Raman spectroscopy. Inset Raman spectra exhibit the presence of RBM, confirming SWNT growth. .... 139

**Figure 4.1:** Set up of well-plate reactor, 5x5 arrays of 3.8 mm circular wells. (A) Substrates are placed on substrate support inside of base plate, with screws facing upwards through 9 bolt holes. (B) Substrate-well seal layer, in this example lubricated PTFE, is placed on top of the substrates, aligning the wells with locations of interest on the substrate. Kalrez is used for experiments performed  $<100$  °C, and lubricated PTFE is used at higher temperatures. (C) The bulk well layer is then loaded on top of the seal layer and screwed tight to isolate each well. Once this is done, the wells are created, and solutions can be loaded. (D) The top seal layer is placed over the wells to prevent evaporation of low volumes and the top plate is screwed down to create a reliable seal. Reaction solutions can also be loaded at this step by piercing the top seal layer with a needle. (E) Side view of the reactor once fully constructed. (F) Vertical scheme of reactor fully constructed. Grey: base plate and top plate. Red: substrate support. Purple: substrates. White: substrate-well seal layer. Yellow: bulk well plate. Blue: top seal layer..... 152

**Figure 4.2:** N-alkylation of 1-naphthylamine in well plate reactor. GC-MS spectra of the resulting product after the reaction ran for 18 hours at 200 °C. These Pd catalysts exhibited a high selectivity for the fully reduced product..... 153

**Figure 4.3:** Configuration of well plate reactor for electrocatalysis (A) Side view schematic of reactor set up, similar to the use for heterogeneous catalysis without the top plate. The working electrode in each well is connected in parallel and the reference and counter electrodes are moved from well to well to test each section. (B) Photograph of well plate reactor testing one of 9 cells. Smaller wells are capable with smaller reference electrodes..... 154

**Figure 4.4:** Catalytic screening of Au-Cu catalysts for oxygen reduction on non-uniform mechanically polished GC. .... 156

**Figure 4.5:** Inconsistent patterning on mechanically polished GC. (A) Dark field optical images of patterned polymer domes on an outward bowed GC substrate. While there are regions of the pattern that resulted in uniform patterns and the PPL array was in proper contact with the substrate, the center of the substrate applied too high of a force resulted in aggregations of patterns and the edges did not contact at some points resulting in no patterns. (B) AFM image of polymer domes patterned on a rough mechanically polished substrate. The resulting polymer domes are non-uniform in shape due to increased roughness pinning the edges of the polymer dome..... 157

**Figure 4.6:** Profilometry measurements of a set of GC substrates and a Si wafer. Due to the mechanical polishing required for GC, large area height variations occur that prevent large area patterning for reliable catalyst screening. .... 158

**Figure 4.7:** Characterization of PAD GC films. AFM images of as fabricated GC films when spin coated at (A) 8000 rpm and (B) 6000 rpm. Faster spin rates resulted in non-uniform films that produced pinholes that were not present in lower spin rates. (C) Raman spectra of GC films. The

D- ( $1350\text{ cm}^{-1}$ ) and G- ( $1590\text{ cm}^{-1}$ ) band peaks are present, along with a smaller 2D and D+G band peak at  $2800\text{ cm}^{-1}$ . ..... 160

**Figure 4.8:** Characterization of patterns on PAD GC. AFM images of (A) polymer domes patterned on PAD GC and (B) the resulting nanoparticles after heat treatment showing high yield of single particle formation. (C) Optical images of polymer domes patterned across the entire patterned substrate showing high pattern uniformity over the necessary scales for combinatorial screening. .... 162

**Figure 4.9:** Characteristic voltage sweep measurements of PAD GC substrates with and without patterned AuCu nanoparticles. The lower turn on voltage and higher peak current indicate that the patterned nanoparticles are electrically connected to the GC substrate and accessible by the reactant solution. .... 163

**Figure 5.1:** Characterization of NPoM substrates. (A) SEM image of thermally treated Ti-Au thin film. (B) AFM image of as deposited Au thin film showing roughness of  $\pm 2\text{ nm}$ . (C) SEM image of polymer nanoreactor on a Cr-Au- $\text{Al}_2\text{O}_3$  substrate after heat treatment. (D) SEM image of polymer nanoreactor on Cr-Au-3MPTS- $\text{SiO}_2$  substrate after heat treatment. .... 173

**Figure 5.2:** Backscattering intensity heatmap at  $630\text{ nm}$  scattering using white light. This is an image of an array of  $40\text{ nm}$  diameter Au Nanoparticles on a  $5\text{ nm}$  gap Mirror substrate. When using a white light excitation with an approximately  $1\text{ }\mu\text{m}$  diameter beam size, the backscattering signal area from each particle matches the white light beam size. Due to the  $3\text{ }\mu\text{m}$  spacing between particles, this allows for each nanoparticle to be individually investigated. .... 176

**Figure 5.3:** Dark field spectra of 40 nm Au nanoparticles on three substrates. The bare nanoparticle on a SiO<sub>2</sub> substrate exhibited limited optical scattering. As the gap between the nanoparticle and the plasmonic thin film is lowered, the resulting spectra increases in intensity and red shifts significantly..... 177

**Figure 5.4:** Theoretical modeling of Au-Au NPoM geometries. (A) Dark field spectra predictions for nanoparticles on SiO<sub>2</sub> (Semi-inf), Au film with 5 and 10 nm SiO<sub>2</sub> gap layers. E-field heat maps of Au nanoparticles on (B) SiO<sub>2</sub>, (C) 10 nm and (D) 5 nm gap substrates..... 178

**Figure 5.5:** Theoretical modeling of AuNi-Au NPoM geometries. The dark field back scattering spectra for the three substrates and the three nanoparticle orientations show a wide range of possible spectra. The greatest intensity and highest wavelength LSPR were found when the Au phase of the AuNi nanoparticle was in direct contact with a 5 nm gap mirror substrate. For each nanoparticle orientation, similar substrate trends were found when compared to the Au-Au geometries. It was found that nanoparticle orientation had an equal contribution to the LSPR, with the rotation of the Janus structure creating overlap in the LSPR between different substrates.. 180

**Figure 5.6:** Experimental spectra of AuNi nanoparticles on different mirror substrates. These trends match theoretical calculations but are difficult to fully characterize due to the lack of orientation control. The determination of the orientation of each nanoparticle is not currently possible due to the thick substrate preventing high resolution TEM characterization. .... 181

**Figure 5.7:** FDTD calculations for AuAg-Au NPoM geometries. .... 182

**Figure 5.8:** Experimental characterization of AuAg-Au NPoM geometry substrates. (A) The dark field scattering spectra of a 70 nm  $\text{Au}_{0.5}\text{Ag}_{0.5}$  nanoparticle on a 5 nm gap substrate produced the two expected LSPR peaks at 500 and 600 nm. (B) When functionalized with BDT, SERS detection was achieved using a single isolated  $\text{Au}_{0.5}\text{Ag}_{0.5}$  spherical nanoparticle (red trace on the nanoparticle, blue trace off of the particle, green trace bulk BDT). ..... 184

**Figure 6.1:** Shape control of patterned SPBCL nanoparticles through secondary treatments. (A) using traditional seed mediated secondary growth treatments, each nanoparticle can be grown into an anisotropic shape, determined by the solution surfactants and reduction rates. (B) Using a novel Bi CVD method, THH nanoparticles can be fabricated at large scales to increase the catalytic activity of each nanoparticle composition. Figure adapted from reference.<sup>276</sup> ..... 192

**Figure 6.2:** Trimetallic phase spray configuration. By introducing a third gaussian spray profile, each profile's linear regime can be overlapped, creating a triangular compositional gradient. . 193

**LIST OF TABLES**

<b>Table 3.1:</b> Range of growth parameters screened for SPBCL Co catalysts deposited on SiO <sub>2</sub> ARES micropillars. ....	126
--	-----

**CHAPTER 1:**  
**INTRODUCTION TO**  
**COMPLEX NANOMATERIALS**



## 1.1 Complex Materials Through History

The discovery of new materials has driven human innovation throughout history and, in certain cases, has defined entire ages of time. From the stone age, to the bronze age, to the iron age, and more recently to the silicon age, new capabilities directly correlate with our access to new materials. The trend through these ages has predominantly been increasing complexity, combining multiple materials together to utilize each material's strengths, or unlocking new properties entirely. Fast forward to today, we are able to fabricate high-performance superalloys, made up to >10 different elements, some making up less than 1% atomically.<sup>1</sup> This opens the ability to optimize each material for each application taking advantage of cooperative properties (e.g. strength,<sup>2</sup> toughness,<sup>3</sup> hardness,<sup>4</sup> chemical reactivity,<sup>5</sup> and chemical resistance<sup>6</sup>) from each component.

The discovery of new materials has traditionally been slow, with inflection points at fundamental discoveries or methods of screening that drastically change the rate of discovery.<sup>7</sup> Even with all of the advances made in developing high throughput methods of materials discovery, the more complex the materials being studied, the larger the parameter space that need to be taken into account. For example, current materials databases list on the order of 100,000 inorganic compounds discovered to date.<sup>8</sup> While this is a massive amount of materials, it is a miniscule number compared to what is possible. Taking a simple calculation of the possible tetra-metallic alloys, not considering crystal structure or relative composition, just composition, there are 2,672,670 possible metal alloys. In order to discover which of these materials are relevant for real-world applications, new methods of screening are required, in which high throughput synthesis methods are matched by high throughput characterization methods.

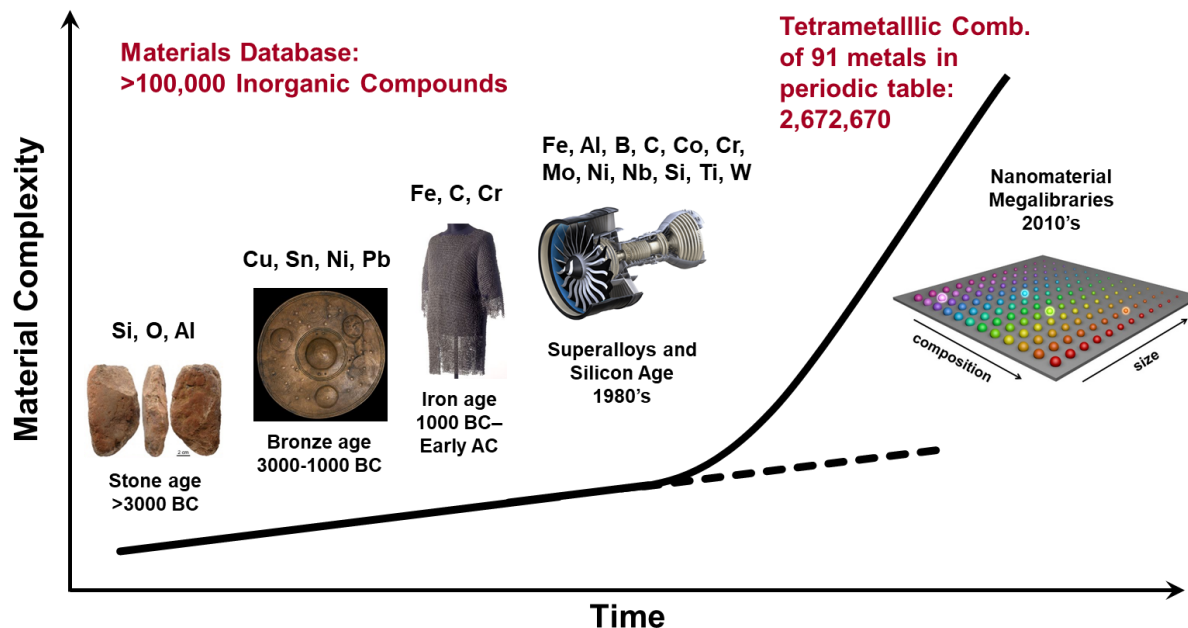


**Figure 1.1:** Material complexity over time. As humans have evolved, so have the materials that are used, with the impact of some materials being so great that ages of history have been named after them. Today, extremely complex materials are used in everyday applications, with materials databases containing hundreds of thousands of different materials. While this is a large number, it pales in comparison to the total number of materials with this given complexity. This thesis will describe novel methods that were developed to increase the rate of material discovery in the nano-realm using nanomaterial Megalibraries.

### 1.1.2 Importance of Nanomaterials

Through human development, the drive of material development has often been to grow larger, transforming small towns into sprawling cities with skyscrapers that can be seen from miles away. More recently, the main technological breakthroughs have been in the opposite direction, towards

the extremely small. With the majority of Americans walking around with a super computer in their pocket, we are currently living in what could be termed the nano-age.<sup>9, 10</sup> Nanomaterials are defined as materials with at least one dimension on the order of 1-100 nanometers. While nanomaterials were used centuries ago (two of the most famous examples are gold-silver nanoparticles in the Lycurgus Cup<sup>11</sup> (Figure 1.2) and carbon nanotubes in Damascus Steel<sup>12</sup>), it would be thousands of years before they were directly studied. One of the first reported scientific studies of nanomaterials was in 1857 when Michael Faraday measured the optical properties of a “Ruby” gold solution of nanoparticles.<sup>13</sup>



**Figure 1.2:** First recorded uses of nanomaterials show their application centuries ago. With the Lycurgus cup taking advantage of the beautiful optical properties that arose when gold and silver nanoparticles were incorporated. Figure adapted from reference.<sup>11</sup>

Today, nanoparticles are used for a wide range of applications, taking advantage of their mechanical,<sup>14</sup> catalytic,<sup>15</sup> and optical<sup>16</sup> properties. These properties are often a direct result of the materials size. For example, graphene and carbon nanotubes are some of the strongest materials in the world.<sup>17</sup> This comes from the fundamental strength of the C-C covalent bonds that make up the entirety of these nanomaterials, which can be fabricated with zero defects,<sup>18</sup> creating a material stronger than steel. Nanoparticles are also of interest for catalytic properties due to their high surface area to volume ratio. When materials are shrunk to the nanoscale, the number of surface atoms can make up over half of the total atoms. These surface atoms are extremely useful for two reasons. First, only the surface atoms interact with the chemical surroundings, meaning the more surface atoms you have, the higher percentage of your material is actively being used. Second, these surface atoms are not fully coordinated. They are missing a complete side of their nearest neighbors in the materials crystal lattice. This makes for high energy surfaces that can be exploited to interact with outside reactants for high efficiency catalysts.<sup>19</sup> Additionally, nanomaterials exhibit unique optical properties due to their size. These optical properties are leveraged through two different methods: plasmonics and quantum confinement. Plasmonics is a physical phenomenon in which clouds of electrons oscillate within a metal nanoparticle.<sup>16</sup> The resonance at which this occurs can be controlled by the composition, size, or shape of the nanoparticle, allowing for extreme control over the wavelengths of interactions. Quantum confinement occurs when the size of the particles is below the exciton Bohr radius (the distance between an electron-hole pair in a bulk crystal).<sup>20</sup> These two phenomenon allow for the tuning of the absorbance and emittance of nanomaterials over wide ranges of optical wavelengths.

Similar to bulk materials, the first studies of nanomaterials were of mono-component materials. As more research into the strengths of nanomaterials has proved fruitful, more complex materials have become a point of interest, wherein researchers are attempting to combine the ideal properties of multiple components into a single nanomaterial.<sup>21</sup>

## 1.2 Synthesis of Complex Nanomaterials

The controlled synthesis of nanomaterials have come a long way since Faraday's preliminary studies in which he varied the concentration of gold salt and observed the effects on the color of the resulting gold nanoparticle solution.<sup>13</sup> As a whole, nanomaterial synthesis methods can be described in one of two ways: top-down or bottom-up.<sup>22</sup> Top-down approaches begin with a bulk material and break it down to nanomaterials. This can be done through mechanical,<sup>23</sup> thermal,<sup>24</sup> physical,<sup>25</sup> and chemical<sup>26</sup> processes. Bottom-up approaches begin with atomic or molecular precursors and combine them to form nanomaterials. Both of these approaches have their own benefits and are useful in certain applications for complex multicomponent nanomaterials.

When fabricating complex nanomaterials, higher precision synthesis controls are required compared to bulk materials. Because nanomaterials consist of a countable number of atoms, atomic variations in their structures can have significant changes in their properties. On the bulk scale, one is able to combine a set amount of starting material and produce a single product made up of those starting materials. On the nanoscale, there are only a few ways to control the starting materials on the same size scale as the final product. These methods are described in detail in 1.2.3. Because multiple products will be formed at the nanoscale, external controls are needed to ensure that each product matches the targeted stoichiometry of the starting materials. Consider an example of a starting solution of a 50:50 mixture. If a single product is formed, it will consist of an identical

50:50 mixture. If two products are formed, there is a continuum of possible products, from two 50:50 products to two 100% products of each composition. This is a simple example that already shows the difficulty of fabricating multicomponent materials, and nanomaterials synthesis will often produce products on the molar scale, greatly increasing the complexity and the number of the possible products. Additionally, these examples only account for pure statistical sampling of the starting material. Real applications require balancing miscibility, phase structures, and interface and surface energies.

### ***1.2.1 Top-Down Nanomaterial Synthesis***

Starting with a bulk-scale material, top-down nanomaterial synthesis techniques enable the fabrication of large quantities of materials. While mechanical and chemical methods are possible,<sup>23,</sup><sup>26</sup> the most common approach, particularly for complex materials, involves thermal or physical methods. These approaches use a bulk source material and either heat them to the point of evaporation or physically bombard them with ions to eject atoms or molecules from the material. The vapor phase material then deposits onto a substrate as a thin film. The growth of the films is determined by the interaction between the deposited material and the substrate and can proceed by one of three pathways: Volmer-Weber island growth, Frank-van der Merwe layer growth, or Stranski-Krastanov layer plus island growth.<sup>27</sup> Island growth occurs when there is a high interface energy between the deposited material and the substrate, leading to aggregations of the deposited material as isolated particles, or islands, until they eventually grow into one another, forming a uniform film.<sup>28</sup> Layer growth describes the formation of a monolayer of the deposited material prior to the addition of a second layer. This occurs when there is a strong interaction between the deposited material and the substrate. Layer plus island growth occurs when a monolayer is initially

formed, but due to a lattice mismatch or lattice orientation,<sup>29</sup> islands begin forming on the deposited monolayers before the film achieve confluence. These films can be heated, causing the thin film to dewet into uniform nanoparticles for catalysis<sup>30</sup> and optical applications.<sup>31</sup>

Physical thin film deposition methods were some of the first methods used for the synthesis and screening of complex nanomaterials. In 1995, Xiang and Schultz et al. combined sequential thin film deposition and physical masking techniques to fabricate large arrays of oxides to screen for superconducting films<sup>32</sup> (Figure 1.3 A). Using these arrays composed of 10,000 sites per square inch, with dimensions of 200x200  $\mu\text{m}$ , they were able to identify two oxide films (BiSrCaCuO and YBaCuO) that demonstrated superconductivity. The same authors were then able to discover new cobalt oxide magnetoresistance materials using a similar screening technique<sup>33</sup> and later translated the technique into a more general methodology that can be applied to investigate luminescent, ferroelectric, dielectric, and magnetic materials (Figure 1.3 B).<sup>34</sup> Similar methods were used by Mao more recently to characterize the optical properties of semiconductors.<sup>35, 36</sup> Alternatively, continuous gradient depositions have been fabricated using a moving mask to control the deposition across a single substrate.<sup>37-39</sup>

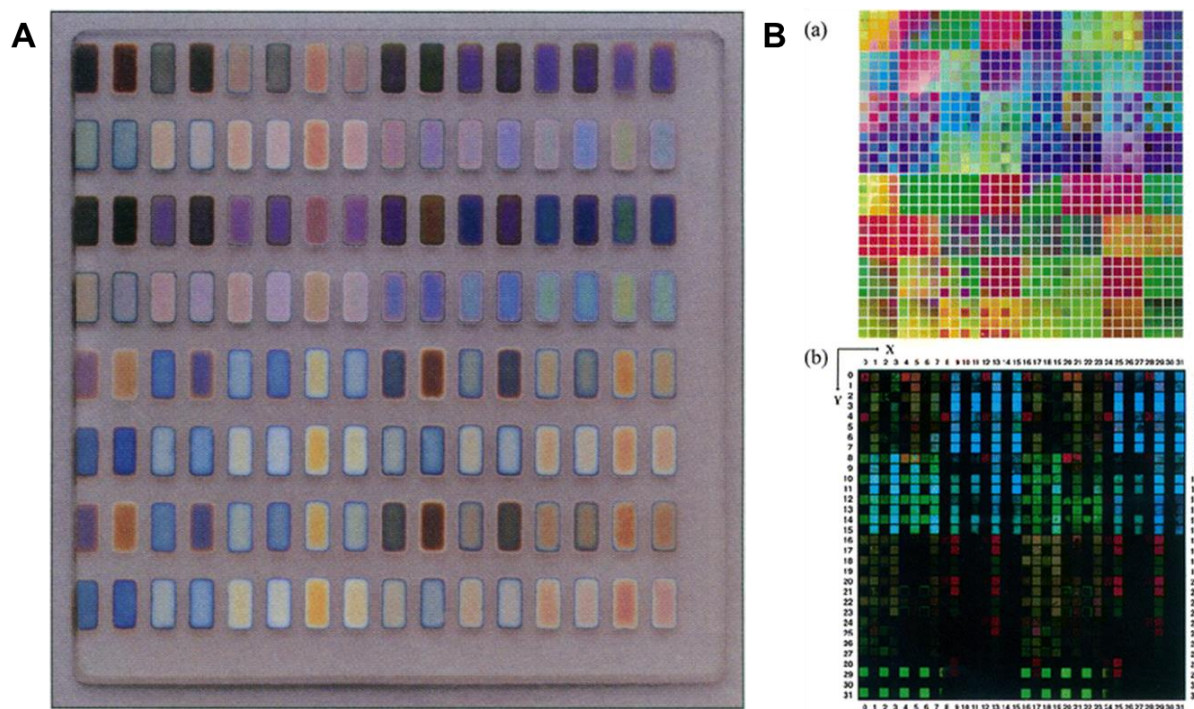


**Figure 1.3:** Combinatorial fabrication of thin film materials. Xiang et al. developed a method of sequential depositions with physical masks to fabricate libraries of nanomaterials, first with (A) 128 different compositions and then expanded to almost 1,000 compositions on a single substrate. These libraries were used to discover (A) superconducting and (B) photoluminescence. Figure adapted from references (A)<sup>32</sup> and (B).<sup>34</sup>

While the methods described above have driven a large amount of materials discovery, they have been largely limited to thin films, which while important, only reach the nanoscale in one dimension: thickness. In 1999, Günther et al. discovered that using the same deposition sources used to fabricate thin films he could form nanoparticles by depositing into a liquid as opposed to onto a solid substrate<sup>40</sup> (Figure 1.4). These deposition processes occur under vacuum, and thus high molecular weight liquids were required for this particular method. Gunther et al. began using



silicone oil but the method was later expanded to include ionic liquids, which can coordinate with the nanoparticles in solution to stabilize them, preventing excessive aggregation.<sup>41, 42</sup> Using ionic liquids, multimetallic nanoparticles have been fabricated using these sputter plasma-in-liquid techniques,<sup>43</sup> including AuAg,<sup>44, 45</sup> AuPd,<sup>46</sup> AuPt,<sup>47, 48</sup> AuCu,<sup>49, 50</sup> PtNi,<sup>51</sup> and, more recently, some pentametallic compositions.<sup>52</sup> These compositions were formed either through the use of alloy sources, sequential deposition, co-deposition, or in one case, a silver source deposited into an ionic liquid containing gold salt, resulting in the reduction of Au onto the Ag particles.<sup>53</sup> When a substrate target is selectively etched to form micro-wells on the surface, and those wells are subsequently filled with a volume of ionic liquid, the combinatorial libraries studied in thin film literature can be directly applied to plasma-in-liquid nanoparticles.<sup>50, 52</sup>

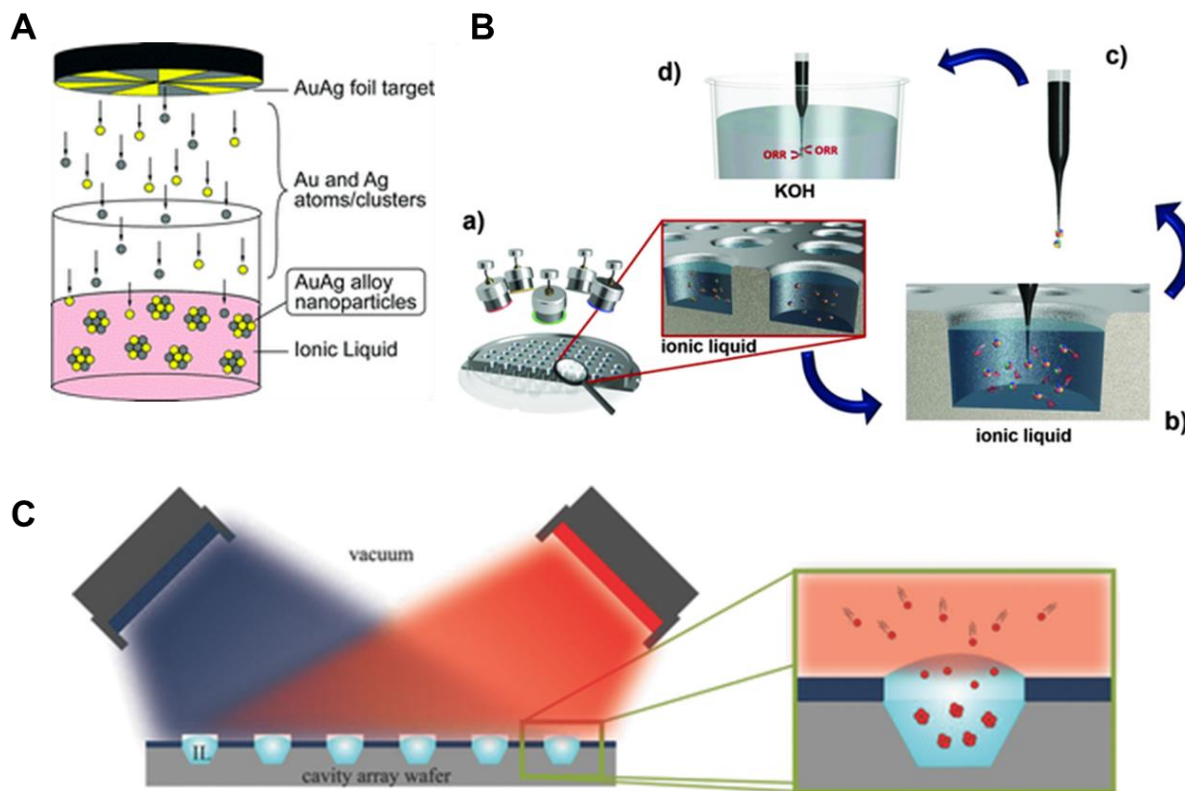


**Figure 1.4:** Fabrication of multimetallic nanoparticles through top-down deposition into ionic liquids. (A) Using alloy targets for deposition, AuAg nanoparticles were fabricated with a composition controlled by the relative composition of the foil target. (B) Pentametallic nanoparticles were fabricated in an ionic liquid and screened for the oxygen reduction reaction, finding a material (Cr-Mn-Fe-Co-Ni) with comparable catalytic activity to Pt, but without any precious metals. (C) Combinatorial co-deposition of AuCu nanoparticles into ionic liquid containing wells allowed for 19 relative compositions to be synthesized on a single substrate. Figure adapted from references (A),<sup>44</sup> (B),<sup>52</sup> and (C).<sup>50</sup>

### ***1.2.2 Bottom-Up Nanomaterial Synthesis***

While there are some top-down methods for synthesizing nanoparticles, the majority of nanoparticle synthesis employs bottom-up methods. Atomic precursors, which are typically metal salts, are decomposed in one of two ways: thermal decomposition or chemical reduction. These two methods have been employed since the beginning of human use of nanomaterials. To turn stained glass red, artisans would add gold salts to molten glass, forming nanoparticles through thermal decomposition. Faraday's first experiments chemically reduced gold salts using phosphorous.<sup>13, 54</sup> These syntheses were standardized almost a century later by Tukevich.<sup>55</sup> Regardless of which method is used, the process of the nanoparticle formation is similar and follows a LaMer plot process<sup>56</sup> (Figure 1.5). In solution, the precursors are highly soluble, typically in the form of metal ion salts. As the salts are decomposed or reduced, they form  $M^0$  metal atoms in solution, which have a much lower solubility. This leads to a super-saturation of the metal atoms, causing them to homogeneously nucleate and begin forming nanoparticles. If the concentration remains at this super-saturation point, through the addition of more  $M^0$  atoms, nucleation will continue to occur. Once particles are formed,  $M^0$  atoms in solution will heterogeneously nucleate on the particle surface and grow the particle larger. Heterogeneous nucleation occurs as soon as nucleation occurs and continues after solution is below the homogeneous nucleation super-saturation point until the solution equilibrium is reached.

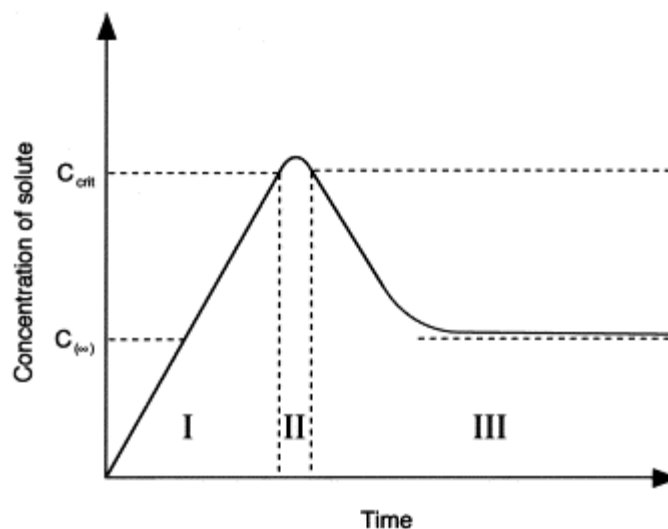


**Figure 1.5:** The growth of nanoparticles in solution follow the schematic explanation of a LaMer plot. Region I represents the prenucleation stage in which the precursors are being decomposed, either thermally or chemically, until  $C_{crit}$  is reached. Once at  $C_{crit}$ , the critical concentration for nucleation, the growth transitions to region II, where nanoparticles begin to nucleate. Nucleation proceeds until the concentration is lowered below  $C_{crit}$  and can be described in region III, the growth stage. The growth stage consists of heterogeneous nucleation on the formed particles, growing them in size until  $C_{\infty}$  is reached, the equilibrium concentration of solute. Figure adapted from reference.<sup>57</sup>

Through these processes, scientists have been able to fine tune the synthesis of homogeneous nanoparticles of almost every of mono-component metal of interest. When expanding to multicomponent nanoparticles, there are many variables that need to be considered, including reduction potentials, nucleation kinetics, growth kinetics, and interface energies. Reduction potentials, in particular, often are the driving force for the kinetics of the synthesis. Different metals

intrinsically have different reduction potentials, with those with more positive reduction potentials being reduced more readily. Practically, this means that if the reduction potentials are close in value, the metals can be co-reduced, each populating the solution with equal quantities of  $M^0$  resulting in uniform nucleation and growth. This allows for simple control of the final particle composition by altering the composition of the metal salts.<sup>58</sup> While other methods have been developed for nanoparticles containing two metals with a large reduction potential difference, such as  $Au_3M$  compositions reported by Schaak et al.,<sup>59,60</sup> these methods are more complex and require extensive optimization to control their relative compositions and homogeneity.

Similarly, thermal co-decomposition of multiple precursors can be performed if the decomposition temperature of the precursors is close in temperature. This approach is easier to control compared to reduction potentials through the use of different salt ligands or solution conditions.<sup>61</sup> Recently, Hu et al. has developed a new way to overcome differences in decomposition temperatures through a technique called carbothermal shock synthesis<sup>62</sup> (Figure 1.6) By mixing salt solutions uniformly and depositing them onto carbon nanofibers, the use of a short electrical pulse results in the rapid heating ( $\sim 10^5$  K/s) of the metal precursors to  $\sim 2000$  K, well above all of the metal salts decomposition temperatures, negating the differences in the precursors' decomposition temperatures. This work has led to the synthesis of high entropy alloy nanoparticles containing up to 8 different elements in a solid solution. This technique was expanded to perform high throughput screening of these nanoparticles for the oxygen reduction reaction.<sup>63</sup>

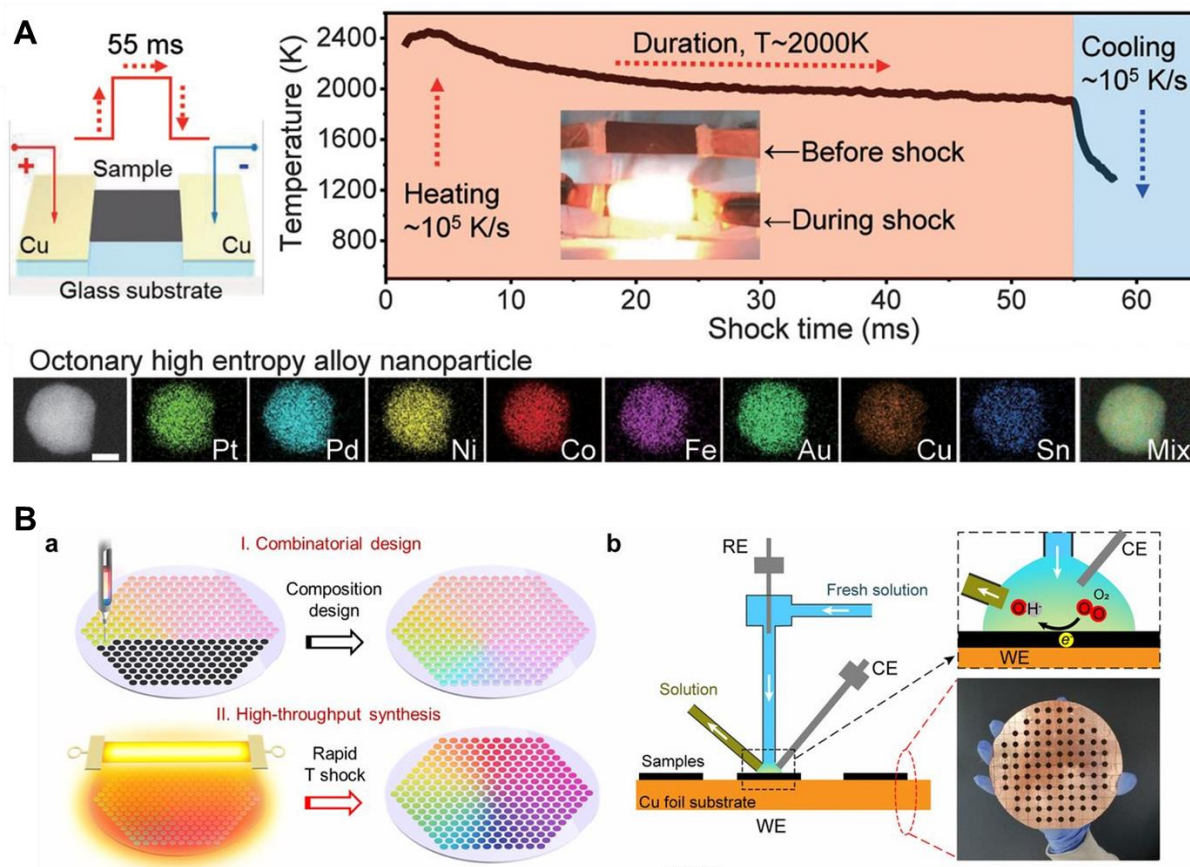


**Figure 1.6:** Carbothermal shock nanoparticle synthesis methods have allowed researchers to overcome large differences in precursor decomposition temperatures to synthesize uniform multimetallic nanoparticles at a high throughput. By heating a carbon fiber substrate containing metal precursors, octonary nanoparticles can be readily synthesized (A). Using ink jet printing, this can be scaled to fabricated combinatorial libraries of 22 different composition nanoparticles containing up to 8 different elements (B). These methods were used to study (A)  $\text{NH}_3$  conversion and (B) the oxygen reduction reaction. Figures adapted from references (A)<sup>62</sup> and (B).<sup>63</sup>

### *1.2.3 Nanoreactor Nanomaterial Synthesis*

Ultimately, current bottom-up synthesis methods are able to access a wide variety of nanoparticle structures through optimized reactions, but each synthesis requires time-intensive study and optimization for each individual structure. This massive phase space is one of the major bottlenecks for the discovery of new nanoparticle materials. Thus, more universal synthesis methods are required to determine which structures are worth further method development and scale-up. The use of nanoreactors is one such promising method in which a set amount of precursor is isolated and thus a single nanoparticle product can be formed. By forming a single product, one is able to overcome the differences in reduction potentials, thermal decomposition temperatures, and growth kinetics through spatial constraints. While one precursor may nucleate first, the second precursor will heterogeneously nucleate onto the first particle. In cases where multiple nucleation events occur, due to the close proximity of the nuclei in the nanoreactor, given enough time, they will eventually aggregate together and form a single product.

One of the first instances of nanoreactors being used for nanoparticle synthesis was in 1991, where Mann et al. utilized a protein cage to isolate the synthesis of iron sulfide and manganese oxide nanoparticles.<sup>64</sup> This was then followed by the use of synthesized block copolymers specially designed to form micelles of controlled size to directly control the size of nanoparticles both in solution<sup>65-68</sup> and on a substrate<sup>69-72</sup> (Figure 1.7 A). Alternatively, single molecule nanoreactors were also used in the form of dendrimers with metal ion coordination groups templated within the dendrimer<sup>73-75</sup> (Figure 1.7 B). While these methods of molecular nanoreactors demonstrated the power of nanoreactors, they still required extensive optimization for each new system. Furthermore, bio-inspired nanoreactors are limited to molecules present in nature that are

stable under the nanoparticle formation conditions, and block copolymer micelles and dendrimers require new molecules for each combination of precursors to overcome metal coordination competition.

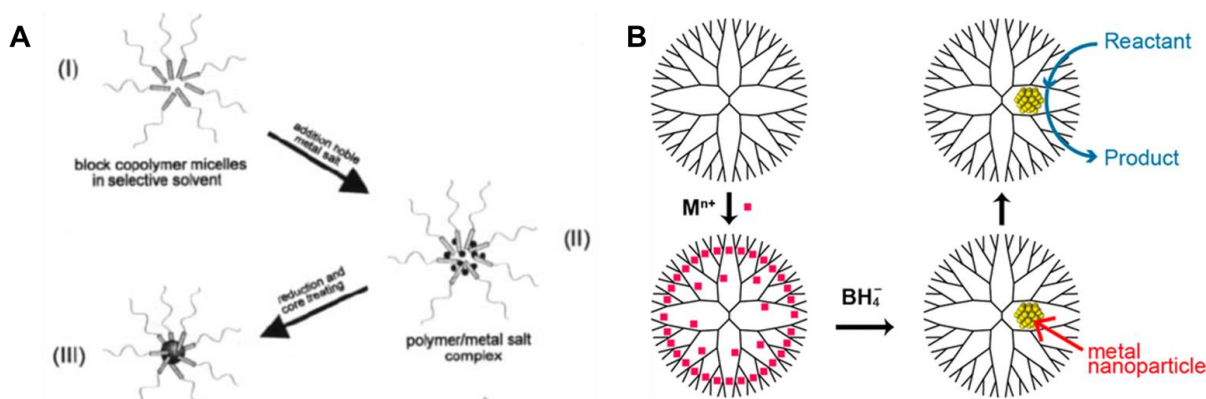


**Figure 1.7:** Molecular nanoreactors were the first methods used to isolate a small quantity of metal precursors to allow the synthesis of a single nanoparticle. While this was first achieved using templated proteins, it was expanded through the use of (A) block copolymer micelles and (B) single molecule dendrimers. Figure adapted from references (A)<sup>69</sup> and (B).<sup>75</sup>

The use of templated nanoreactors provided a breakthrough by addressing most of the limitations of the previously described molecular defined nanoreactors. Using either naturally mesoporous films,<sup>76-78</sup> selectively patterned substrates,<sup>79, 80</sup> or droplet-based microfluidics,<sup>81-83</sup> nanoreactors could be formed regardless of their contents, greatly increasing the flexibility of the syntheses. In this thesis, a particularly powerful nanoreactor technique, scanning probe block copolymer lithography (SPBCL), is presented (Figure 1.8).<sup>84</sup> Using a nanopatterning technique known as dip-pen nanolithography<sup>85</sup> (DPN), an AFM cantilever can be used to deposit extremely small volumes of a solution onto a substrate. When a hydrophobic surface is used, isolated



nanodomains containing similar metal ion coordinated block copolymers to those used in micelle nanoreactors are formed. Due to the site isolation of each nanoreactor, this technique has been used to study the formation of nanoparticles in nanoreactors.<sup>86-88</sup> By using a composition independent lithography technique, these nanoreactors have been used to synthesize complex nanoparticles from 2 to >50 nm in size<sup>89</sup> over a wide range of metallic<sup>90-92</sup> and oxide<sup>93</sup> compositions and comprised of up to 7 different elements.<sup>94</sup> This synthesis technique can then be scaled up to deposit millions of nanoreactors in parallel across cm<sup>2</sup> areas using polymer pen lithography (PPL)<sup>95</sup> (Figure 1.9) PPL is a cantilever-free patterning platform that uses massive arrays of polydimethylsiloxane (PDMS) pyramidal pens and xyz-piezo scanners move and deposit the nanoreactors in unison.



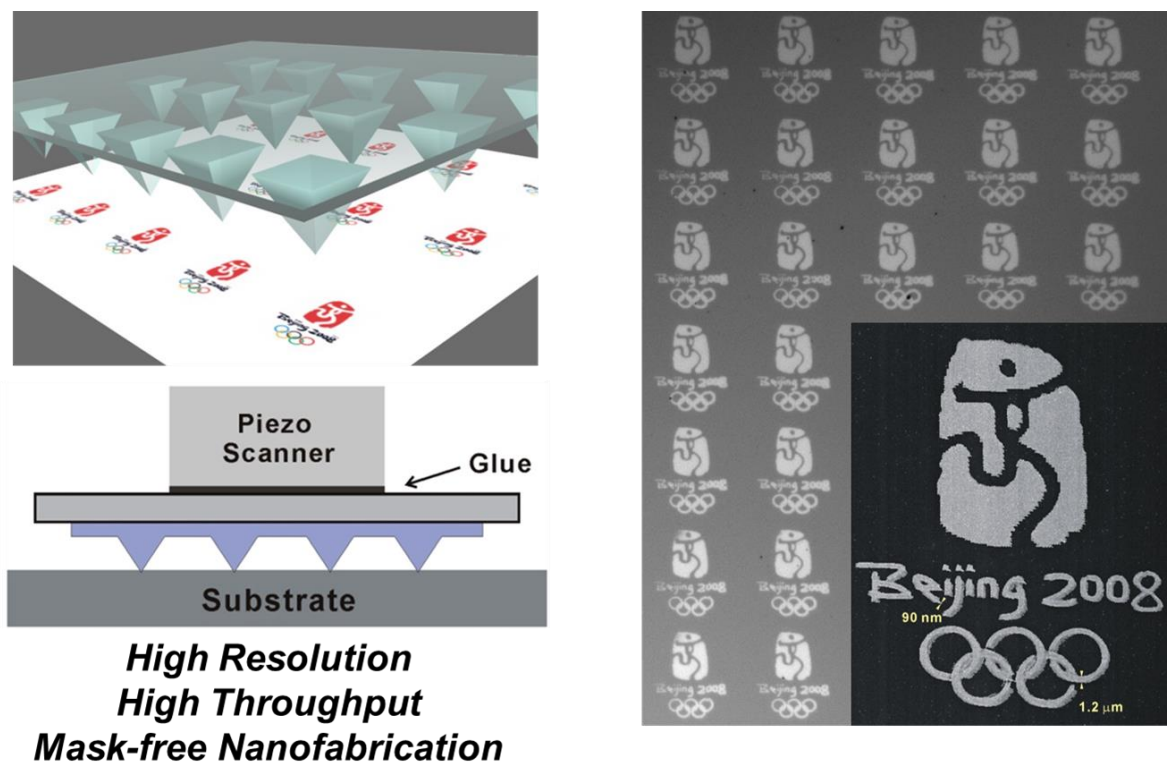


**Figure 1.9:** Polymer pen lithography (PPL) is a tip-based lithography that uses thousands of polymer pyramids to deposit material onto a surface in unison. PPL, combined with SPBCL, allows for large areas of multimetallic nanoparticles to be synthesized on a single substrate. Figure adapted from reference.<sup>95</sup>

### 1.3 Nanomaterial Screening Platforms

Ultimately, for any new material to be useful, synthesizing them is only half of the battle. Characterizing these massive phase spaces is equally important. Many methods of high throughput screening of nanomaterials have been modeled after those performed in the biological realm, such as universal peptide synthesis<sup>96</sup> or combinatorial drug discovery.<sup>97</sup> Similar to biological assays, there are two methods of characterizing material properties: directly and indirectly. Direct

measurements are used when the property in question is directly accessible by a characterization technique, such as electrical probes<sup>32</sup> or laser X-ray fluorescence and diffraction.<sup>35,36</sup> For catalytic applications, electrochemistry is the most promising candidate for high throughput screening due to the direct measurement of current as an indicator of catalytic activity, either through scanning electrochemical microscopy<sup>98</sup> or array reactors.<sup>99,100</sup> These direct measurements are useful in their ability to definitively measure the material's properties but are often limited in throughput due to their serial nature, though rapid assessments methods have been used to increase their efficiency.<sup>101,102</sup> Indirect measurements are used when a signal from the property in question is not easily directly measurable by any characterization method. One of the most common indirect measurements is the use of fluorescent dyes that are sensitive to a change in the system caused by the property of interest. In electrochemistry, one common example is the use of pH sensitive dyes (Figure 1.10), such as quinine,<sup>103-105</sup> which elicit a change in the optical signal as a function of pH and thus can be used to indirectly determine catalytic activity.<sup>106</sup> Another common example is the production of gas bubbles from water splitting which can also indirectly measure catalytic activity in parallel.<sup>107</sup>



preventing new reactants from binding. Alternatively, with the massive data sets being produced through high throughput experimental screening, future experiments are now being directed by through the implementation of machine learning.<sup>113-116</sup> For the highest rate of materials discovery to be truly reached, computational methods need to be paired with equally high throughput experimental synthesis and characterization methods.

#### 1.4 Scope of Thesis

This dissertation outlines a new high throughput nanomaterial synthesis method aimed to increase the rate of multimetallic nanoparticle materials discovery. The ability to synthesis precisely controlled nanoparticles across large areas and phase spaces in parallel and subsequently characterize them is crucial to driving the field of nanomaterials forward. The study of this platform, both of its fabrication and of the resulting properties found, are significant advancements in the field of nanomaterials discovery.

Chapter 2 reports the fabrication of massive nanoparticle libraries using SPBCL and PPL to deposit attoliter volume nanoreactors onto multiple substrates. Developing methods to deposit controlled quantities and compositionally defined nanoreactors opened the ability the synthesize millions of nanoparticles on a single substrate with their size and composition spatially encoded for subsequent characterization. Chapter 3 reports these nanoparticle libraries being utilized for their ability to catalyze the growth of single walled carbon nanotubes (SWNTs). Using a high throughput screening platform, the autonomous research system (ARES), laser induced heating of thermally isolated micropillars containing the deposited catalysts was leveraged to screen nanoparticle catalysts at a higher resolution than previously reported in literature. This work resulted in the discovery of a new catalysts, Au<sub>3</sub>Cu, not previously found in literature for this

application. Chapter 4 reports the use of customized reactors for the reliable screening of isolated sections of these nanoparticle arrays for heterogeneous catalysis. By creating multiple wells across the patterned substrates, each section can be individually accessed for its ability to perform both heterogeneous and electrocatalytic activity. Chapter 5 reports the fabrication of a novel substrate for the study of multimetallic nanoparticles on mirrors for optical characterization. These mirror substrates were designed to undergo the harsh conditions needed for the nanoparticle synthesis while maintaining their well-defined structure. Using a mirror substrate, the signal from a single nanoparticle was increased by an order of magnitude and the first multimetallic nanoparticle-on-mirror was studied.

This dissertation significantly increased the rate of material fabrication, and analysis, through these complex nanomaterial libraries. By fabricating large arrays on single substrates, the vast phase space of multicomponent nanoparticles can be shrunk to a manageable size and characterized through the methods described. The platform presented herein represents important steps towards determining design rules for structure-function relationships of these extremely complex materials. Ultimately, this will lead to an enhanced understanding of the fundamental properties of these materials, driving future materials discovery.

**CHAPTER 2:**  
**FABRICATING NANOMATERIAL**  
**COMBINATORIAL MEGALIBRARIES**

This chapter is based, in part, on the research described in the following publications:

Hedrick, J.L.; Brown, K.A.; Kluender, E.J.; Cabezas, M.D.; Chen, P.-C.; Mirkin, C.A. “Hard Transparent Arrays for Polymer Pen Lithography” *ACS Nano* **2016**, 10, 3144-3148.

Kluender, E.J.; Hedrick, J.L.; Brown, K.A.; Rao, R.; Meckes, B.; Du, J.S.; Moreau, L.M.; Maruyama, B.; Mirkin, C.A. “Catalyst discovery through megalibraries of nanomaterials” *Proceedings of the National Academy of Sciences* **2019**, 116, 40-45.



## 2.1 Background

In much the same ways bulk scale alloys fundamentally changed the materials that humans use, multicomponent nanomaterials have had profound impacts with discovery of each new material. This has been true for both physical (magnetic<sup>117</sup> and plasmonic<sup>118</sup>), chemical (heterogenous catalysis<sup>119</sup> and electrochemical catalysis<sup>120</sup>), and hybrid (taking advantage of both physical and chemical properties, such as surface-enhanced Raman spectroscopy<sup>121</sup> and biological imaging<sup>122</sup>) applications. While each of these applications have shown great promise, discovery of new nanomaterials, especially those made up of more than two components, has proven to be an extremely arduous process. This is due to the extreme precision syntheses needed at the nanoscale, where nanometer, and even atomic, changes will greatly alter the materials properties. Additionally, the parameter space for multicomponent materials explodes exponentially when size is added to composition and structure.

Traditional metal nanoparticle synthesis has employed colloidal synthesis methods – reducing a metal salt through chemical reagents and nucleating small nanoparticles that continue to grow as more metal atoms are reduced, following the trends in a LaMer Plot.<sup>56</sup> These methods have proven extremely powerful to synthesize large quantities of monometallic or compositionally uniform nanoparticles. While there are some examples of homogenous multimetallic nanoparticles synthesized in solution, they often requiring multiple steps and optimization for each composition.<sup>58-60</sup> This is due to the difficulty in controlling reduction, nucleation, and growth of two different elements in a single solution because each metal salt has different reduction potentials and interface energies. These imbalances lead to a wide distribution of products, whereby one element will nucleate before the second or third element leading to some final

population of monometallic particles. This problem is exacerbated when the two elements are immiscible. Scanning probe block copolymer lithography (SPBCL)<sup>84</sup> is able to overcome this challenge by shrinking the reaction to a single attoliter-scale polymer nanoreactor, and allowing synthesis of a single product in each reactor, up to 7 elements.<sup>94</sup> The power of SPBCL is that this phenomenon occurs regardless of the elements in the nanoreactor, permitting synthesis of particles made up of immiscible elements, making it one of the most universal nanoparticle synthetic methods developed.

Benefits gained from using isolated nanoreactors are accompanied by the bottle neck of having to produce millions of individual nanoreactors. Initial SPBCL studies were performed using AFM probes<sup>85</sup> to deposit hundreds to thousands of nanoreactors on TEM grids for high resolution imaging to fully characterize the resulting nanoparticles. While this has been a valuable tool for the fundamental study of particle formation in the polymer nanoreactor, thousands of nanoparticles on a TEM grid do not lend themselves to high-throughput property characterization. To scale up to millions, and even billions, of nanoparticles, polymer pen lithography (PPL)<sup>95</sup> can be used to deposit nanoreactors across cm-scale substrates. PPL uses an elastomeric array of pyramidal pens that each act as an isolated probe to deposit nanoreactors onto a surface. By attaching this array to a three-axis xyz piezo motor, each of the pens are able to deposit hundreds to thousands of nanoreactors in parallel. In the past, these PPL arrays have been used similarly to the AFM probes and were only used as a method to increase the quantity of nanoparticles synthesized. In order to create a screening platform employing these techniques, the scale of PPL needs to be paired with the precision and universality of SPBCL.

For any combinatorial materials screening platform, fabrication of the library of materials in a controlled and reproducible manner is essential for the resulting hits from screening to be reliable. The closest screening platform to nanoparticles, in terms of material scale, has been thin films.<sup>32, 35, 36</sup> By using alloyed elemental sources, sequential deposition and annealing, or co-deposition, the composition of multicomponent thin films has been scaled to hundreds of compositions on a single sample. While these techniques were uniquely powerful in increasing the number of materials on a single substrate, they were still limited to 800  $\mu\text{m}$  x 800  $\mu\text{m}$  areas and did not achieve the scale of nanoparticles where new properties can arise. To reach nanoparticle scale, techniques developed in thin film deposition were translated to PPL and SPBCL using a novel spray coating method to load different block copolymer solutions, inks, onto each pen on the PPL array. This allows for the large-scale fabrication of multimetallic nanoparticles on a single substrate with composition and size spatially encoded. In addition to controlling the ink on each pen in the PPL array, to ensure that is the only variable changing, each pen needs to deposit ink in the same manor across cm-scale areas uniformly. In this chapter, the transformation of PPL into a uniform patterning method to fabricate combinatorial arrays of nanoparticles with size and composition spatially encoded will be established, allowing for the subsequent screening in later chapters.

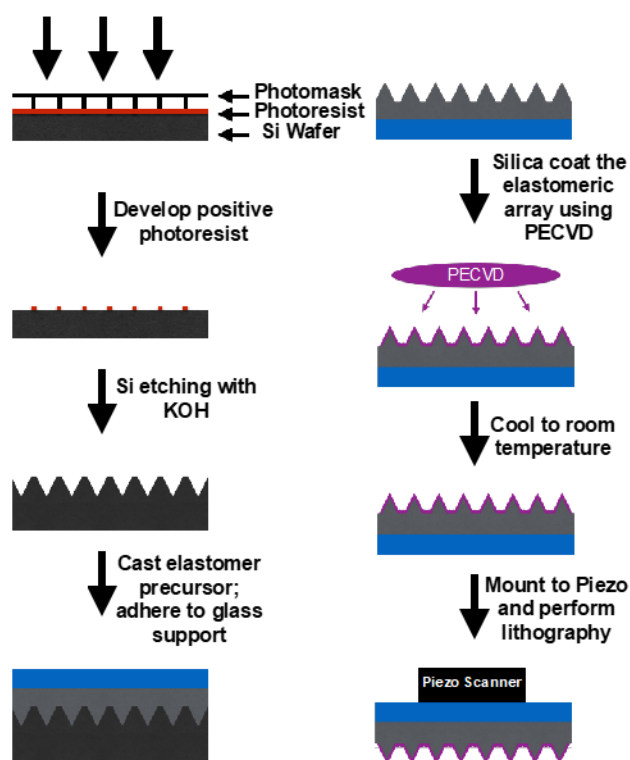
## 2.2 Results and Discussion

### 2.2.1 *Hard Transparent Arrays for Force Independent Uniform Features*

Polymer pen lithography (PPL) was invented specifically to address the challenge of depositing soft materials over large areas with nanoscale resolution.<sup>95, 123</sup> It is a cantilever-free scanning probe technique that uses an array of elastomeric pyramidal pens, connected to a transparent rigid glass slide with a thick elastomeric backing layer, to deposit nanoscale features in a massively parallel format across centimeter-scale areas. When each pen comes into contact with a surface, it deforms in two ways: pen deformation that increases the pen-sample contact area and backing-layer deformation that does not change the pen-sample contact area. While the increase of contact-area upon deformation is useful as a means to vary feature size,<sup>124-126</sup> it limits the minimum achievable feature size and uniformity across large areas. As a result, the minimum feature size achieved by PPL is larger than the smallest features written by its cantilever-based predecessor dip-pen nanolithography (DPN) by a factor of  $\sim 3$ .<sup>85, 127-133</sup> Additionally, PPL arrays are inconsistent and tend to have pen to pen height variations on the order of 1-2  $\mu\text{m}$  resulting in feature size variations between pens.<sup>127</sup> For PPL, there is nearly a 1:1 relationship between extension past first contact and feature size, so this effect can be quite significant when considering the desire to write uniform large scale arrays of sub-micron features.<sup>127, 134, 135</sup>

Interestingly, if the elastomeric pens are replaced with rigid silicon pens (while retaining the elastomeric backing layer), force-independent patterning is possible.<sup>136, 137</sup> This technique, known as hard-tip, soft-spring lithography (HSL), offers an 8  $\mu\text{m}$  range in extension over which the feature size does not change. The drawback to HSL is that making each pen array consumes a specialty 50- $\mu\text{m}$  thick Si wafer, in contrast to PPL which utilizes pen arrays that can be molded nearly

indefinitely from a single Si mold. Additionally, HSL pens are not transparent, which precludes their use for patterning with energy *via* optical methods.<sup>138, 139</sup> Other noteworthy attempts to improve resolution of PPL have relied on using pen arrays composed of other polymers or hard polymer pens on a soft elastomer support.<sup>140-142</sup> These approaches reduce the feature size dependence on force by at most  $\sim 1/4$ , but none have produced extension-independent patterning.



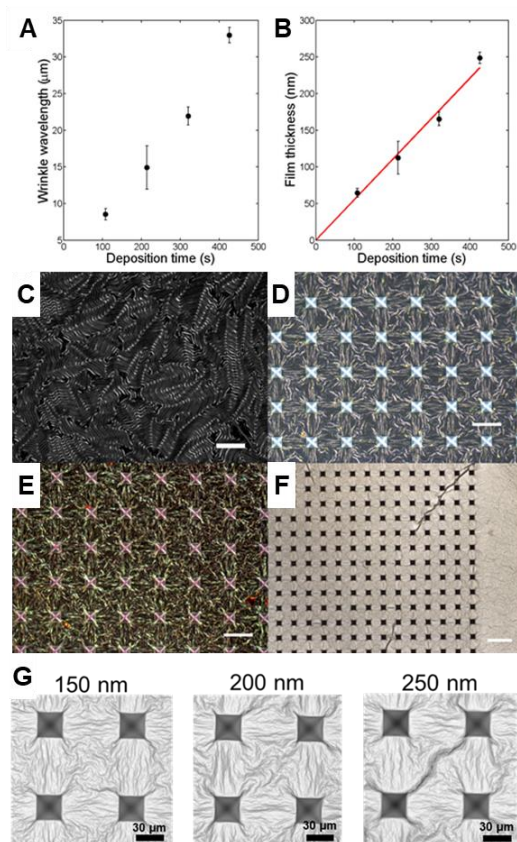
**Figure 2.1:** Schematic of the fabrication process for hard transparent polymer pen arrays.

Figure adapted from reference.<sup>143</sup>

Here, a new cantilever-free pen array architecture is presented that affords the ability to write with high resolution in an extension-independent manner using transparent pen arrays that are simple modifications of inexpensive PPL pen arrays. The central hypothesis of this work is that, by coating PPL pen arrays with a thin hard layer, the tip of each pyramid will retain its shape during patterning, and all strain due to pen-sample contact will be absorbed by the elastomeric backing layer (Figure 2.1). Specifically, coating PPL pen arrays composed of polydimethylsiloxane (PDMS) with silica using plasma-enhanced chemical vapor deposition (PECVD) was found to be an effective way to construct pen arrays capable of patterning small molecules and polymers at high resolution without dependence on pen-sample contact force.

In principle, the presence of a conformal hard layer could enable pen arrays to write in a consistently high-resolution and extension-independent manner. However, depositing a hard material on a soft material is challenging, often resulting in buckling<sup>144-146</sup> and delamination.<sup>147</sup> To address this problem, a low temperature PECVD process was developed to minimize the degree of thermal expansion that would lead to residual strain between the hard layer and the elastomeric pen array. Specifically, this deposition process was carried out at 200 °C using 900 mTorr with 500 sccm SH<sub>4</sub>, 1420 sccm O<sub>2</sub>, and 30 W of high frequency power. By performing spectroscopic ellipsometry of films grown on Si wafers, a growth rate of  $0.92 \pm 0.01$  nm/s was extracted with a refractive index of  $1.49 \pm 0.01$  at a wavelength of 630 nm, as expected for silica. While silica films grown on PDMS films could not be measured using ellipsometry due to the buckling pattern that emerged, this periodic buckling pattern itself was used to compute the film thickness (Figure 2.2 A,C).<sup>148</sup> By assuming that the modulus of the silica film is the same as bulk silica, the rate of deposition of silica on the PDMS surface was calculated to be  $0.55 \pm 0.03$  nm/s (Figure 2.2 B).

In order to determine the optimal thickness of silica that would allow for force-independent patterning, PPL pen arrays were coated with silica films of different thicknesses and subsequently evaluated for their morphology and behavior during pen-sample contact. When the thickness was less than 100 nm, the force on the pens during contact caused the thin silica layer to delaminate from the pen (Figure 2.2 E). In contrast, when the thickness was greater than 250 nm, the buckling effect was so great that it substantially deformed the pens and perturbed the uniformity of the pen array (Figure 2.2 F). Pen arrays with ~175 nm thick silica films were found to be optimal compromises that mitigated both these effects (Figure 2.2 D). While CVD-grown silica was found to be robust for patterning, it previously has been noted that exposing a PDMS film to an O<sub>2</sub> plasma forms a silica film on the surface of the PDMS.<sup>149</sup> This observation could explain the change in writing performance of PPL pen arrays following repeated exposure to O<sub>2</sub> plasma; however, this approach to depositing silica layers is impractically slow for generating robust hard layers. In addition to using PECVD methods of deposition, it was found that sequential deposition using electron beam physical vapor deposition (E-Beam PVD) could be used to fabricate these SiO<sub>2</sub> coated pen arrays. When using E-Beam PVD, a crucible of SiO<sub>2</sub> is exposed to an electron beam that sublimates the SiO<sub>2</sub> and deposits it onto a target. If the entire 175 nm of SiO<sub>2</sub> is deposited continuously in a single run, the pen array heats up resulting in significant bowing and subsequent buckling between pens. By depositing in ~25 nm increments, with sufficient time between depositions for the array to cool, these pen arrays could be fabricated using PVD (Figure 2.2 G).



**Figure 2.2:** (A) Wrinkle wavelength as a function of silica thickness. (B) Silica thickness as a function of deposition time (slope  $0.55 \pm 0.03$  nm/s). (C) Bright-field image of silica deposited onto a slab of PDMS, 200  $\mu\text{m}$  scale bar. (D) Dark-field image of hard transparent array when it is at the goldilocks thickness of 175 nm, 50  $\mu\text{m}$  scale bar. (E) Shattered hard transparent array pens after patterning when silica thickness is too thin at 83 nm, 50  $\mu\text{m}$  scale bar. (F) Bright-field image of hard transparent array when silica thickness is too large, here 250 nm, buckling goes through the pens, 100  $\mu\text{m}$  scale bar. (G) Optical images of SiO<sub>2</sub> films deposited on PDMS pen arrays using E-beam deposition. These trends agree with PECVD growth SiO<sub>2</sub>. Figure adapted from reference.<sup>143</sup>



In order to explore the force-dependent feature size of polymer arrays versus hard transparent arrays, 16-mercaptohexadecanoic acid (MHA) features were patterned onto gold whereby each pen wrote 25 individual dots in an array that varied in extension across the pattern with a constant dwell time. MHA was chosen because it is well-known to form monolayers on gold and has been patterned extensively by PPL and DPN.<sup>130</sup> Features written by polymer arrays were observed using atomic force microscopy (AFM) to be square with edge lengths that increase with extension (Figure 2.3 B,D). The square morphology originates from the deformation of the square pyramidal pens during patterning. In contrast, features written by hard transparent arrays were found to be independent of pen-sample force over a 5  $\mu\text{m}$  extension range (Figure 2.3 A). PPL performed with hard transparent arrays, similar to conventional DPN, generates circular features with dwell time-dependent diameters (diffusion-mediated).<sup>126</sup>

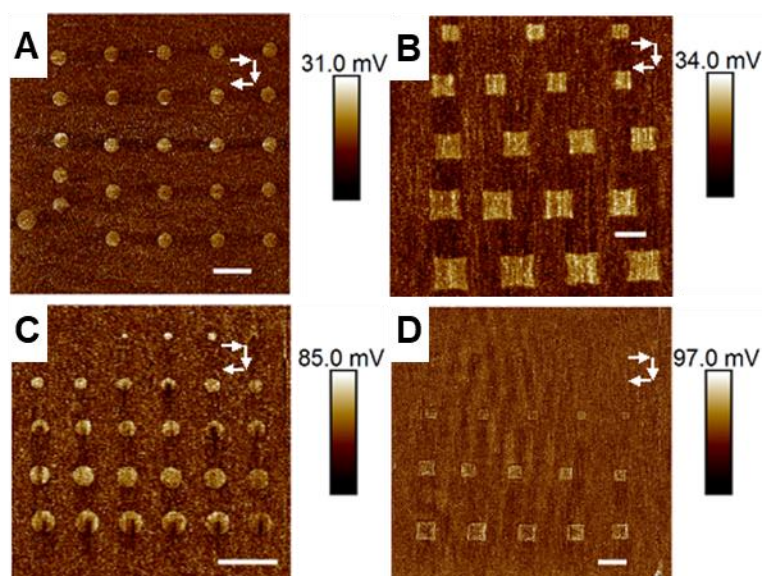


**Figure 2.3:** Patterning MHA using (A) a hard transparent array and (B) a polymer array, both with an extension sweep over 5  $\mu\text{m}$  piezo range with 100  $\mu\text{m/s}$  extension and withdraw speed and 5 second dwell time. Patterning MHA using (C) a hard transparent array and (D) a polymer array, both with an extension sweep covering 5  $\mu\text{m}$  piezo range with 1.5  $\mu\text{m/s}$  extension and withdraw speed and no dwell time at full extension., All scale bars are 2.5  $\mu\text{m}$ . Images were taken using lateral force microscopy using AFM. Figure adapted from reference.<sup>143</sup>

While force-independent patterning will allow for more consistent patterns, intentionally varying pen deformation allows one to pattern macroscopic gradients by tilting the pen array in relation to the patterning surface, which enables nanocombinatoric patterns with a gradient of features.<sup>124, 126, 150-152</sup> In order to retain this ability using hard transparent arrays, it was hypothesized that tilting the array and approaching the surface slowly would result in a positionally-dependent pen-sample contact time, providing a gradient of feature sizes as a result of an increase in diffusion time between the pen and substrate. To test this hypothesis, a patterning

experiment was performed in which extension was increased over a 5  $\mu\text{m}$  range with a 1.5  $\mu\text{m/s}$  approach and retraction speed. At most, this would result in a  $\sim 3$  s difference in pen-sample contact time for every micron difference in extension. Indeed, after patterning, MHA features ranging from 250 nm to 1  $\mu\text{m}$  in a smooth size gradient were observed (Figure 2.3 C). This is an important capability as it allows one to contemplate constructing nanocombinatoric arrays for experiments with PPL arrays coated with silica by making gradients of feature sizes.<sup>124, 153</sup>

To test these arrays for scanning probe block copolymer lithography (SPBCL), polymer arrays and hard transparent arrays were used to pattern a square dot array with an extension that varied over 5  $\mu\text{m}$  after being inked with a 5 mg/mL solution of the block copolymer poly(ethylene oxide)-*b*-poly(2-vinyl pyridine) (PEO-*b*-P2VP,  $M_n=2.8\text{-}1.5$  kg $\cdot\text{mol}^{-1}$ ) in water. The approach speed was 100  $\mu\text{m/s}$ , which indicates that varying extension over a 5  $\mu\text{m}$  range had a negligible effect on pen-sample contact time. Following patterning, AFM imaging revealed that features written by conventional polymer arrays exhibited a large square contact area while those written by hard transparent arrays had small round contact areas that were independent of extension (Figure 2.4 A,C). Furthermore, as with patterning alkanethiols on gold, it was possible to vary the feature size of polymers by changing approach speed. Specifically the pen extension was varied by 4.2  $\mu\text{m}$  while writing a dot array with an approach speed of 3  $\mu\text{m/s}$ , resulting in gradients of feature sizes from 40 to 160 nm (Figure 2.4 B,C).

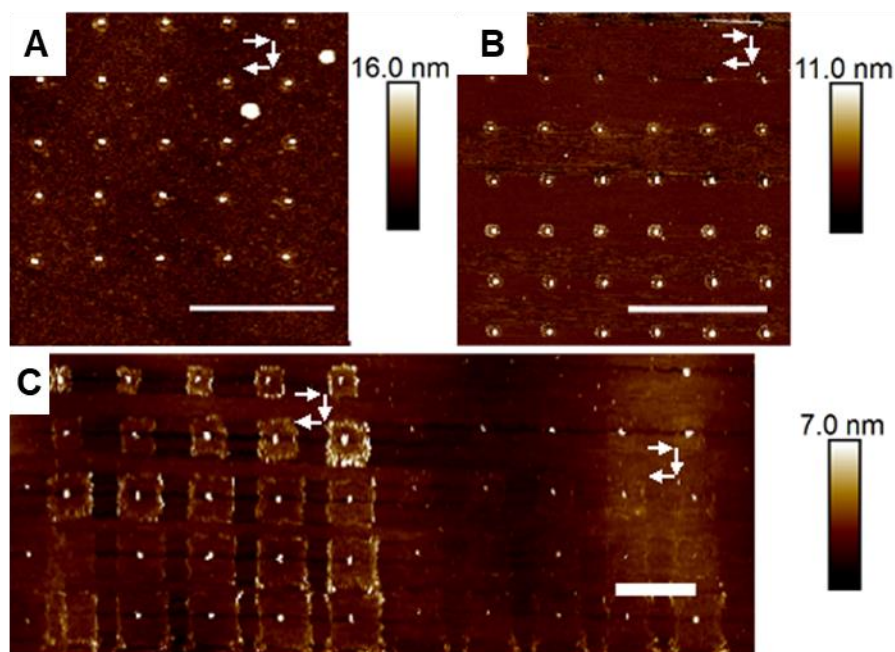


**Figure 2.4:** Patterning polymer ink with an (A) extension sweep over 5  $\mu\text{m}$  piezo range with 100  $\mu\text{m}/\text{s}$  extension and withdraw speed using hard transparent arrays and a dwell time of 2.5 s at full extension, (B) hard transparent arrays extension sweep over 4.2  $\mu\text{m}$  piezo range with 3  $\mu\text{m}$  extension and withdraw with no dwell time at full extension, and (C) PPL extension sweep over 5  $\mu\text{m}$  piezo range with the left half corresponding to the conditions in (D) and the right half corresponding to (B). Scale bars are 2.5  $\mu\text{m}$ . Images were taken with AFM in tapping mode.

Figure adapted from reference.<sup>143</sup>

One major, and previously undiscussed, problem associated with pen deformation is that it can limit feature pitch. While small molecules that covalently bind to the patterning surface are robust after patterning, large molecules that physically adsorb to a surface, such as PEO-*b*-P2VP, can be disturbed after patterning because they behave as fluids in the high-humidity environment needed for patterning.<sup>154, 155</sup> Because of this, if the pen-sample contact diameter is on the order of the feature pitch, the pen will absorb neighboring features when patterning each feature. With polymer arrays, this manifests as a row of features merging into a single large feature. This is mitigated with hard transparent arrays due to the lack of pen deformation. Specifically, by patterning PEO-*b*-P2VP, hard transparent arrays yielded feature pitches of 175 nm with a hexagonal array (Figure 2.5 A,B). By switching from a square pattern array to hexagonal pattern array, feature density was further increased by ~15%. The capability of patterning smaller pitches indicates that it is possible to pattern extraordinary numbers of features. Specifically, by patterning 14,641 polymer dots with each of the four hundred thousand pens in a 14.5 cm<sup>2</sup> array, it was possible to generate a total of 5.9 billion polymer dot features (Figure 2.5 C,D).

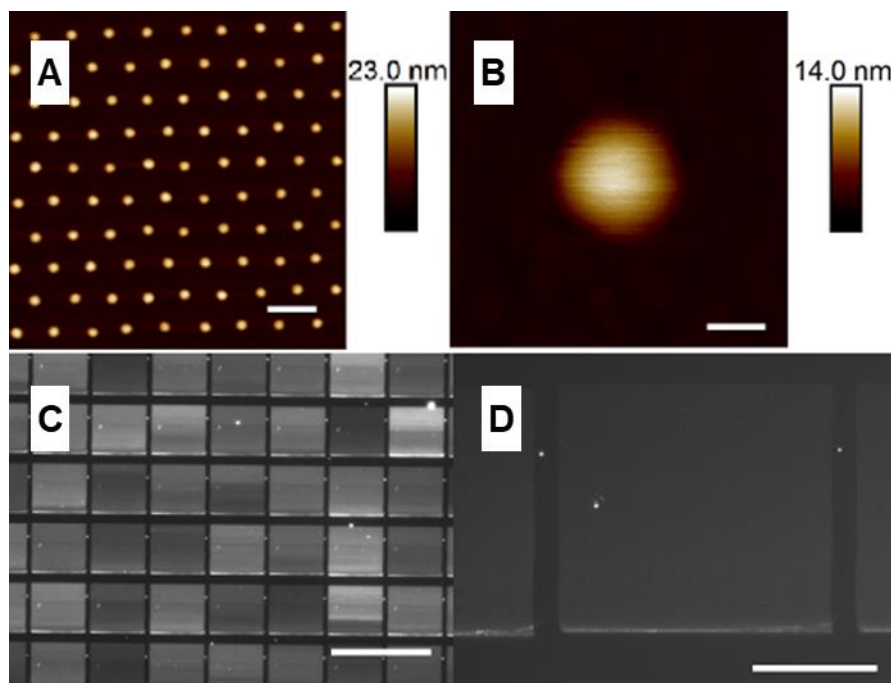


**Figure 2.5:** (A) AFM of a dot array with a 175 nm pitch in a hexagonal pattern array written using hard transparent array, 150 nm scale bar. (B) Single polymer feature with a circle of small droplets from original meniscus, 20 nm scale bar. (C) Dark-field optical microscopy of array with 500 nm pitch written using hard transparent array with PPL with 14,641 features written per pen, 100  $\mu\text{m}$  scale bar, and (D) zoomed in image pattern made from a single pyramidal pen, 25  $\mu\text{m}$  scale bar. Figure adapted from reference.<sup>143</sup>

In this work, it is shown that the use of hard transparent arrays allows one to write higher density and more reliable patterns than are possible using traditional polymer pen arrays. While this silica coating was found to render patterning of polymers and small molecules to be force-independent, it also enabled a method of writing gradients with force-independent probes. Importantly, hard transparent arrays are a simple post-modification of polymer pen arrays,

indicating that the barrier to adoption is extremely modest. When combined with a technique like SPBCL,<sup>84, 156</sup> one can create high-density nanoparticle arrays for the investigation of nanoparticle properties such as plasmonics, nanomagnetism, and catalysis.<sup>90, 91, 157</sup> Ultimately, the ability to directly write billions of discrete uniform features on a surface is a significant advance for nanolithography and has opened avenues for using cantilever-free scanning probe lithography as a combinatorial discovery tool.

### ***2.2.2 Blade Coating PDMS Pen Arrays for Large Area Patterning***

For the patterning of combinatorial libraries of nanoparticles, pen arrays that uniformly pattern over large areas are required. While MHA patterning has traditionally been used to show the ability of PPL to pattern over large areas, when patterning polymer inks, the force of interaction between the pen and the substrate needs to be controlled to a greater extent to ensure identical patterning between pens. This is due to the different ink deposition methods. MHA, similar to other thiols on gold surfaces, deposits by forming a self-assembled monolayer (SAM) through molecular transport.<sup>158, 159</sup> Functionally, this means that as long as the pen is in contact with the substrate and is coated with ink, a SAM feature will be deposited. For the deposition of aqueous polymer inks that are used in SPBCL, the force, retraction speed, pen-ink and surface-ink interactions all play significant roles, and a polymer feature is only deposited if the capillary bridge is ruptured.<sup>154, 159</sup> This requires the meniscus between the pen and the substrate to be controlled for every pen and for the meniscus to be broken at the same point. If the meniscus is broken sooner, the feature will be larger. If it is broken later, more ink will have returned to the pen, resulting in a smaller feature. Adequate control is relatively easy on the pen-to-pen scale, and  $\sim 1 \mu\text{m}$  differences from pen height variations do not significantly alter the features that form and can predominantly be overcome by

hard transparent coatings. Where the meniscus formation and rupturing can begin to play a more significant role is when pen arrays are larger than 1x1 cm and contain hundreds of thousands to millions of pens. Consider this simple calculation. For a perfectly flat 2x2 cm plane to be within 1  $\mu\text{m}$  of parallel to another perfectly flat 2x2 cm plane, there is  $0.002^\circ$  alignment range of freedom. When patterning over these large areas, if there is an angle greater than  $0.002^\circ$  between the substrate and the pen array, there will be size differences in the resulting features. Importantly, this calculation also assumes a perfectly flat pen array backing layer.

When fabricating PPL arrays, a PDMS elastomer is thermally cured between a glass slide and a selectively etched hydrophobic Si master that is a negative image of the pyramidal pens.<sup>134</sup> After the PDMS is fully cured, the pen array can be peeled out of the hydrophobic Si master, as the PDMS covalently bonds to the Si-OH groups on the glass slide. Traditionally, the Mirkin group has used a rigid PDMS (h-PDMS) formulation that retains sub-100 nm features when removed from Si masters.<sup>142</sup> This formulation is able to reliably cure pen arrays that are up to 2x2 cm in scale. When patterning 2x2 cm areas, it is essential to use a pen array that is at least 1-2 cm larger than the patterning area due to edge effects of the pen array.

Due to the larger size arrays needed for large area patterning, softer PDMS formulations are needed. Specifically, Sylgard 184 (s-PDMS) was used. When changing to this softer elastomer and increasing the pen array size, a bowing effect was observed. This bowing presents itself during patterning in the center of the array coming into contact with the substrate before any of the edges, indicating that it was not due to misalignment (Figure 2.6). Because the pens in the center contact the surface more than 2  $\mu\text{m}$  before the edge pens, inconsistent patterning resulted. This bowing contributed to a change in the PDMS backing layer after the array was removed from the master,



resulting in a rounded pen array instead of a flat plane of pens. It was hypothesized that this bowing must be due to a relaxation of forces that were created during the curing process while the PDMS was between the glass slide and the Si master. These forces were not great enough to bow smaller arrays made out of h-PDMS due to the smaller area and higher Young's Modulus of the h-PDMS. The force that is hypothesized to be causing the bowing is the internal stress caused by the crosslinking and cooling of the PDMS.<sup>160, 161</sup> While these stresses are locally isotropic, the geometry of the pen arrays leads to anisotropic effects. The dimensions of a 100  $\mu\text{m}$  array on a 2x2 in glass slide, which is used for 4x4 cm pen arrays, is 50.8x50.8x0.1 mm, leading to a 500:1 stress imbalance. Additionally, once the array is removed from the Si master, the relaxation of the internal stresses is also anisotropic because it is pinned on the glass slide. This leads the PDMS backing layer to relax, pulling volume from the edges of the array towards the middle, pushing out the center of the array.

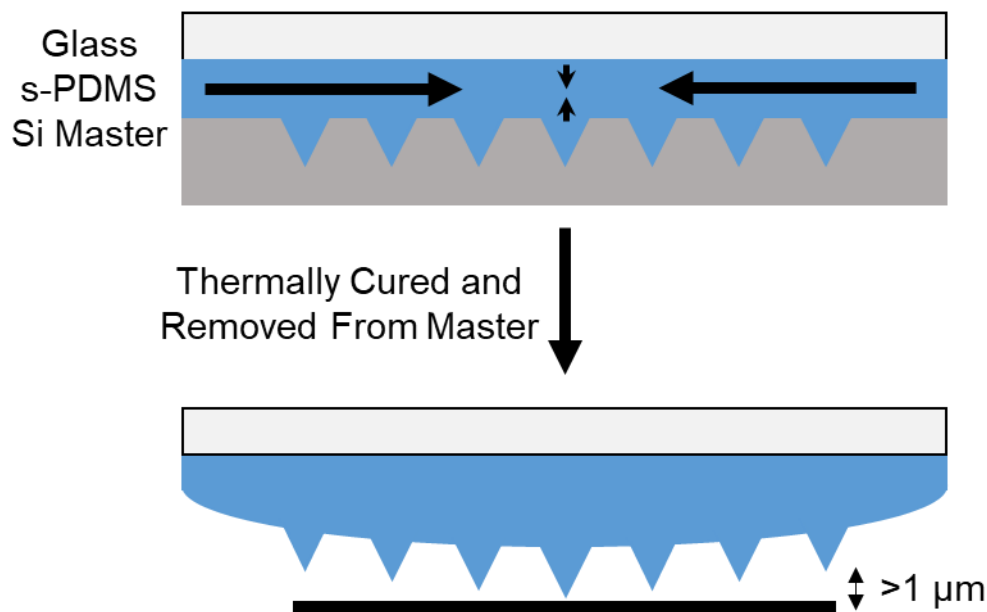


**Figure 2.6:** Schematic of pen array bowing that occurs when large area pens are made of s-PDMS.

To prevent the stress relaxation from bowing the pen arrays, it was hypothesized that if the PDMS was fully cured without the glass slide present before being attached to the glass slide, once removed from the Si master, the pen array would retain its flat plane geometry. In order to fabricate uniform layers of PDMS to cure prior to glass slide attachment, a blade coating method was developed. By using guard rails on either side of the pen array area of the Si master, a razor blade could be brought across the Si master, creating a film of uniform and controlled thickness (Figure 2.7 A). Additional pinpoints were added on either side of the pen array area to ensure the PDMS film did not retract into the pen array. If these were not present, due to the hydrophobic nature of the Si master, the PDMS would retract from the edges of the wafer and lead to thicker sections at the edges and the film uniformity would be lost. This PDMS film would then be fully cured without

a glass slide present. By curing each layer individually, the PDMS backing layer could be made thick enough (<400  $\mu\text{m}$  up to 1 mm) that the bowing would no longer occur with s-PDMS over these larger areas. h-PDMS was also able to be cured over these larger areas in thin films without the presence of a glass slide. This process could be repeated multiple times with different formulations of PDMS, allowing for the fabrication of multilayered PDMS arrays. Similar to previous work with photocurable elastomers,<sup>140</sup> resulting pen arrays have the joint advantages of both h-PDMS (pen rigidity and limited pen deformation) and s-PDMS (soft backing layer for increased backing layer deformation) (Figure 2.7 B). To fabricate these arrays, an s-PDMS-h-PDMS-s-PDMS array was made. By performing profilometry measurements, it was found that the bowing was almost entirely removed through this blade coating method (Figure 2.8). Through hard transparent pen arrays made using this blade coating method, reliable large area pen arrays were fabricated for combinatorial library fabrication.

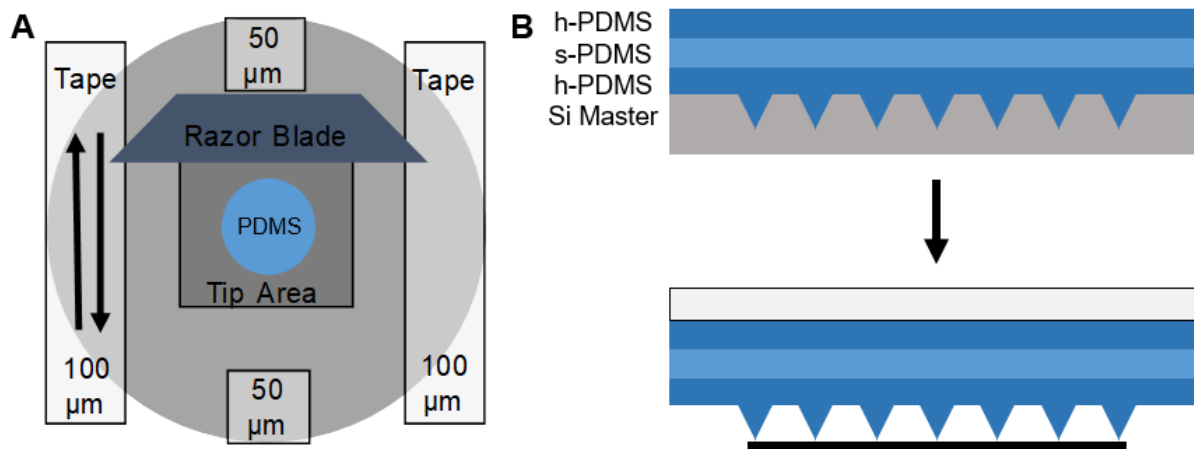


**Figure 2.7:** (A) Schematic of blade coating technique. Scotch tape (50-70 μm thick) was used as guard rails to control layer thickness, and to pin the film at each edge of the wafer. Multiple blade coating and curing steps were sequentially performed to create multilayered pen arrays. (B) Schematic of blade coated arrays. By curing each layer without the glass slide present, the internal stresses were able to relax before the glass slide was attached.

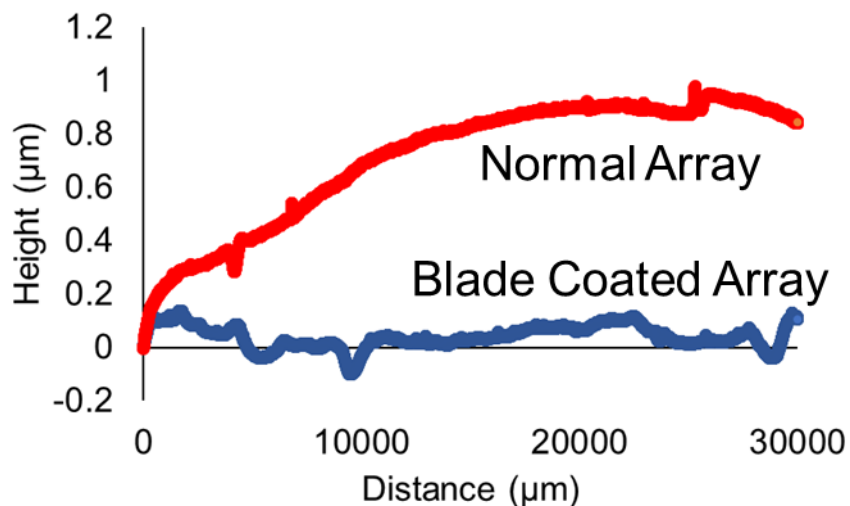


**Figure 2.8:** Profilometry measurements of PDMS pen arrays from the same Si master. The normal array was fabricated in one curing step of s-PDMS. The blade coated array was made in three curing steps out of s-PDMS, h-PDMS, and attached to a glass slide with s-PDMS.

### 2.2.3 Sequential Inking of Multiple Wells on PPL Array

Using SPBCL and PPL techniques, massive arrays of multimetallic nanoparticles can be deposited in an ordered pattern on a single surface. PEO-*b*-P2VP ink solutions with different metal salt precursors can be spin coated, drop cast, or spray coated onto a PPL array. The composition of the ink on each pen directly correlates to the composition of the ink in the nanoreactors that particular pen patterns on the surface, which in turn directly controls the composition of the final nanoparticle that is formed in each nanoreactor.<sup>91</sup> Due to the direct correlation of the final particle's composition, if the ink on each individual pen in an array is controlled, massive libraries of compositionally controlled nanoparticles could be deposited on a single substrate. Previous methods have been developed using ink jet printing and a Si mold of wells, where a PPL array

dips each pen into a well to ink the array before patterning.<sup>151</sup> While this method was able to ink 1600 wells, and consequently ink 1600 pens, it was limited to 3 different ink compositions. This technique is fundamentally limited in throughput due to the requirement of inkjet printing ink solutions into each well. In order to fully realize the power of PPL and SPBCL, the inking of each pen needs to be controlled over cm-scale areas regardless of the density of the pens in the array.

To scale up the inking procedure to larger pen arrays, a drop casting method with segregated wells was developed. This method uses 3D printed wells (made of acrylonitrile butadiene styrene, ABS) to segregate the pen array into 9 different sections, taking advantage of the elastomeric PDMS to form a seal between each well (Figure 2.9). By compressing the wells into the PPL array, a different ink solution can be drop cast into each well and allowed to dry. In order to allow a uniform wetting across the entire well, more ink was required than traditional inking methods and dilute PEO-b-P2VP ink (1-2 mg/ml compared to the standard 5 mg/ml) was used to prevent excess ink loading. By creating a seal between each well, there was no leakage between the wells, and the composition of each well's ink was maintained during drying of the ink. After the ink was dried, the wells were removed, and the array was used to pattern onto a hexamethyldisilazane (HMDS) treated SiO<sub>2</sub> substrate. Resulting patterns match perfectly with the inked pen arrays with a 4 pen (600 μm) gap present between each well (Figure 2.10). While this method destroys the pens that were under each well, it does allow for each composition to be completely segregated for later screening. Using this inking technique, the number of different ink compositions on a single array was increased by three-fold compared to ink jet deposition methods.



**Figure 2.9:** Photographs of 3D printed 3x3 wells sealed with PPL array. Clamps were used to compress the wells into the elastomeric PDMS to for a seal between each well.

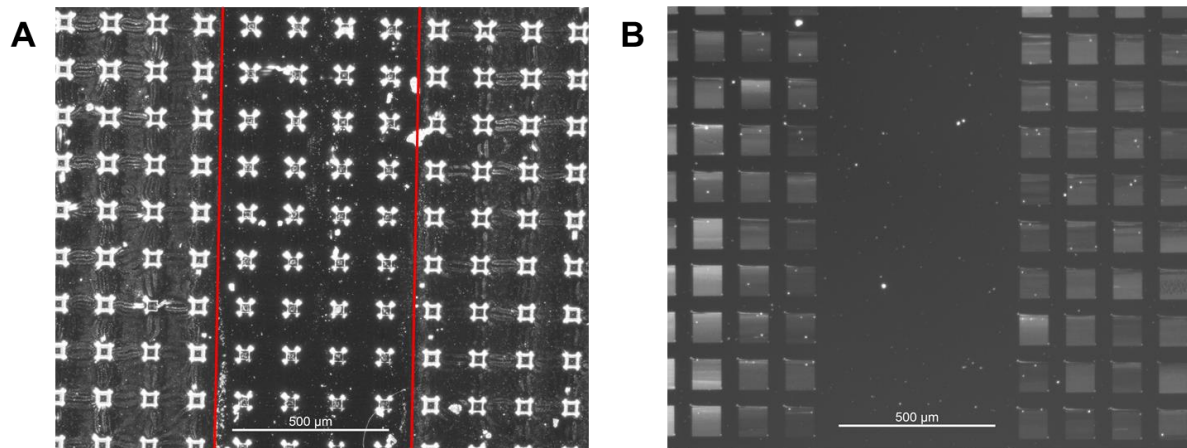


**Figure 2.10:** Dark field optical images of (A) inked pen array and (B) the resulting polymer dome patterns on a  $\text{SiO}_2$  substrate. The red line indicates the edge of the well wall.

While using compression sealed wells and drop casting was sufficient for these 3x3 well designs, as the well size becomes smaller (below 5x5 mm), drop casting is no longer a viable method. When ink is drop cast into the well, it forms a meniscus between the well walls, which leads to a larger quantity of ink near the wall compared to the center of the well. On larger wells, the variation in the inking of the pens is much less pronounced as the meniscus is able to slowly drop down as the ink dries. For smaller wells, the ink dries too quickly, and as a result, the pens on the edge of the well have significantly more ink per pen, which leads to a variation in the polymer dome size throughout the well when patterned. In order to ink a single pen array with more than 9 inks, a sequential spray coating method was introduced. Using an air brush with a 0.15 mm needle, small volumes (as low as 50  $\mu$ l) of a PEO-*b*-P2VP aqueous solution can be sprayed on a pen array. While the air brush's overall spray profile resembles a Gaussian distribution of ink, if the pen array is far enough away, there is a region in the center of the profile that can be treated as a fixed constant quantity at the peak of that Gaussian. The center of the spray profile was marked by a cross to ensure that the exposed section could be aligned to the center of the Gaussian distribution (Figure 2.11 A). To selectively spray different inks onto different sections of the pen array, five different masks (one for the entire array and four to select which section is exposed (Figure 2.11 B)) were 3D printed out of ABS to selectively cover all but 1 of the 16 sections at a time. Each section of the array can then be individually sprayed with a different ink, resulting in a pen array with 16 different compositions of ink. Using this inking technique, a blade coated pen array with a hard gold coating (Au/s-PDMS/h-PDMS/s-PDMS/glass slide) was inked with 15 different inks, leaving one section blank as a control (Figure 2.11 C). This pen array was then used to pattern arrays of polymer domes on a HMDS treated conductive Si substrate. The



resulting patterns were uniform across the entire array (Figure 2.12), indicating a uniform quantity of ink on each section of the pen array. Using this method, the number of different inks that can be loaded on a single array has now been increased by more than a factor of five compared to ink jet methods. Additionally, the only limitation to the size of each section, and therefore the number of sections that there can be on one pen array, is the quality of the mask. Due to 3D printing limitations, the walls between each section were required to be 1 mm thick, leading to the decision to use a 4x4 array of 3x3 mm wells for a 1.5x1.5 cm array. If these masks were machined out of metal, each well could, in theory, be less than 1x1 mm, with 0.5 mm walls, resulting in up to 100 different inks on each pen array.

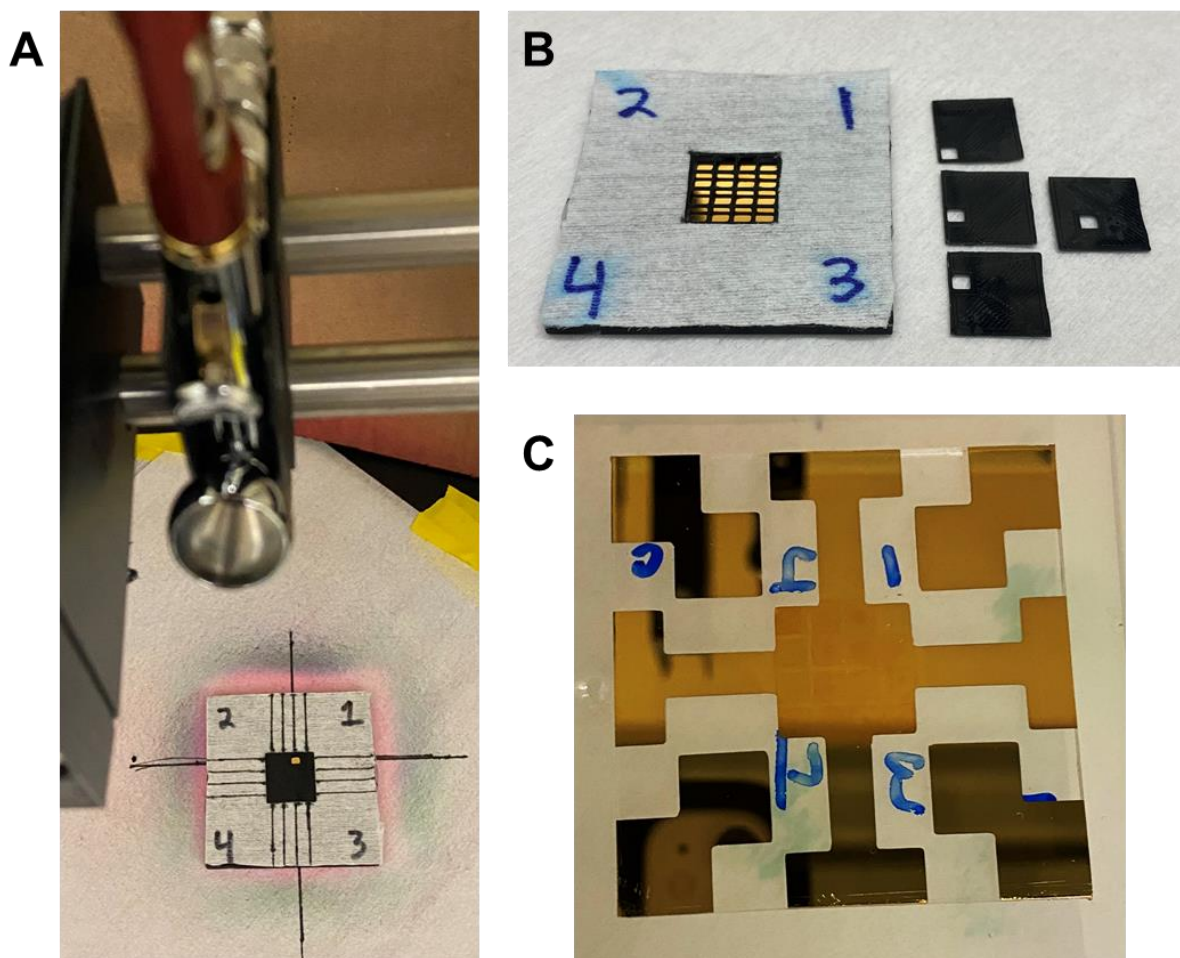


**Figure 2.11:** (A) Photograph of the spray system set up. The center of the spray profile is aligned with the exposed section of the pen array. (B) Photograph of the masks used to expose selected sections of the pen array. The large mask is covered with an absorbent material to prevent excess ink from contaminating the pen array. Each of the smaller masks are used to expose four different sections depending on their orientation. (C) Photograph of pen array sprayed with 15 different inks (the top right section was left blank as a control).

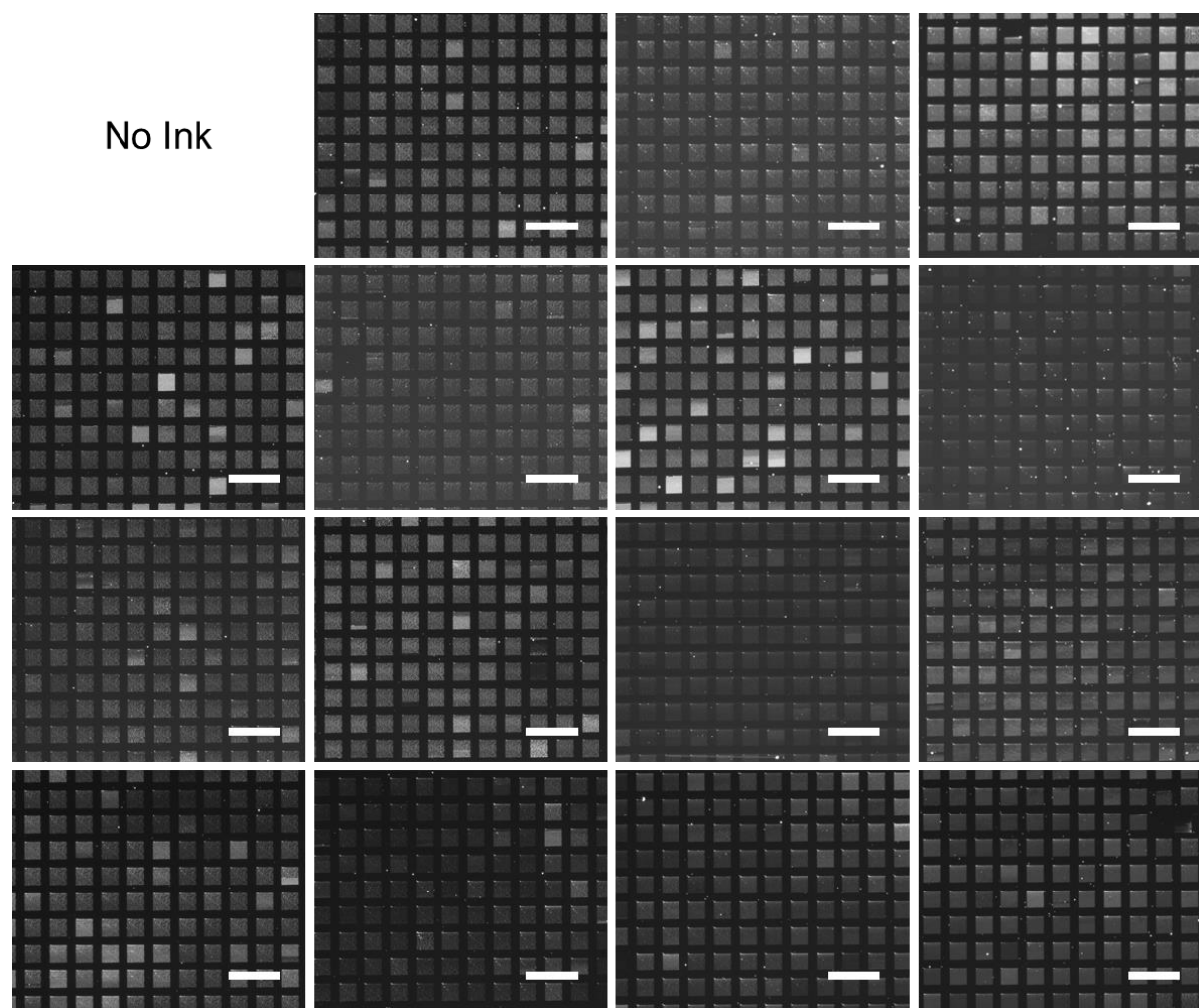


**Figure 2.12:** Dark field optical images of polymer dome arrays patterned on HMDS treated conductive Si by a sequentially spray coated pen array. Each image is from a different sprayed section of the pen array. All scale bars are 300  $\mu\text{m}$ .

#### ***2.2.4 Spray Coating Pen Arrays for Continuous Composition and Size Gradients***

When looking at thin film screening platforms, the highest rate of materials discovery in terms of compositional screening is achieved using gradients made through sputtering co-deposition.<sup>162-164</sup> To translate this method to SPBCL and PPL, an analogous system to sputter co-deposition is air brush spray coating. Both produce Gaussian deposition profiles that can be altered by varying deposition/spray rate and distance between the source and target. In order to explore the combination of PPL with pen array spray-coating as a method for generating combinatorial libraries, the radial distribution of ink deposition was evaluated by performing a spray-coating operation on a target substrate held at various distances from the nozzle. Quantitative evaluation of this distribution was done by imaging the substrate and examining the intensity of the image in a line across the center of the image (Figure 2.13 B). When the intensity profile was fit to a Gaussian function, there was a nearly linear section from 0.15 to 0.85 of normalized intensity. The full width half max (FWHM) of radial spray distribution increased proportionally to the air brush-sample separation distance in a manner such that the FWHM was 0.27 times the separation, which illustrates that this coating method could be readily adjusted to accommodate any array size (Figure 2.13 C). From this, adjustment of the air brush distance and placement can be systematically accomplished based on the array size. To increase capabilities, a second air brush was utilized to create overlapping profiles that result in a combinatorial gradient that can be reliably modeled (Figure 2.13 A). Utilizing the relationship between the linear region of the sprayed surface and the nozzle-sample distance, we found that inking a typical 1.5 cm wide PPL pen array with a gradient that varies from approximately 15 to 85% requires two spray air brushes with a separation of 5 cm that are positioned 20 cm from the pen array.

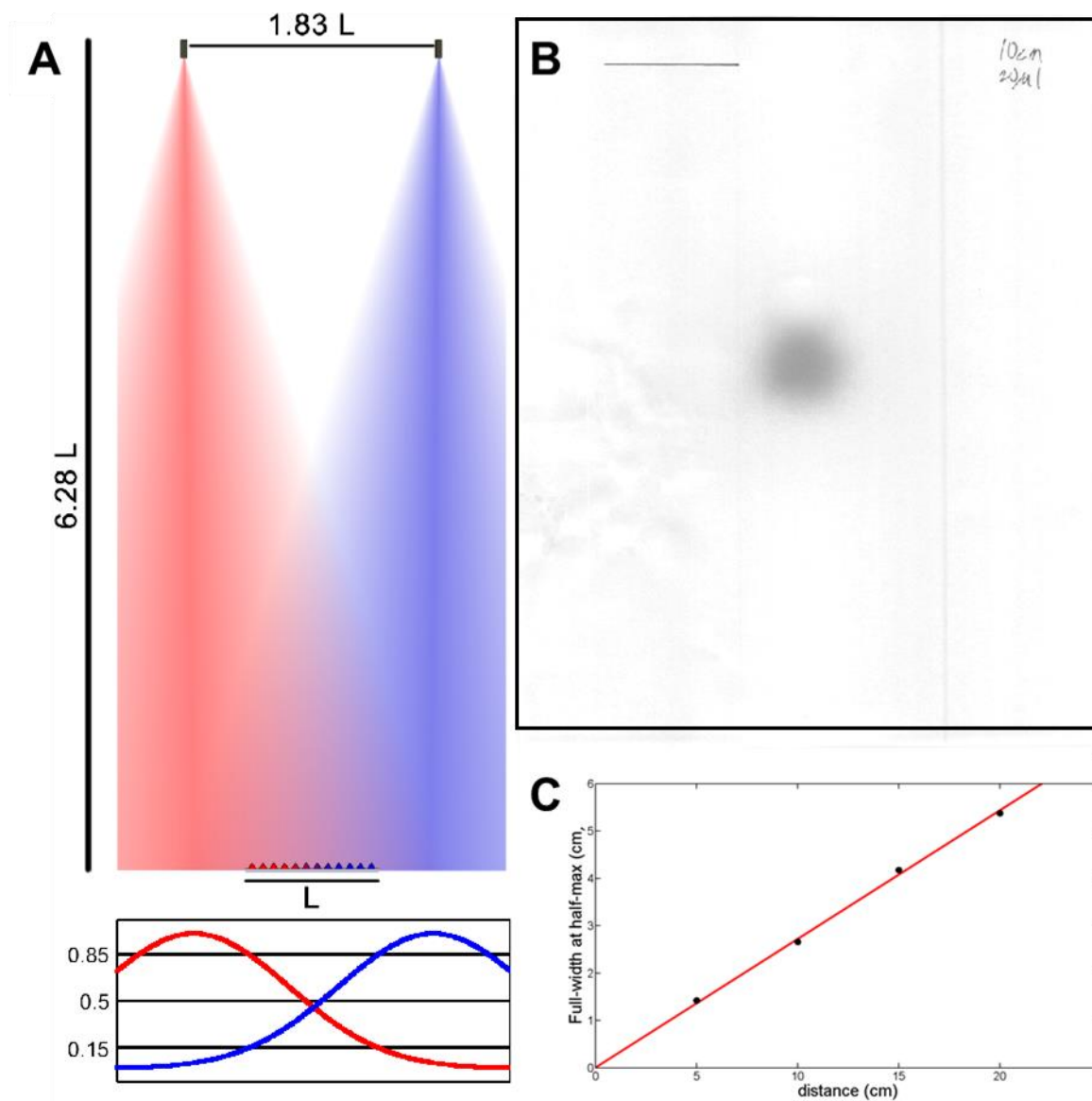


**Figure 2.13:** Scalability of spray-coating with different arrays. (A) Diagram of how to position air brushes relative to PPL array based on size, (B) scanned spray used to quantify spray profile, (C) linear full width half max slope showing a linear scaling trend for PPL arrays. Figure adapted from reference.<sup>165</sup>

While spray-coating a uniform film on a flat surface is a well understood problem, forming a compositional gradient on a surface decorated with a periodic array of pyramidal pens could introduce problems stemming from inhomogeneous drying and diffusion of the constituent materials. Considering a small molecule with a diffusion constant  $D \sim 3.5 \times 10^{-6} \text{ cm}^2/\text{s}$ , one may estimate the time  $t$  over which molecules will diffuse a distance  $x$  using a diffusion equation  $t = x^2/2D$ .<sup>166</sup> In particular, for a 1.5 cm wide pen array with a pen-to-pen pitch of 120  $\mu\text{m}$ , the molecule will diffuse between pens in  $\sim 20$  s and across the whole array in  $\sim 400$  days, suggesting an extremely long window over which drying can occur and still maintain the compositional gradient. Importantly, we hypothesize that allowing enough time for diffusion to occur around a specific pen may be very important, as it could allow for localized diffusive mixing of the multicomponent ink sprayed near a given pen (Figure 2.14).<sup>144, 167</sup>

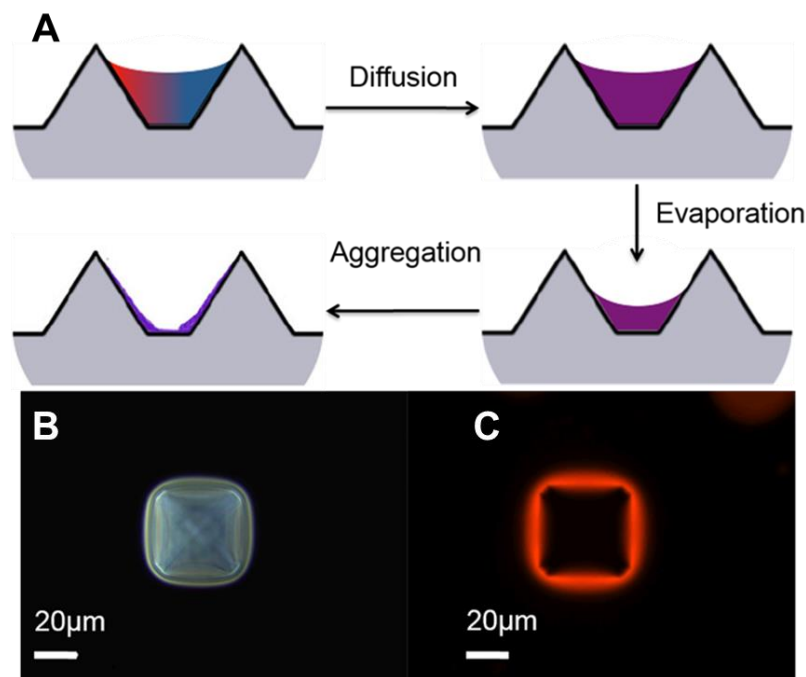


**Figure 2.14:** Evaporative self-assembly of diffused ink around pyramidal pens. (A) Proposed mechanism of ink evaporation following spray coating in which evaporation and diffusion leads to homogenous mixing of the inks and preferential deposition of the ink on the pens. Optical image of a single pen under (B) dark field and (C) fluorescence showing preferential inking at the base of the pen. Figure adapted from reference.<sup>165</sup>

To evaluate the potential for reliably transferring the gradient formed on the PPL array to an underlying substrate (Si/SiO<sub>2</sub>), two aqueous inks, consisting of Rhodamine 6G or Sulfo-Cyanine5 NHS Ester in poly(ethylene oxide)-*b*-poly(2-vinylpyridine) (PEO-*b*-P2VP), were prepared and studied. These dyes were chosen because they can be spectrally distinguished using fluorescence microscopy. The inking procedure consisted of simultaneously spraying the two inks, each aimed at the center of opposing edges of the PPL pen array, and then allowing the solutions

to completely dry prior to patterning (Figure 2.15 D). During the drying process, the ink deposited onto the array mixes between neighboring pens, and the ink dries around the base of the pens before global mixing occurs. After drying, a gradient could be seen by eye across the PPL array (Figure 2.16 A). To characterize the gradient, the whole PPL array was imaged with a confocal microscope. In order to maintain the high resolution required to visualize the nanoscale features across the whole array, thousands of images were taken on two tracks, one for each fluorophore, and subsequently stitched and stacked to make a single image with 268 million pixels (Figure 2.16 B). To verify that spray-coated PPL pen arrays can be used to pattern surfaces with the same compositional gradient, the dual spray-coated PPL array was used to print polymer domes onto a substrate that was imaged in the same way as the array (Figure 2.15 A,C). The counter-propagating changes in fluorescence contrast indicate that the spray-coating was effective and created a red-blue, left-to-right gradient. To quantify the distribution of the ink, the image stacks were averaged to construct a profile plot of fluorescence intensity (Figure 2.15 B). The fluorescence intensity plots demonstrate the potential for dual spray-coating to generate near linear gradients of ink composition on PPL pen arrays.



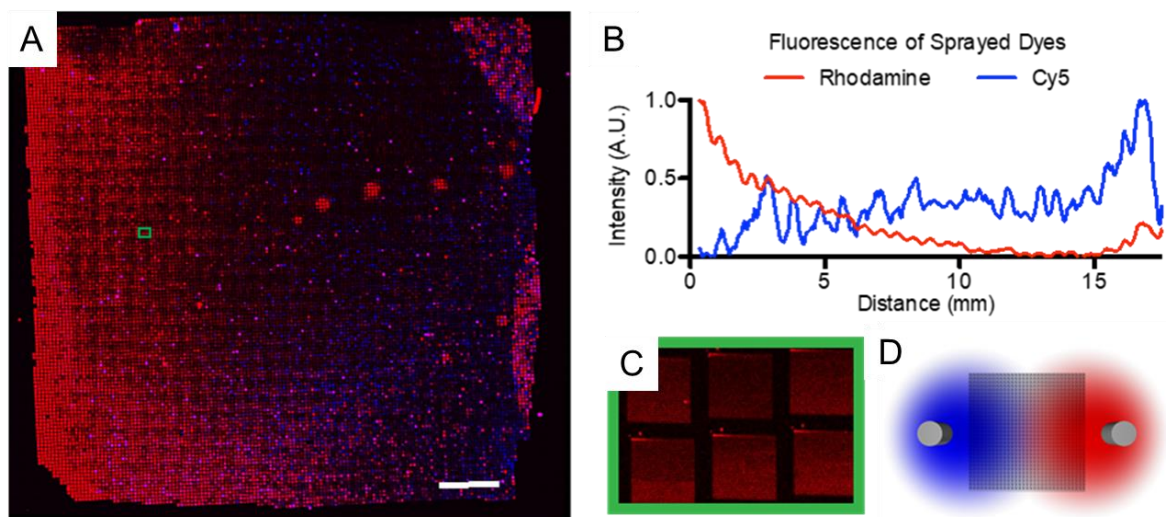


**Figure 2.15:** Large scale gradients of patterned nanomaterials. (A) Stitched confocal fluorescence image of a compositional gradient of two different fluorophores in patterned polymeric domes, scale bar is 2 mm, and (B) fluorescence intensity across of each region. (C) A magnified fluorescence image showing a single tile from (A), illustrating the dot arrays pattern, as well as the resolution of (A). (D) Schematic of the airbrush position during spraying.

Figure adapted from reference.<sup>165</sup>

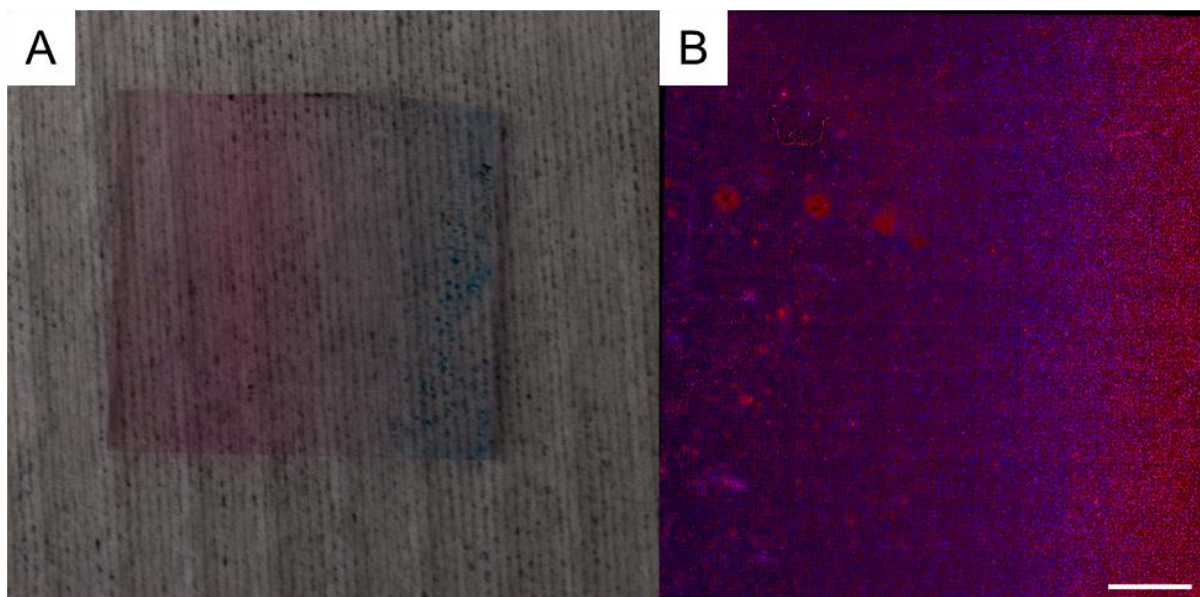


**Figure 2.16:** PPL array spray-coated with a composition gradient. (A) Photograph and (B) confocal micrograph of the composition gradient spray coated onto the PPL array. Figure adapted from reference.<sup>165</sup>

While prior experiments focused on patterning gradients with easy to detect fluorophores to visualize and characterize the gradients, it is important to validate that combinatorial libraries can be generated using substances where the function can, in principle, dramatically change across the array. When combined with SPBCL, catalytically-active multimetallic nanoparticles with gradients of composition can be readily synthesized. To determine if combining SPBCL and dual spray-coating can be used to generate compositional gradients, we explored the patterning of metal ion-loaded block copolymers that can be compositionally quantified using X-ray fluorescence (XRF)<sup>168</sup>. To explore the patterning of these inks, a pen array was dual spray-coated using aqueous solutions of PEO-*b*-P2VP, one with auric acid and the other with sodium tetrachloropalladate.

Following spray-coating, this pen array was used to pattern features on a silicon wafer. After heat treatment to form nanoparticles in each polymer dome (Figure 2.17 B), the substrate was characterized using XRF, which allowed for the calculation of the local atomic ratio of Au to Pd in sections across the array (Figure 2.17 A). As expected, the atomic ratio of Au-to-total Au and Pd varied from 9 to 88%. Qualitatively, it is observable that going from the Au-rich (right) to Pd-rich (left) side of the substrate, the Au  $L\beta$  fluorescence intensity decreases while the Pd  $K\alpha$  fluorescence intensity increases as would be expected (Figure 2.18). Such a trend was observed not only for the silicon-dioxide wafer substrate sample, but also when a quartz glass substrate was used (Figure 2.19). This demonstrates that a gradient sample can be created independent of substrate. Quantitative analysis of the Au and Pd relative atomic percentages were conducted using corrected areas under the Pd  $K\alpha$  (21177 eV) and Au  $L\beta$  (11443 eV) fluorescence lines, with peak areas fit to a Gaussian distribution after background subtraction. Intensity values were corrected for dead-time, incident beam intensity, elemental cross-sections,<sup>169</sup> detector efficiency, and attenuation due to species present between the sample and detector at the relative fluorescence line energies.

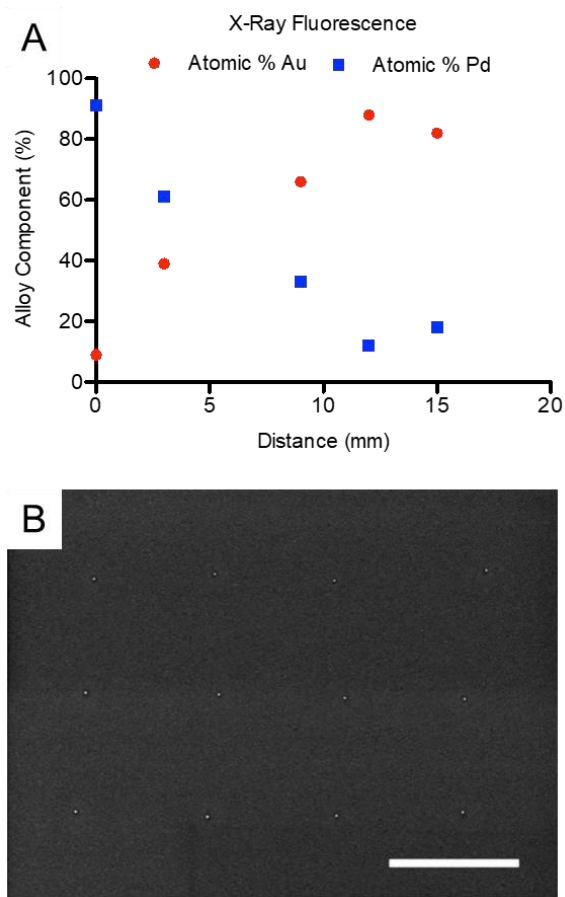


**Figure 2.17:** 14 million bimetallic nanoparticles synthesized in parallel with a compositional gradient. (A) X-ray fluorescence profile of AuPd alloy composition of SPBCL patterned array taken with a 3 mm slit, note that the last point is at the edge of the array. (B) SEM of SPBCL AuPd nanoparticles. Scale bar is 2  $\mu\text{m}$ . Figure adapted from reference.<sup>165</sup>

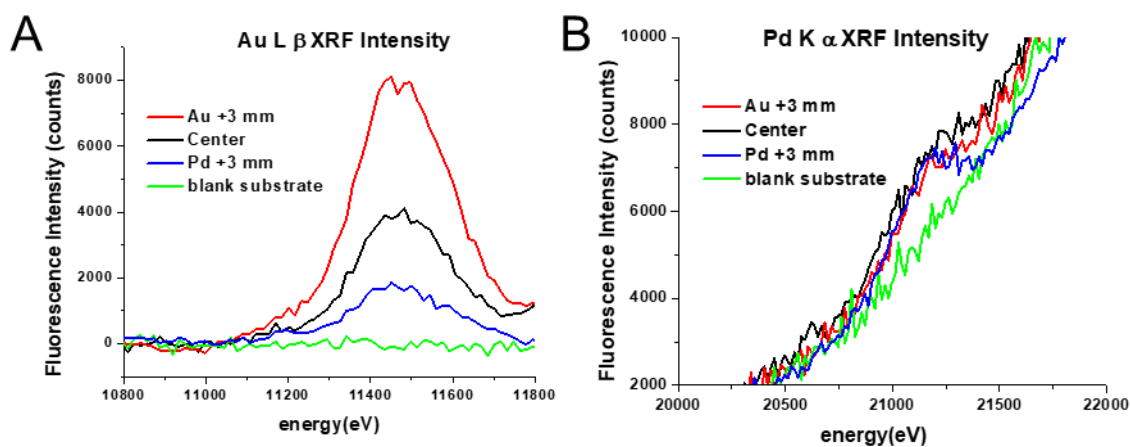


**Figure 2.18:** Au L $\beta$  and Pd K $\alpha$  Fluorescence Intensities. The Au L $\beta$  fluorescence line intensity (A) increases towards the Au-rich side of the sample and decreases towards the Pd-rich side. No signal is observed for the case of a blank substrate (green). The Pd K $\alpha$  fluorescence line intensity (B) decreases towards the Au-rich side of the sample and increases to a well-defined peak (blue) towards the Pd-rich side of the spectrum. +3 Au refers to a 3 mm offset from the sample center towards the Au-rich side, and +3 Pd refers to a 3 mm offset from the sample center towards the Pd-rich side. Figure adapted from reference.<sup>165</sup>

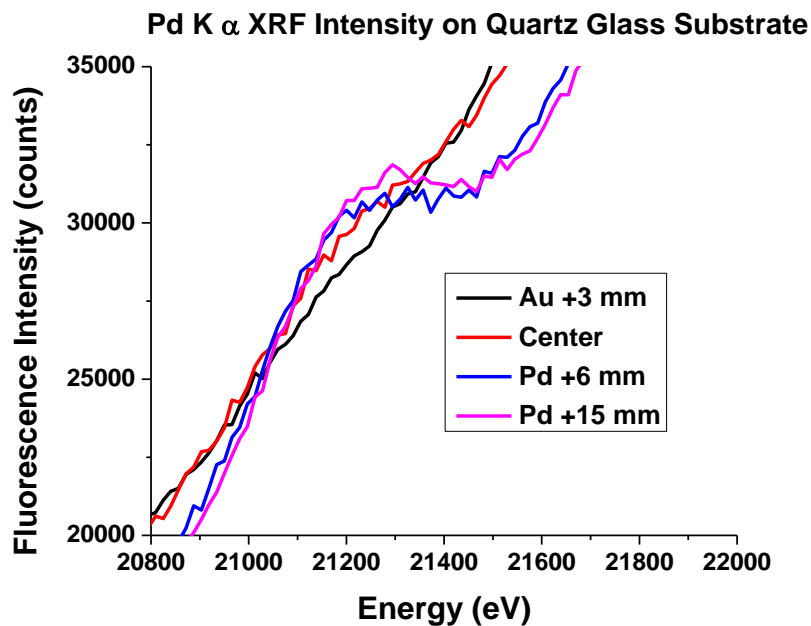


**Figure 2.19:** Pd K $\alpha$  XRF Intensity from sample patterned on quartz glass substrate. Qualitatively, it is observable that from the Au-rich side of the sample (black) to the Pd-rich side of the sample (blue and pink) that the Pd K $\alpha$  fluorescence intensity increases. This demonstrates that a gradient Au-Pd sample can be patterned independent of substrate. Figure adapted from reference.<sup>165</sup>

While the ability to generate patterns with compositional gradients on the nanoscale is novel and potentially useful, realizing combinatorial patterns with control over the size and composition of every feature in the pattern is the ultimate goal for high throughput screening. In addition to inking the pen arrays with uniform quantities of ink while varying their composition, it is possible to vary the quantity of ink on each pen. It is important to note that while similar linear gradients have been previously achieved by patterning with pen arrays that have been deliberately tilted to

change pen-sample contact area or contact time across the array, controlling feature size with ink loading affords the option of realizing non-linear gradients in patterned feature size.<sup>124, 170</sup> In order to explore the ability of spray-coating to generate such combinatorial libraries, a dual spray-coating experiment was performed in which the two airbrushes were loaded with the same polymer-fluorophore inks previously used, but were aimed above two adjacent corners of the pen array (rather than along a line that passes through the center of the array) (Figure 2.21 E). The dual gradient as sprayed on the pen array can be seen by eye (Figure 2.20 A) and mapped via fluorescence confocal microscopy (Figure 2.20 B). Subsequently, PPL was performed with each pen in the array being used to print a  $30 \times 30$  array of dot features (Figure 2.21 D). Given that this  $126 \times 126$  pen array contained 15,876 pens, the final pattern was composed of over 14 million discrete polymer features. To characterize this massive array of features, large-scale fluorescence images were acquired, which clearly showed a macroscopic gradient in fluorescence across the patterned surface (Figure 2.21 A). Indeed, the average fluorescence intensity is well described by a linear gradient across the entire patterned surface horizontally (Figure 2.21 B). Also, fluorescence intensity and atomic force microscopy (AFM) data show a non-linear size gradient of features ranging from  $1.10 \pm 0.02 \mu\text{m}$  to  $642 \pm 46 \text{ nm}$  in diameter and  $17 \pm 1$  to  $3.6 \pm 0.8 \text{ aL}$  in volume going from the top of the array to the bottom (Figure 2.21 C,F,G). Through this fabrication method, massive libraries of nanostructures can be deposited in unison with their size and composition spatially encoded. Translating these fluorescent dyes to SPBCL inks, this results in a significant increase in the synthetic throughput of complex nanoparticles.

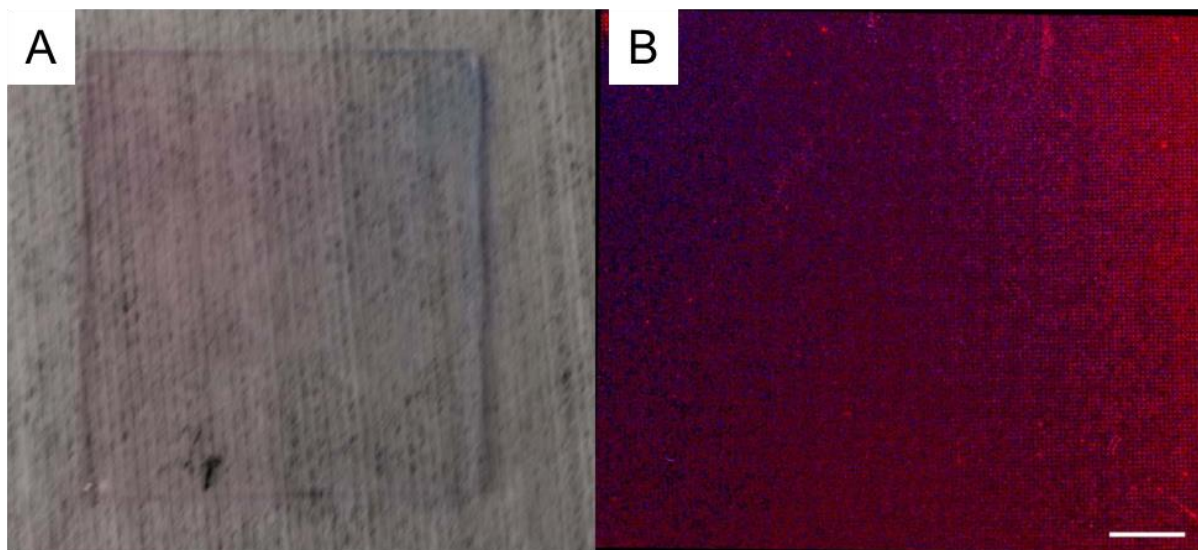


**Figure 2.20:** PPL array spray-coated with both a size and composition gradient. (A) Photograph and (B) confocal micrograph of the composition and size gradient spray coated onto the PPL array. Figure adapted from reference.<sup>165</sup>



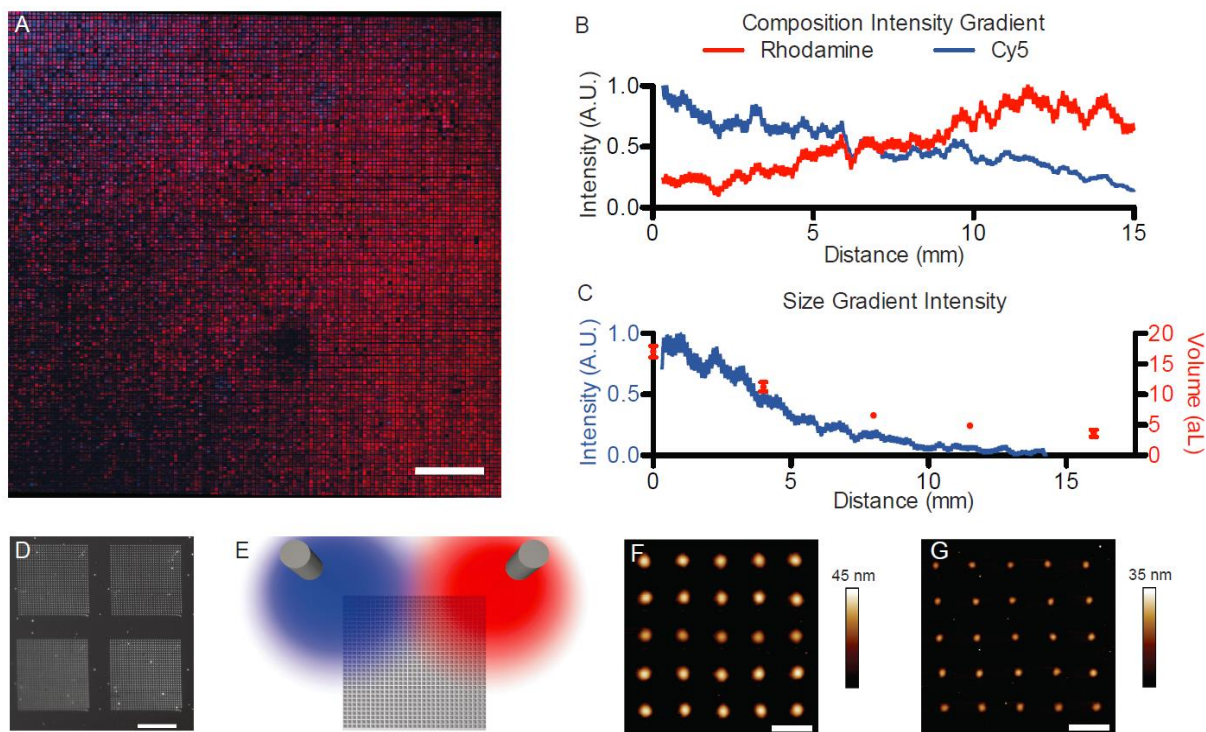


**Figure 2.21:** Large scale nanopatterned gradients of composition and size. (A) Stitched confocal fluorescence image of compositional and size gradients of two fluorophores in polymeric domes. Scale bar is 2 mm. (B) Average fluorescence intensity of each fluorophore across the array and (C) average total fluorescence intensity in the vertical axis plotted with the average volume of individual features as measured by AFM. (D) High resolution darkfield micrograph of a region showing the patterns written by four pens, scale bar is 50  $\mu\text{m}$ . (E) Schematic of the airbrush position during spraying. (F) AFM of the largest patterned features ( $1.10 \pm 0.02 \mu\text{m}$ ) at the top of the array, and (G) AFM of the smallest patterned features ( $642 \pm 46 \text{ nm}$ ) at the bottom of the array, scale bars are 3  $\mu\text{m}$ . Figure adapted from reference.<sup>165</sup>

## 2.3 Experimental Methods

### 2.3.1 Fabrication PPL Arrays

PPL arrays were fabricated as previously reported.<sup>95, 134</sup> For hard transparent coated PPL arrays using PECVD, they were then inserted into PECVD chamber to be coated with silica at 900 mTorr while introducing 500 sccm SH<sub>4</sub> and 1420 sccm O<sub>2</sub> and 30 W of high frequency power for 320 s with a base plate temperature of 200 °C using a STS LpX CVD. For E-beam coated pen arrays, PPL arrays were loaded into the E-beam chamber of a using a Kurt J. Lesker Co. PVD 75 electron-beam evaporator and pumped down below  $1 \times 10^{-7}$  Torr. Depositions were done in 25 nm increments, with 20 minutes of cool down between each deposition, up to 175 nm in total.

For blade coated pen arrays, standard Si masters were used. Strips of tape, generally 2 for ~100 μm thick layers, were laid down on either side of the wafer, in addition to two small pieces on the opposite ends. One ml of uncured PDMS was deposited on one edge of the master. A razor blade, or glass slide, was then slowly pulled across the wafer in a single smooth movement to coat the master in a flat thin layer of PDMS. If air bubbles were present or portions of the master remained uncovered, the razor blade was brought back across the wafer until the layer was uniform. This PDMS was then cured for ~10 min at 80 °C, to the point of solidifying but still tacky to the touch. The process was repeated until the desired thickness was reached. To attach the PDMS array and blade coated backing layer to a glass slide, a small amount of PDMS was placed in the center of the master and the glass slide (oxygen plasma treated for 2 min at 60 W to present -OH surface groups) was placed on top. This final array was then fully cured at 80 °C for 4 hours before being peeled out of the master.

### 2.3.2 Patterning

Patterning was performed using a Park XE-150 in a humidity control chamber at a relative humidity between 70-95 % and at room temperature with a 30 min incubation period prior to patterning. For patterning with Au coated pen arrays, a TERA-Fab M series instrument was used.

### ***2.3.3 MHA Ink and Substrate Preparation***

Solutions of 10 mM MHA in ethanol were spray coated on PPL arrays after a 2 min oxygen plasma treatment at 60 W. Au-coated Si wafers were prepared using a Kurt J. Lesker Co. PVD 75 electron-beam evaporator, depositing 5 nm Ti followed by 35 nm Au.

### ***2.3.4 SPBCL Ink and Substrate Preparation***

Solutions of PEO-*b*-P2VP, ranging from 1-5 mg/ml, were prepared in water. For instances where nanoparticles were subsequently formed, metal salts were added to the polymer ink solution. These polymer inks were drop cast or spray coated onto PPL arrays after a 2 min oxygen plasma treatment at 60 W. The substrates used in this chapter were all oxides and were made hydrophobic through vapor coating in a desiccator for 24 hours with a 1:1 solution of hexane and HMDS.

### ***2.3.5 SPBCL Nanoparticle Synthesis***

In order to convert polymer features into nanoparticles, the substrate was put into a tube furnace and thermally annealed. The heating conditions were programmed as follows: ramp to 120 °C under Ar (flow rate: 1.1 L/min) in 1 hour, hold at 120 °C for 48 hours, then cool back to room temperature in 4 hours, switch the atmosphere into H<sub>2</sub> (flow rate: 4.2 L/min), ramp to 500 °C in 2 hours, hold at 500 °C for 12 hours, and finally cool down to room temperature over 6 hours. Metal precursors aggregate during the first step, followed by nanoparticle formation and reduction at 500 °C under H<sub>2</sub>.

### **2.3.6 *Imaging***

Atomic force microscope (AFM) measurements were performed on a Dimension Icon (Bruker) to obtain 3D profiles of the patterns. Images were processed in Nanoscope Analysis. Confocal images were taken with a Zeiss LSM 800 Confocal Microscope. Images were processed with ImageJ and Zen Blue. Maximum intensity projections of confocal stacks were generated for each tile. Tiles were stitched with vignette corrections. Intensity plots were created from 500 pixel moving averages.

### **2.3.7 *X-Ray Fluorescence***

Data was collected at sector 5 BMD of the Advanced Photon Source. Fluorescence spectra were collected at an incident energy of 24.8 keV using two four-element Vortex ME-4 silicon drift diode detectors. The sample was placed in a glancing-incidence geometry with respect to the X-ray beam, at an angle of  $\sim 0.1^\circ$ . A horizontal slit size of 3 mm was used and the sample translated in order to probe the Au-Pd gradient at various points on the sample. The vertical slit size was adjusted according to footprint calculation, such that the entire sample length would be measured, in order to both maximize fluorescence counts from the elements of interest and achieve a global representation of the Au-Pd gradient.

## **2.4 Summary**

Herein, a comprehensive method of fabricating combinatorial libraries of materials was established through the use of PPL and SPBCL. Through the deposition of a hard coating onto a PDMS pen array, a force-independent patterning technique was developed. Using this coating, the deformation caused by pen-substrate contact was entirely transferred to the flexible backing layer, thus preventing any pen deformation. With no pen deformation, it is now possible to extend the

entire array further towards the substrate, allowing for the pen array to push through pen to pen height variations. Additionally, by maintaining a small contact area with the surface, smaller polymer dome features were able to be patterned closer together. Ultimately through this method, the total number of features that could be patterned onto a single surface was raised to over 406 million per  $\text{cm}^2$  area. In a similar aim, a new method of PDMS pen array fabrication was created. By blade coating multiple layers of PDMS into the Si master, global variations in the pen array were able to be overcome. Internal stresses that previously caused large scale bowing of the elastomer backing layer were negated, both through thicker PDMS layers and stiffer PDMS layers that limited the deformation caused by those stresses. With these pen arrays, the area that could be reliably patterned was raised from  $1 \text{ cm}^2$  to over  $9 \text{ cm}^2$ .

These methods were developed to ensure consistent patterning over large areas, which is necessary for the combinatorial deposition of nanomaterial libraries. To take advantage of the large area patterning capabilities, two methods of systematically controlling the ink that was loaded onto each pen of the pen array were described. First, a sequential coating method which used the isolation of segmented wells across the pen array, which raised the number of compositions that could be coated on a single pen array without sacrificing the total pens that could be inked. Due to the control of this method, parallel patterning of 16 different compositions of ink could be patterned, each completely isolated from each other composition. This method of inking is ideal for any application that requires at least a  $3 \times 3 \text{ mm}$  area of patterned material to analyze. For applications where the quantity of material needed is much smaller, a second gradient inking method can be used. Utilizing two spray sources with Gaussian distribution spray profiles, the linear regimes of each spray profile can be overlapped to form a two-way compositional gradient

between the two sources. Due to the continuous nature of the spray profiles, the gradient created is also continuous, leading to each pen across the array to contain a distinct composition of ink. In addition to composition gradients, the spray sources can be moved to two corners of the array, causing perpendicular gradients of size and composition. Through these methods, combinatorial libraries of over 14 million discrete features was deposited onto a single substrate with 15,876 distinct compositions and sizes spatially encoded. Paired with SPBCL, these patterning techniques open up the possibility to perform high-throughput screening of multimetallic nanoparticles at a rate not previously possible.

**CHAPTER 3:**  
**SCREENING CATALYST COMPOSITION FOR THE CHEMICAL VAPOR**  
**DEPOSITION GROWTH OF CARBON NANOTUBES**

This chapter is based, in part, on the research described in the following publication:

Kluender, E.J.; Hedrick, J.L.; Brown, K.A.; Rao, R.; Meckes, B.; Du, J.S.; Moreau, L.M.; Maruyama, B.; Mirkin, C.A. Catalyst discovery through megalibraries of nanomaterials *Proceedings of the National Academy of Sciences* **2019**, 116, 40-45.

### 3.1 Background

Carbon nanotubes (CNT) have experienced considerable scientific interest since their confirmed discovery in 1991 due to their enhanced materials properties.<sup>171</sup> CNTs consist of a rolled sheet of graphene, with diameters ranging from below 1 nm to 10's of nm and lengths ranging from nm's to cm's, resulting in one of the largest aspect ratios of any nanomaterial.<sup>172</sup> The angle at which the graphene sheet is wrapped into a cylinder, also known as the chirality, determines the diameter and electric band structure of the CNT. Depending on the chirality, single walled carbon nanotubes (SWNT) exhibit either metallic and semi-conductive behavior, with band gaps ranging from 0 to 1.5 eV.<sup>173, 174</sup> These electrical properties make CNTs an appealing material for transistors (with single CNTs<sup>175, 176</sup> as well as bulk CNT thin films<sup>177</sup>), light emitting diodes,<sup>178</sup> photovoltaics (both as the active layer<sup>179</sup> and the transparent electrode<sup>180</sup>), and sensors for gases<sup>181</sup> and biological molecules.<sup>182</sup>

CNTs were first synthesized by introducing an extreme amount of energy to graphite, either photonic<sup>183</sup> or electric,<sup>184</sup> with transition metals embedded. These first synthesis methods were extremely dirty, creating multiple carbon nanomaterials including fullerenes and amorphous carbon and routinely had CNT yields as low as 20%. The metal powders were initially added to the graphite with the hope of encapsulating single metallic atoms within fullerene molecules, specifically Co, Ni, and Fe. While this was achieved, it was also discovered that the addition of cobalt metal powder produced rubbery sheets on the fabrication chamber walls. These sheets consisted of large webs of CNTs covered in amorphous carbon, and a secondary purification step was needed to isolate CNTs. This technique was optimized using a nickel-cobalt catalyst, producing large ropes of bundled SWNTs covered in amorphous carbon with a CNT yield of



70%.<sup>185</sup> The first growth of isolated CNTs using CVD used a tube furnace heated above 1000 °C and benzene gas was flowed through the chamber along with hydrogen. The addition of iron catalyst particles produced CNTs with diameters on the order of 2 nm.<sup>186</sup> This primitive CVD method, while much cleaner than laser ablation and arc discharge, still produced a wide range of products, with amorphous carbon often coating large portions of the CNTs. One of the first examples of current CVD CNT growth was produced in 1996 using iron particles embedded in SiO<sub>2</sub>.<sup>187</sup> The mesoporous silica substrates were made by a sol-gel process using a tetraethoxysilane-iron nitrate solution. The solution was dried, calcined, and reduced to form the final substrate used for CNT growth. The growth atmosphere was composed of 9% acetylene in nitrogen at a growth temperature of 700 °C. Resulting CNTs formed a film of aligned MWNTs, perpendicular to the silica substrate.

In addition to the transition metals initially used (Co, Ni, Fe), the library of metal nanoparticles that are catalytically active for CVD growth of CNTs has been expanded to include almost every metal on the periodic table. CNTs have been successfully grown from other transition metals (Mn,<sup>188-190</sup> Cr,<sup>189, 190</sup> Mo<sup>189, 190</sup>), platinum group metals (Pd,<sup>189, 191</sup> Pt,<sup>189-191</sup> Ru<sup>192</sup>), noble metals (Au,<sup>189-191, 193</sup> Ag,<sup>191</sup> Cu<sup>189, 191, 194</sup>), carbon family elements (Si,<sup>195</sup> Ge,<sup>195</sup> Sn,<sup>189, 190</sup> Pb<sup>189</sup>), and even lanthanides (Gd,<sup>196</sup> Eu<sup>196</sup>). Regardless of composition, the nanoparticle catalyst plays 3 major roles in CNT growth: surface diffusion of carbon for graphitic formation, templating graphene cap nucleation, and maintaining a reactive nanotube rim for sustained growth. In addition to these functions, the nanoparticle may also catalyze the chemical decomposition of the carbon precursor. Initially, it was thought that high carbon solubility or carbide formation, two properties of the transition metals that first exhibited catalytic activity, was vital to CNT formation due to the ability

to absorb the carbon precursor before precipitating CNTs.<sup>197</sup> This hypothesis was based on the vapor-liquid-solid (VLS) mechanism of other nanowire growths.<sup>198</sup> VLS growth of CNTs was challenged by the discovery of catalytically active noble metal catalysts with negligible carbon solubility or carbide formation. The VLS mechanism may still be accurate for metals with high carbon solubility, but for metals with lower solubilities, the carbon precursor is likely adsorbed onto the particle surface as opposed to absorbed into the particle. Currently, there is no conclusive experimental or theoretical evidence that carbon absorbance plays a larger role than carbon adsorbed on the surface.<sup>199</sup>

Gas flow used for CNT growth plays a role equivalent to the catalyst. The main component of the growth atmosphere is the carbon precursor that decomposes into the carbon that comprises the final CNT. There is a wide range of carbon-containing molecules that have been used for CNT growth, including simple hydrocarbons,<sup>200</sup> alcohols,<sup>201</sup> and aromatic compounds.<sup>202</sup> In a special case, a specific precursor ( $C_{96}H_{54}$ ) was adsorbed onto a Pt surface.<sup>203</sup> The metal surface catalyzed cyclodehydrogenation, forming a  $sp^2$  cap. Once formed, the cap was then elongated through traditional precursor growth. While complex carbon precursors have exhibited equal success for CNT growth, the most common molecules used are methane, acetylene, ethylene, and ethanol. These carbon precursors are preferred for scientific study due to their gaseous state and simplicity. Larger carbon precursors have more decomposition pathways leading to less control of which carbon species are interacting with the catalyst particles. Depending on the catalyst, precursor, and growth temperature, carbon precursors can either be catalytically cracked by the nanoparticle<sup>204</sup> or thermally decomposed.<sup>205</sup> The amount of carbon precursor also effects the efficiency of the growth, where the reaction can be either gas limited or surface limited.<sup>206</sup> By using *in situ* Raman

spectroscopy, the G-band peak ( $sp^2$  Raman peak for CNTs at  $1590\text{ cm}^{-1}$ ) can be measured as a function of time and fit to a growth equation, calculating the initial growth rate,  $v$ , and growth lifetime,  $\tau$ . At lower partial pressures of precursor, the growth is gas-phase diffusion limited. With less carbon being added to the reactor, the growth proceeds at a slower rate but lasts longer. As the partial pressure of carbon increases, the growth rate increases and the lifetime decreases, until they both level out in the catalyst surface limited regime. Other gases are often included in the growth atmosphere, acting as inert carrier gases (Ar,  $N_2$ ) or as active components ( $H_2$ ,<sup>207</sup>  $NH_3$ ,<sup>208</sup>  $H_2O$ ,<sup>209</sup>  $CO_2$ ). Hydrogen and ammonia are added as reducing agents to maintain the catalyst in a metallic phase, which is significantly more active than oxide phases. Water and carbon dioxide act as weak oxidizing agents. In small quantities, they are not strong enough to fully oxidize the nanoparticles, but etch amorphous carbon, preventing non-graphene carbon from forming around the catalyst, poisoning the surface. In larger quantities, they impede growth by oxidizing the catalyst and etching CNTs.

The holy grail of CNT growth is chiral selectivity. The chirality is indexed using the notation  $(n,m)$ , where  $n$  and  $m$  are the number of lattice unit vectors between the two points on the graphene lattice that are connected to make the CNT.<sup>210</sup> There are two SWNTs with special names: zigzag (where  $m=0$ ) and armchair (where  $n=m$ ). The electronic properties of SWNTs directly depend on their chirality and can be split into three different categories: metallic, quasi-metallic, and semiconducting. SWNTs are metallic (no band gap) when  $n=m$ , quasi-metallic (small band gap) when  $n-m$  is divisible by 3, and semiconducting (large band gap up to 1.5 eV) for all other cases.<sup>173</sup> Due to the correlation between the chirality and electronic properties, for electronic devices to use CNTs on a large scale, a method of synthesizing homogenous chiral CNTs is necessary. Bottom

up methods of synthesizing CNTs have been proposed for chiral selective growth. Fullerene,  $C_{60}$ , molecules have been opened using thermal oxidation and CNTs have been grown off of the cap formed.<sup>211</sup> Individual building block rings of cycloparaphenylenes have been synthesized<sup>212</sup> in attempts to made to build CNTs layer by layer, but these efforts have yet to be successful due to the complexity of side products.<sup>213</sup> CNT caps have also been synthesized using a complex carbon precursor and a cyclodehydrogenation reaction, resulting in highly uniform final CNTs.<sup>203</sup> Additionally, short SWNTs of homogenous chirality can be used as templates for longer CNT growth.<sup>214</sup> This secondary growth is necessary due to the short length of the CNTs sorted by DNA-based chromatography,<sup>215</sup> density centrifugation,<sup>216</sup> and temperature gel chromatography.<sup>217</sup>

Controlling the chirality of SWNTs grown from CVD has proven to be the most viable method of chiral control. Using iron nanoparticle catalysts on a  $SiO_2$  support, increasing the  $H_2:Ar$  ratio during catalyst conditioning caused a drastic increase in the yield of metallic tubes, going from 18 to 91%.<sup>218</sup> Inversely, incorporating a plasma source to the CVD process synthesized >90% semiconducting tubes.<sup>219</sup> Another found a 96% semiconducting selectivity using an Al support and acetylene as a carbon source.<sup>220</sup> Building on the effects of plasma on CNT selectivity, free electron laser (FEL) irradiation was used during the CVD growth using a CoMo catalysts supported on  $SiO_2$ .<sup>221</sup> Five irradiation wavelengths were tested: 532, 800, 1300, 1650, and 1400 nm. All wavelengths limited the number of chirality's grown, with 800 nm producing the most homogeneous population, only growing CNTs of 6 chirality's, all of which are semiconducting. Multimetallic nanoparticles have exhibited enhanced CNT growth caused by the alloying of multiple active metals. A trimetallic catalyst composed of Al, Cu, and Fe in three phases ( $i-Al_6Cu_{25.5}Fe_{12.5}$ ,  $\omega-Al_7Cu_2Fe$ , and  $\epsilon-Al_2O_3$ ) on a  $SiO_2$  support, grew (9,9) armchair SWNTs with

50% selectivity.<sup>222</sup> It is possible that one phase produced enhanced chiral selectivity and a more precisely synthesized catalyst would increase the selectivity further, as the relative amount of the alloying elements plays a substantial role on catalytic activity. In a study of the  $\text{Ni}_x\text{Fe}_{1-x}$  alloy system, relative composition changed the chiral profile of the resulting CNTs.<sup>223</sup> Mapping the chirality's through photoluminescence, the chiral indices present evolve continuously with increasing Fe content. It is proposed that this is due to the increase in lattice spacing in the nanoparticle with increasing Fe% and the shift from fcc to bcc phase. Finally, the state of the arc CVD catalyst for CNT growth is the  $\text{W}_6\text{Co}_7$  catalyst.<sup>224</sup> This catalyst has a high melting temperature which is believed to maintain the crystalline structure at the 1030 °C growth temperature. This sustained crystalline structure produced highly selective growth of (12,6) chiral SWNTs at greater than 92%. These initial particles were synthesized using a molecular cluster, an extremely uniform catalyst that is difficult to scale, but the WCo system has also been reproduced using sputtered catalysts with 70% (12,6) selectivity.<sup>225</sup>

Based on the studies mentioned above, it is clear that CNT growth is a complex system that is controlled by many factors, both in the catalyst and the growth conditions. With multimetallic nanoparticles exhibiting enhanced catalytic activity, it is necessary to use precise and tunable particle syntheses to accurately elucidate the catalyst-CNT relationship. A method that meets this criteria is scanning probe block copolymer lithography (SPBCL).<sup>84</sup> Based off traditional block copolymer micelle lithography,<sup>226</sup> an attoliter-volume nanodome of block copolymer, with metal ions coordinated to one block, is patterned onto a surface using tip-directed nanolithography, either on a small area with dip-pen nanolithography (DPN)<sup>85</sup> or across a cm scale substrate with polymer pen lithography (PPL).<sup>95</sup> By varying the metal precursors coordinated to the initial block

copolymer, the composition of the final particle can be precisely controlled, and synthesize up to septametallic particles.<sup>94</sup> Due to the closed system created in the polymer dome, all of the metal atoms in a feature aggregate into a single nanoparticle, allowing for the synthesis of particles that would be significantly more difficult to synthesize in traditional solution synthesis. While these particles have not been shown to be catalytically active for CNT growth, traditional block copolymer micelle lithography synthesized particles have exhibited catalytic activity.<sup>193, 227</sup>

In order to perform effective screening of CVD CNT growth, both the catalyst synthesis and growth analysis need to be high throughput. Laser induced heating is a promising method for rapid growths, specifically the autonomous research system (ARES). In ARES, thermally isolated catalyst-coated micron-scale silicon pillars can be instantaneously heated to CNT growth temperatures and cooled back to room temperature. In a low-pressure chamber, the growth atmosphere can be precisely controlled by backfilling with Ar, H<sub>2</sub>, and carbon precursors. Analysis can also occur *in situ*, collecting Raman spectroscopy using the heating laser as an excitation laser. Initial studies using this system have measured growth rates of CNTs as a function of chirality.<sup>228</sup> Once the growths are performed and *in situ* data is collected, each pillar can be further analyzed *ex situ* using all available methods. There is a direct relationship between laser power and pillar temperature, allowing for large temperature ranges to be screened for catalytic activity. This has been used to reveal the impact of a solid to liquid phase change in iron catalysts.<sup>229</sup> Due to the instantaneous analysis of the growths, this system has also been used to create the first-of-its-kind closed-loop iterative experimental apparatus for materials discovery.<sup>116</sup> By incrementally changing the growth parameters, the system can apply machine learning to grow CNTs at targeted growth

rates. In this chapter, SPBCL, PPL, and laser induced CVD will be used to screen the effects of catalyst composition on SWNT growth.

## 3.2 Results and Discussion

### 3.2.1 *Fabrication of Micropillar Substrates*

Equally important to synthesizing cm-scale continuous compositional nanoparticle gradients, described in Chapter 2, is developing methods to measure the properties of the resulting nanoparticles. The property measured in this chapter is each nanoparticle's ability to catalyze the growth of SWNTs in a CVD reaction, using laser-induced heating in the Autonomous Research System (ARES). ARES matches the high-throughput nanoparticle synthesis technique with an equally high-throughput screening technique. Utilizing substrates containing thousands of thermally isolated silicon micropillars (10  $\mu\text{m}$  diameter and height), each pillar can be instantaneously heated to SWNT growth temperatures (700-900  $^{\circ}\text{C}$ ) using a 6 W laser (532 nm) inside a vacuum chamber containing a reducing agent ( $\text{H}_2$ ) and a hydrocarbon source ( $\text{C}_2\text{H}_4$ ). This heating laser is also used as a Raman excitation laser to measure the Raman peaks from the growing SWNTs, namely the low frequency, diameter-dependent radial breathing modes (RBMs) (between 100-300  $\text{cm}^{-1}$ , corresponding to SWNT diameters ranging from  $\sim 0.8 - 2.5$  nm), disorder-induced D band (at  $\sim 1350$   $\text{cm}^{-1}$ ), and the graphitic G band (at  $\sim 1590$   $\text{cm}^{-1}$ ). In previous literature, ARES substrates are 5x5  $\text{mm}^2$  in dimension and contains a 12x12 array of numbered patches, spaced 400  $\mu\text{m}$  apart, each consisting of a 5x5 array of 10  $\mu\text{m}$  diameter pillars, spaced 50  $\mu\text{m}$  apart.

In order to fully utilize the large area composition gradients capable through polymer pen lithography (PPL), large area uniform thermally isolated micropillar substrates are required. To achieve this goal, a fabrication method to form thermally isolated micropillars, based off of the

process used to fabricate PPL pen array masters,<sup>134</sup> was developed using a silicon-on-insulator (SOI) wafer (Figure 3.1). The substrates were designed to have the same pillar-to-pillar and patch-to-patch distances as the traditional ARES substrates, but each substrate would be 1.6x1.6 cm and contain a 40x40 array of patches, compared to the 12x12 patch arrays on the 5x5 mm substrates.

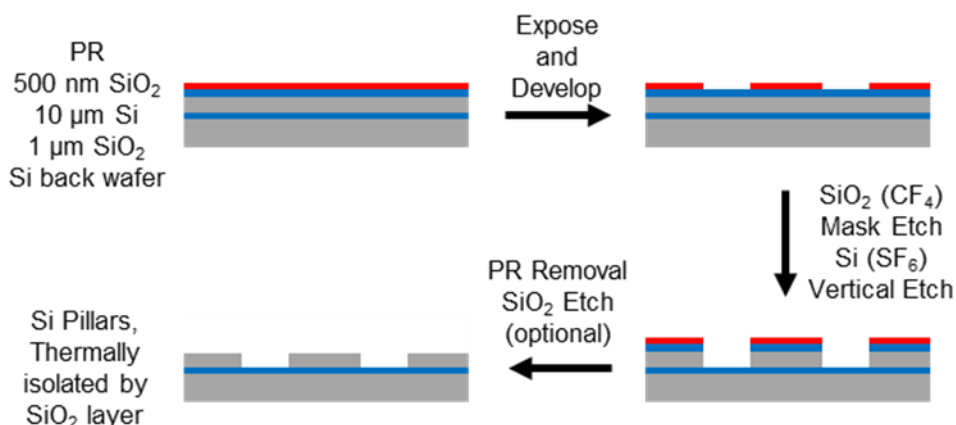


**Figure 3.1:** Scheme of micropillar fabrication using SOI Wafer.

To optimize the fabrication process, Si wafers were first used before SOI wafer (which are significantly more expensive). First, 500 nm of SiO<sub>2</sub> was deposited onto a polished Si wafer to act as a hard mask during the etching of the Si, which will make up the bulk of the pillars. Next, a photoresist was spin coated, exposed, and developed. S1805 photoresist, a positive resist (exposed areas are more soluble to developer), was used to produce the circular micropillars required for ARES. Due to the small isolated features required for micropillar fabrication, extremely short development times were used (<3 seconds), with longer developments (>5 seconds) fully removing all pillar features. The development time can be increased slightly by a longer bake time prior to exposure, but the size of the features still require a shorter development time. Once the



photolithography was optimized, the hard mask was etched using a  $\text{CF}_4$  dry etch, a highly selective  $\text{SiO}_2$  reactive ion etching process when in the presence of oxygen,<sup>230</sup> with an etch rate of  $\sim 20$  nm/min. This etch process uses directional plasma to form ions that primarily etch vertically into the substrate. During this step it is vital to fully remove all of the  $\text{SiO}_2$  hard mask where subsequent Si etch will occur. When there is incomplete removal of the  $\text{SiO}_2$ , even a few nm, the bottom of the Si trench will not be smooth and etch rates will be non-uniform, due to the high selectivity of the following Si  $\text{SF}_6$  etch.<sup>231</sup> With the hard mask formed, a deep etch to produce the bulk of the micropillar was performed using  $\text{SF}_6$ . Initial Si etches were performed with the same reactive ion etch process as the  $\text{SiO}_2$  etch, using a continuous process with the directional plasma driving a predominantly vertical etch. Due to the depth of the Si etch compared to the  $\text{SiO}_2$  hard mask etch,  $10\ \mu\text{m}$  vs  $500\ \text{nm}$ , respectively, the Si etch process began to undercut the hard mask (Figure 3.2 A). While the plasma is directional, scattering events prevent vertical wall formation from directional plasma alone. Vertical walls are necessary for the ARES micropillars, as each pillar needs to be made of the same, controlled amount of material. This is required due to the laser heating mechanism of ARES. Ensuring that each pillar reaches the same temperature at the same laser power is vital for the reproducibility of each growth experiment. To achieve vertical walls and mitigate etching from scattered molecules, a cyclical etch-deposition process, the Bosch process,<sup>232</sup> was used. The Bosch process oscillates between etch and deposition steps on the order of seconds. The etch step is identical to the continuous process, a directional plasma producing reactive ions that selectively etch Si. Each etch step is followed by a deposition step, where a fluoropolymer is deposited on the entire substrate, including the newly etched walls. When the process switches back to the etch step, the directional plasma sputters the fluoropolymer deposited

on the bottom of the substrate, exposing the bottom of the trench to the reactive ions for continued etching. The scattered ions do not have enough energy to sputter off the fluoropolymer and etch the side walls, preventing the undercutting seen with continuous etching. This deposited passivation layer adds an additional directionality to the etch process, producing near perfect vertical walls (Figure 3.2 B). The ridging seen on these pillars is due to the slight undercutting during each etch step, before the exposed wall is passivated (Figure 3.2 C). Each cycle of the etch process producing one ridge, the wall smoothness can be controlled by changing the length of each etch step. Shorter cycle times produce smoother walls but requiring more cycles for the same etch depth. When using SOI wafers, the buried oxide layer controls the final pillar height, as the  $\text{SF}_6$  etch does not etch  $\text{SiO}_2$ , halting the etching process. Once the Si micropillars are etched, the remaining photoresist and  $\text{SiO}_2$  hard mask can be removed, using piranha etching and HF etching, respectively.

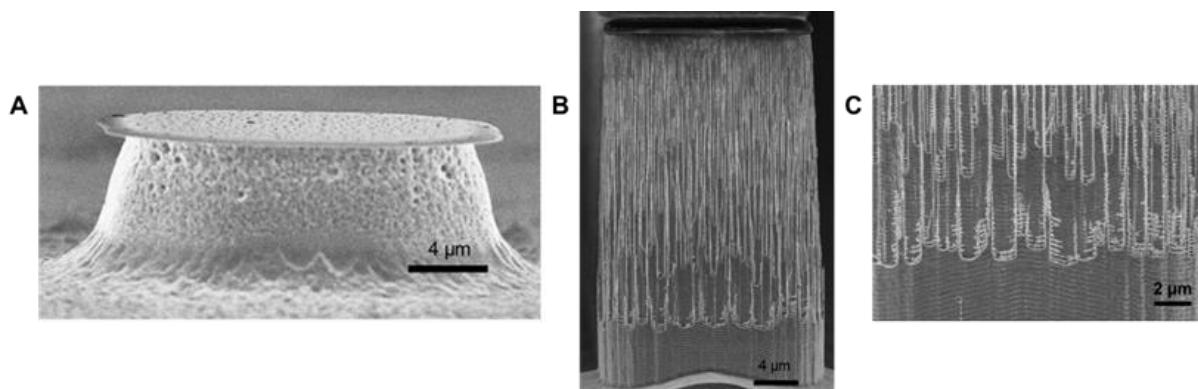


**Figure 3.2:** SEM images of micropillars etched into Si wafers. (A) Hard mask undercutting occurs when the SF<sub>6</sub> Si etch is ran continuously for the entire etch process. (B) By using the Bosch process and oscillating between etch and passivation steps, near vertical pillar walls are formed, producing micropillars up to 40 μm tall. (C) Ridging occurs on the walls of the micropillars produced by the Bosch process. Each ridge is created by one etch-deposition cycle.

While Si wafers were used for optimizing the fabrication process, SOI wafers are required to produce thermally isolated micropillars for the ARES substrates. This is achieved by etching a 10 μm Si micropillar supported on a >1 μm thick buried oxide layer, which acts as a thermal insulator and prevents any heat generated in the pillar from dissipating into the wafer. When pillars are not thermally isolated by the buried oxide layer, they are not able to heat up to CNT growth temperatures (>700 °C) due to heat diffusion to the backing wafer. It is also important to thermally isolate each pillar from the neighboring pillars to prevent pillar-to-pillar heating cross talk. To test these large area ARES substrates, a traditional CNT CVD catalyst, 0.8 nm Fe thin film, was sputter coated onto a micropillar substrates. Due to the size of the ARES growth chamber, only 1x1 cm substrates are able to fit, require the dicing of the 1.6 cm substrate into 4 segments prior to growths.

Using these test catalysts, CNT growths were performed in the ARES system at a variety of temperatures and growth atmospheres. To test that the pillars did not alter the performance of the deposited catalysts, the growth trends as a function of temperature were examined. CNT growths were performed in the ARES chamber under 20 torr pressure containing ethylene and hydrogen. CNTs were grown over a wide range of temperatures ranging from 700 to greater than 900 °C, with secondary SEM images confirming extensive CNT growth (Figure 3.3 A). The growth kinetics also agreed with literature precedent (Figure 3.3 B). Growths performed at higher temperatures exhibited faster initial growth kinetics, but quickly plateaued. This is due to excess decomposition of ethylene that drives initial growth but eventually encases the catalysts in amorphous carbon, preventing further growth. While growths performed at lower temperatures grew at slower rates, they proved to have longer growth lifetimes as there is limited amorphous carbon formation at this temperature, resulting in a larger final amount of CNTs produced.

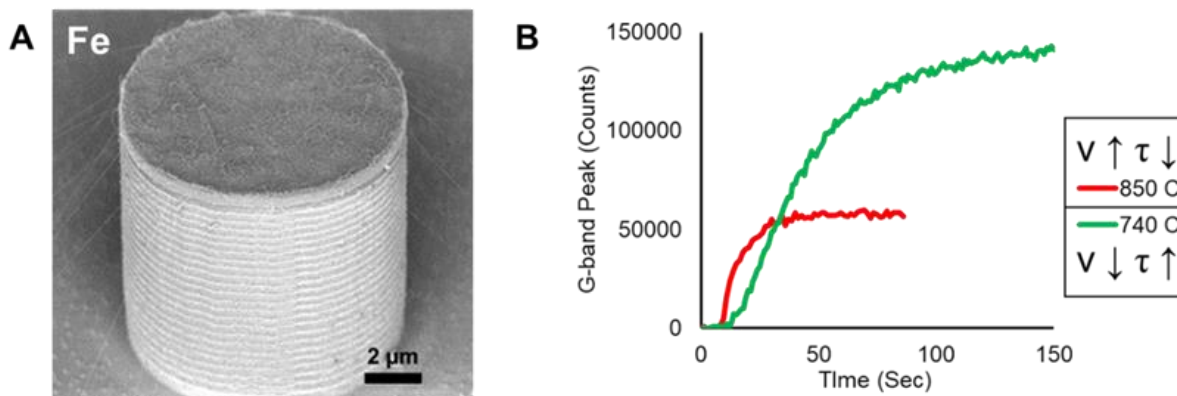


**Figure 3.3:** (A) SEM image of SWNTs grown on ARES micropillar using a 0.8 nm Fe film catalyst. (B) G-band peak integration measurements from *in situ* Raman spectra collected during growths at two temperatures. Higher growth temperatures exhibited faster growth kinetics but short lifetimes, while lower temperatures produced slower growth kinetics and longer lifetimes.

In addition to Raman characterization, we attempted AFM characterization of particles and resulting SWNTs. This was not possible due to the roughness of the pillar surface being greater than the size of the features of interest (particles ~3 nm, SWNTs ~1.5 nm, surface roughness ~6 nm) (Figure 3.4 A). The surface roughness was found to be caused by the SiO<sub>2</sub> hard mask used during the pillar fabrication process, either from incomplete removal or secondary scattering occurring during the etching process. To overcome this source of surface roughness, it was determined that by dropping the temperature at which the dry etch process was performed, it was possible to use photoresist as a mask for the vertical etch process, removing the SiO<sub>2</sub> from the process entirely. Using only photoresist leads to a gentler fabrication process with fewer steps. Substrates were then fabricated using photoresist as a mask at different temperatures during the SF<sub>6</sub> etching step. When the etching process was performed at 0 °C, the Si did not etch uniformly,

leading to a rough substrate between the pillar (Figure 3.4 C i). The temperature of the substrate was then raised to 10 °C (the recommended lowest temperature for substrates used in the Bosch Process), but the resulting etch removed the photoresist and lost the uniformity of the photolithography pattern (Figure 3.4 C iii). It was then determined that using a substrate temperature of 5 °C was optimal for performing uniform etches without fully removing the photoresist mask (Figure 3.4 C ii). While the PR mask was not fully removed at 5 °C, it was chemically altered from its initial state and was no longer able to be removed by an acetone wash, as was previously accomplished when the DRIE was performed at 0 °C. Instead, a O<sub>2</sub> plasma treatment (30 W for 5 min) was used to fully remove the residual PR mask, leaving a polished Si surface that was easily functionalized with HMDS to be made hydrophobic for SPBCL patterning. This modified process proved to be simpler and produced uniform pillars with a significant reduction in surface roughness (Figure 3.4 B). After these micropillar samples are fabricated, the top surface of the pillar, where the catalyst is deposited, can be altered to a wide variety of oxide surfaces. Typically, either Al<sub>2</sub>O<sub>3</sub> or SiO<sub>2</sub> are used as supports for CNT growth to prevent catalyst aggregation and often play a large role in the resulting CNT growth.<sup>233</sup> For Al<sub>2</sub>O<sub>3</sub>, an ALD process can be performed using sequential pulses of Al(CH<sub>3</sub>)<sub>3</sub> and water, forming a monolayer of Al<sub>2</sub>O<sub>3</sub> during each cycle. To produce SiO<sub>2</sub> supports, a dry thermal oxidation method can be used. By heating the substrate to 900 °C for 4 hours in air, the surface of Si micropillars will be oxidized, forming a SiO<sub>2</sub> surface. For both of these methods, the surface roughness/smoothness is retained from the Si pillar prior to treatment.

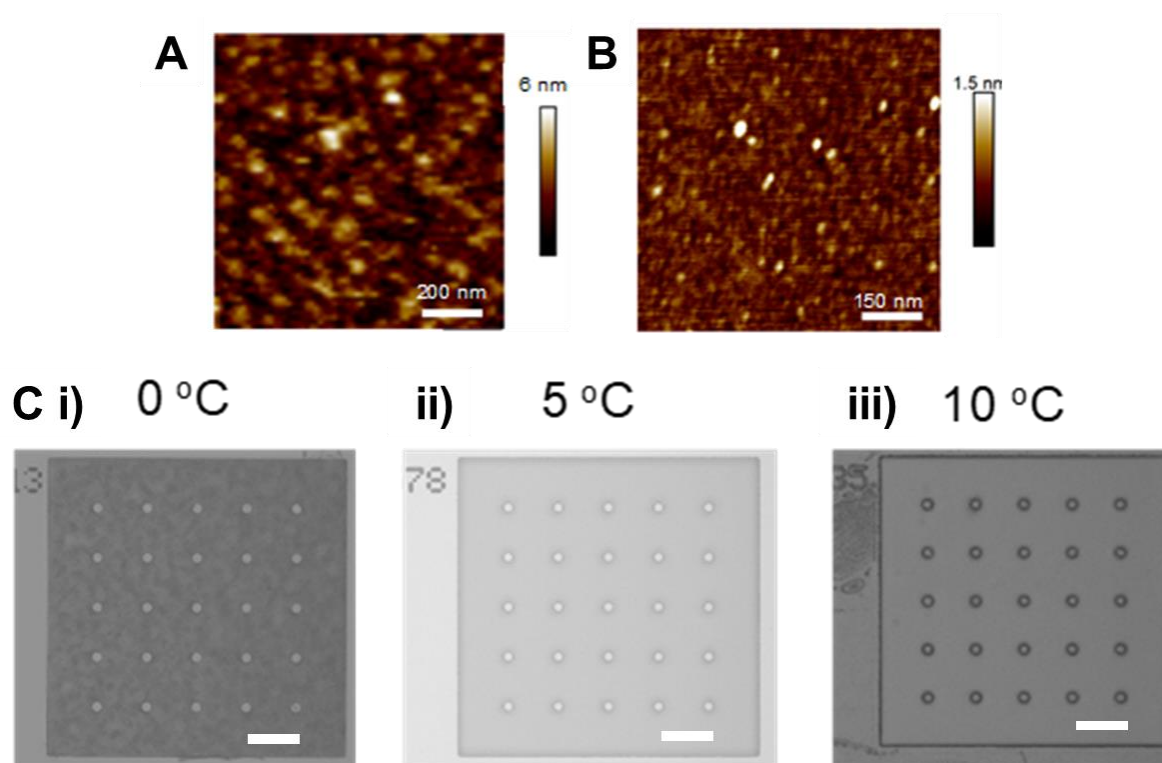


**Figure 3.4:** AFM micrographs of the top surfaces of micropillars made using (A) SiO<sub>2</sub> and (B) photoresist as the hard mask during Bosch process etching. (B) Optical image of micropillars fabricated using photoresist as a hard mask performed at (i) 0, (ii) 5, and (iii) 10 °C. Scale bars are 50 μm.

### 3.2.2 Investigating Effects of Growth Conditions on SPBCL Catalysts

Prior to the combinatorial screening of multimetallic scanning probe block copolymer lithography (SPBCL) synthesized catalysts in the ARES system, it first needs to be confirmed that SPBCL is a viable catalyst synthesis method. When using SPBCL nanoparticles as SWNT catalysts, two potential hurdles arise. For the majority of SPBCL studies, 20-50 nm particles have been synthesized for ease of imaging. To be catalytically active for SWNT growth, catalyst

nanoparticles need to be in a much smaller size regime (2-5 nm in diameter). When synthesizing nanoparticles through SPBCL, there are two approaches to control the resulting nanoparticle size, either shrinking the polymer nanoreactor's size or decreasing the metal precursor loading. To achieve the 2-5 nm size range required for this application, both approaches were required. It was determined that a sub-300 nm diameter polymer dome with a 256:1 pyridine to metal salt loading was sufficient in forming a nanoparticle that was in the catalytically active size regime.

In addition to particle size, the excess presence of carbon in the SPBCL process needs to be considered. One of the main causes for catalyst poisoning prior to or during SWNT growth is an excess of amorphous carbon that coats the catalyst particle and terminates growth or prevents SWNT growth entirely. There are two main sources of carbon in the SPBCL process that need to be accounted for prior to SWNT growth: surface bound hexamethyldisilazane (HMDS) and residual polymer dome. For SPBCL patterning to be performed, it is required that the patterned substrate be hydrophobic to ensure isolated polymer nanodomains are formed. HMDS is used to treat oxide surfaces, reacting with surface -OH groups to form a methylated hydrophobic surface. This surface decomposes during the particle formation heat treatment but is not fully removed. Additionally, the polymer dome is a large source of carbon that directly interacts with the surface of the nanoparticle. During the heat treatment process, the sample is raised to 500 °C, under a hydrogen atmosphere, resulting in decomposition of the polymer but not complete removal. The nanoparticles formed through SPBCL are therefore covered in a thin (1-2 nm) layer of amorphous carbon. Two methods were used to clean substrates prior to SWNT growth: oxygen plasma cleaning and calcination. Using oxygen plasma, at 30 W for 5-10 minutes, all of the amorphous carbon can be removed. The drawbacks of this technique are two-fold, plasma devices are not



universally prevalent, and are high energy, which can cause the catalyst nanoparticle to structurally change as high energy oxygen atoms are being driven into it. For these two reasons, it was determined that a calcination method, extended heating in the presence of oxygen, was more suitable to this application. A wide range of calcination treatments were investigated, all with positive results. It was found that temperatures ranging from 350 to 700 °C were suitable for the removal of amorphous carbon, with the former taking 1-2 hours and the later taking as little as 15 minutes. Additionally, as calcination and CVD growth of SWNTs are done in tube furnaces, substrates patterned with SPBCL particles can undergo calcination and SWNT growths in the same system sequentially, limiting any contamination or lag time in the system. Using these sample preparation methods (using the low metal loading and <300 nm polymer domes (Figure 3.5)), cobalt nanoparticles, with a nanoparticle-to-nanoparticle distance of 750 nm, were synthesized on an ALD Al<sub>2</sub>O<sub>3</sub> substrate, made hydrophobic by HMDS. These nanoparticles underwent a 700 °C calcination in air for 15 minutes, followed by a SWNT growth under a 50:10:1 Ar:H<sub>2</sub>:C<sub>2</sub>H<sub>4</sub> atmosphere at 800 °C for 10 minutes. The resulting SWNT were characterized by scanning electron microscopy (SEM) and Raman spectroscopy (Figure 3.6). Due to the density of nanoparticles and high aspect ratio of the SWNTs, there was a significant amount of SWNT bundling, making isolated characterization of each SWNT difficult. In all future studies for combinatorial screening, the nanoparticle spacing was maintained above 2 μm to prevent this bundling from occurring. These tube furnace CVD growths were also performed with Au, Ag, and Pt nanoparticles on SiO<sub>2</sub> substrates, all resulting in SWNT growth, demonstrating the flexibility of this synthetic platform.

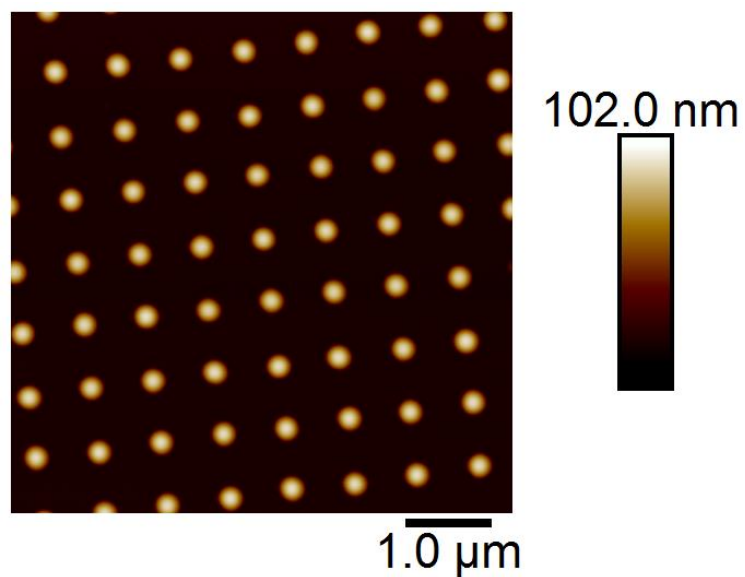


**Figure 3.5:** AFM micrograph of polymer domes containing Co precursors patterning on ALD  $\text{Al}_2\text{O}_3$ , made hydrophobic with HMDS. The polymer domes were spaced by 750 nm and were 275 nm in diameter.

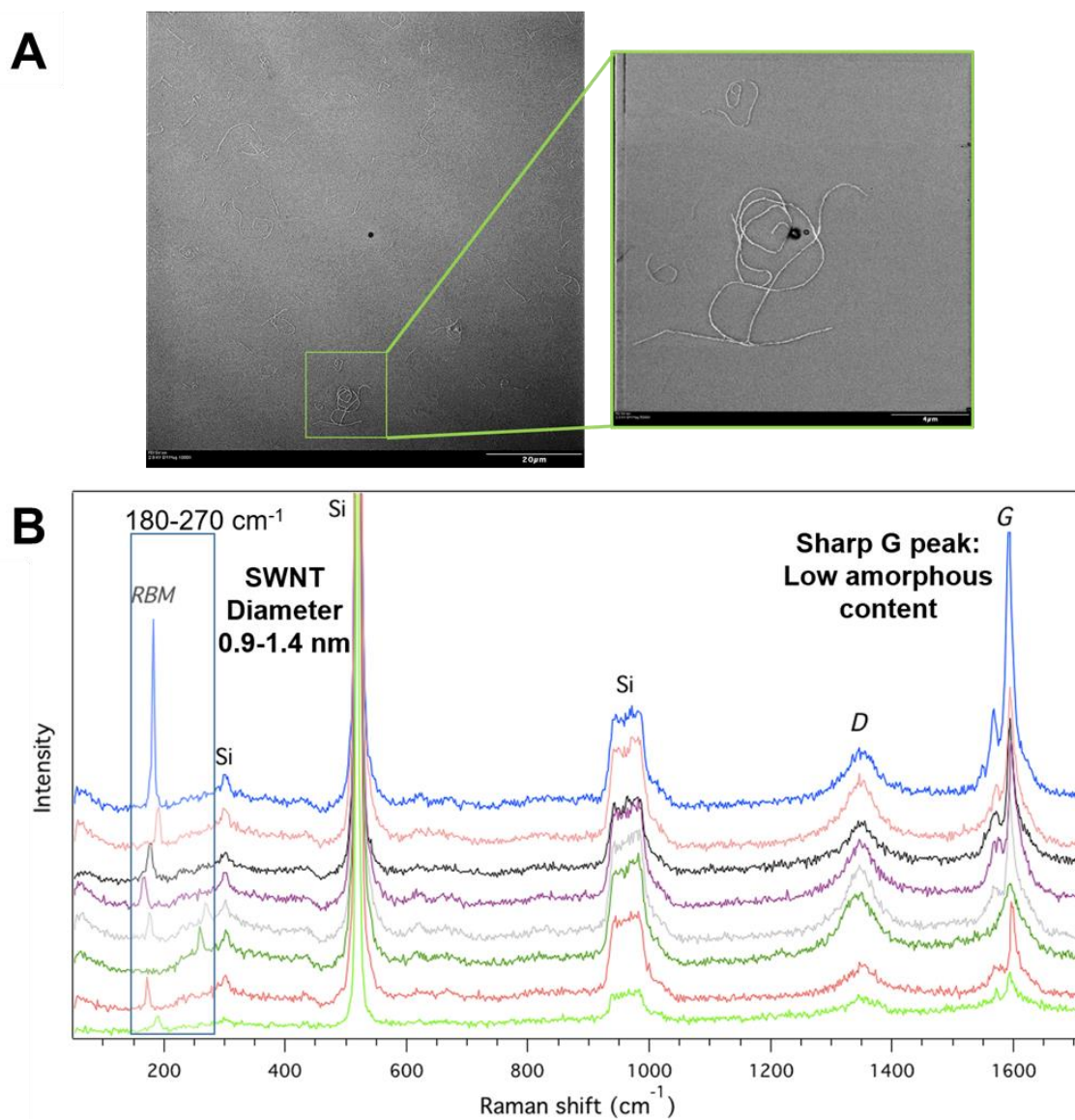


**Figure 3.6:** SWNTs grown from SPBCL synthesized Co nanoparticle catalysts. (A) SEM micrographs of the SWNTs, inset showing excessive bundling. (B) Raman spectrum of SWNTs, sharp G peaks indicate low defect SWNTs. Presence of radial breathing modes (RBMs) confirms SWNT growth, and fourth from bottom (grey trace) exhibit more than one RBM confirming bundling seen in SEM.

With confirmation of SPBCL nanoparticles as viable catalysts for the CVD growth of SWNTs, the next steps were to pair SPBCL with the autonomous research system (ARES) through the deposition of polymer domes on top of ARES micropillars. A polymer pen array was fabricated with 15  $\mu\text{m}$  base length pyramidal pens with the same spacing as the pillars on an ARES substrate. Using a rotational stage and an xyz piezo motor to align the pen array with the substrate (Figure 3.7 A), attoliter polymer domes with metal precursor containing PEO-*b*-P2VP ink were deposited in an ordered array on top of HMDS treated micro-pillars (Figure 3.7 B). Across a 1.5x1.5 cm substrate, for each pen to be aligned and pattern on each micropillar, the xy tilt is required to be within  $0.003^\circ$  tilt alignment and the rotational alignment within  $0.01^\circ$  alignment, all done by hand. Following the three-step heat treatment to synthesize catalytically active nanoparticles, SPBCL nanoparticles were deposited on ARES micropillars allowing for high-throughput SWNT growth and *in situ* characterization.

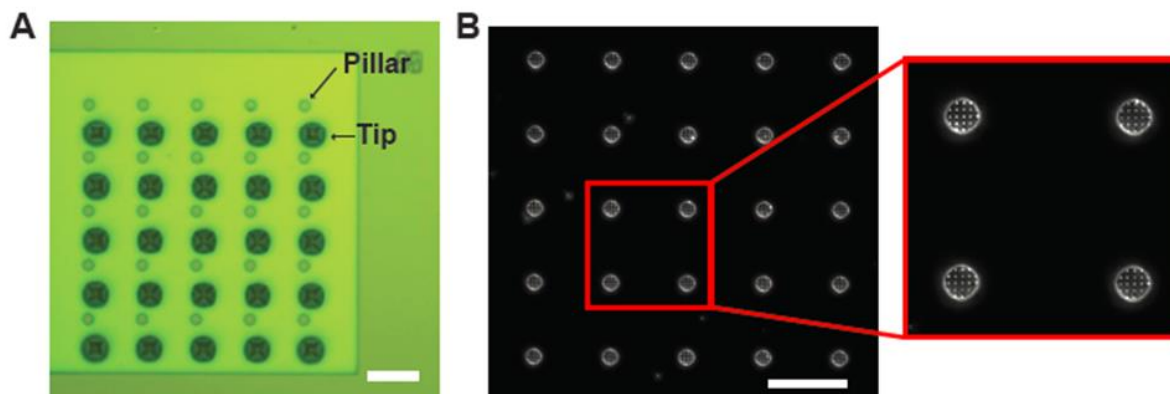


**Figure 3.7:** Patterning SPBCL nanoparticles onto ARES micropillars. (A) Image of the pen arrays aligned with the ARES micropillars, scale bar is 50  $\mu\text{m}$ . (B) Dark field optical image, scale bar is 50  $\mu\text{m}$ , with expanded inset of four pillars of the nano-dome polymer features in a square array on top of the micropillars. Figure adapted from reference.<sup>165</sup>

To study the effects of growth parameters using the ARES platform with SPBCL catalysts, the same Co catalysts deposited on the flat  $\text{Al}_2\text{O}_3$  substrate were patterned on  $\text{SiO}_2$  ARES micropillars. The temperature and partial pressures of ethylene, hydrogen, carbon dioxide, and water, as well as the total pressure, were tested across wide ranges. The upper and lower limit of the growth conditions tested, in addition to the optimal conditions found, are shown in Table 3.1. Through this screening, in addition to an optimal growth atmosphere, two growth peaks are observed as a function of temperature. A possible cause for the two peaks in catalytic activity at 900 and 950  $^\circ\text{C}$  could be a phase change from solid to liquid catalyst that has been reported in previous studies in the ARES system.<sup>229</sup> In addition to these Co catalysts, it was confirmed that Au, Ag, Cu, and AuCu alloy particles were also catalytically active when deposited on  $\text{SiO}_2$  ARES micropillars.

**Table 3.1:** Range of growth parameters screened for SPBCL Co catalysts deposited on SiO<sub>2</sub> ARES micropillars.

Parameter	C <sub>2</sub> H <sub>4</sub> (torr)	H <sub>2</sub> (torr)	CO <sub>2</sub> (torr)	H <sub>2</sub> O (ppm)	P (torr)	T (°C)	t (sec)
Upper Limit	56.25	12	3.636	35	75	1000	200+
Lower Limit	3.659	2.857	0.122	3	5	680	< 3
Optimal	30x	10x	1x	10	30	900, 950	n/a

### 3.2.3 Combinatorial Screening of Bimetallic SPBCL Catalysts

With the catalytic activity confirmed, and the ability to deposit these nanoparticles on ARES micropillars achieved, the full capabilities of SPBCL synthesis when paired with PPL, combinatorial gradients, was utilized. Au-Cu alloy catalysts were initially studied due to their full miscibility at the nanoscale over all compositions,<sup>92, 234</sup> and the literature precedent that both elements have been used for SWNT growth as monometallic particles.<sup>191, 235</sup> For this catalyst screen, it was decided to study only SWNT growth, thus no size gradient was included due to the size restriction (2-5 nm) of catalytically active particles for SWNT growth. The nanoparticles used in SWNT growths were ~2.5 nm in size and are composed of Au and Cu uniformly mixed in the nanometer scale (Figure 3.8). When particles are larger than this size regime, multiwalled CNTs are the primary product. In order to analyze the catalytic activity of the full Au<sub>x</sub>Cu<sub>1-x</sub> system, a 1.5 cm wide pen array, consisting of pens which align with the micropillar substrate, was spray-

coated with 5 mg/ml Poly(ethylene oxide)-*b*-poly(2-vinyl pyridine) (PEO-*b*-P2VP,  $M_n=2.8\text{-}b\text{-}1.5\text{ kg}\cdot\text{mol}^{-1}$ ) solutions using two different spray sources. The Gaussian spray profiles' linear regimes were overlapped across the pen array (Figure 3.9 A,B). The compositional gradient was characterized to be from  $X = 0.12$  to  $X = 0.85$  (Figure 3.9 C).

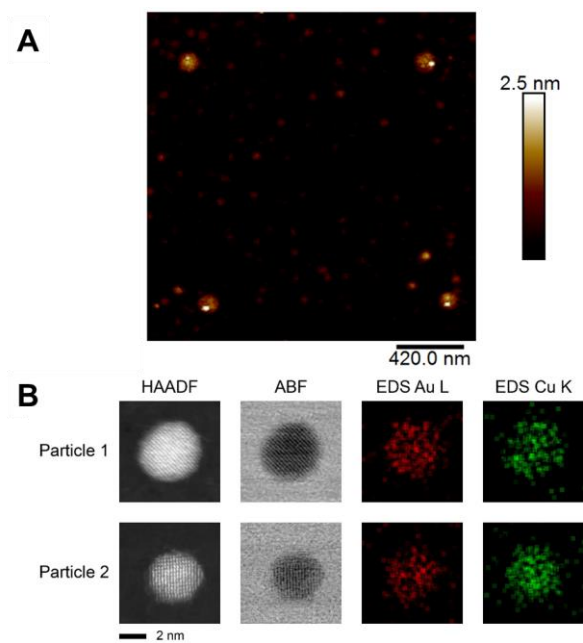


**Figure 3.8:** Characterization of AuCu alloy catalysts used in compositional screen. (A) AFM of AuCu particles in catalytically active size regime prior to calcination. AFM of AuCu particles on top of ARES micropillar with heights of  $\sim 2.5$  nm. This AFM was performed prior to calcination with residual carbon from the patterned polymer nanoreactor still present surrounding each nanoparticle (B) Scanning transmission electron microscopy of Au-Cu alloy nanoparticles in catalytically active size regime. The particles were synthesized on an electron-transparent silicon nitride thin film but have similar sizes as the ones on ARES micropillars and show a homogenous alloy structure. From left to right: high-angle annular dark field (HAADF) images, annular bright field (ABF) images, energy-dispersive X-ray spectroscopy (EDS) elemental mapping results for Au L and Cu K lines. All images share the same scale bar of 2 nm. HAADF and ADF images were denoised using the block-matching and 3D filtering (BM3D) method. Figure adapted from reference.<sup>165</sup>



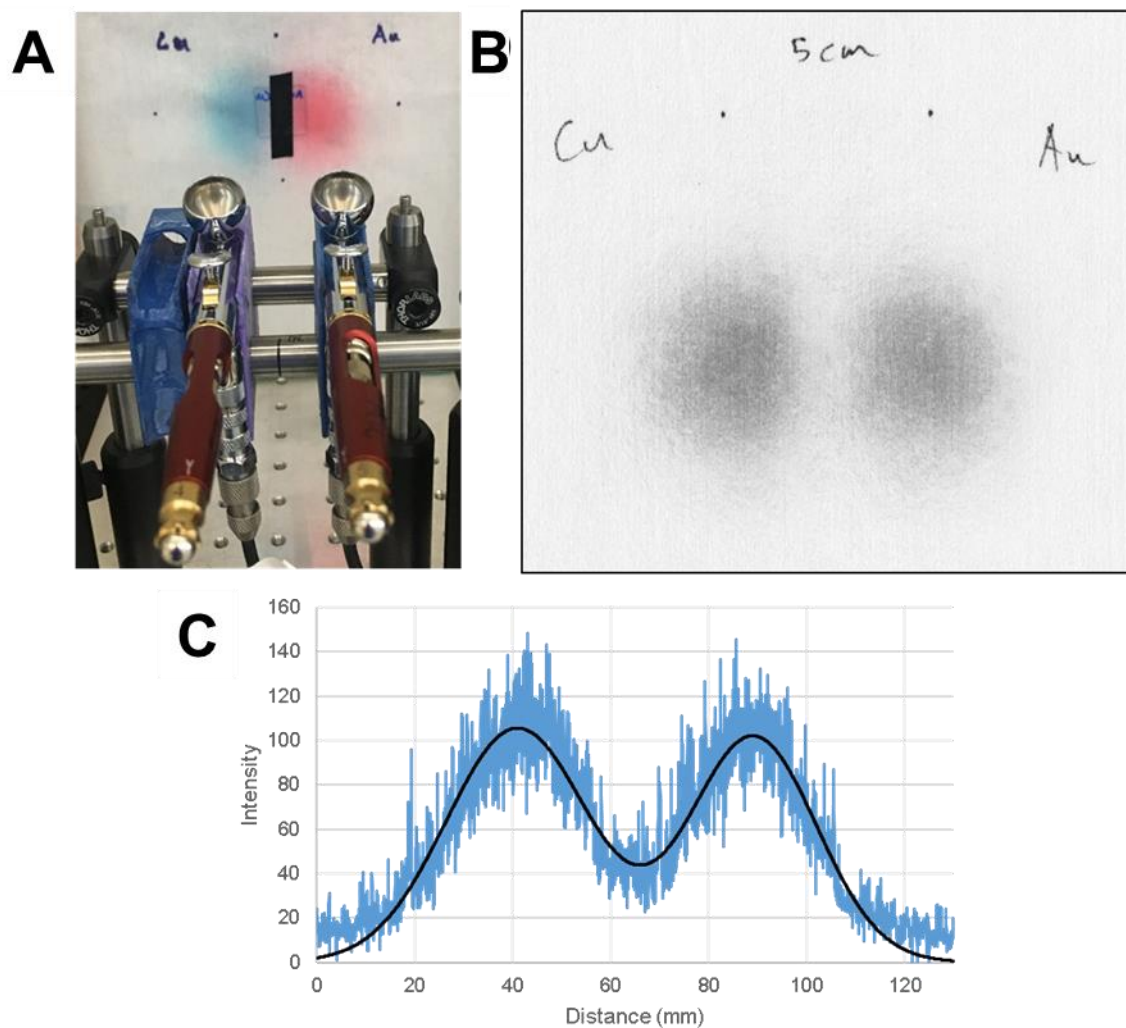


**Figure 3.9:**  $\text{Au}_x\text{Cu}_{1-x}$  Composition gradient. (A) Photograph of air brushes spraying Au and Cu PEO-*b*-P2VP inks onto a pen array. (B) Optical scan of spray profiles for Au and Cu sources. (C) Spray profile intensity across the center of both spray profiles, fit to a double Gaussian curve. This fit was used to calculate the composition as a function of position across the pen array.

This compositional gradient was patterned onto three 5 mm wide ARES micropillar substrates, requiring the 1.5 cm gradient to be split evenly into three sub-gradients. Each substrate was patterned using a third of the pen array, resulting in three gradients with ~24% composition change from edge to edge. Across each ARES substrate, there are 12 columns of patches. Assuming the variation of final particle composition has a distribution of roughly 5%, each vertical column of patches can be treated as a single composition, with a 2% composition change from column to column (Figure 3.10). The particle composition is this precise over the entire array due to the tight correlation between ink composition and resulting particle composition, which has been studied in detail.<sup>91, 92</sup> This compositional gradient was investigated prior to the fabrication of 1.6 cm ARES micropillar substrates. All other compositional screens used the larger substrates, which require a single patterning process but result in the same compositional resolution due to the identical micropillar configuration. All three substrates were heat treated to form catalytically active particles and placed into the ARES reaction chamber. Growths were performed in two temperature ranges: 700-800 °C and 800-900 °C. Each pillar was individually heated to the growth temperature under a total pressure of 20 torr, consisting of C<sub>2</sub>H<sub>4</sub> (partial pressure 13.5 torr) and H<sub>2</sub> (6.5 torr). SWNT growth occurred over 1 min. These growth conditions were determined to be the optimal temperature and growth atmosphere through a growth condition screen using Au<sub>0.5</sub>Cu<sub>0.5</sub> alloy catalysts. Following each growth, the laser power was turned down and a low-power 30 s Raman scan was collected at room temperature. The integrated intensity of the G band peak, normalized to the 950 cm<sup>-1</sup> Si peak, from this room temperature scan (labeled G<sub>max</sub>) is proportional to the yield of the SWNTs on the micropillar. Ten growths were performed for each nanoparticle composition, five in each temperature range, amounting to a total of 360 growth experiments.

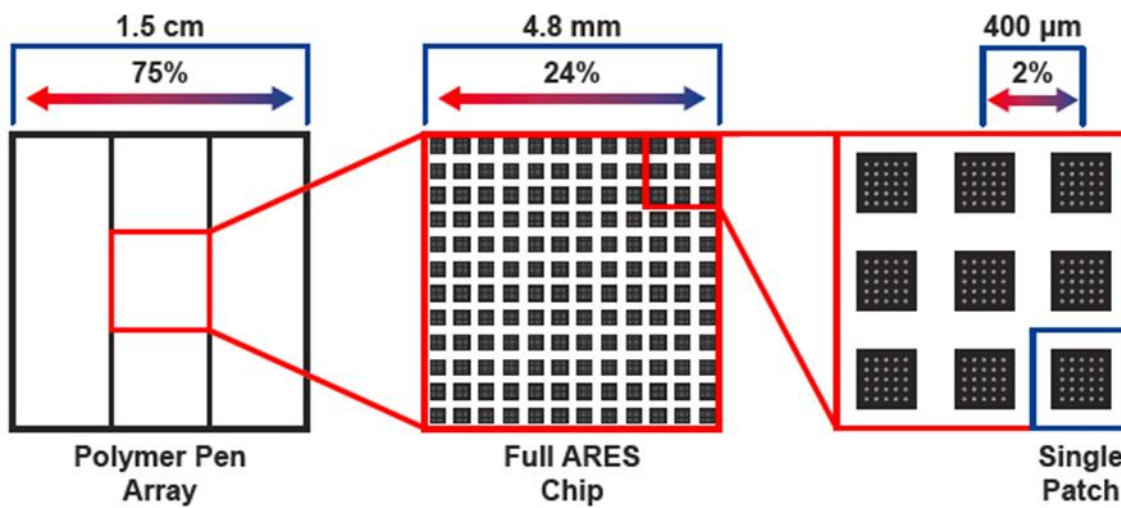


**Figure 3.10:** Compositional breakdown of the 75% composition gradient across three 5 mm substrates. Figure adapted from reference.<sup>165</sup>

The average  $G_{\max}$  values were analyzed as a function of nanoparticle composition, visualizing the growths performed at 700-800 °C (Figure 3.11 A) with representative Raman spectra in the G-band region of the SWNTs are shown for five different alloy compositions (Figure 3.11 C). Growths performed between 800-900 °C were also analyzed (Figure 3.11 B). The largest increase in catalytic activity was found at  $x=0.75$  for both growth temperatures. While this composition was not previously known for its ability to catalyze SWNT growth, it has been shown to have enhanced catalytic activity in electrochemistry, with  $\text{Au}_3\text{Cu}$  exhibiting a peak activity for the reduction of  $\text{CO}_2$  greater than any other composition in the Au-Cu system.<sup>236</sup> Moreover, higher overall SWNT yield was observed in the lower-temperature range. Taking melting point depression into account, these growth temperatures are near the melting points of AuCu nanoalloys, with particles containing a higher gold content having higher melting temperatures<sup>234</sup>. Thus,

the lower (700-800 °C) and higher (800-900 °C) growth temperatures may correspond to solid and liquid catalysts, respectively. Furthermore, it has been shown previously that average particle size increases with Au content owing to the larger lattice constant of Au compared to Cu.<sup>237</sup> In this study, the molar metal loading was kept constant across our gradient, yet the average SWNT diameter increases with Au content (Figure 3.12), which can be attributed to the increase in lattice constant. These SWNT diameters were measured using *ex situ* Raman spectroscopy, correlating the radial breathing modes to the corresponding SWNT diameters for each composition.

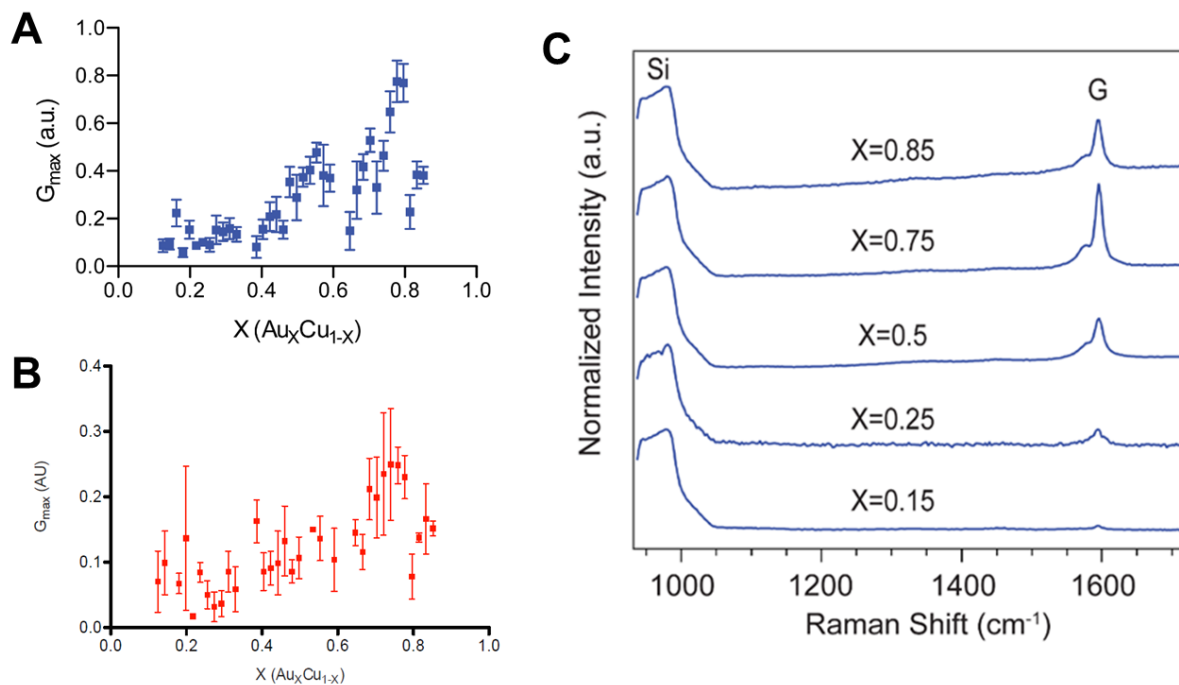


**Figure 3.11:** Compositional breakdown of catalytic activity. (A) Integrated intensity of the SWNT Raman G band as a function of catalyst composition for growths performed between 700 °C and 800 °C. Error bars represent SEM. (B) Growths performed between 800 °C and 900 °C. The  $G_{\max}$  peaks at  $X = 0.75$  suggests  $\text{Au}_3\text{Cu}$  is the composition that exhibits the highest catalytic activity for SWNT growth. (C) Representative Raman spectra from growths on ARES micropillars at five compositions normalized to the Si peak. Figure adapted from reference.<sup>165</sup>

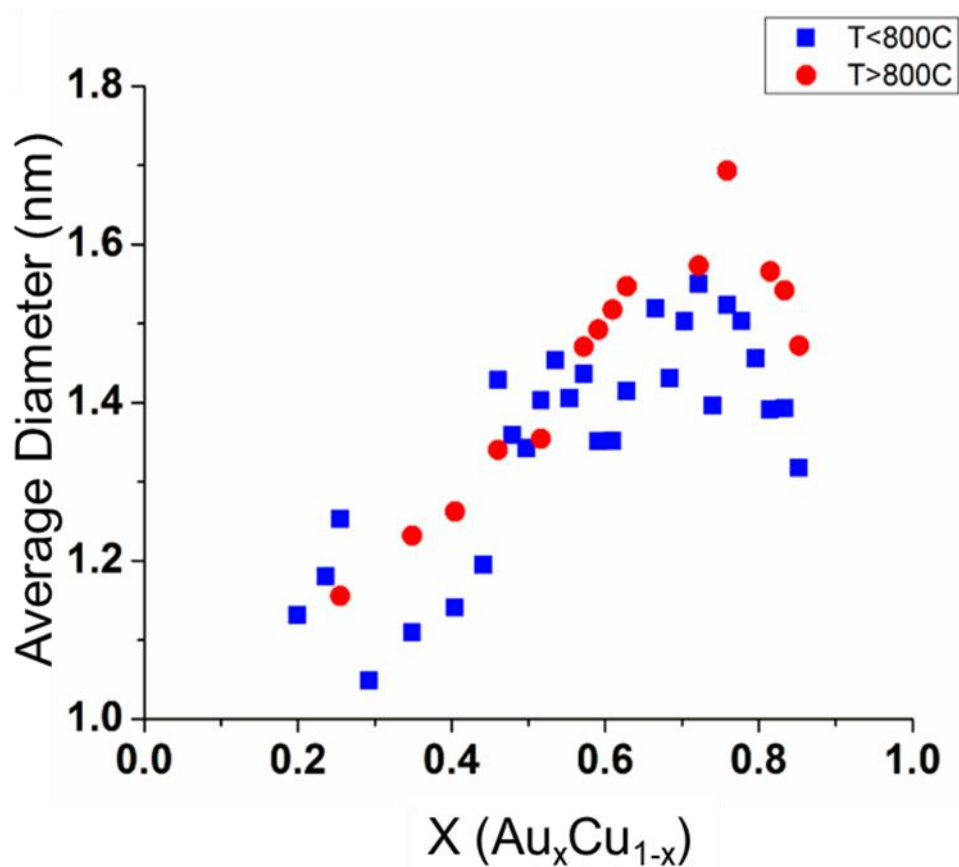


**Figure 3.12:** Average SWNT diameter as a function of Au content. RBMs were collected across the compositional array. The diameter of a SWNT is inversely proportional to the RBM ( $d=248/\text{RBM}$ ). Figure adapted from reference.<sup>165</sup>

These observations of enhanced catalytic activity at Au<sub>3</sub>Cu were not limited to the ARES experiments. The results were independently confirmed with more traditional tube furnace-based thermal CVD growth experiments, where the appropriate amounts of Au and Cu were used in the form of salts (auric acid and cupric nitrate) dissolved in ethanol followed by dip coating of SiO<sub>2</sub> substrates. Samples were made at compositions of X = 0, 30, 50, 70, and 100. While the products

from these growths exhibited a higher D-band intensity due to an excess of ethylene being present (the tube furnace growths were performed at atmospheric pressure, while ARES growths were carried out at 20 torr; excess ethylene leads to more disordered C), the G-band trends for the growths performed with the SPBCL-synthesized particles were mirrored using this more conventional particle synthesis and growth method (Figure 3.13).

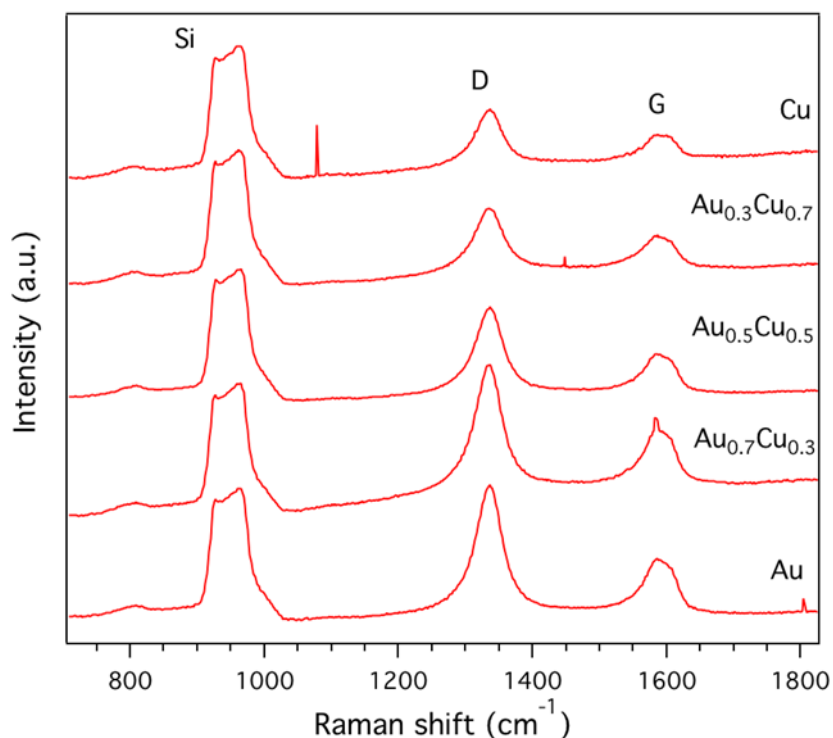


**Figure 3.13:** Raman spectra of SWNTs grown from dip coated catalyst. Raman spectra exhibit similar trends to those seen in SPBCL ARES spectra, with an increased catalytic activity at  $\sim$ Au<sub>3</sub>Cu. Figure adapted from reference.<sup>165</sup>

Following the catalyst hit found at  $\text{Au}_3\text{Cu}$ , the next focus was on expanding the Au-Cu system to include Ni. Ni was chosen for two reasons. First, it is a metal traditionally used in SWNT growth. Second, the Au-Cu-Ni phase diagram exhibits a wide range of particles structures due to the miscibility of Cu with both Au and Ni and the immiscibility of Au and Ni. On the nanoscale, this is expressed in alloy (Au-Cu, Cu-Ni) and Janus (Au-Ni) structures being present depending on composition. We chose the Cu-Ni bimetallic system as the first gradient to investigate as Cu and Ni have been shown to form an alloy structure.<sup>92</sup> A Cu-Ni composition gradient of PEO-*b*-P2VP was spray coated onto a 2 cm hard transparent coated PPL array and subsequently patterned onto a 40-patch, 1.6 cm wide ARES micropillar substrates. Multiple patterns were produced using the same gradient to allow for different growth procedures on the same underlying nanoparticle gradient. The nanoparticles were formed using the traditional SPBCL two step heat treatment, followed by a calcination to remove excess carbon. One substrate was loaded into the ARES system for high throughput growth. After the chamber was evacuated, it was back filled with 20 mTorr of growth atmosphere (15 mTorr  $\text{C}_2\text{H}_4$ , 5 mTorr  $\text{H}_2$ , 2 ppm  $\text{H}_2\text{O}$ ). Preliminary growths were performed, varying the growth temperature, until an optimal temperature was found at  $\sim 840$  °C. With the conditions found for the Cu-Ni system, growths were performed across the 40 patches, 5 pillars in each patch, 200 growths total. Using the G band peak, normalized to the Si peak, the growths were analyzed for the total amount of SWNT's grown (Figure 3.14). A peak in catalytic activity was found at 75% Ni, a composition of  $\text{CuNi}_3$ . Similar to the catalyst hit found at  $\text{Au}_3\text{Cu}$ , this catalyst composition had not previously been discovered as an ideal catalyst for SWNT growth, but had been seen as a composition with enhanced catalytic activity for other applications, this time for hydrogenation of vegetable oils.<sup>238</sup>



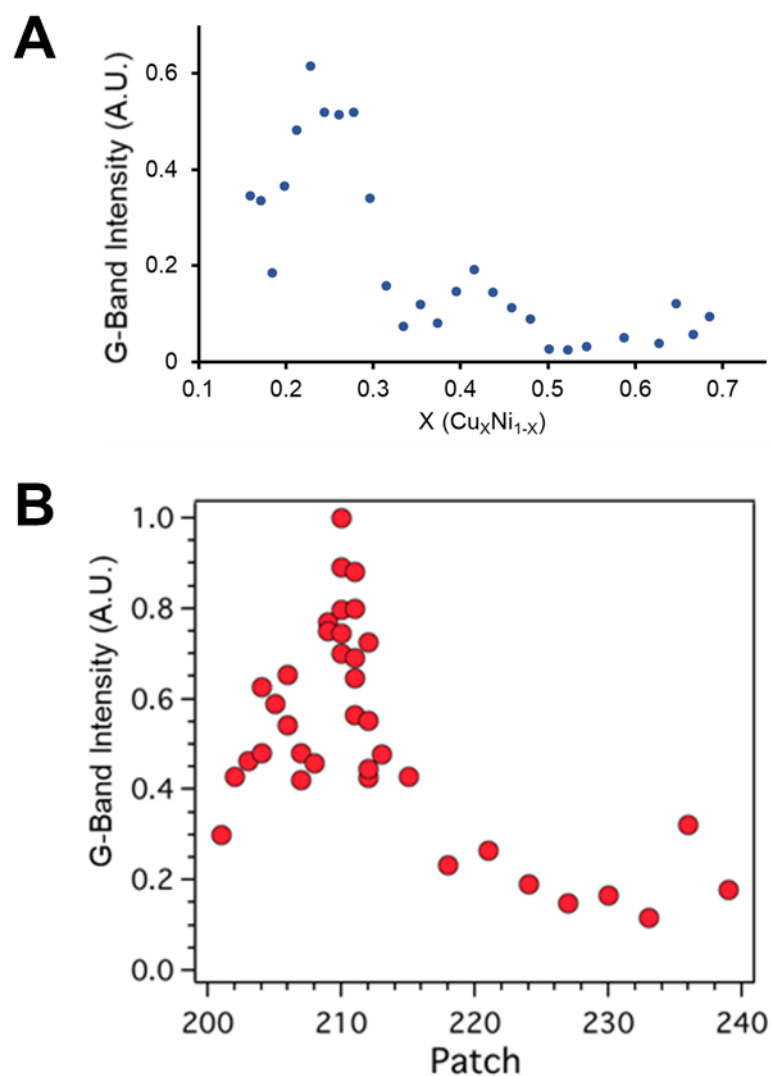


**Figure 3.14:** G-band intensity, normalized to the Si Raman peak, as a function of Cu-Ni composition. (A) 200 growths performed in ARES, resulting in a catalyst hit at CuNi<sub>3</sub>. (B) The same catalyst peak was found using traditional tube furnace growth, *ex situ* Raman spectra was used to collect a representative spectrum from the center pillar of each patch (Patch 210, on this gradient, correlates with the composition CuNi<sub>3</sub>)

In addition to the growths performed in the ARES system, a second gradient on ARES micropillars was used in a traditional tube furnace growth. The entire 40 patch gradient was calcinated under air, followed by a growth performed under Ar, C<sub>2</sub>H<sub>4</sub>, and H<sub>2</sub> at 840 °C. Post-growth, *ex situ* Raman spectra were collected across the gradient (Figure 3.14 B), with more spectra collected at the composition which exhibited the highest catalytic activity, CuNi<sub>3</sub>. This data agrees with the findings from the growths performed using laser induced CVD in the ARES system. This again confirms that the SPBCL catalyst hits found using this screening platform are not limited to the ARES system and can be extrapolated to other growth methods.

The screening of the Au-Cu-Ni bimetallic composition phase space was continued with the investigation of Au-Ni bimetallic nanoparticles. Using the same parameters as the Cu-Ni gradient (2 cm SiO<sub>2</sub>-coated tips, sprayed with linear composition gradient, patterned onto a 1.6 cm micropillar substrate), multiple patterns were prepared. After heat treatment to synthesize the nanoparticles, a calcination process was performed (650 °C for 15 minutes), followed by a SWNT growth at 840 °C under an atmosphere of H<sub>2</sub>, Ar, and C<sub>2</sub>H<sub>4</sub>, flowed at rates of 100, 500, and 20 sccm, respectively. The analysis of this growth was performed by collecting a single Raman spectrum from the center of pillars across a row of patches. This analysis exhibits an increase in G band intensity with increased Ni content (Figure 3.15). The Au-Ni system was the first system encountered that did not have any catalyst hits found, but instead a global trend. This is hypothesized to be caused by the immiscibility of the two elements, and the resulting G-Band intensity that is solely dependent on the quantity of Ni, the more dominant catalytic composition, present on the sample.

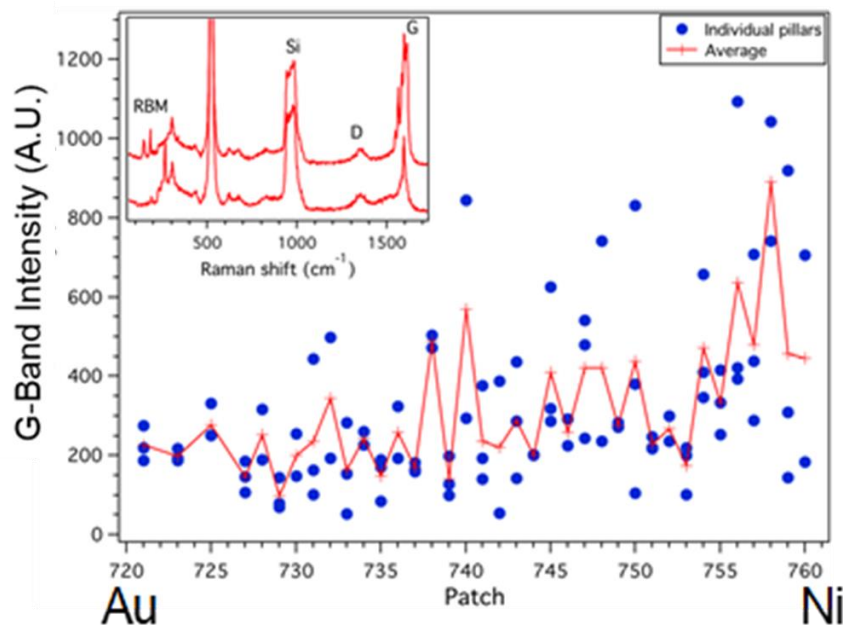


**Figure 3.15:** G-band intensity as a function composition of Au-Ni nanoparticles. SWNT growth was performed in a tube furnace with analysis completed with *ex situ* Raman spectroscopy. Inset Raman spectra exhibit the presence of RBM, confirming SWNT growth.

### 3.3 Experimental Methods

#### 3.3.1 Fabrication of Micropillar Substrates

Using a silicon on insulator (SOI) wafer, (Si device thickness 10  $\mu\text{m}$ , buried oxide thickness  $\geq 1 \mu\text{m}$ ), a hard mask, if used, was deposited (typically  $\text{SiO}_2$  through E-beam deposition). Next, a positive photoresist, S1805, was spin coated onto the wafer at 4000 RPM, resulting in a film thickness of  $\sim 450 \text{ nm}$ . Photolithography was then performed using similar bake, exposure, and develop methods used in fabricating Si masters for PPL arrays. Once the photoresist mask was produced, if a hard mask was used, the  $\text{SiO}_2$  hard mask was etched, either by wet etching with HF or dry etching with  $\text{CF}_4$  followed by the removal of the photoresist by acetone. If no hard mask

was used, i.e. the photoresist is used as the mask for the Bosch cycle etch, a second hard bake treatment was performed at 115 °C for 5 minutes. With the mask formed, a Bosch cycle etching procedure was performed, oscillating between an etch step ( $\text{SF}_6$ ) and a protective deposition step ( $\text{C}_4\text{F}_8$ ). This procedure was performed until the Si had been etched down to the buried oxide layer, producing thermally isolated Si pillars on a  $\text{SiO}_2$  film. Finally, the mask used was removed. If a hard mask was used, a wet HF etch was performed to remove the  $\text{SiO}_2$  hard mask. While this will also etch the exposed buried oxide layer, the hard mask (~500 nm) should be completely removed prior to complete etching of the buried oxide layer ( $\geq 1 \mu\text{m}$ ). If hard baked photoresist was used as a mask, an oxygen plasma cleaning treatment (5 min at 30-60 W) was performed to remove all remaining photoresist. Before catalysts were deposited on the micropillar surface, the top of the micropillar was modified to become an oxide surface, either  $\text{Al}_2\text{O}_3$  or  $\text{SiO}_2$ . For  $\text{Al}_2\text{O}_3$ , an ALD method was used to deposit 3-5 nm of  $\text{Al}_2\text{O}_3$  through sequential reactions of  $\text{Al}(\text{CH}_3)_3$  and water, forming a monolayer of  $\text{Al}_2\text{O}_3$  for during each cycle. For  $\text{SiO}_2$ , the Si pillar was thermally oxidized through a dry oxidation treatment (4 hr at 900 °C in air). For patterning, these pillar were made hydrophobic by vapor treatment, using a 1:1 hexamethyldisilazane:hexane solution in a sealed desiccator for 24 hours.

### ***3.3.2 Tube Furnace Growth of SWNTs***

Substrates with catalytic nanoparticles were loaded into the center zone of a 1-inch diameter quartz tube furnace. A calcination process was performed under air at 350-700 °C for 15 min to 2 hours. The furnace was then heated to the SWNT growth temperature (750-1000 °C) under a constant flow of argon (500 sccm) and hydrogen (200 sccm). Once the furnace reached the growth temperature, SWNT growth was initiated by flowing in controlled amounts of a hydrocarbon

precursor (ethylene or ethanol) for 5-15 min. Following the growth period, the furnace was turned off and allowed to cool to room temperature under a constant argon stream.

### **3.3.3 ARES Growth of SWNTs**

For high throughput SWNT growth, a laser-induced system was used (ARES). Before being placed into the vacuum chamber, the substrate with pillars was calcinated in a tube furnace under air at 350-700 °C for 15 min to 2 hours to remove residual carbon from the nanoparticles. After loading the substrate into the ARES chamber, it was pumped down to a base pressure of  $\sim 1 \times 10^{-6}$  torr overnight followed by backfilling the chamber with H<sub>2</sub> to the growth pressure. Using a 532 nm laser, as both a heating source and a Raman excitation laser, 10  $\mu\text{m}$  pillars were heated to the growth temperature under the growth atmosphere (20-50 torr containing varying partial pressures of C<sub>2</sub>H<sub>4</sub> and H<sub>2</sub>). The temperature was measured using the ratio of the Stokes and anti-Stokes Si Raman peaks. The G-band carbon peak was integrated as a measurement of carbon deposited on the pillar to calculate the growth kinetics. Due to a noisy Raman signal in the low frequency range, radial breathing modes (RBM) were measured using post-growth Raman maps.

### **3.3.4 Imaging and Characterization of Nanoparticles and Resulting SWNTs**

To collect AFM measurements of patterned polymer domes or nanoparticles, a Dimension Icon (Bruker) was used to perform tapping mode measurements. For the analysis of features on top of micropillars, it was vital to align the AFM cantilever with the center of the pillar to ensure the system did not crash into the side of the pillar. Images were processed in Nanoscope Analysis software. To investigate SWNT products from tube furnace growths and to analyze RBM on ARES micropillars, additional Raman spectra were collected *ex situ* using a standard Raman microscope (Renishaw InVia; 514.5-nm excitation).

To collect scanning transmission electron microscopy on the Au-Cu nanoparticle catalysts, polymer nanoreactors containing Au and Cu precursor ions were deposited on 15-nm silicon nitride membranes using dip pen nanolithography and thermally treated under the same conditions as used on ARES micropillars. Scanning transmission electron microscopy imaging was performed on a JEOL ARM200 equipped with a CEOS probe corrector and dual energy-dispersive X-ray spectroscopy detectors. The high-angle annular dark-field images were collected with a collection angle of 68–280 mrad, and annular bright-field images were collected with a collection angle of 8–34 mrad.

### **3.3.5 SWNT Catalyst Screening Platform Optimized Workflow**

Polymer pen arrays were made using Si masters, which contained pyramidal pits with a pitch and density to align with ARES substrates. Two polymer solutions, each containing a different metal, were prepared and shaken overnight. Concurrently, the micropillar substrates were treated with HMDS to make them hydrophobic. The next morning, the pen array was spray coated with a composition gradient and used to pattern polymer domes onto the micropillars, using the spray profiles to assign a specific composition to each patch number on the substrate. That night, the substrates were loaded into a tube furnace under an Ar or H<sub>2</sub> atmosphere and stepwise heat treated to form a bimetallic nanoparticle in each polymer dome. Before being loaded into the ARES vacuum chamber, a calcination was performed under air in a tube furnace to remove any residual carbon resulting from decomposition of the polymer dome. The growth gases were back filled into the ARES vacuum chamber and allowed to equilibrate. Growths were performed across the entire gradient over 2-3 days. The *in situ* Raman spectra were analyzed using peak integration

calculations. From start to finish, the screening platform allowed for comprehensive combinatorial screening of multimetallic nanoparticles in 5–6 days.

### 3.4 Summary

Herein, the first property screened using combinatorial libraries synthesized using PPL and SPBCL was described, the catalytic ability to grow SWNTs. First, a substrate was fabricated to allow for isolated heating of micropillars using laser induced heating. Through a multistep etching process, thermally isolated Si micropillars (10  $\mu\text{m}$  tall and 10  $\mu\text{m}$  in diameter) on a  $\text{SiO}_2$  film were fabricated. These micropillars can be exposed to a high energy laser (532 nm, 6 W maximum power) which instantaneously heats the pillar to 700-1200  $^\circ\text{C}$ . This laser can also be used as an excitation laser to collect *in situ* Raman spectra of the SWNTs that are grown on the micropillar. When catalysts are deposited on top of these micropillars, hundreds of individual SWNT growths, with product analysis, can be performed in the time it would take to perform a single tube furnace growth due to the ability to instantaneous heat and cool each micropillar. This allows for a higher number of catalysts and growth conditions to be screened, greatly increasing the throughput of materials discovery.

To fully take advantage of throughput of both the laser induced heating SWNT growth and the SPBCL and PPL combinatorial nanoparticle libraries, they were first proved to be compatible. SPBCL catalysts were confirmed to be catalytically active for SWNT growth when they are synthesized in the correct size regime (2-5 nm in diameter) and properly heat treated (complete calcination to remove excess carbon residues). When properly synthesized on a flat substrate, multiple SPBCL catalysts (Co, Pt, Ag, Pt) were found to be catalytically active for the growth of

SWNTs. To pair SPBCL catalysts with the micropillar substrates, a rotational stage was added to the patterning process to align custom made PPL arrays to align each pen with a micropillar. By patterning polymer domes on top of each micropillar, various homogenous nanoparticles (Co, Ni, Au, Ag, Cu, AuCu 1:1 alloy) were deposited and screened for optimal growth conditions.

With the confirmation of the compatibility of the two techniques (synthesis and screening), combinatorial libraries of multimetallic nanoparticles were deposited onto micropillar arrays. Due to the spacing of the micropillar patches, a near continuous gradient of AuCu alloy catalysts were screened with a ~2% compositional resolution, the highest nanoparticle screening resolution to date. Across two different temperature ranges, multiple trends were found, including a new catalyst hit that was discovered at the composition Au<sub>3</sub>Cu. This process was repeated to complete the Au-Cu-Ni bimetallic systems, including a traditional SWNT catalyst in Ni. Another previously unknown catalyst hit was found at CuNi<sub>3</sub>. In the AuNi system, which, at the 20-50 nm size range studied in literature, does not form an alloyed particle but instead a Janus structure, was found to contain a trend of increasing catalytic activity as a function of Ni content. Using these techniques (SPBCL and PPL for synthesis and ARES for screening), a new high throughput screening platform was developed with a throughput of catalyst screening dramatically higher than traditional methods with a greatly increased compositional resolution.



**CHAPTER 4:**  
**COMBINATORIAL SCREENING OF**  
**CATALYTIC PROPERTIES**

This chapter is based, in part, on the research described in the following publication:

Du, J.S.; Kluender, E.J.; Liu, M.; Ivankin, A.; Chen, P.C.; Hedrick, J.L.; Wolverson, C.; Dravid, V.P.; Mirkin, C.A. "Combinatorial Assessment of Au-Cu Alloy and Intermetallic Nanoparticle Electrocatalysts" in preparation for submission

#### 4.1 Background

Catalysts are responsible for a massive percentage of the world's GDP. Almost the entirety of chemical processes (90%) require a heterogeneous catalyst.<sup>239</sup> These catalyst materials are vital to the synthesis of a wide range of chemicals, from drug synthesis<sup>240</sup> to fuel production.<sup>241</sup> A catalyst is defined as a material or chemical that lowers the energy required for a chemical reaction, often allowing for reactions to undergo that would not be possible without the catalyst, while remaining present after the reaction has occurred. The majority of these catalysts are heterogeneous catalysts which consist of a material on a surface that chemically interacts with reactants in a solution or gas. By using heterogeneous catalysts, the catalysts no longer need to be separated from the resulting products, removing a purification step that is required from homogeneous catalysts. Nanomaterials have proven to be an ideal system for these catalysts due to their high surface area to volume ratio and high surface energy.<sup>242</sup> By the simple nature of being extremely small, a large percentage of the atoms that make up nanoparticles are on the surface and can directly interact with the surrounding chemicals. Additionally, by having these surface atoms that are on curved surfaces, they often contain a higher percentage of dangling bonds that allow for advantageous interactions with chemical reagents.

Catalysts are measured by two properties: efficiency and selectivity. Efficiency is a direct measurement of how well the catalyst is able to transform one chemical into another. When there is a direct chemical pathway which results in one set of reactants turning into one set of products, using high efficiency catalysts is the goal. This is an ideal situation though, as most chemical reactions have multiple pathways and can result in multiple different products. Selectivity is the measurement of just that, the ability of the catalyst to undergo a select chemical pathway, resulting

in a homogeneous product. This is often more important than efficiency, particularly in the pharmaceutical industry where complex molecules need to undergo specific chemical reactions.<sup>243</sup>

For each reaction, the ideal catalyst can vary wildly. Due to the specificity of the surface-reactant and surface-product interactions required for efficient and selective catalysts, each reaction performs differently on a surface. To tailor a specific catalyst to a specific reaction, controlling the atomic surface structure is required. While some metals have proven to be extremely catalytically active for a wide range of reactions (Pt,<sup>120</sup> Pd<sup>243</sup>), they are often expensive materials. To mitigate the cost and to improve activity (both efficiency and selectivity), alloy materials have been studied.<sup>21, 51, 52</sup> Through the alloying of multiple elements, the surface energies can be controlled, altering the surface-analyte interactions for each reaction.<sup>244</sup> This requires not only composition control, but also crystal phase control, as a random mixed alloy would act differently than an ordered structure.<sup>245</sup> Catalytic processes which are based on the chemisorption and desorption of molecules, are highly sensitive to the local atomic arrangement near the catalyst surface. Particularly, even if the overall elemental composition is similar, the crystal structure or chemical ordering of nanoparticle electrocatalysts could lead to drastically different electrochemical properties presumably due to the different electron structure, strain, and chemisorption sites.

While these controls allow for the specific tailoring of catalysts to reactions, it opens up a massive parameter space. The discovery of new catalysts has predominantly been driven by computational methods predicting surfaces of interest.<sup>109, 111, 246</sup> While this has been a valuable resource for materials discovery, ultimately, they are only calculated predictions and experimental limitations may prevent a theoretically perfect catalyst. Scanning probe block copolymer

lithography (SPBCL) synthesis of multimetallic nanoparticles is an ideal method for investigating these predicted structures of interest. Due to the nanoreactors used in SPBCL, it is capable of synthesizing a wide range of complex multimetallic nanoparticles regardless of their composition.<sup>91, 92, 94</sup> Paired with polymer pen lithography (PPL),<sup>95</sup> these nanoparticles can be deposited onto a wide variety of substrates for different catalytic reactions and rapidly probed for their activity, greatly increasing the throughput of material discovery. This was first shown in a study of hydrogen evolution catalysts, computational methods led to the testing of two compositions that were predicted to have ideal hydrogen binding energies: AuCuPt and AuNiPt.<sup>244</sup> Upon synthesis of these materials, it was discovered that while AuCuPt performed as predicted (7 times more active than traditional Pt catalysts per Pt atom), AuNiPt did not perform nearly as well and was only as active as AuPt by itself. With this information, the particle's phase structure was investigated using TEM and it was found that the AuCuPt formed a homogenous alloy (same as used in the computational predictions), but the AuNiPt segregated into a Ni-AuPt Janus structure. Ultimately, for any screening platform to be used to its full potential, it requires powerful computational predictors combined with experimental measurements. This chapter will overview the development of this screening platform for the selective characterization of nanoparticle catalysts with composition spatially encoded. These studies seek to improve the field's ability to rapidly probe complex nanoparticles for catalytic activity, driving the discovery of new materials.

## 4.2 Results and Discussion

### 4.2.1 *Universal Well-Plate Reactor for Heterogeneous Catalysis*

With great control of composition and phase structure, SPBCL has the capability of being an ideal synthetic method for screening for new catalyst nanomaterials. In addition to showing catalytic activity for the growth of single walled carbon nanotubes in Chapter 3, SPBCL catalysts have been shown to be catalytically active for a hydrogenation reaction.<sup>91</sup> By altering the nanoparticles composition, an alloy of Pd and Au was found to have higher catalytic activity for the reduction of 4-nitrophenol. This was valuable as a proof-of-concept for catalytic activity, but its catalytic methodology was extremely rudimentary (drop casting a reactant onto a substrate with deposited nanoparticles) and not suitable for high throughput screening of libraries of materials on a single substrate. To allow for the analysis of multiple locations of a single substrate, a well-plate reactor was designed to investigate isolated sections of a single samples. This required a set of materials that is able to form reliable sealed reactors on multiple locations of a substrate and be compatible with extreme catalytic condition, specifically non-aqueous volatile solvents and high temperatures. Additionally, the most promising application of SPBCL catalysts is in the field of electrocatalysis, requiring each section to be electrically isolated.

To investigate individual locations on the library for their catalytic properties, a modified well-plate reactor was developed that allows for the isolation of specific locations of the substrates under a variety of conditions. The reactor is made of 6 separate layers to allow for reliable sealing and isolation of each well: a base plate, a substrate support, a substrate-well seal layer, a bulk well plate, a top seal, and a top plate (Figure 4.1). The base plate is made of a hard metal (in this case stainless steel) with holes for screws to be ran through each layer to forms seals at the bulk well

and top plate levels. The substrate support is made of thermally conductive elastomer to allow for heating of the sample through the base plate, while limiting the hard-to-hard contact between the substrate and the metal base plate that can cause fracturing of the substrate. The substrate-well seal layer will be discussed later. The bulk well plate is made of a hard plastic or metal and makes up the majority of the well volume and forms the isolated wells. The top seal is made of chemically inert elastomer, same material as substrate-well seal layer, to prevent solvent in low-volume wells from evaporating, particularly when using volatile solvents. The top plate is made of a hard metal to compress the top seal and isolate the small solution volumes in the wells. The most important layer of the reactor is the substrate-well seal layer. This layer needs to be pliable enough to form a reliable seal between the wells without cracking the substrate, while also being stable enough to withstand extreme chemical conditions. For screening performed at low temperatures (<100 °C), kalrez, a fluoropolymer, was used. It exhibited limited swelling under a wide variety of solvents and produced isolated wells for >48 hours of testing. For higher temperatures (>100 °C), a polytetrafluoroethylene (PTFE) layer, coated in a perfluoropolyether lubricant, was used. This PTFE layer was used at high temperatures because kalrez absorbs solvent at higher temperatures, causing problematic swelling and well-to-well leakage. Both seal layers produced isolated wells for >48 hours without leaching any impurities into the solvents loaded into each well. With this reactor set up, individual reactions can be performed at isolated locations of the substrate under a variety of extreme chemical conditions. To investigate the stability of this reactor during a reaction of interest, a substrate was fabricated consisting of Pd nanoparticles and loaded into the reactor to run a N-alkylation reaction using lubricated PTFE seal layers. 50  $\mu$ l of an o-xylene solution, containing 1 M 1-naphthylamine, 500 mM benzyl alcohol and a saturated  $\text{FeCl}_3 \cdot 6\text{H}_2\text{O}$  cocatalyst,

was loaded into a reactor well. The reaction ran for 18 hours at a reactor base plate temperature of 200 °C. After completion of the reaction, another 50 µl of o-xylene was added to the well and the entire 100 µl was removed and analyzed using gas chromatography-mass spectroscopy (GC-MS) (with a dodecane internal standard). While this reaction was performed with extreme excess of 1-naphthylamine, the product formed with a selectivity for the fully reduced product (Figure 4.2). This reactor shows the capability to be ran at high temperatures with a wide range of reactants and solvents, allowing for the universal screening of catalytic reactions using substrate-based catalysts. While this well-plate reactor was initially designed to screen a composition and size gradient sample synthesized using SPBCL and PPL, it can also be used for reaction condition screening of a more traditionally produced homogenous substrate.

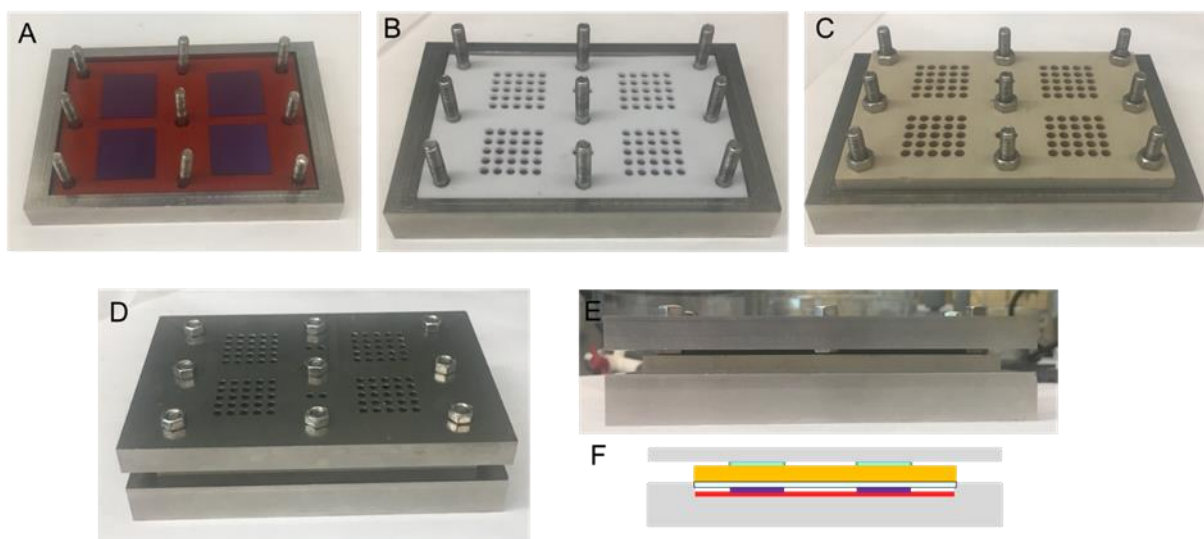


**Figure 4.1:** Set up of well-plate reactor, 5x5 arrays of 3.8 mm circular wells. (A) Substrates are placed on substrate support inside of base plate, with screws facing upwards through 9 bolt holes. (B) Substrate-well seal layer, in this example lubricated PTFE, is placed on top of the substrates, aligning the wells with locations of interest on the substrate. Kalrez is used for experiments performed  $<100$  °C, and lubricated PTFE is used at higher temperatures. (C) The bulk well layer is then loaded on top of the seal layer and screwed tight to isolate each well. Once this is done, the wells are created, and solutions can be loaded. (D) The top seal layer is placed over the wells to prevent evaporation of low volumes and the top plate is screwed down to create a reliable seal. Reaction solutions can also be loaded at this step by piercing the top seal layer with a needle. (E) Side view of the reactor once fully constructed. (F) Vertical scheme of reactor fully constructed. Grey: base plate and top plate. Red: substrate support. Purple: substrates. White: substrate-well seal layer. Yellow: bulk well plate. Blue: top seal layer.



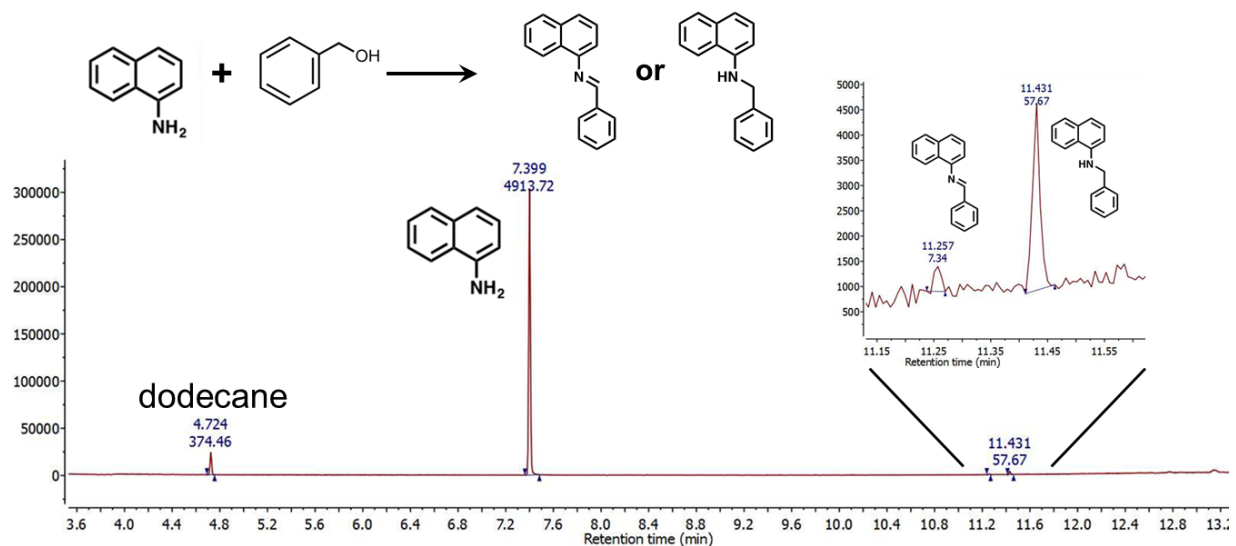


**Figure 4.2:** N-alkylation of 1-naphthylamine in well plate reactor. GC-MS spectra of the resulting product after the reaction ran for 18 hours at 200 °C. These Pd catalysts exhibited a high selectivity for the fully reduced product.

This reactor set up was originally investigated for the used in heterogeneous reactions performed for the chemical transformations of different organic molecules. While this is a viable use of the system, the low turnover of the catalysts due to the low catalyst loading and limited diffusion (two difficulties that are often overcome by high surface area catalyst supports) make it more challenging to produce high throughput testing of results as reactions need to run for longer times. Another application of this reactor is electrocatalysis, which allows for the instantaneous measurement of catalytic activity by measuring IV curves. The well configuration is readily modifiable for a wide range of well sizes, allowing for both low volume heterogeneous catalysis (with volumes ~10  $\mu$ l) as well as larger wells with enough space for electrodes to perform

electrocatalytic screening without the top plate (Figure 4.3). By loading a conductive substrate into the reactor and sealing the bulk well plate to form an open top reactor.

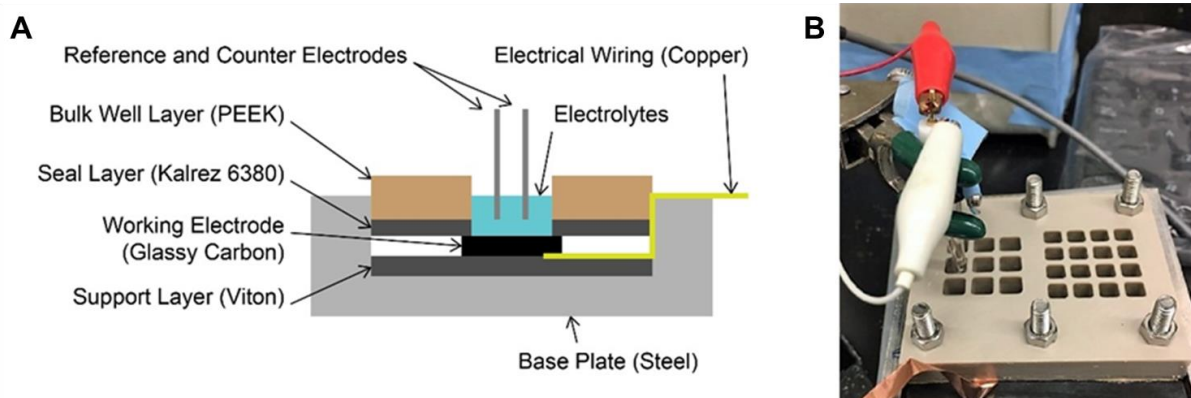


**Figure 4.3:** Configuration of well plate reactor for electrocatalysis (A) Side view schematic of reactor set up, similar to the use for heterogeneous catalysis without the top plate. The working electrode in each well is connected in parallel and the reference and counter electrodes are moved from well to well to test each section. (B) Photograph of well plate reactor testing one of 9 cells. Smaller wells are capable with smaller reference electrodes.

#### 4.2.2 Electrochemical screening of AuCu on glassy carbon films

To perform electrocatalytic screening of bimetallic nanoparticles, Au-Cu nanoparticles were chosen as an ideal test system. They had been extensively studied for their crystal structure and have traditionally been studied for electrocatalytic applications.<sup>236</sup> For SPBCL catalysts to be used as electrocatalysts they need to be patterned onto a conductive substrate. To deposit the isolated nanoreactors that power the SPBCL technique, the surface that is used needs to be hydrophobic to ensure high contact angles with the polymer domes and prevent multiple nanoreactors from aggregating during the patterning and heat treatment processes. This has led to the used of oxide

surfaces due to the ease of silane chemistry to functionalize the surface. While there are some conductive oxides, such as indium tin oxide, their conductivity is not resilient to the heat treatments under reducing atmospheres required for nanoparticle formation through SPBCL.

Therefore, glassy carbon (GC) substrates were used in place of oxide surfaces. GC is a carbon species that is halfway between graphene and amorphous carbon, being made up of entangled ribbons of layers of graphene.<sup>247</sup> This produces a thermally stable conductive substrate that maintains its conductivity even under high temperatures in reducing atmospheres. To make GC hydrophobic enough to pattern nanoreactors onto, it can be functionalized by hexafluorobenzene (HFB). By spin coating HFB onto GC, the  $\pi$ - $\pi$  interactions between the HFB and  $sp^2$  carbon result in a stable hydrophobic surface. To test the viability of the glassy carbon as a working electrode substrate, mechanically polished GC substrates, treated with HFB, were patterned with  $Au_3Cu$ , AuCu, and  $AuCu_3$  composition nanoparticles. Using the well plate reactor described previously (Figure 4.3), oxygen reduction reaction (ORR) tests were performed (each well contained 400  $\mu$ l of 0.1 M KOH). It was found that  $Au_3Cu$  exhibited the lowest turn on voltage and AuCu exhibited the highest current at its peak (Figure 4.4). While this was a positive proof-of-concept for the viability of GC substrates, these trends proved difficult to scientifically explain. Specifically, the lower onset voltage for  $Au_3Cu$  and higher absolute current for AuCu.

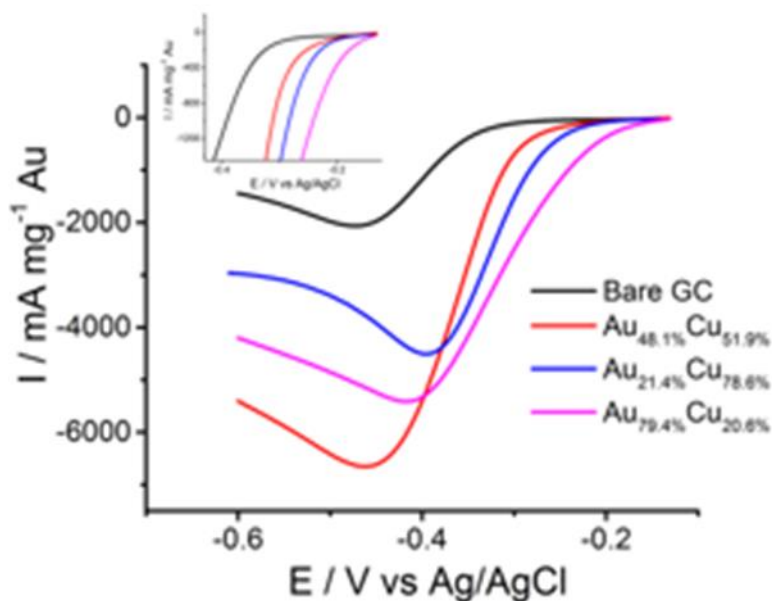


**Figure 4.4:** Catalytic screening of Au-Cu catalysts for oxygen reduction on non-uniform mechanically polished GC.

It was determined that the variations in the IV curves, while partially due to nanoparticle composition, could also be caused by variations in the substrate preparation, specifically the uniformity of the GC substrate. Under further investigation of the mechanically polished GC surface, it was found to have both nano and macro variations that would greatly impact the patterned polymer domes. First, the local roughness of the substrates varied greatly from sample to sample, resulting in inconsistent patterning and irregularly shaped polymer domes caused by pinning of the polymer dome's edges at rough locations of the substrate (Figure 4.5 B). Second, large area bowing (Figure 4.6), attributed to the physical polishing process performed, led to inconsistent patterning over large areas, preventing the full utilization of SPBCL and PPL for

screening large libraries of nanomaterials. Similar to how bowing of the PPL array effects the resulting patterning (Section 2.2.2), bowing of the substrate, even on the order of a micron, can lead to massive patterning discrepancies (Figure 4.5 A).

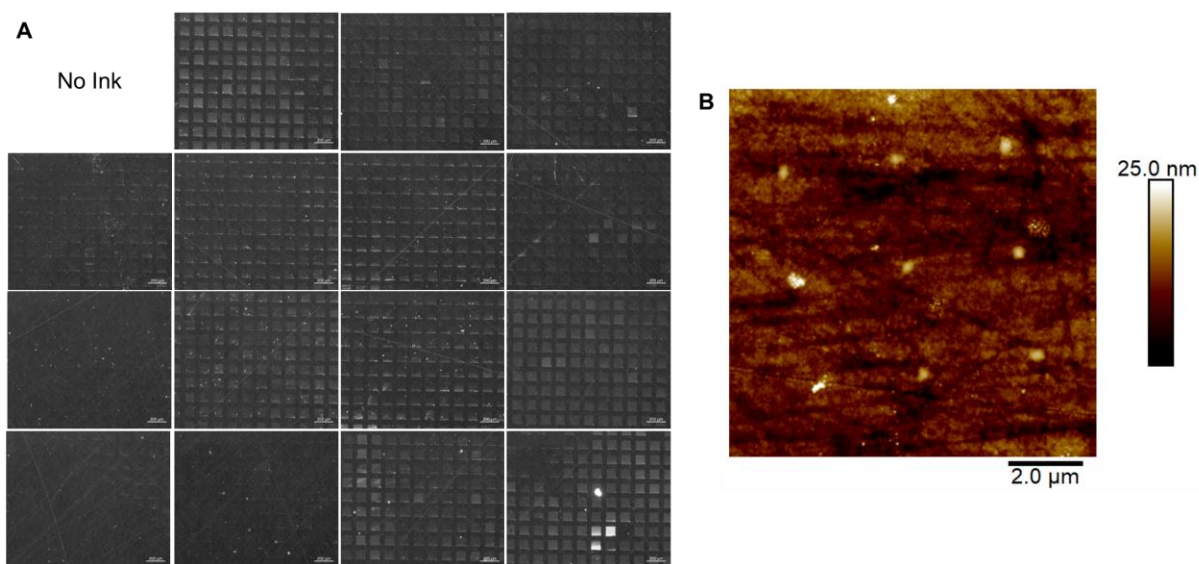


**Figure 4.5:** Inconsistent patterning on mechanically polished GC. (A) Dark field optical images of patterned polymer domes on an outward bowed GC substrate. While there are regions of the pattern that resulted in uniform patterns and the PPL array was in proper contact with the substrate, the center of the substrate applied too high of a force resulted in aggregations of patterns and the edges did not contact at some points resulting in no patterns. (B) AFM image of polymer domes patterned on a rough mechanically polished substrate. The resulting polymer domes are non-uniform in shape due to increased roughness pinning the edges of the polymer dome.

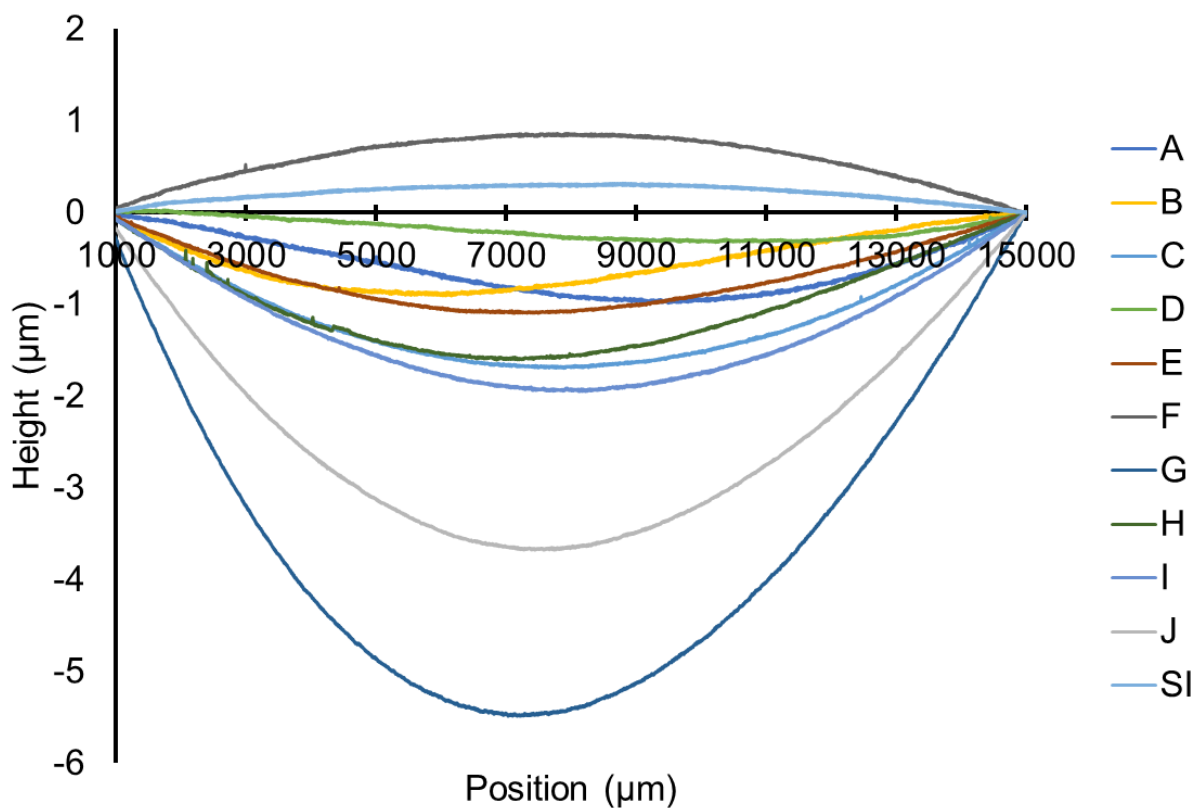


**Figure 4.6:** Profilometry measurements of a set of GC substrates and a Si wafer. Due to the mechanical polishing required for GC, large area height variations occur that prevent large area patterning for reliable catalyst screening.

Ultimately it was determined that mechanically polished substrates would not be viable for large area patterning and screening. To produce reliable conductive substrates that were flat both on the nano and the macro scale, a thin film deposition method was developed. A thin GC film was formed on top of a conductive Si substrate through polymer assisted deposition (PAD).<sup>248</sup> On a Si or SiO<sub>2</sub> substrate, an aqueous solution of polyethylenimine (PEI) and glucose was spin coated at spin rates ranging from 4-8 krpm. These wafers were then heat treated under a 10:1 Ar:H<sub>2</sub>

atmosphere at 1000 °C for 5 min, ramping with a rate of 2 °C per min. After cooling back to room temperature, these substrates were characterized by AFM and Raman spectroscopy. To the eye, the substrates appeared to retain the polished surface of the underlying Si wafer. By AFM, the bulk of the samples exhibited a surface roughness of approximately +/- 1.5 nm (Figure 4.7 B). When spin rates were above 6000 rpm, pinholes occurred (Figure 4.7 A) that would prevent single particle formation once patterned on, indicating spin rates below 6000 rpm were necessary for screening substrates. Raman spectroscopy confirmed the presence of sp<sup>2</sup> carbon and matches literature spectra of GC (Figure 4.7 C). These substrates were found to be as conductive as the mechanically polished GC substrates and would prove to be a viable substrate for electrochemical testing.

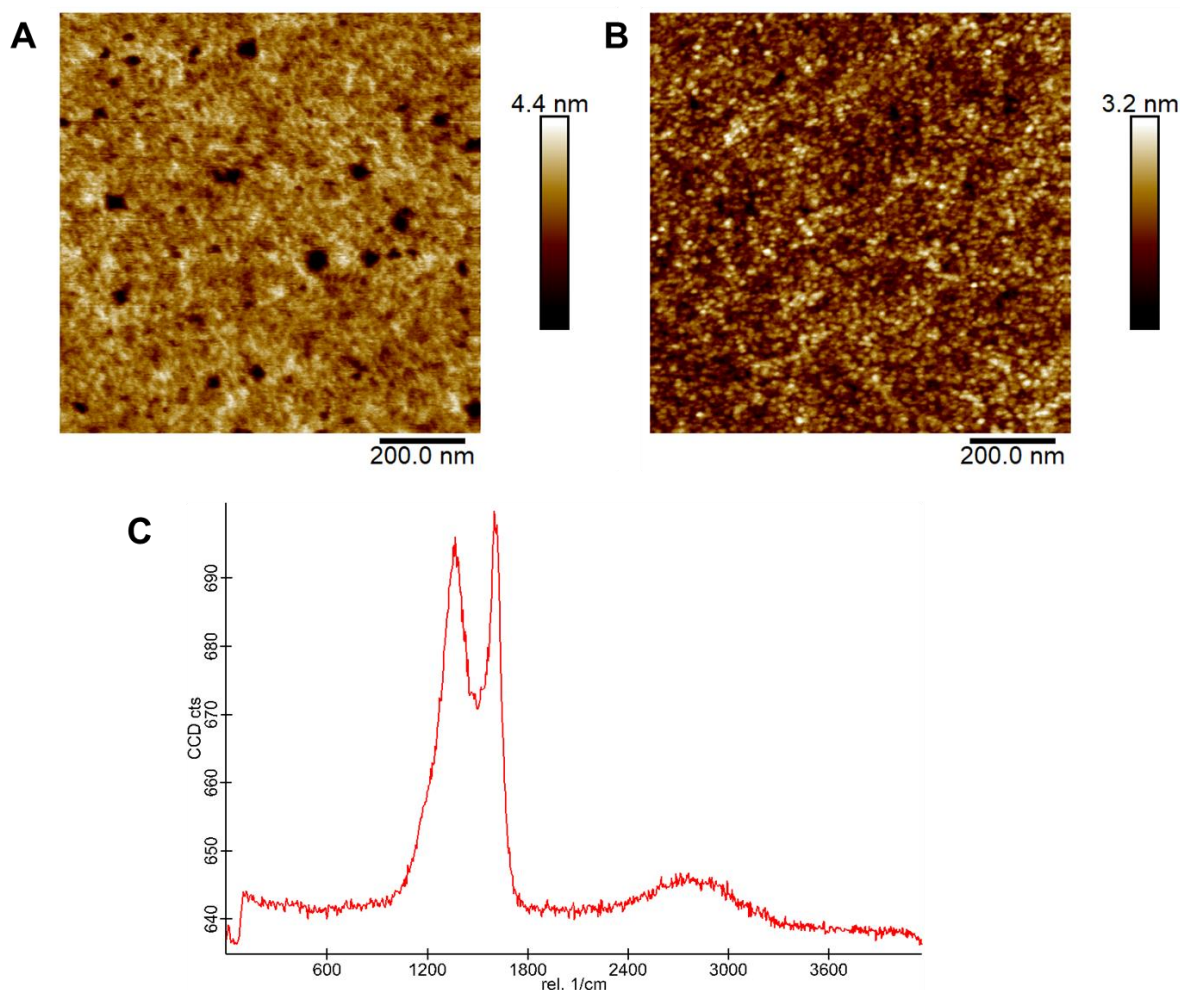


**Figure 4.7:** Characterization of PAD GC films. AFM images of as fabricated GC films when spin coated at (A) 8000 rpm and (B) 6000 rpm. Faster spin rates resulted in non-uniform films that produced pinholes that were not present in lower spin rates. (C) Raman spectra of GC films. The D- ( $1350\text{ cm}^{-1}$ ) and G- ( $1590\text{ cm}^{-1}$ ) band peaks are present, along with a smaller 2D and D+G band peak at  $2800\text{ cm}^{-1}$ .

Using PAD GC films on conductive Si as electrodes, AuCu nanoparticles needed to be deposited on it for screening. To examine the ability to pattern SPBCL inks onto PAD GC films,



they were treated with HFB in the same method as the mechanically polished GC and AuCu loaded polymer ink was patterned with the same conditions. The resulting polymer domes were uniform in shape (Figure 4.8 A) and homogeneous in size across the entire patterned area (Figure 4.8 C). This patterned sample was then heat treated to form nanoparticles and characterized with AFM, showing high yield of single particle formation in each polymer dome. The PAD GC films resulted in more uniform electrode for the fabrication of multimetallic libraries of nanoparticles. In order to test the electrochemical activity of these nanoparticles, ORR reaction was ran using 0.1 M KOH and the AuCu nanoparticles showed an enhanced catalytic activity relative to the bare PAD GC film (Figure 4.9).

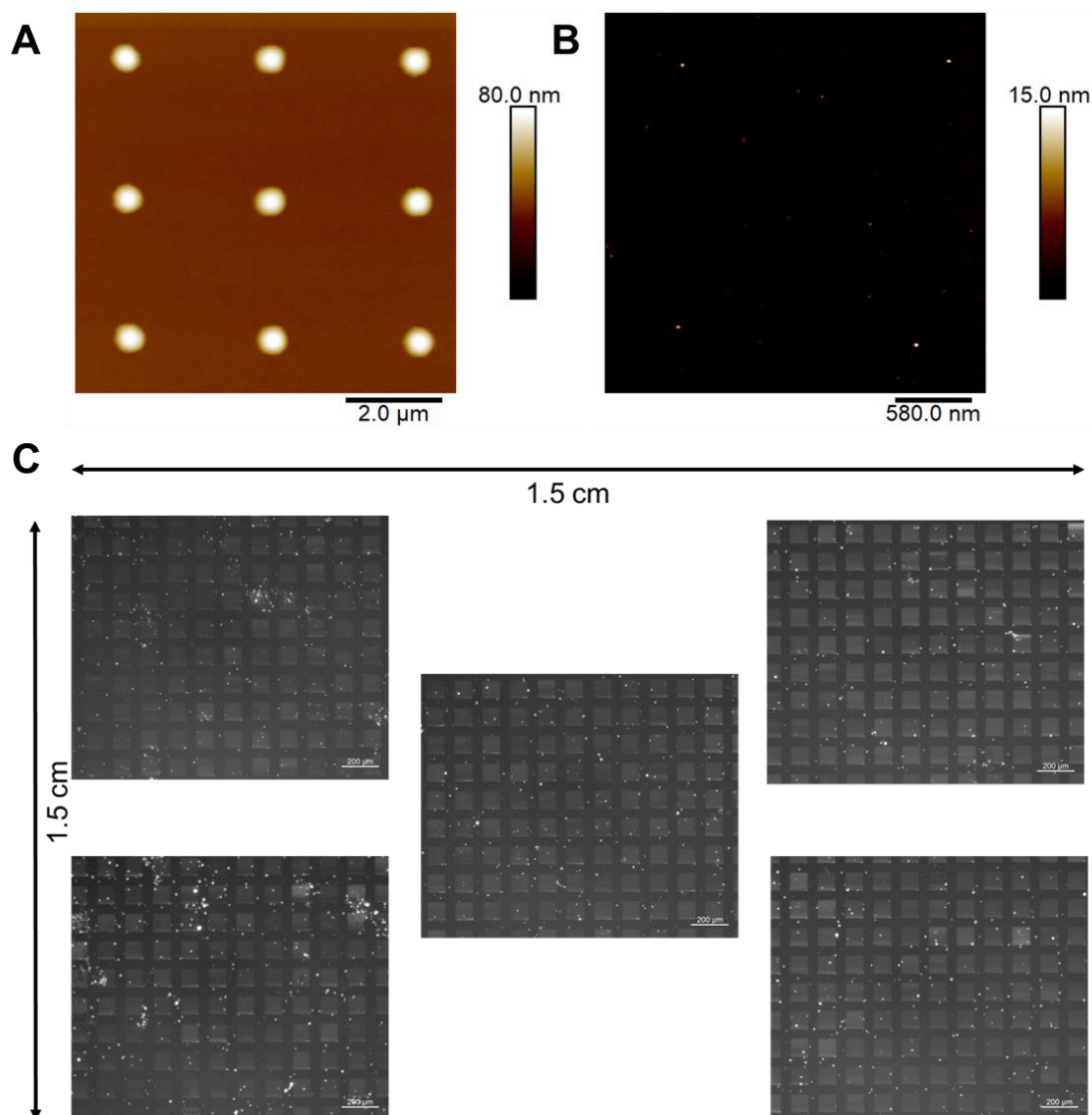


**Figure 4.8:** Characterization of patterns on PAD GC. AFM images of (A) polymer domes patterned on PAD GC and (B) the resulting nanoparticles after heat treatment showing high yield of single particle formation. (C) Optical images of polymer domes patterned across the entire patterned substrate showing high pattern uniformity over the necessary scales for combinatorial screening.

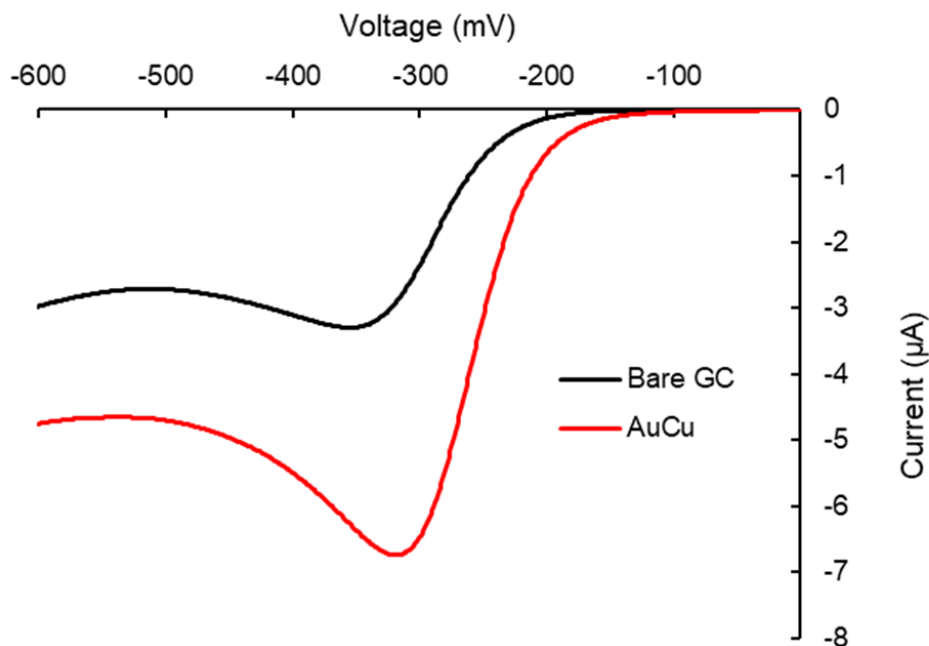


**Figure 4.9:** Characteristic voltage sweep measurements of PAD GC substrates with and without patterned AuCu nanoparticles. The lower turn on voltage and higher peak current indicate that the patterned nanoparticles are electrically connected to the GC substrate and accessible by the reactant solution.

### 4.3 Experimental Methods

#### 4.3.1 Fabrication of PAD GC

To prepare substrates for large area electrochemical screening, a polymer assisted deposition method was used. An aqueous solution of 0.1 g/ml polyethylenimine (PEI) and 0.4 g/ml glucose was prepared and shaken overnight. The concentration of PEI was always kept constant and the thickness of the resulting films could be controlled by the concentration of glucose. This solution

was spin coated onto a Si or SiO<sub>2</sub> wafer at a spin rate of 6000 rpm for 1 min. Then the sample was placed under a 10:1 Ar:H<sub>2</sub> atmosphere for 1 hour. The substrates were then heated to 1000 °C over the course of 8.5 hours, held at 1000 °C for 5 minutes and then allowed to cool to room temperature. These substrates were then made hydrophobic by a hexafluorobenzene (HFB) treatment. 200 µl of HFB was deposited on the substrate for 30 seconds, the excess HFB was removed via spin coating at 2500 rpm for 1 min. The resulting substrates were then hydrophobic enough to be used as patterning substrates for the deposition of SPBCL polymer inks.

#### **4.3.2 *Well-plate Electrochemical Measurements***

To perform oxygen reduction electrochemical measurements in the well-plate reactors, 0.1 M KOH solutions were prepared and bubbled with oxygen to ensure a saturated reaction solution for all measurements. Linear sweep voltammetry measurements were performed on an Epsilon Eclipse Workstation. Ag/AgCl reference and Pt wire counter electrodes were used in each well. Each sweep was performed from an initial potential of 0 mV to a final potential of -600 mV, with a 10 mV/s scan rate, sampling at 1 mV.

#### **4.4 *Summary***

Herein, the analysis of multimetallic nanoparticles for electrocatalytic activity was investigated. First, the properties available for screening was expanded to include heterogeneous and electrocatalytic activity. To isolate individual sections of the combinatorial arrays of nanoparticles, a universal well-plate reactor was fabricated. Using the same dimensions as a traditional 384-well plate system traditionally used for high throughput screening in biological systems, a 6-layer reactor created the necessary forces to seal each well of the reactor with the substrate. The materials used in the reactor depended on the specific reaction it is used for, with extreme conditions

requiring PTFE seal layers. For electrochemical reactions, a flexible fluoropolymer, Kalrez, was used to for reliable seals at significantly lower pressures. Through this reactor, patterned nanoparticle libraries were able to be used for combinatorial screening of nanoparticle catalytic properties.

With a universal reactor to screen catalytic activity, combinatorial libraries of AuCu nanoparticles were fabricated onto conductive substrates to determine an optimal catalyst for half of the water splitting reaction, the oxygen reduction reaction (ORR). In order to pattern large area substrates with uniform patterns, a new conductive substrate was fabricated, consisting of a conductive Si surface coated in a thin glassy carbon film deposited through polymer assisted deposition. This substrate produced a flat substrate to align with the large area PPL array to facilitate the uniform patterning required for screening.

**CHAPTER 5:**  
**SCREENING OPTICAL PROPERTIES OF**  
**MULTIMETALLIC NANOPARTICLES ON PLASMONIC MIRRORS**

This chapter is based, in part, on the research described in the following publication:

Kluender, E.J.; Bourgeois, M.R.; Cherqui, C.R.; Schatz, G.C.; Mirkin, C.A. “Multimetallic Nanoparticles on Mirrors for SERS Detection” in preparation for submission to *ACS Photonics*

## 5.1 Background

The physical properties of nanoparticles have been of significant human interest for a long time, their plasmonic properties in particular. In fact, nanoparticles were used for their optical properties before nanoparticles themselves were even discovered. One of the earliest uses of nanoparticles for optical properties was in the famous Lycurgus cup, made in 4<sup>th</sup> century Rome.<sup>11</sup> The glass used in this cup, dichroic glass, consisted of normal glass with gold or silver nanoparticles dispersed throughout. This gave the glass a color changing effect depending on the direction light is hitting the glass, with transmitted light making it appear red and reflected light appearing green. More recently, nanoparticles plasmonic properties have been exploited for numerous applications, especially in the fields of microscopy,<sup>249</sup> sensors,<sup>250</sup> and even medicinal applications.<sup>251</sup> Plasmonic nanoparticles exhibit these optical properties due to the electron within the nanoparticle interacting with incoming electromagnetic radiations. When interfaced with a dielectric, the nanoparticles electron density will oscillate within and slightly outside of the nanoparticle, creating localized surface plasmons (LSPs).

Nanoparticles are of such interest in the field of plasmonics due to their flexibility, with the LSP of a single nanoparticle is tied to the composition,<sup>252</sup> size, shape,<sup>16</sup> and electromagnetic environment. Using these three variables, nanoparticles are able to interact with light at any wavelength, from UV to IR. In the visible regime, Ag, Au, and Cu are considered plasmonic materials, with their absorption peaks falling between 400 and 600 nm.<sup>252</sup> In the UV, Al nanoparticles are often used in plasmonic applications such as solar cells to extend the region of light utilized.<sup>253</sup> The wavelength of the plasmonic resonant frequency can be tuned through composition by alloying these materials together. For example, by alloying Au and Ag, the location

of the LSP resonance shifts from ~400 nm for pure Ag to ~540 nm for pure Au, following an almost linear trend between the two as a function of relative composition.<sup>254</sup> In addition to controlling the interactions of a single nanoparticle, plasmonic nanoparticles also exhibit coupling effects when multiple plasmonic nanoparticles are brought together, with the specific geometries and separation distances drastically enhancing the strength of the interaction as well as controlling the location of the plasmonic resonance.<sup>255, 256</sup>

Significant experimental advances have enabled fine control over interparticle interactions allowing rational engineering of electromagnetic hot spots and ultra-small mode volumes. Such systems often require fine control over interparticle separation and nanoparticle orientation to facilitate strong plasmon-plasmon interactions. This nanoparticle on mirror (NPoM) geometry, consisting of a thin plasmonic film under an ultra-thin passivation layer supporting a nanoparticle, has gained traction owing to less demanding fabrication requirements.<sup>257, 258</sup> Rather than interactions occurring between discrete nanoparticles, electromagnetic coupling in NPoM structures takes place between LSPs in the nanoparticle and their images induced in the underlying thin film. This allows for the study of reproducible single particles with plasmonic near-field magnitudes comparable to those achieved in dimer systems. Furthermore, by tuning the thickness of the passivation layer, the strength of the electromagnetic coupling between nanoparticle and substrate can be controlled.<sup>259, 260</sup>

While plasmonic nanoparticles have been used over a wide range of applications, sensing has been on the forefront due to the tunability of the different structures. From shifting the LSP resonance by adsorbing an analyte<sup>261</sup> to quenching fluorescent dyes,<sup>262</sup> plasmonic nanomaterials have allowed rapid probing for many specialized sensors. One method that has produced the lowest



limit of detection, even down to a single molecule,<sup>263</sup> is surface-enhanced Raman spectroscopy (SERS). By adsorbing a molecular analyte to the surface of a plasmonic surface, a laser with a wavelength near the LSPR can be used as an excitation source for Raman spectroscopy. The laser's interaction with the nanoparticle creates a field enhancement that leads to a great increase in the Raman signal. The field enhancement occurs twice, first for exciting the analyte by enhancing the incoming laser source and a second time enhancing the Raman scattered photons, leading to what is known as the  $E^4$  enhancement. Au and Ag are traditionally used as SERS surfaces due to their plasmonic resonances in the visible regime where Raman spectroscopy is predominantly performed.

In this chapter, study of the plasmonic properties of SPBCL nanoparticles is performed. First, a mirror substrate is fabricated that is compatible with the sequential heat treatments required for SPBCL synthesis. Second, monometallic NPoM geometries are studied, investigating the effect of gap size. Finally, the first multimetallic NPoM geometry was produced, creating a substrate that exhibited the SERS detection from a single nanoparticle.

## 5.2 Results and Discussion

### 5.2.1 Fabrication of Thermally Stable Mirror Substrates

Scanning probe block copolymer lithography (SPBCL) is an extremely powerful nanoparticle synthetic technique that uses attoliter volume nanoreactors to create complex multimetallic nanoparticles on substrates in ordered arrays.<sup>84, 90-92, 94</sup> This technique has been proven to be a useful tool for screening multimetallic nanoparticles for their chemical properties<sup>165, 244</sup> but can also be used to investigate their physical properties, specifically their optical properties. Synthesizing isolated nanoparticles with controlled composition and size over large areas can be

studied for bulk measurements for catalysis. For the study of optical properties, laser measurements will only hit a single nanoparticle and white light measurements will either be focused on a single nanoparticle or interact with large areas of the substrate without nanoparticles. Therefore, studying SPBCL nanoparticles for optical properties is limited to single particle studies. Initially, this may seem to be a bottle neck for the discovery of new optical materials, but it can also be leveraged to increase the power of the platform. The structure of each deposited nanoparticle can be directly correlated to its optical properties due to the controlled spatial encoding of each nanoparticle. For fundamental studies of single nanoparticles, there are electron imaging techniques that are able to measure the optical signal from a single isolated nanoparticle,<sup>264</sup> but these techniques require specialized instrumentation. Most optical measurements will either take bulk solution measurements or study aggregated nanoparticles which exhibit enhancement from coupling. Neither of these methods are available to SPBCL nanoparticles as they are isolated and spaced microns apart. To increase the intensity of the signal for single nanoparticles, nanoparticle on mirror (NPoM) geometries are required to functionally dimerize the nanoparticle using a plasmonic thin film with a spacer layer.

The majority of literature on NPoM plasmonics use nanoparticles synthesized in solution followed by coordination with a separately fabricated thin film substrate. For the use of SPBCL nanoparticles on a mirror substrate, the synthesis of the nanoparticles will occur on the thin film substrate. For this study, Au thin films are used as the mirror substrate due to their higher stability compared to Ag thin films which are readily oxidized when exposed to air. While Au films can be made hydrophobic, through simple thiol functionalization, and polymer nanoreactors can be patterned directly on them, there are two challenges to achieving suitable NPoM geometries:

thermal stability and heterogeneous nucleation. During the SPBCL process, the substrates are heated to 150 °C to aggregate the metal precursors and 500 °C to fully reduce the metal precursors and decompose the polymer dome to leave a single nanoparticle. For a mirror substrate to be compatible with the SPBCL fabrication process it needs to retain its structure during these heat treatment steps without dewetting, or surface roughness. This requires an adhesion layer between the Au thin film and the underlying substrate (typically SiO<sub>2</sub>) due to the limited chemical interaction between Au (a noble metal) and the substrate, as well as a surface passivation. For electron beam (E-beam) deposition, either Ti or Cr are used as adhesion layers for Au on SiO<sub>2</sub>. Both have a reasonable interaction strength with both the oxide substrate and the Au film on top, increasing the film's overall stability. For most pure Au thin film applications, Ti adhesion layers are chosen, as Cr alloys with the Au at the interface.<sup>265</sup> When picking a composition for the adhesion layer, the thermal stability is key for the NPoM application. For this reason, Cr was found to be the better adhesion layer. While Cr alloys with the Au film at the interface, this interaction is independent of temperature and the alloy phase is thermally stable up to 1000 °C.<sup>266</sup> When Ti-Au thin films are heated, due to the immiscibility of Au and Ti, the Ti layer diffuses through the Au thin film at the grain boundaries, creating a discontinuous Au surface (Figure 5.1 A).<sup>267</sup>

Using Cr to increase the thermal stability of the Au thin film, the surface also requires a passivation layer to prevent heterogeneous nucleation of the metal precursors in the nanoreactor on the Au film. If a polymer nanoreactor were to be patterned onto the Au film and the two-step heating process for SPBCL particle formation was performed, all of the metal precursors would reduce onto the bare Au surface and the concentration of metal precursor's in the nanoreactor would not reach the levels necessary for homogeneous nucleation. To prevent this from occurring,

a passivation layer, with controlled thickness is required. In addition to passivating the Au film during the particle formation, the thickness of this layer is a critical variable in the NPoM geometry system. In most NPoM studies, organic molecular layers are used to control the gap between nanoparticle and thin film, either through self-assembled monolayers (SAMs)<sup>268</sup> or coating the nanoparticle in a core-shell structure.<sup>269</sup> Due to the roughness of the E-beam deposited Au film (Figure 5.1 B), these molecular layers are not thick enough to prevent heterogeneous nucleation on the film. Another common method of creating a gap layer is atomic layer deposition (ALD) of  $\text{Al}_2\text{O}_3$ ,<sup>270</sup> which allows for the formation of sub-nm films. While these films prevented the heterogeneous nucleation on the thin film noted above, the island growth of  $\text{Al}_2\text{O}_3$  on the Au film during the ALD process, which is due to the non-continuous formation of the first atomic layer, created small pinholes that each nucleate a single nanoparticle and prevent complete aggregation of a single nanoparticle in the nanoreactor (Figure 5.1 C).

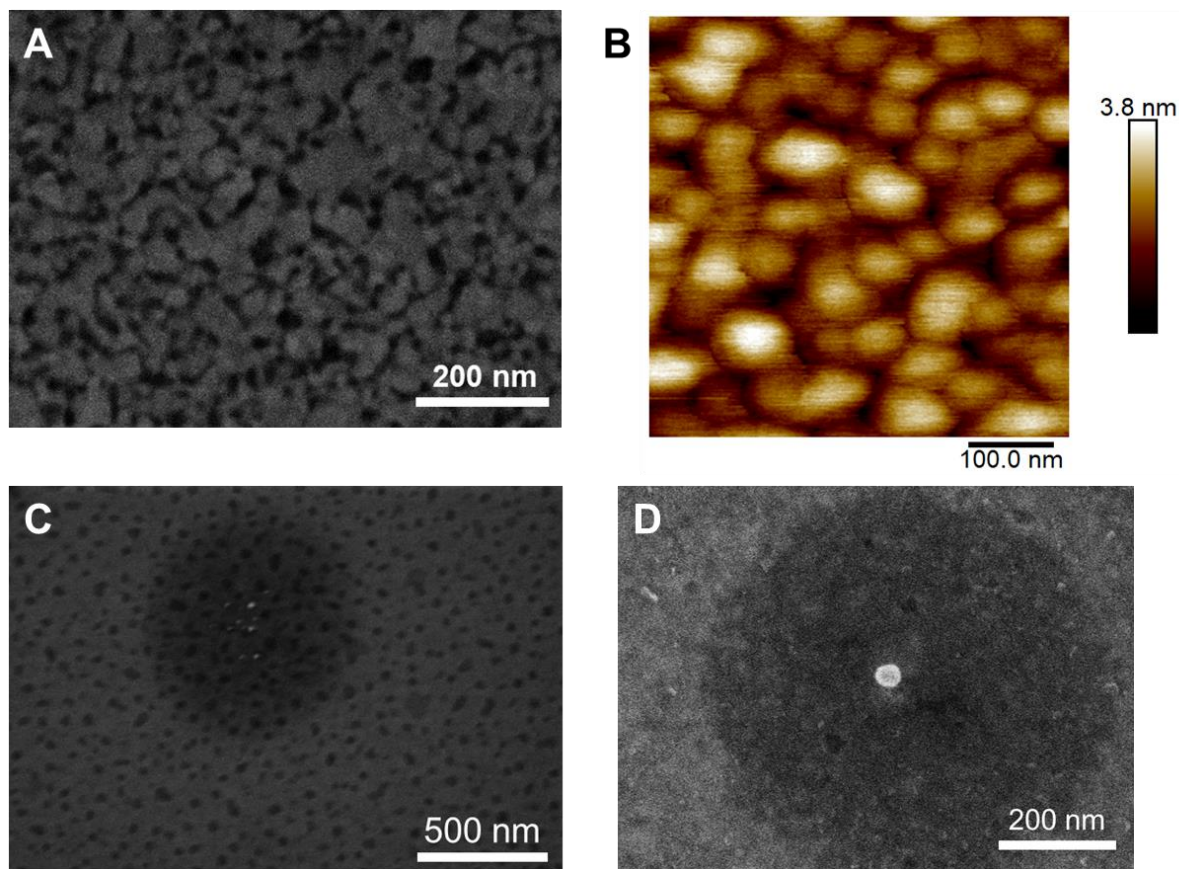


**Figure 5.1:** Characterization of NPoM substrates. (A) SEM image of thermally treated Ti-Au thin film. (B) AFM image of as deposited Au thin film showing roughness of  $\pm 2$  nm. (C) SEM image of polymer nanoreactor on a Cr-Au-Al<sub>2</sub>O<sub>3</sub> substrate after heat treatment. (D) SEM image of polymer nanoreactor on Cr-Au-3MPTS-SiO<sub>2</sub> substrate after heat treatment.

Ultimately, it was determined that a physical deposition method was required to form a homogeneous passivation layer thick enough to prevent heterogeneous nucleation on the surface. To achieve this, a SiO<sub>2</sub> layer was deposited through E-beam deposition using a molecular adhesion layer. Similar to the deposition of Au onto a SiO<sub>2</sub> substrate, the adhesion layer is required to form

a uniform, thermally stable thin film. For this application, the Au thin film was treated with a thiolated silane ((3-mercaptopropyl)trimethoxysilane or 3MPTS) in an ethanol solution overnight. The thiol bonds to the Au surface and presents a silane for the deposited SiO<sub>2</sub> to adhere to. Using this SiO<sub>2</sub>-Cr-Au-3MPTS-SiO<sub>2</sub> substrate, SPBCL nanoreactors are able to be deposited onto the mirror substrate and thermally treated to form single nanoparticles in each polymer dome (Figure 5.1 D). This substrate geometry opens up the possibility to synthesize any SPBCL mono- or multimetallic nanoparticle on a mirror substrate to enhance the scattering intensity relative to the single nanoparticles, facilitating the study of their optical properties.

### **5.2.2 Au nanoparticles on mirror substrates**

Using the thermally stable substrate described in section 5.2.1, the first system studied was a simple monometallic Au nanoparticle on a 50 nm Au thin film. In this system, there is one variable that is easily controlled to investigate its role on the optical properties: the SiO<sub>2</sub> gap layer thickness. During the substrate preparation, the SiO<sub>2</sub> layer that is deposited on the Au thin film can be deposited as thin as 4 nm. This limit was determined by the original Au film roughness (Figure 5.1 B), ensuring that the SiO<sub>2</sub> layer thickness was double the film's roughness to prevent any possibility of the Au film being accessible to the precursors in the polymer dome. To investigate the role of the gap between the nanoparticle and mirror film, three samples of ~40 nm diameter Au nanoparticles were prepared above the following substrates: 4 nm SiO<sub>2</sub> on 50 nm Au film, 8 nm SiO<sub>2</sub> on a 50 nm Au film, and a bare SiO<sub>2</sub> substrate as a "semi-infinite" gap layer. These samples were fabricated using dip pen nanolithography and were all patterned and heat treated identically. In addition to experimental investigation, computation predictions were used compare the trends between the gap layers.

These samples were then analyzed using confocal dark field microscopy, using a white light source. By spacing each nanoparticle 3  $\mu\text{m}$  apart from their nearest neighbor, the spectra from a single nanoparticle was able to be collected. Using a piezo stage, maps were collected of the nanoparticle arrays, showing that each nanoparticle had its own signal that did not overlap with the neighboring nanoparticles (Figure 5.2). This allows for single particle measurements to be made and correlated with SEM and AFM images to connect individual structures to individual spectra. Over the three samples of varying gap thickness, two trends emerged: the signal intensity and resonant wavelength both increased as the thickness of the gap layer decreased (Figure 5.3). As expected, the single nanoparticle on the semi-infinite  $\text{SiO}_2$  substrate had the weakest scattering signal and peaked at approximately 560 nm. This is slightly red shifted from a spherical 40 nm nanoparticles in solution, which was attributed to the interaction with the higher-index  $\text{SiO}_2$  substrate, which also promotes some amount of nanoparticle anisotropy (non-unity aspect ratio), as well as the presence of residual amorphous carbon from the SPBCL fabrication. The presence of a higher refractive index material (amorphous carbon is approximately  $n=1.9-2^{271}$ ) surrounding the nanoparticle will also result in a red shifting of the LSPR peak by up to 20 nm.<sup>272</sup> As the thickness of the gap layer is reduced to 8 nm and then to 4 nm, the LSPR peak further red shifted to 580 nm and 620 nm, respectively. This red shift arises from the longitudinal (head-to-tail) coupling between the LSP excited in the nanoparticle and its image induced in the Au substrate, the strength of which increase with decreasing gap thickness. Note that the gap thicknesses used in this study are large enough ( $>1$  nm) that carrier tunneling between nanoparticle and substrate is not expected to occur. The longitudinal coupling underlying the gap-mod formation also leads to a larger net dipole moment and increased scattering cross section. The nanoparticle on a 4 nm gap

film showed a 10-fold increase in measured dark field scattering compared to the single nanoparticle on the SiO<sub>2</sub> substrate.

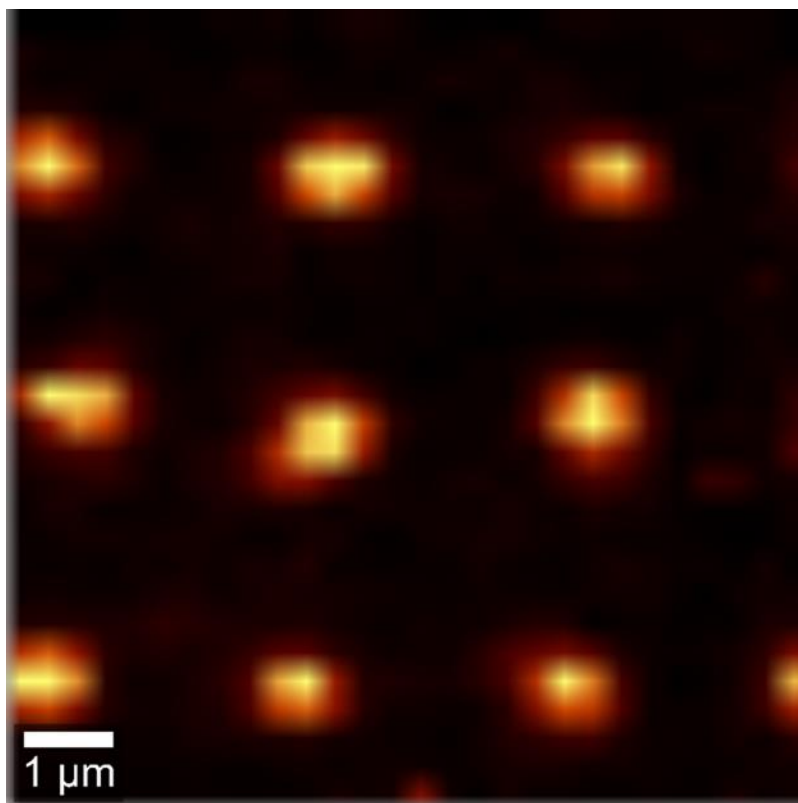


**Figure 5.2:** Backscattering intensity heatmap at 630 nm scattering using white light. This is an image of an array of 40 nm diameter Au Nanoparticles on a 5 nm gap Mirror substrate. When using a white light excitation with an approximately 1  $\mu\text{m}$  diameter beam size, the backscattering signal area from each particle matches the white light beam size. Due to the 3  $\mu\text{m}$  spacing between particles, this allows for each nanoparticle to be individually investigated.



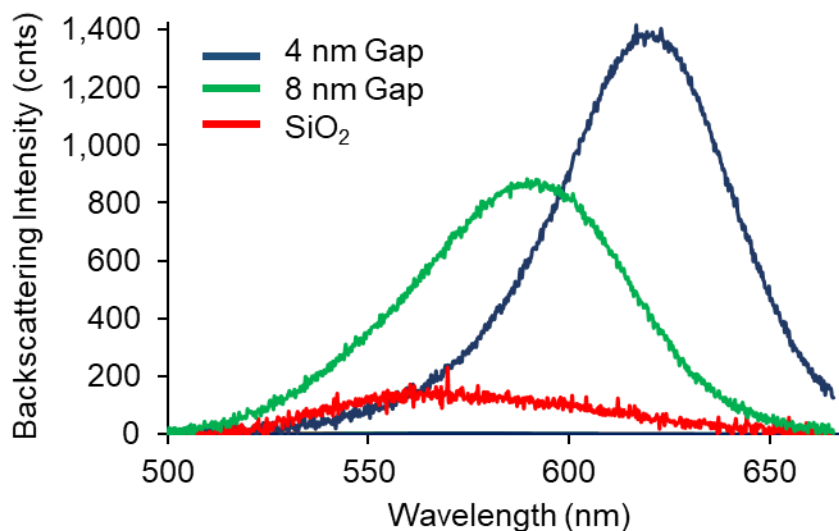


**Figure 5.3:** Dark field spectra of 40 nm Au nanoparticles on three substrates. The bare nanoparticle on a SiO<sub>2</sub> substrate exhibited limited optical scattering. As the gap between the nanoparticle and the plasmonic thin film is lowered, the resulting spectra increases in intensity and red shifts significantly.

Near- and far-field optical properties of the NPoM structures were simulated using the finite-difference time-domain method (FDTD). The same samples were calculated as were examined experimentally, with the gaps rounded to 5 and 10 nm. The trends found in the theoretical models matched those in the experimental results, increase in intensity of approximately 10-fold and a red-shift of approximately 60 nm. The absolute positions of each peak were slightly blue shifted compared to experimental results, likely due to the presence of amorphous carbon surrounding the nanoparticle that was not included in the theoretical predictions. Using E-field heat maps to visualize the spectra, the LSPR peaks were found to lead to the largest increase in E-field at the

junction between the nanoparticle and the substrate, with an additional increase on the opposite side of the nanoparticle. This matches literature precedent and explains the trends observed in the experimental results.

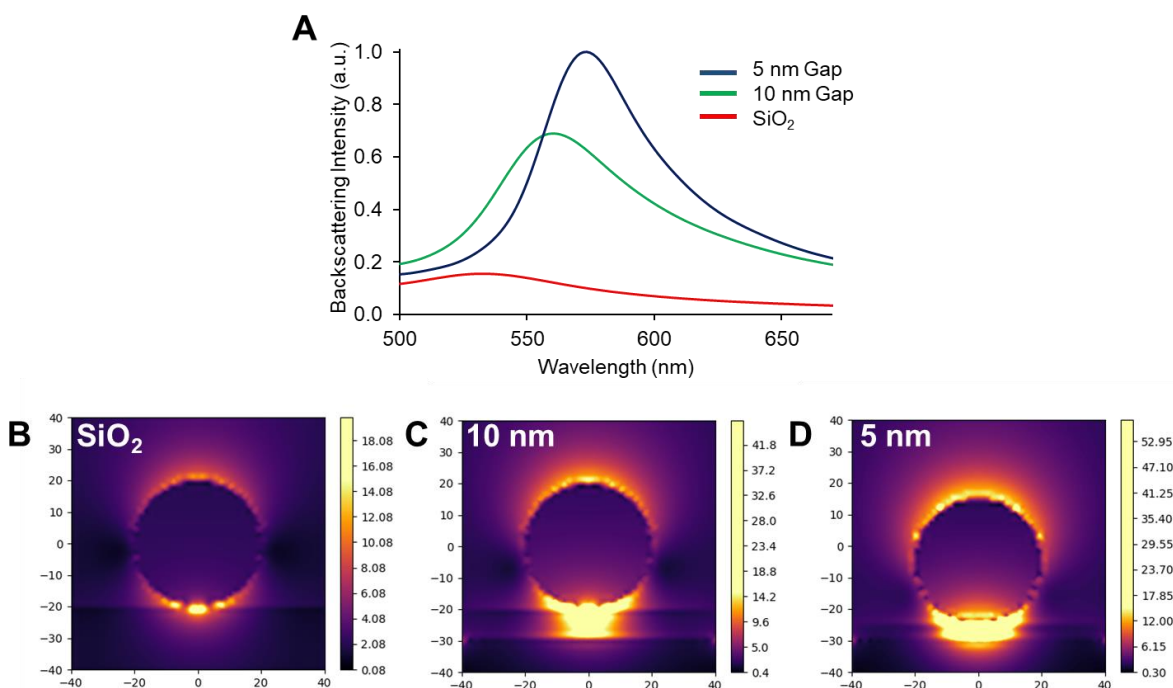


**Figure 5.4:** Theoretical modeling of Au-Au NPoM geometries. (A) Dark field spectra predictions for nanoparticles on SiO<sub>2</sub> (Semi-inf), Au film with 5 and 10 nm SiO<sub>2</sub> gap layers. E-field heat maps of Au nanoparticles on (B) SiO<sub>2</sub>, (C) 10 nm and (D) 5 nm gap substrates.

### 5.2.3 Multimetallic Nanoparticles on Mirror Substrates

Having determined that 4 nm gap layers led to the maximum enhancement of the mirror substrates studied, the next variable to examine is nanoparticle composition, a system that has yet to be investigated in NPoM literature. The two proposed compositions of interest were AuAg and

AuNi. Using SPBCL, both compositions can be readily synthesized by controlling the ratios of the metal salts in the polymer inks. Au and Ag are completely miscible over the entire phase space and forms a homogeneous alloy at every relative composition. Due to the immiscibility of Au and Ni, the AuNi nanoparticle forms a Janus structure, with two separate Au and Ni phases. To preempt the experimental examination of these systems, computational predictions were calculated. On the same three substrates used in the Au system, calculations for the dark field scattering spectra for  $\text{Au}_{0.5}\text{Ag}_{0.5}$  and  $\text{Au}_{0.5}\text{Ni}_{0.5}$  were performed.

When running calculations for the AuNi nanoparticles, it was determined that the orientation of the Janus structure played a large role in the structure's spectra. When the Au phase of the nanoparticle was in direct contact with the mirror substrate, the signal was almost twice as large as when the Au phase is oriented upwards or when the interphase is perpendicular to the substrate (Figure 5.5). The overall trends for the different substrates followed the same general trends, increased intensity and red shift as the gap became smaller, but the orientation played a larger role. Even for the 5 nm gap substrates, if the nanoparticle's nickel phase was in contact with the substrate or the interphase was perpendicular, the intensity would be lower than a nanoparticle with the gold phase in contact with a 10 nm gap substrate. In addition to intensity, there is a small red shift when the gold phase was in contact compared to other orientations. When AuNi nanoparticles were synthesized on these substrates, the resulting spectra varied drastically, with the average spectra of 5 nanoparticles for each sample showing the red shift trend, but not the entire intensity trend (Figure 5.6). This is a result of the SPBCL synthesis process having no control over particle orientation. The nanoparticle structure is consistent throughout the sample, but once the nanoparticle is synthesized, how it is oriented with respect to the substrate is random. Imaging

the orientation of SPBCL nanoparticles is possible with TEM and EDS, but for the NPoM substrates, the samples are too thick for TEM, and SEM EDS does not have the resolution required to determine Janus nanoparticle orientation. It may be possible to measure the nanoparticle orientation using scanning tunneling microscopy.

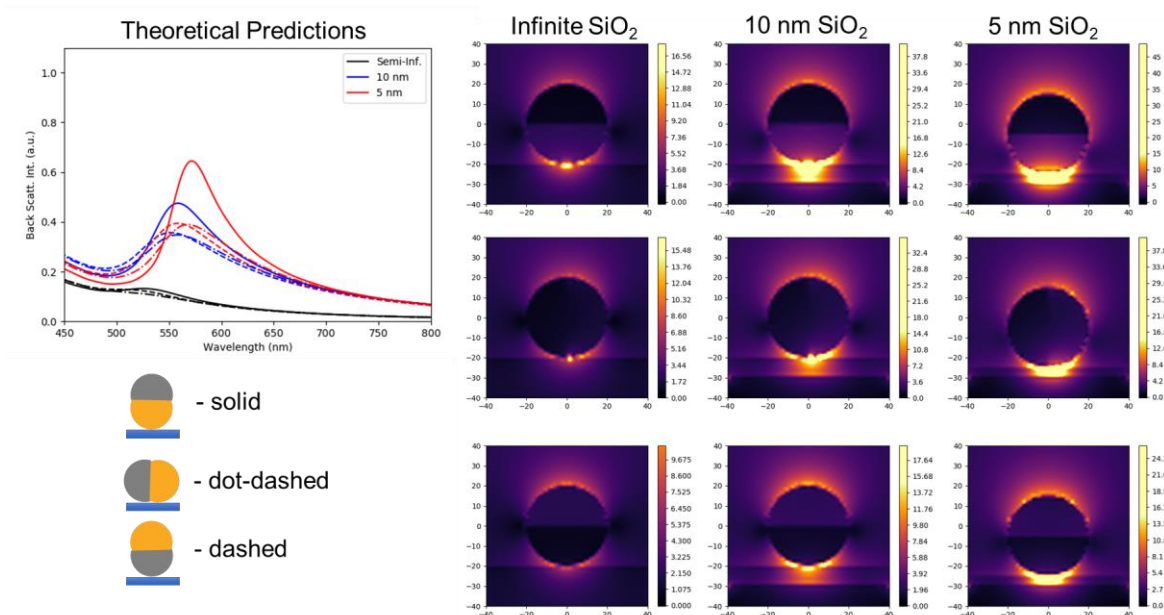


**Figure 5.5:** Theoretical modeling of AuNi-Au NPoM geometries. The dark field back scattering spectra for the three substrates and the three nanoparticle orientations show a wide range of possible spectra. The greatest intensity and highest wavelength LSPR were found when the Au phase of the AuNi nanoparticle was in direct contact with a 5 nm gap mirror substrate. For each nanoparticle orientation, similar substrate trends were found when compared to the Au-Au geometries. It was found that nanoparticle orientation had an equal contribution to the LSPR, with the rotation of the Janus structure creating overlap in the LSPR between different substrates.

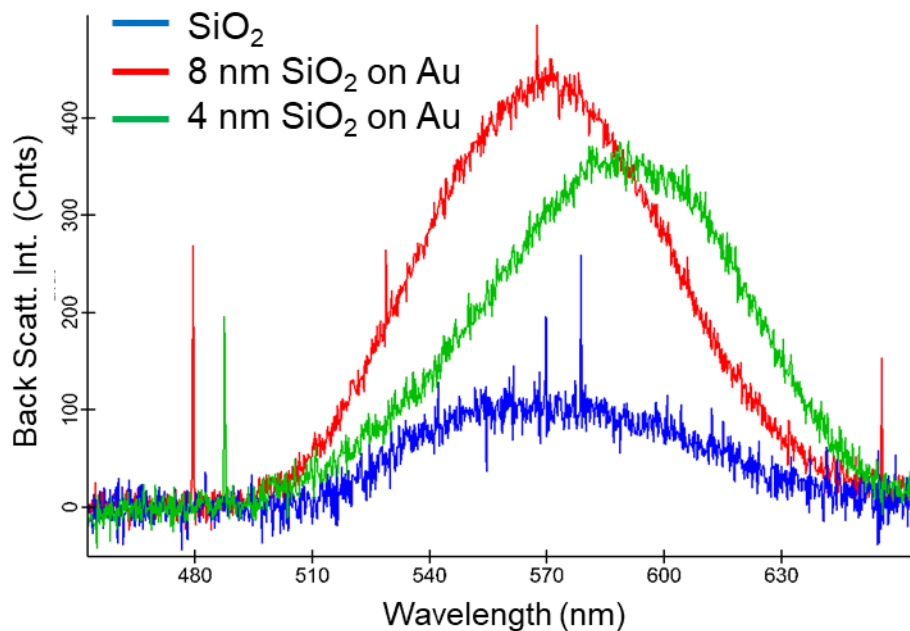


**Figure 5.6:** Experimental spectra of AuNi nanoparticles on different mirror substrates. These trends match theoretical calculations but are difficult to fully characterize due to the lack of orientation control. The determination of the orientation of each nanoparticle is not currently possible due to the thick substrate preventing high resolution TEM characterization.

The AuAg nanoparticle calculations produced three distinctly different spectra dependent on the substrate it was placed on. Each sample produced a single spectrum due to the alloy structure formed by AuAg nanoparticles (Figure 5.7). For a AuAg nanoparticle on a SiO<sub>2</sub> substrate, the spectra matched literature precedent, producing a single LSPR peak at ~470 nm, roughly halfway between pure Au and pure Ag. When placed on a mirror substrate, that LSPR peak split into two peaks, one slightly red shifted from the original 470 nm peak and one emerging close to 575 and 590 nm for the 10 nm and 5 nm substrates, respectively. When on a 10 nm gap mirror substrate,

these two peaks were both roughly the same intensity. On a 5 nm gap mirror substrate, the 590 nm peak was significantly greater in intensity compared to the 460 nm peak, which lowered compared to the 10 nm gap substrate peak at the same wavelength. This indicates that the peak at 470 nm does not involve strong interaction with the underlying substrate and the 560 nm is the gap mode between the mirror and nanoparticle as it increases in intensity as the gap is shrunk and is not present when the nanoparticle is on bare  $\text{SiO}_2$ .

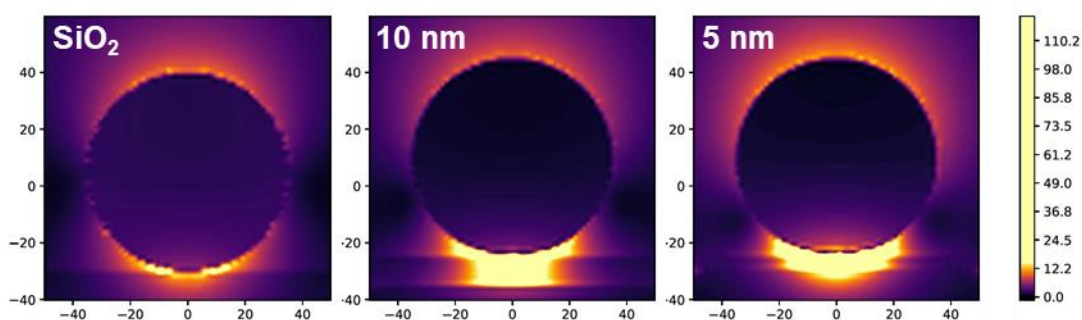
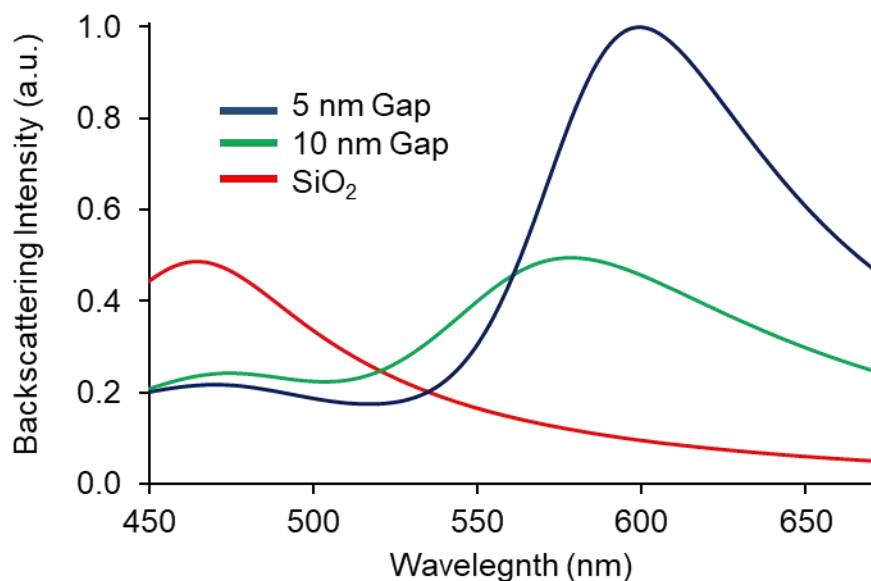


**Figure 5.7:** FDTD calculations for AuAg-Au NPoM geometries.

To confirm the theoretical predictions, 70 nm AuAg nanoparticles were deposited onto a 4 nm gap layer substrate using DPN. This was followed by an oxygen plasma treatment (5 min at 30 W) to remove any excess amorphous carbon that remained after the SPBCL heat treatment. The dark field scattering spectra matched theoretical predictions, with two peaks present, 490 and 600 nm, and the gap mode peak exhibiting roughly double the intensity (Figure 5.8 A). With the confirmation of the plasmonic properties, their use as SERS active materials was investigated. The oxygen plasma treatment removed any contaminants on the nanoparticle, leaving the bare surface to be functionalized with 1,4-benzenedithiol (BDT). Raman spectroscopy was performed on an isolated nanoparticle, using a 633 nm laser for excitation which aligns with the gap mode of the dark field spectra. Using this substrate preparation, SERS detection of BDT was achieved using a single nanoparticle (Figure 5.8 B). While the signal is relatively low, the ability to detect a molecule using a single spherical nanoparticle has limited literature precedent, as the majority of SERS measurements rely on anisotropic nanoparticles with sharp vertices or multiple nanoparticle conjugates.

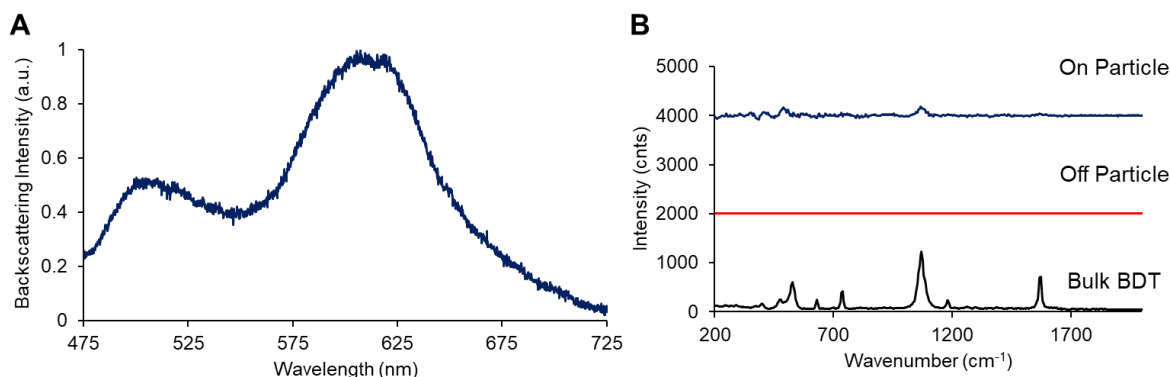


**Figure 5.8:** Experimental characterization of AuAg-Au NPoM geometry substrates. (A) The dark field scattering spectra of a 70 nm Au<sub>0.5</sub>Ag<sub>0.5</sub> nanoparticle on a 5 nm gap substrate produced the two expected LSPR peaks at 500 and 600 nm. (B) When functionalized with BDT, SERS detection was achieved using a single isolated Au<sub>0.5</sub>Ag<sub>0.5</sub> spherical nanoparticle (red trace on the nanoparticle, blue trace off of the particle, green trace bulk BDT).

### 5.3 Experimental Methods

#### 5.3.1 Fabrication of NPoM Samples

To fabricate the thermally stable substrate used for SPBCL NPoM samples, first the thin film mirror was deposited. Using E-beam deposition (Kurt J. Lesker PVD 75 E-beam Evaporator), 5 nm of Cr followed by 50 nm Au were deposited. It is crucial for the Cr to be in the metallic state, as any oxidation will limit the thermal stability during the heat treatment. After deposition of the Au film, the substrate was treated overnight in a 10 mM 3MPTS solution in dry ethanol. If the ethanol was not completely dry, the 3MPTS will hydrolyze and silica will crash out of solution preventing a uniform monolayer from forming on the Au surface. The substrate was then reloaded into the E-beam evaporator for the deposition of a SiO<sub>2</sub> passivation layer, where 4-10 nm of SiO<sub>2</sub>



were deposited. When deposited using E-beam evaporation, SiO<sub>2</sub> does not melt, which leads to a gradient in the thickness of the deposited film over cm scale areas. This inconsistency prevents the ability of using internal thickness sensors in the E-beam evaporator, so in order to measure the exact gap thickness of the substrates, AFM characterization is required. To pattern on these substrates with DPN, they were made hydrophobic through a hexamethyldisilazane (HMDS) treatment, where the substrate was placed in a sealed desiccator overnight with a 50:50 solution of HMDS and hexane.

To form the nanoparticles on these mirror substrates, 5 mg/ml solutions of poly(ethylene oxide)-*b*-poly(2-vinylpyridine) (PEO-*b*-P2VP) were prepared with metal salts of the final nanoparticles composition. For Au, Ni, and Ag containing nanoparticles, HAuCl<sub>4</sub>, Ni(NO<sub>3</sub>)<sub>2</sub>, and AgNO<sub>3</sub> were used, respectively. The solutions containing Ni and Ag were brought to a pH below 4 by the addition of nitric acid to prevent polymer micelle formation. To pattern the polymer solutions, 2 μl of the solution was drop cast onto a HMDS treated SiO<sub>2</sub> substrate and allowed to dry in a 70% humidity chamber. Using a Park XE-150 modified AFM, a DPN tip array was dip coated in the now concentrated PEO-*b*-P2VP solution. This ink was then patterned onto the mirror substrates in ordered arrays with 3 μm between each feature to ensure no crosstalk occurred during optical characterization. Once the polymer domes were patterned onto the substrate, they were heat treated in a tube furnace under a H<sub>2</sub> atmosphere, first at 150 °C for 12 hours to aggregate the metal precursors and then at 500 °C for 4-6 hours to reduce the precursors and decompose the residual polymer dome. For nanoparticles on mirror substrates, the second treatment is required to be shorter to ensure the stability of the mirror and passivation layers. Additionally, this heat treatment is required to be performed under a H<sub>2</sub> atmosphere to keep the Cr adhesion layer fully

reduced throughout the process. If the application required the surface of the nanoparticle to be free of amorphous carbon left from the decomposed polymer dome, an oxygen plasma treatment was used to remove it. This treatment, while more aggressive than traditional thermal calcination methods, allowed the excess carbon to be removed within minutes and from a top-down approach which retained the mirror substrate stability.

### **5.3.2 Characterization of NPoM Samples**

For the optical and Raman spectroscopy characterization of the NPoM samples, a confocal Raman microscope (Witec alpha300 R) was used. Using a 50x dark field objective and a white light LED source, the nanoparticles were located, and a single nanoparticle was focused on. White light scattering spectra were collected using the 50x dark field objective, with 10-30 second integration times. For SERS measurements, the NPoM substrates were placed in a 10 mM 1,4-benzenedithiol in dry ethanol for 2 hours. After repeated washing with pure ethanol, the nanoparticles were found using white light excitation with the dark field objective. A low powered 633 nm laser was then focused on the nanoparticle. It is vital to use the laser at powers below 1 mW due to the high intensity of the laser when focused onto a single nanoparticle on the surface. If the laser is above 1 mW, the nanoparticle may melt, and any chemically adsorbed molecules will be removed. For the physical characterization of NPoM substrates, AFM (Bruker Dimension Icon) and SEM (Hitachi SU8030) were used.

### **5.3.3 Finite Difference Time Domain Calculations**

The finite-difference time domain (FDTD) method is a numerical method of solving Maxwell's equations in the time domain. This is accomplished by propagating any incident fields in both space and time across a simulation region, which encloses the material system and is

terminated by specifying a set of boundary conditions. The propagation of the fields is accomplished using the leapfrogging algorithm developed by Yee,<sup>273</sup> which uses central finite-differencing on spatially-offset cartesian grids for the  $\mathbf{E}$  and  $\mathbf{H}$  fields to evaluate the curl of the  $\mathbf{E}$  and  $\mathbf{H}$  fields, respectively, at time step  $t_n$ . Inspection of Maxwell's equations makes plain that the curl of  $\mathbf{E}$  ( $\mathbf{H}$ ) at time step  $t_n$  can be used to evaluate  $\mathbf{H}$  ( $\mathbf{E}$ ) at time step  $t_{n+1}$ . This procedure is repeated for each time step until some termination criterion is reached. Frequency domain quantities can be determined once the simulation has finished by performing a discrete Fourier transform on time domain data.

The intensity of back-scattered light and near-field spatial distributions of the NPOM structures were calculated using the implementation of the FDTD method by Lumerical Inc. (version 8.16.871). A cross section through the X-Z plane of the 2,000 nm x 2,000 nm x 2,000 nm simulation region of the 40 nm diameter NP above a 100 nm Au thin film situated above a semi-infinite SiO<sub>2</sub> half space. The simulation region is terminated using perfectly matched layer (PML) absorptive boundary conditions. Two overlapping total-field scattered-field (TFSF) sources were used to inject counter-propagating plane wave fields along the  $\pm X$ -directions and polarized along the Z-axis in order to approximate the dark-field excitation of the gap mode supported by the NPoM system. The TFSF sources include both the incident and scattered fields within the interior of the TFSF boundary, while only the scattered field is present on the exterior. Therefore, calculation of the net electromagnetic flux integrated over the enclosing regions on the interior and exterior of the TFSF sources allows the calculation of the absorption and scattering cross sections, respectively. The spectrum of back-scattered light was evaluated by integrating the flux of the

scattered field across a finite 500 nm x 500 nm planar region displaced 800 nm above the NP, which corresponds to a half-collection angle of approximately 17.35 degrees.

Near-fields spatial distributions of the electric field and back-scattering spectra were calculated for 40 nm diameter Au and Ag monometallic NPs, AgAu alloy NPs, and AuNi Janus NPs. Fits to the bulk dielectric function data of Johnson and Christy were used for the monometallic Au, Ni, and Ag components,<sup>274</sup> and a parameterized dielectric function for the AuAg alloy was taken from the literature.<sup>275</sup>

#### 5.4 Summary

Herein, the optical properties of multimetallic nanoparticles were investigated, utilizing NPoM geometries to enhance the signal generated from a single patterned nanoparticle. First, a thermally stable substrate was developed that was able to withstand the extended treatment at high temperatures required for SPBCL nanoparticle synthesis. Using the proper adhesion layers between the multilayered films, it was found that a SiO<sub>2</sub>-Cr-Au-3MPTS-SiO<sub>2</sub>-HMDS substrate was able to be patterned on with DPN and survive the SPBCL heat treatment. Using this substrate, Au nanoparticles were first investigated to determine the effect of the gap thickness on the LSP of the nanoparticle-mirror structure. Using this substrate, with a gap thickness of 4 nm, it was found to increase the intensity of the plasmonic signal by a factor of 10. Additionally, the gap thickness could be used to control the LSPR peak location, with a thinner gap leading to a larger red shift in the peak, allowing for the peak to be shifted anywhere between 560 nm and 620 nm. By enhancing the signal of a single nanoparticle, the throughput of the analysis was increased due to the lower integration times required to collect a high signal and did not require specialized instrumentation.

In addition to studying a monometallic system, AuNi and AuAg nanoparticles were investigated, the first multimetallic NPoM geometry study reported to date. Using SPBCL, the composition of the nanoparticles can be readily controlled by changing the concentrations of the metal precursors in the polymer ink. This allows the thermally stable mirror substrate to be used to study a wide range of nanoparticle compositions. In this chapter it was found that AuNi nanoparticles require an orientation control that is not currently accessible to the platform, as the Janus structure of the AuNi nanoparticle resulted in multiple presenting LSPR's depending on orientation. This technique in the future could be used to elucidate the exact structure function relationship for these complex structures, but imaging techniques need to be developed in order to take full advantage of the platform. AuAg alloy nanoparticles were also investigated, as they presented a single LSPR for each composition-gap system. It was found that there are two LSPR peaks that arise when the  $\text{Au}_{0.5}\text{Ag}_{0.5}$  nanoparticle is deposited on a mirror substrate: a nanoparticle peak and a gap peak. The ratio of these peaks is determined by the thickness of the gap layer. Using these AuAg NPoM substrates, SERS detection of BDT was achieved using a single nanoparticle. This opens up the ability use more complex nanoparticle structures for SERS detection in which each phase of a Janus nanoparticle could be designed to adsorb a different molecule, leading to a more versatile SERS detection platform.

**CHAPTER 6:**  
**FUTURE OUTLOOK**

There are many ways in which the work presented in this thesis can continue. While the new screening platform described three different applications (SWNT growth, catalysis, and plasmonics), only a small portion of the structures of interest were investigated and was limited to bimetallic spherical systems. When looking at the materials landscape of nanomaterials, there are billions of different compositions that can be accessed and studied for each application, as well as different shaped nanoparticles. Before going into further detail on the future directions of the applications presented in this work, the further development of the nanoparticle library platform will be addressed. With respect to synthesis, the inclusion of shape control will primarily be the focus. Through the control of nanoparticle composition, the structure of the nanoparticle (alloy vs Janus vs multiphase) can be determined by the phase diagram of the elements that make up the nanoparticle, but the nanoparticle will be relatively spherical due to the thermal treatments. The Janus structured nanoparticles will become oval in shape to decrease the interface area. In order to create a bare particle, the polymer dome needs to be removed, which is currently done by high temperature treatments which result in thermodynamic products. Shape of these patterned nanoparticles can be altered through secondary treatments to form more catalytically active or optically interesting shapes. Using seed mediated growth protocols, the nanoparticles can be grown into different shapes (Figure 6.1 A). These protocols have been widely used in solution synthesis of metallic nanoparticles and can be translated to SPBCL nanoparticles on a surface. Additionally, this also opens the ability to investigate the exact growth mechanism of these anisotropic nanoparticles due to the site isolation of each SPBCL nanoparticles allowing for 1-to-1 starting material product analysis, compared to population analysis in solution. Through Bi modifications, the nanoparticles can be transformed into tetrahexahedral (THH) nanoparticles (Figure 6.1 B).

These THH nanoparticles present high index  $210$  facets that greatly increase the nanoparticles catalytic activity. By adding the control of nanoparticle shape to the composition and size gradients, the parameter space that is accessible greatly increases.

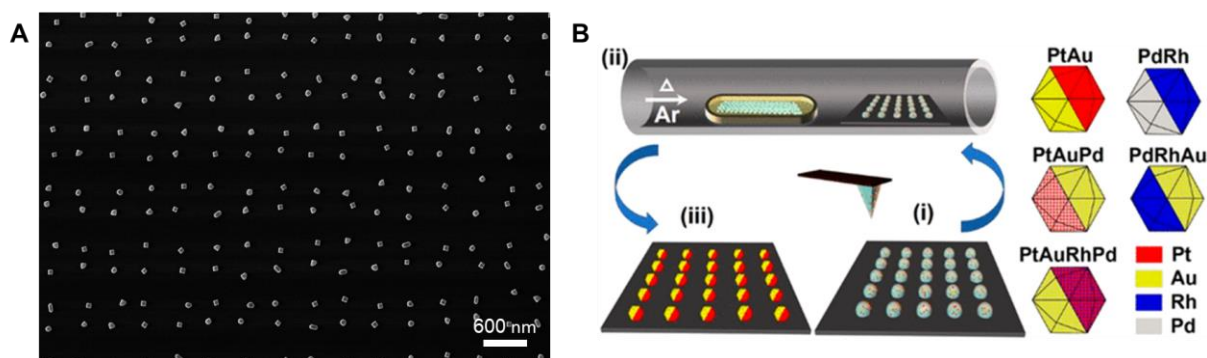


**Figure 6.1:** Shape control of patterned SPBCL nanoparticles through secondary treatments. (A) using traditional seed mediated secondary growth treatments, each nanoparticle can be grown into an anisotropic shape, determined by the solution surfactants and reduction rates. (B) Using a novel Bi CVD method, THH nanoparticles can be fabricated at large scales to increase the catalytic activity of each nanoparticle composition. Figure adapted from reference.<sup>276</sup>

In addition to shape control, expanding beyond bimetallic systems is necessary to achieve the full reach of the screening platforms. This can be achieved with the two air brushes by using multimetallic inks in each brush. For example, the left ink could contain  $M_A M_B$  and the right ink could contain  $M_A M_C$ . By spraying the linear gradient using these two inks, the gradient would range from  $M_{A0.5} M_{B0.43} M_{C0.07}$  to  $M_{A0.5} M_{B0.07} M_{C0.43}$ , based off a typical 15:85-85:15 percentage gradient. Changing the relative compositions in each ink will allow the entire phase space to be spanned. A more interesting method of expanding the compositional phase space accessible would



be to introduce a 3<sup>rd</sup> air brush, creating a triangular 3 composition spray profile (Figure 6.2Figure 6.2:). This was preliminarily studied and achieved but was not applied to any applications. This would allow the trimetallic nanoparticle phase space to be examined in greater detail. Previously, it had been shown that across a trimetallic system, multiple phases become stable at different relative compositions, spanning both Janus and alloy systems. By patterning these systems, the entire composition and structure phase space can be studied on a single substrate.

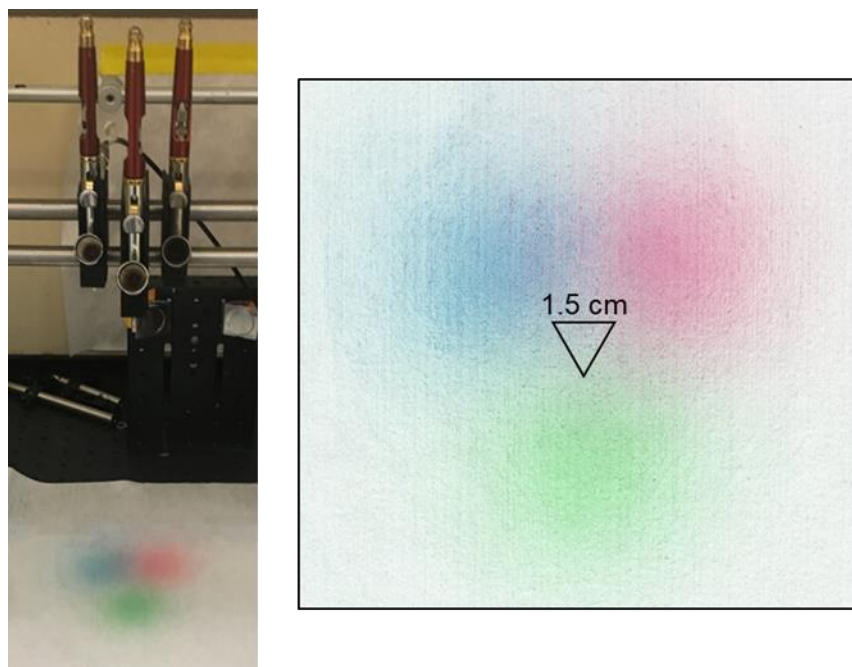


**Figure 6.2:** Trimetallic phase spray configuration. By introducing a third gaussian spray profile, each profile's linear regime can be overlapped, creating a triangular compositional gradient.

The ARES screening technique powered the highest resolution of nanoparticles composition to date and can continue to be used to as a powerful screening tool for SWNT growth. In this work, the three bimetallic systems in the Au-Cu-Ni system were investigated for their ability to grow

SWNTs. Two main directions for future work would be to expand composition and study chirality. Using refractory metals, such as W, would be initial avenues to study, as they have shown to have high catalytic activity and selectivity. Additionally, by using the tri-gradient (Figure 6.2) trimetallic nanoparticles could be investigated. While there are some limited studies into multimetallic nanoparticles past bimetallic for SWNT growth, there have been no complete studies of any trimetallic systems. Studying more complex compositions is the easiest direction to continue this work, but the most impactful would be to find a chiral selective catalyst. The main factor preventing SWNTs from wide usage is the lack of synthesis methods for homogeneous populations due to the wide range of electronic structures across the different chirality's. For example, a small portion of metallic SWNTs will inevitably short any device made out of a largely semiconductor population. Current limitations on the throughput of the chirality analysis is the need of radial breathing mode (RBM) mapping through secondary Raman characterization. The collaborators on this project at AFRL at Wright Patterson Air Force Base have begun developing analytical methods to perform high throughput diameter and chiral determination using the *in situ* Raman spectra collected in the ARES instrument. The implementation of this analysis would allow for the screening of not only absolute catalytic activity, but also selectivity, greatly increasing the power of the screening platform.

Following from Chapter 4, the proof-of-concept of the universal sealed well plate reactor will be expanded to functional screens for catalytic activity and selectivity. Unfortunately, due to the Covid-19 pandemic, the full characterization of the AuCu composition phase space on the stable PAD GC is still ongoing. As a whole, the screening of heterogeneous catalysts and electrocatalysts has the possibility to greatly impact almost every aspect of human life. While this may seem like

a dramatic claim, the use of catalysts for drug synthesis, fuel production, polymer synthesis, and other material fabrication processes, leads to a massive global impact of a new catalyst. Even finding a catalyst that performs 1% better in a billion-dollar industry, will have its impact felt. The well plate reactor system is a functional screening platform, and does produce *in situ* measurements for electrochemical reactions, but ultimately will not match the throughput of the synthesis platform. Similar to the throughput of ARES, for a screening platform to reach its potential, a *in situ* detection method with 100  $\mu\text{m}$  resolution is required. Work towards this aim will likely use fluorescent or thermal imaging in a microfluidic reactor. Microfluidics, and even nanofluidics,<sup>277</sup> flow extremely small volumes of reactants over a catalyst, greatly increasing the interactions between the catalyst on the surface and the solution. These fluidic devices can be made out of transparent materials and can often be ran at high temperatures and pressures provided the proper materials are chosen. Fluorescent dyes have been used in literature as a direct and indirect measurement of catalytic activity.<sup>105</sup> For direct measurements, either the reactant or product are required to be fluorescent, limiting the chemicals accessible. Indirect measurements have traditionally used pH sensitive dyes, which are powerful in electrochemical reactions which often produce  $\text{H}^+$  or  $\text{OH}^-$  ions as byproducts. Thermal characterization has the most promise as a universal screening technique as a large majority of catalytic reactions are exothermic. This will require a sensitive IR camera, but provided the catalytic turnover is great enough, which would be the case for optimized catalysts of interest, large arrays of nanoparticles can be screened in parallel, determining catalytic efficiency directly by the heat generated. Developing these screening methods will overcome the bottleneck of analysis for these catalytic reactions.

In Chapter 5, the plasmonic properties of multimetallic nanoparticles were the first physical property examined for SPBCL nanoparticles. Using the nanoparticle on mirror (NPoM) geometry, the signal was enhanced by an order of magnitude. Using SPBCL nanoparticles in this geometry show promise as single nanoparticle sensors, as well as a method of studying the plasmonic properties of complex multimetallic nanoparticles. Developing methods of controlling, or at least imaging, the orientation of Janus nanoparticles will increase this platform's impact. In addition to plasmonic properties, the other physical property of interest is magnetism. By patterning magnetically active nanoparticles, magnetic force microscopy (MFM) can be used to image the magnetic moments of single nanoparticles. Additionally, the investigation of plasmonic-magnetic hybrid materials (such as AuNi) allow for the study of the effects of magnetic fields on plasmonics. Similar to how the NPoM uses a plasmonic thin film to boost the plasmonic activity of the nanoparticles patterned on them, a magnetic thin film could also be used to increase the magnetic signal. Studying the entire spectrum of electromagnetic properties of nanoparticles will allow for the discovery of new materials for sensors, signal generators, or optical electronics.

Overall, the ability to synthesize these massive arrays of nanoparticles opens up a wide range of applications that were not previously accessible. The daunting task of screening the entire nanomaterial landscape is overwhelming when each structure of interest is synthesized individually. By fabricating these arrays in parallel, the rate of material discovery can skyrocket. The bottleneck will continue to be on the characterization of the nanoparticle arrays, but as the work in this thesis has shown, the rate of analysis can be greatly increased by shrinking the combinatorial library onto a single substrate. Ultimately, the future outlook of this work will be determined by scientist's ability to develop screening techniques to match the synthetic throughput.

There are countless chemical reactions that can be improved by nanoparticle catalysts, it is just a matter of how fast they can be found in the massive materials landscape. Hopefully, this platform will become the magnet that helps scientists find that needle in a haystack.

## REFERENCES

1. Weber, J.H., *Nickel-based Superalloys: An Overview*, in *Encyclopedia of Materials: Science and Technology*, K.H.J. Buschow, et al., Editors. 2001, Elsevier: Oxford. p. 6154-6155.
2. Inoue, A.; Ohtera, K.; Kita, K.; Masumoto, T. New amorphous Mg-Ce-Ni alloys with high strength and good ductility *Japanese journal of applied physics* **1988**, 27, L2248-L2251.
3. Horimura, H.; Matsumoto, N.; Okamoto, K., *High strength and high toughness aluminum alloy*. 1994, Google Patents.
4. Krasnowski, M.; Kulik, T. Nanocrystalline Al-Fe intermetallics—light weight alloys with high hardness *Intermetallics* **2010**, 18, 47-50.
5. Holmblad, P.M.; Larsen, J.H.; Chorkendorff, I. Modification of Ni (111) reactivity toward CH<sub>4</sub>, CO, and D<sub>2</sub> by two - dimensional alloying *The Journal of chemical physics* **1996**, 104, 7289-7295.
6. Hashimoto, K.; Kumagai, N.; Yoshioka, H.; Habazaki, H.; Kawashima, A.; Asami, K.; Zhang, B.P. Recent studies of chemical properties of amorphous alloys *Materials Science and Engineering: A* **1991**, 133, 22-25.
7. Science, N.; Council, T., *Materials genome initiative for global competitiveness*. 2011: Executive Office of the President, National Science and Technology Council.
8. Jain, A.; Ong, S.P.; Hautier, G.; Chen, W.; Richards, W.D.; Dacek, S.; Cholia, S.; Gunter, D.; Skinner, D.; Ceder, G.; Persson, K.A. Commentary: The Materials Project: A materials genome approach to accelerating materials innovation *APL Materials* **2013**, 1, 011002, 1-11.
9. Pagliaro, M., *Nano-Age: How Nanotechnology Changes our Future*. 2010. 196.
10. *National Nanotechnology Initiative (NNI)*. [cited 2020; Available from: <http://www.nano.gov/>].
11. Freestone, I.; Meeks, N.; Sax, M.; Higgitt, C. The Lycurgus cup—a roman nanotechnology *Gold bulletin* **2007**, 40, 270-277.
12. Reibold, M.; Paufler, P.; Levin, A.A.; Kochmann, W.; Pätzke, N.; Meyer, D.C. Carbon nanotubes in an ancient Damascus sabre *Nature* **2006**, 444, 286-286.
13. Faraday, M. X. The Bakerian Lecture.—Experimental relations of gold (and other metals) to light *Philosophical Transactions of the Royal Society of London* **1857**145-181.

14. Kinloch, I.A.; Suhr, J.; Lou, J.; Young, R.J.; Ajayan, P.M. Composites with carbon nanotubes and graphene: An outlook *Science* **2018**, 362, 547-553.
15. Narayanan, R.; El-Sayed, M.A. Catalysis with Transition Metal Nanoparticles in Colloidal Solution: Nanoparticle Shape Dependence and Stability *The Journal of Physical Chemistry B* **2005**, 109, 12663-12676.
16. Eustis, S.; El-Sayed, M.A. Why gold nanoparticles are more precious than pretty gold: Noble metal surface plasmon resonance and its enhancement of the radiative and nonradiative properties of nanocrystals of different shapes *Chemical Society Reviews* **2006**, 35, 209-217.
17. Krishnan, A.; Dujardin, E.; Ebbesen, T.W.; Yianilos, P.N.; Treacy, M.M.J. Young's modulus of single-walled nanotubes *Physical Review B* **1998**, 58, 14013-14019.
18. Coleman, J.N. Liquid Exfoliation of Defect-Free Graphene *Accounts of Chemical Research* **2013**, 46, 14-22.
19. Zhou, Z.-Y.; Tian, N.; Huang, Z.-Z.; Chen, D.-J.; Sun, S.-G. Nanoparticle catalysts with high energy surfaces and enhanced activity synthesized by electrochemical method *Faraday discussions* **2009**, 140, 81-92.
20. Ekimov, A.I.; Efros, A.L.; Onushchenko, A.A. Quantum size effect in semiconductor microcrystals *Solid State Communications* **1985**, 56, 921-924.
21. Gilroy, K.D.; Ruditskiy, A.; Peng, H.-C.; Qin, D.; Xia, Y. Bimetallic Nanocrystals: Syntheses, Properties, and Applications *Chemical Reviews* **2016**, 116, 10414-10472.
22. Iqbal, P.; Preece, J.; Mendes, P., *Nanotechnology: The "Top-Down" and "Bottom-Up" Approaches*. 2012.
23. Yadav, T.; Yadav, r.m.; Singh, D. Mechanical Milling: a Top Down Approach for the Synthesis of Nanomaterials and Nanocomposites *Nanoscience and Nanotechnology* **2012**, 2, 22-48.
24. Nagase, K.; Shimizu, Y.; Miura, N.; Yamazoe, N. Electrochromism of gold - vanadium pentoxide composite thin films prepared by alternating thermal deposition *Applied Physics Letters* **1994**, 64, 1059-1061.
25. Yang, P.Y., *Sputter deposition process*. 1996, Google Patents.
26. Chen, J.S.; Zhu, T.; Yang, X.H.; Yang, H.G.; Lou, X.W. Top-Down Fabrication of  $\alpha$ -Fe<sub>2</sub>O<sub>3</sub> Single-Crystal Nanodiscs and Microparticles with Tunable Porosity for Largely Improved Lithium Storage Properties *Journal of the American Chemical Society* **2010**, 132, 13162-13164.
27. Harsha, K.S., *Principles of vapor deposition of thin films*. 2005: Elsevier.

28. Dolbec, R.; Irissou, E.; Chaker, M.; Guay, D.; Rosei, F.; El Khakani, M.A. Growth dynamics of pulsed laser deposited Pt nanoparticles on highly oriented pyrolytic graphite substrates *Physical Review B* **2004**, 70, 201406-1-4.
29. Eaglesham, D.J.; Cerullo, M. Dislocation-free Stranski-Krastanow growth of Ge on Si(100) *Physical Review Letters* **1990**, 64, 1943-1946.
30. Yahyazadeh, A.; Khoshandam, B. Carbon nanotube synthesis via the catalytic chemical vapor deposition of methane in the presence of iron, molybdenum, and iron–molybdenum alloy thin layer catalysts *Results in Physics* **2017**, 7, 3826-3837.
31. Thouti, E.; Chander, N.; Dutta, V.; Komarala, V.K. Optical properties of Ag nanoparticle layers deposited on silicon substrates *Journal of Optics* **2013**, 15, 035005, 1-7.
32. Xiang, X.-D.; Sun, X.; Briceno, G.; Lou, Y.; Wang, K.-A.; Chang, H.; Wallace-Freedman, W.G.; Chen, S.-W.; Schultz, P.G. A combinatorial approach to materials discovery *Science* **1995**, 268, 1738-1740.
33. Briceño, G.; Chang, H.; Sun, X.; Schultz, P.G.; Xiang, X.D. A Class of Cobalt Oxide Magnetoresistance Materials Discovered with Combinatorial Synthesis *Science* **1995**, 270, 273-275.
34. Xiang, X.-D. COMBINATORIAL MATERIALS SYNTHESIS AND SCREENING: An Integrated Materials Chip Approach to Discovery and Optimization of Functional Materials *Annual Review of Materials Science* **1999**, 29, 149-171.
35. Mao, S.S. High throughput growth and characterization of thin film materials *Journal of crystal growth* **2013**, 379, 123-130.
36. Mao, S.S. High throughput combinatorial screening of semiconductor materials *Applied Physics A* **2011**, 105, 283-288.
37. Fukumura, T.; Ohtani, M.; Kawasaki, M.; Okimoto, Y.; Kageyama, T.; Koida, T.; Hasegawa, T.; Tokura, Y.; Koinuma, H. Rapid construction of a phase diagram of doped Mott insulators with a composition-spread approach *Applied Physics Letters* **2000**, 77, 3426-3428.
38. Hasegawa, K.; Ahmet, P.; Okazaki, N.; Hasegawa, T.; Fujimoto, K.; Watanabe, M.; Chikyow, T.; Koinuma, H. Amorphous stability of HfO<sub>2</sub> based ternary and binary composition spread oxide films as alternative gate dielectrics *Applied surface science* **2004**, 223, 229-232.
39. Takahashi, R.; Kubota, H.; Murakami, M.; Yamamoto, Y.; Matsumoto, Y.; Koinuma, H. Design of combinatorial shadow masks for complete ternary-phase diagramming of solid state materials *Journal of combinatorial chemistry* **2004**, 6, 50-53.



40. Wagener, M.; Günther, B. Sputtering on liquids – a versatile process for the production of magnetic suspensions? *Journal of Magnetism and Magnetic Materials* **1999**, 201, 41-44.
41. Torimoto, T.; Okazaki, K.-i.; Kiyama, T.; Hirahara, K.; Tanaka, N.; Kuwabata, S. Sputter deposition onto ionic liquids: Simple and clean synthesis of highly dispersed ultrafine metal nanoparticles *Applied physics letters* **2006**, 89, 243117, 1-3.
42. Torimoto, T.; Tsuda, T.; Okazaki, K.i.; Kuwabata, S. New frontiers in materials science opened by ionic liquids *Advanced Materials* **2010**, 22, 1196-1221.
43. Nguyen, M.T.; Yonezawa, T. Sputtering onto a liquid: interesting physical preparation method for multi-metallic nanoparticles *Science and Technology of Advanced Materials* **2018**, 19, 883-898.
44. Okazaki, K.-i.; Kiyama, T.; Hirahara, K.; Tanaka, N.; Kuwabata, S.; Torimoto, T. Single-step synthesis of gold–silver alloy nanoparticles in ionic liquids by a sputter deposition technique *Chemical Communications* **2008**691-693.
45. Čempel, D.; Nguyen, M.T.; Ishida, Y.; Tokunaga, T.; Yonezawa, T. Ligand free green plasma-in-liquid synthesis of Au/Ag Alloy nanoparticles *New Journal of Chemistry* **2018**, 42, 5680-5687.
46. Shirai, H.; Nguyen, M.T.; Čempel, D.; Tsukamoto, H.; Tokunaga, T.; Liao, Y.-C.; Yonezawa, T. Preparation of Au/Pd bimetallic nanoparticles by a microwave-induced plasma in liquid process *Bulletin of the Chemical Society of Japan* **2017**, 90, 279-285.
47. Suzuki, S.; Suzuki, T.; Tomita, Y.; Hirano, M.; Okazaki, K.-i.; Kuwabata, S.; Torimoto, T. Compositional control of AuPt nanoparticles synthesized in ionic liquids by the sputter deposition technique *CrystEngComm* **2012**, 14, 4922-4926.
48. Deng, L.; Nguyen, M.T.; Shi, J.; Chau, Y.-t.R.; Tokunaga, T.; Kudo, M.; Matsumura, S.; Hashimoto, N.; Yonezawa, T. Highly Correlated Size and Composition of Pt/Au Alloy Nanoparticles via Magnetron Sputtering onto Liquid *Langmuir* **2020**, 36, 3004-3015.
49. Suzuki, S.; Tomita, Y.; Kuwabata, S.; Torimoto, T. Synthesis of alloy AuCu nanoparticles with the L1 0 structure in an ionic liquid using sputter deposition *Dalton Transactions* **2015**, 44, 4186-4194.
50. König, D.; Richter, K.; Siegel, A.; Mudring, A.-V.; Ludwig, A. High-Throughput Fabrication of Au–Cu Nanoparticle Libraries by Combinatorial Sputtering in Ionic Liquids *Advanced Functional Materials* **2014**, 24, 2049-2056.
51. Zhou, Y.-Y.; Liu, C.-H.; Liu, J.; Cai, X.-L.; Lu, Y.; Zhang, H.; Sun, X.-H.; Wang, S.-D. Self-Decoration of PtNi Alloy Nanoparticles on Multiwalled Carbon Nanotubes for Highly Efficient Methanol Electro-Oxidation *Nano-Micro Letters* **2016**, 8, 371-380.

52. Löffler, T.; Meyer, H.; Savan, A.; Wilde, P.; Garzón Manjón, A.; Chen, Y.-T.; Ventosa, E.; Scheu, C.; Ludwig, A.; Schuhmann, W. Discovery of a Multinary Noble Metal-Free Oxygen Reduction Catalyst *Advanced Energy Materials* **2018**, 8, 1802269, 1-7.
53. Suzuki, T.; Okazaki, K.-i.; Kiyama, T.; Kuwabata, S.; Torimoto, T. A facile synthesis of AuAg alloy nanoparticles using a chemical reaction induced by sputter deposition of metal onto ionic liquids *Electrochemistry* **2009**, 77, 636-638.
54. Rosenstein, L. RED PHOSPHORUS AS A REDUCING AGENT *Journal of the American Chemical Society* **1920**, 42, 883-889.
55. Turkevich, J.; Stevenson, P.C.; Hillier, J. A study of the nucleation and growth processes in the synthesis of colloidal gold *Discussions of the Faraday Society* **1951**, 11, 55-75.
56. Sugimoto, T. Underlying mechanisms in size control of uniform nanoparticles *Journal of Colloid and Interface Science* **2007**, 309, 106-118.
57. Sugimoto, T.; Shiba, F.; Sekiguchi, T.; Itoh, H. Spontaneous nucleation of monodisperse silver halide particles from homogeneous gelatin solution I: silver chloride *Colloids and Surfaces A: Physicochemical and Engineering Aspects* **2000**, 164, 183-203.
58. Liu, Y.; Chi, M.; Mazumder, V.; More, K.L.; Soled, S.; Henao, J.D.; Sun, S. Composition-Controlled Synthesis of Bimetallic PdPt Nanoparticles and Their Electro-oxidation of Methanol *Chemistry of Materials* **2011**, 23, 4199-4203.
59. Vasquez, Y.; Luo, Z.; Schaak, R.E. Low-temperature solution synthesis of the non-equilibrium ordered intermetallic compounds Au<sub>3</sub>Fe, Au<sub>3</sub>Co, and Au<sub>3</sub>Ni as nanocrystals *Journal of the American Chemical Society* **2008**, 130, 11866-11867.
60. Bondi, J.F.; Misra, R.; Ke, X.; Sines, I.T.; Schiffer, P.; Schaak, R.E. Optimized synthesis and magnetic properties of intermetallic Au<sub>3</sub>Fe<sub>1-x</sub>, Au<sub>3</sub>Co<sub>1-x</sub>, and Au<sub>3</sub>Ni<sub>1-x</sub> nanoparticles *Chemistry of Materials* **2010**, 22, 3988-3994.
61. Bönnemann, H.; Brand, R.; Brijoux, W.; Hofstadt, H.W.; Frerichs, M.; Kempter, V.; Maus - Friedrichs, W.; Matoussevitch, N.; Nagabhushana, K.; Voigts, F. Air stable Fe and Fe-Co magnetic fluids—synthesis and characterization *Applied organometallic chemistry* **2005**, 19, 790-796.
62. Yao, Y.; Huang, Z.; Xie, P.; Lacey, S.D.; Jacob, R.J.; Xie, H.; Chen, F.; Nie, A.; Pu, T.; Rehwoldt, M.; Yu, D.; Zachariah, M.R.; Wang, C.; Shahbazian-Yassar, R.; Li, J.; Hu, L. Carbothermal shock synthesis of high-entropy-alloy nanoparticles *Science* **2018**, 359, 1489-1494.
63. Yao, Y.; Huang, Z.; Li, T.; Wang, H.; Liu, Y.; Stein, H.S.; Mao, Y.; Gao, J.; Jiao, M.; Dong, Q.; Dai, J.; Xie, P.; Xie, H.; Lacey, S.D.; Takeuchi, I.; Gregoire, J.M.; Jiang, R.; Wang, C.; Taylor,

- A.D.; Shahbazian-Yassar, R.; Hu, L. High-throughput, combinatorial synthesis of multimetallic nanoclusters *Proceedings of the National Academy of Sciences* **2020**, 117, 6316-6322.
64. Meldrum, F.C.; Wade, V.J.; Nimmo, D.L.; Heywood, B.R.; Mann, S. Synthesis of inorganic nanophase materials in supramolecular protein cages *Nature* **1991**, 349, 684-687.
65. Antonietti, M.; Wenz, E.; Bronstein, L.; Seregina, M. Synthesis and characterization of noble metal colloids in block copolymer micelles *Advanced Materials* **1995**, 7, 1000-1005.
66. Seregina, M.V.; Bronstein, L.M.; Platonova, O.A.; Chernyshov, D.M.; Valetsky, P.M.; Hartmann, J.; Wenz, E.; Antonietti, M. Preparation of Noble-Metal Colloids in Block Copolymer Micelles and Their Catalytic Properties in Hydrogenation *Chemistry of Materials* **1997**, 9, 923-931.
67. Menezes, W.G.; Zielasek, V.; Dzhardimalieva, G.I.; Pomogailo, S.I.; Thiel, K.; Wöhrle, D.; Hartwig, A.; Bäumer, M. Synthesis of stable AuAg bimetallic nanoparticles encapsulated by diblock copolymer micelles *Nanoscale* **2012**, 4, 1658-1664.
68. Mbenkum, B.N.; Diaz-Ortiz, A.; Gu, L.; van Aken, P.A.; Schutz, G. Expanding micelle nanolithography to the self-assembly of multicomponent core-shell nanoparticles *J Am Chem Soc* **2010**, 132, 10671-10673.
69. Möller, M.; Spatz, J.P.; Roescher, A. Gold nanoparticles in micellar poly(styrene)-b-poly(ethylene oxide) films—size and interparticle distance control in monoparticulate films *Advanced Materials* **1996**, 8, 337-340.
70. Spatz, J.P.; Mössmer, S.; Hartmann, C.; Möller, M.; Herzog, T.; Krieger, M.; Boyen, H.-G.; Ziemann, P.; Kabius, B. Ordered Deposition of Inorganic Clusters from Micellar Block Copolymer Films *Langmuir* **2000**, 16, 407-415.
71. Kim, S.-S.; Sohn, B.-H. Template-assisted self-assembly of diblock copolymer micelles for non-hexagonal arrays of Au nanoparticles *RSC Advances* **2016**, 6, 41331-41339.
72. Glass, R.; Arnold, M.; Cavalcanti-Adam, E.A.; Blümmel, J.; Haferkemper, C.; Dodd, C.; Spatz, J.P. Block copolymer micelle nanolithography on non-conductive substrates *New Journal of Physics* **2004**, 6, 101-101.
73. Crooks, R.M.; Zhao, M.; Sun, L.; Chechik, V.; Yeung, L.K. Dendrimer-Encapsulated Metal Nanoparticles: Synthesis, Characterization, and Applications to Catalysis *Accounts of Chemical Research* **2001**, 34, 181-190.
74. Scott, R.W.J.; Wilson, O.M.; Crooks, R.M. Synthesis, Characterization, and Applications of Dendrimer-Encapsulated Nanoparticles *The Journal of Physical Chemistry B* **2005**, 109, 692-704.

75. Yamamoto, K.; Imaoka, T.; Tanabe, M.; Kambe, T. New Horizon of Nanoparticle and Cluster Catalysis with Dendrimers *Chemical Reviews* **2020**, 120, 1397-1437.
76. Fukuoka, A.; Araki, H.; Sakamoto, Y.; Sugimoto, N.; Tsukada, H.; Kumai, Y.; Akimoto, Y.; Ichikawa, M. Template synthesis of nanoparticle arrays of gold and platinum in mesoporous silica films *Nano Letters* **2002**, 2, 793-795.
77. Besson, S.; Gacoin, T.; Ricolleau, C.; Boilot, J.-P. Silver nanoparticle growth in 3D-hexagonal mesoporous silica films *Chemical Communications* **2003**360-361.
78. Fukuoka, A.; Araki, H.; Kimura, J.-i.; Sakamoto, Y.; Higuchi, T.; Sugimoto, N.; Inagaki, S.; Ichikawa, M. Template synthesis of nanoparticle arrays of gold, platinum and palladium in mesoporous silica films and powders *Journal of Materials Chemistry* **2004**, 14, 752-756.
79. Barton, J.E.; Odom, T.W. Mass-Limited Growth in Zeptoliter Beakers: A General Approach for the Synthesis of Nanocrystals *Nano Letters* **2004**, 4, 1525-1528.
80. Jibril, L.; Chen, P.C.; Hu, J.; Odom, T.W.; Mirkin, C.A. Massively Parallel Nanoparticle Synthesis in Anisotropic Nanoreactors *ACS Nano* **2019**, 13, 12408-12414.
81. Shestopalov, I.; Tice, J.D.; Ismagilov, R.F. Multi-step synthesis of nanoparticles performed on millisecond time scale in a microfluidic droplet-based system *Lab on a Chip* **2004**, 4, 316-321.
82. Chan, E.M.; Alivisatos, A.P.; Mathies, R.A. High-Temperature Microfluidic Synthesis of CdSe Nanocrystals in Nanoliter Droplets *Journal of the American Chemical Society* **2005**, 127, 13854-13861.
83. Liu, L.; Xiang, N.; Ni, Z. Droplet-based microreactor for the production of micro/nanomaterials *ELECTROPHORESIS* **2020**, n/a, 833-851.
84. Chai, J.; Huo, F.; Zheng, Z.; Giam, L.R.; Shim, W.; Mirkin, C.A. Scanning probe block copolymer lithography *Proc Natl Acad Sci U S A* **2010**, 107, 20202-20206.
85. Piner, R.D.; Zhu, J.; Xu, F.; Hong, S.; Mirkin, C.A. "Dip-Pen" Nanolithography *Science* **1999**, 283, 661-663.
86. Chai, J.; Liao, X.; Giam, L.R.; Mirkin, C.A. Nanoreactors for studying single nanoparticle coarsening *J Am Chem Soc* **2012**, 134, 158-161.
87. Chen, P.C.; Du, J.S.; Meckes, B.; Huang, L.; Xie, Z.; Hedrick, J.L.; Dravid, V.P.; Mirkin, C.A. Structural Evolution of Three-Component Nanoparticles in Polymer Nanoreactors *J Am Chem Soc* **2017**, 139, 9876-9884.

88. Du, J.S.; Chen, P.-C.; Meckes, B.; Kluender, E.J.; Xie, Z.; Dravid, V.P.; Mirkin, C.A. Windowless Observation of Evaporation-Induced Coarsening of Au–Pt Nanoparticles in Polymer Nanoreactors *Journal of the American Chemical Society* **2018**, 140, 7213-7221.
89. Chen, P.-C.; Liu, Y.; Du, J.S.; Meckes, B.; Dravid, V.P.; Mirkin, C.A. Chain-End Functionalized Polymers for the Controlled Synthesis of Sub-2 nm Particles *Journal of the American Chemical Society* **2020**, 142, 7350-7355.
90. Liu, G.; Eichelsdoerfer, D.J.; Rasin, B.; Zhou, Y.; Brown, K.A.; Liao, X.; Mirkin, C.A. Delineating the pathways for the site-directed synthesis of individual nanoparticles on surfaces *Proc Natl Acad Sci U S A* **2013**, 110, 887-891.
91. Chen, P.C.; Liu, G.; Zhou, Y.; Brown, K.A.; Chernyak, N.; Hedrick, J.L.; He, S.; Xie, Z.; Lin, Q.Y.; Dravid, V.P.; O'Neill-Slawecki, S.A.; Mirkin, C.A. Tip-Directed Synthesis of Multimetallic Nanoparticles *J Am Chem Soc* **2015**, 137, 9167-9173.
92. Chen, P.-C.; Liu, X.; Hedrick, J.L.; Xie, Z.; Wang, S.; Lin, Q.-Y.; Hersam, M.C.; Dravid, V.P.; Mirkin, C.A. Polyelemental nanoparticle libraries *Science* **2016**, 352, 1565-1569.
93. Du, J.S.; Chen, P.C.; Meckes, B.; Xie, Z.; Zhu, J.; Liu, Y.; Dravid, V.P.; Mirkin, C.A. The Structural Fate of Individual Multicomponent Metal-Oxide Nanoparticles in Polymer Nanoreactors *Angew Chem Int Ed Engl* **2017**, 56, 7625-7629.
94. Chen, P.-C.; Liu, M.; Du, J.S.; Meckes, B.; Wang, S.; Lin, H.; Dravid, V.P.; Wolverton, C.; Mirkin, C.A. Interface and heterostructure design in polyelemental nanoparticles *Science* **2019**, 363, 959-964.
95. Huo, F.; Zheng, Z.; Zheng, G.; Giam, L.R.; Zhang, H.; Mirkin, C.A. Polymer pen lithography *Science* **2008**, 321, 1658-1660.
96. Merrifield, R.B. Solid phase peptide synthesis. I. The synthesis of a tetrapeptide *Journal of the American Chemical Society* **1963**, 85, 2149-2154.
97. Ecker, D.J.; Crooke, S.T. Combinatorial Drug Discovery: Which Methods Will Produce the Greatest Value? *Bio/Technology* **1995**, 13, 351-360.
98. Prochaska, M.; Jin, J.; Rochefort, D.; Zhuang, L.; DiSalvo, F.J.; Abruña, H.D.; Dover, R.B.v. High throughput screening of electrocatalysts for fuel cell applications *Review of Scientific Instruments* **2006**, 77, 054104, 1-8.
99. Smotkin, E.S.; Jiang, J.; Nayar, A.; Liu, R. High-throughput screening of fuel cell electrocatalysts *Applied Surface Science* **2006**, 252, 2573-2579.

100. Shinde, A.; Jones, R.J.R.; Guevarra, D.; Mitrovic, S.; Becerra-Stasiewicz, N.; Haber, J.A.; Jin, J.; Gregoire, J.M. High-Throughput Screening for Acid-Stable Oxygen Evolution Electrocatalysts in the (Mn–Co–Ta–Sb)O<sub>x</sub> Composition Space *Electrocatalysis* **2015**, 6, 229-236.
101. Jiang, R.; Chu, D. A combinatorial approach toward electrochemical analysis *Journal of Electroanalytical Chemistry* **2002**, 527, 137-142.
102. Guerin, S.; Hayden, B.E.; Lee, C.E.; Mormiche, C.; Owen, J.R.; Russell, A.E.; Theobald, B.; Thompsett, D. Combinatorial Electrochemical Screening of Fuel Cell Electrocatalysts *Journal of Combinatorial Chemistry* **2004**, 6, 149-158.
103. Reddington, E.; Sapienza, A.; Gurau, B.; Viswanathan, R.; Sarangapani, S.; Smotkin, E.S.; Mallouk, T.E. Combinatorial Electrochemistry: A Highly Parallel, Optical Screening Method for Discovery of Better Electrocatalysts *Science* **1998**, 280, 1735-1737.
104. Jayaraman, S.; Hillier, A. Electrochemical synthesis and reactivity screening of a ternary composition gradient for combinatorial discovery of fuel cell catalysts *Measurement Science and Technology* **2004**, 16, 5-13.
105. Choi, W.C.; Kim, J.D.; Woo, S.I. Quaternary Pt-based electrocatalyst for methanol oxidation by combinatorial electrochemistry *Catalysis Today* **2002**, 74, 235-240.
106. Lin, X.; Zheng, L.; Gao, G.; Chi, Y.; Chen, G. Electrochemiluminescence Imaging-Based High-Throughput Screening Platform for Electrocatalysts Used in Fuel Cells *Analytical Chemistry* **2012**, 84, 7700-7707.
107. Xiang, C.; Suram, S.K.; Haber, J.A.; Guevarra, D.W.; Soedarmadji, E.; Jin, J.; Gregoire, J.M. High-Throughput Bubble Screening Method for Combinatorial Discovery of Electrocatalysts for Water Splitting *ACS Combinatorial Science* **2014**, 16, 47-52.
108. Saal, J.E.; Kirklin, S.; Aykol, M.; Meredig, B.; Wolverton, C. Materials Design and Discovery with High-Throughput Density Functional Theory: The Open Quantum Materials Database (OQMD) *JOM* **2013**, 65, 1501-1509.
109. Hautier, G.; Jain, A.; Ong, S.P. From the computer to the laboratory: materials discovery and design using first-principles calculations *Journal of Materials Science* **2012**, 47, 7317-7340.
110. Greeley, J.; Jaramillo, T.F.; Bonde, J.; Chorkendorff, I.; Nørskov, J.K. Computational high-throughput screening of electrocatalytic materials for hydrogen evolution *Nature Materials* **2006**, 5, 909-913.
111. Kabir, S.; Artyushkova, K.; Serov, A.; Kiefer, B.; Atanassov, P. Binding energy shifts for nitrogen-containing graphene-based electrocatalysts – experiments and DFT calculations *Surface and Interface Analysis* **2016**, 48, 293-300.

112. Li, X.; Gao, H. DFT Analysis of NO Adsorption on the Undoped and Ce-Doped LaCoO<sub>3</sub> (011) Surface *Materials* **2019**, *12*, 1379, 1-15.
113. Meredig, B.; Agrawal, A.; Kirklin, S.; Saal, J.E.; Doak, J.W.; Thompson, A.; Zhang, K.; Choudhary, A.; Wolverton, C. Combinatorial screening for new materials in unconstrained composition space with machine learning *Physical Review B* **2014**, *89*, 094104, 1-7.
114. Hegde, V.I.; Aykol, M.; Kirklin, S.; Wolverton, C. The phase stability network of all inorganic materials *Science Advances* **2020**, *6*, eaay5606.
115. Rohr, B.; Stein, H.S.; Guevarra, D.; Wang, Y.; Haber, J.A.; Aykol, M.; Suram, S.K.; Gregoire, J.M. Benchmarking the acceleration of materials discovery by sequential learning *Chemical Science* **2020**, *11*, 2696-2706.
116. Nikolaev, P.; Hooper, D.; Webber, F.; Rao, R.; Decker, K.; Krein, M.; Poleski, J.; Barto, R.; Maruyama, B. Autonomy in materials research: a case study in carbon nanotube growth *NPJ Computational Materials* **2016**, *2*.
117. Akbarzadeh, A.; Samiei, M.; Davaran, S. Magnetic nanoparticles: preparation, physical properties, and applications in biomedicine *Nanoscale research letters* **2012**, *7*, 144-144.
118. Yu, H.; Peng, Y.; Yang, Y.; Li, Z.-Y. Plasmon-enhanced light-matter interactions and applications *npj Computational Materials* **2019**, *5*, 45, 1-14.
119. Singh, S.B.; Tandon, P.K. Catalysis: a brief review on nano-catalyst *J Energy Chem Eng* **2014**, *2*, 106-115.
120. Zhang, C.; Shen, X.; Pan, Y.; Peng, Z. A review of Pt-based electrocatalysts for oxygen reduction reaction *Frontiers in Energy* **2017**, *11*, 268-285.
121. Sharma, B.; Frontiera, R.R.; Henry, A.-I.; Ringe, E.; Van Duyne, R.P. SERS: Materials, applications, and the future *Materials today* **2012**, *15*, 16-25.
122. Wu, C.; Bull, B.; Szymanski, C.; Christensen, K.; McNeill, J. Multicolor conjugated polymer dots for biological fluorescence imaging *ACS nano* **2008**, *2*, 2415-2423.
123. Braunschweig, A.B.; Huo, F.; Mirkin, C.A. Molecular printing *Nat Chem* **2009**, *1*, 353-358.
124. Giam, L.R.; Massich, M.D.; Hao, L.; Shin Wong, L.; Mader, C.C.; Mirkin, C.A. Scanning probe-enabled nanocombinatorics define the relationship between fibronectin feature size and stem cell fate *Proc Natl Acad Sci U S A* **2012**, *109*, 4377-4382.
125. Zhong, X.; Bailey, N.A.; Schesing, K.B.; Bian, S.; Campos, L.M.; Braunschweig, A.B. Materials for the preparation of polymer pen lithography tip arrays and a comparison of their printing properties *Journal of Polymer Science Part A: Polymer Chemistry* **2013**, *51*, 1533-1539.

126. Liao, X.; Braunschweig, A.B.; Zheng, Z.; Mirkin, C.A. Force- and time-dependent feature size and shape control in molecular printing via polymer-pen lithography *Small* **2010**, 6, 1082-1086.
127. Brown, K.; Eichelsdoerfer, D.; Shim, W.; Rasin, B.; Radha, B.; Liao, X.; Schmucker, A.; Liu, G.; Mirkin, C. A cantilever-free approach to dot-matrix nanoprinting. *Proceedings of the National Academy of Sciences* **2013**, 110, 12921-12924.
128. Weeks, B.L.; Noy, A.; Miller, A.E.; De Yoreo, J.J. Effect of Dissolution Kinetics on Feature Size in Dip-Pen Nanolithography *Physical Review Letters* **2002**, 88, 255505-1-4.
129. Ginger, D.S.; Zhang, H.; Mirkin, C.A. The evolution of dip-pen nanolithography *Angew Chem Int Ed Engl* **2004**, 43, 30-45.
130. Salaita, K.; Wang, Y.; Mirkin, C.A. Applications of dip-pen nanolithography *Nat Nano* **2007**, 2, 145-155.
131. Vega, R.A.; Shen, C.K.; Maspoeh, D.; Robach, J.G.; Lamb, R.A.; Mirkin, C.A. Monitoring single-cell infectivity from virus-particle nanoarrays fabricated by parallel dip-pen nanolithography *Small* **2007**, 3, 1482-1485.
132. Smith, J.C.; Lee, K.-B.; Wang, Q.; Finn, M.G.; Johnson, J.E.; Mrksich, M.; Mirkin, C.A. Nanopatterning the Chemospecific Immobilization of Cowpea Mosaic Virus Capsid *Nano Letters* **2003**, 3, 883-886.
133. Liu, X.; Fu, L.; Hong, S.; Dravid, V.P.; Mirkin, C.A. Arrays of Magnetic Nanoparticles Patterned via "Dip-Pen" Nanolithography *Advanced Materials* **2002**, 14, 231-234.
134. Eichelsdoerfer, D.J.; Liao, X.; Cabezas, M.D.; Morris, W.; Radha, B.; Brown, K.A.; Giam, L.R.; Braunschweig, A.B.; Mirkin, C.A. Large-area molecular patterning with polymer pen lithography *Nat Protoc* **2013**, 8, 2548-2560.
135. Zhou, Y.; Xie, Z.; Brown, K.A.; Park, D.J.; Zhou, X.; Chen, P.C.; Hirtz, M.; Lin, Q.Y.; Dravid, V.P.; Schatz, G.C.; Zheng, Z.; Mirkin, C.A. Apertureless cantilever-free pen arrays for scanning photochemical printing *Small* **2015**, 11, 913-918.
136. Shim, W.; Braunschweig, A.B.; Liao, X.; Chai, J.; Lim, J.K.; Zheng, G.; Mirkin, C.A. Hard-tip, soft-spring lithography *Nature* **2011**, 469, 516-520.
137. Eichelsdoerfer, D.J.; Brown, K.A.; Boya, R.; Shim, W.; Mirkin, C.A. Tuning the spring constant of cantilever-free tip arrays *Nano Lett* **2013**, 13, 664-667.
138. Liao, X.; Brown, K.A.; Schmucker, A.L.; Liu, G.; He, S.; Shim, W.; Mirkin, C.A. Desktop nanofabrication with massively multiplexed beam pen lithography *Nat Commun* **2013**, 4, 2103-2010.



139. Huo, F.; Zheng, G.; Liao, X.; Giam, L.R.; Chai, J.; Chen, X.; Shim, W.; Mirkin, C.A. Beam pen lithography *Nat Nanotechnol* **2010**, *5*, 637-640.
140. Xie, Z.; Shen, Y.; Zhou, X.; Yang, Y.; Tang, Q.; Miao, Q.; Su, J.; Wu, H.; Zheng, Z. Polymer pen lithography using dual-elastomer tip arrays *Small* **2012**, *8*, 2664-2669.
141. Schmid, H.; Michel, B. Siloxane Polymers for High-Resolution, High-Accuracy Soft Lithography *Macromolecules* **2000**, *33*, 3042-3049.
142. Odom, T.W.; Love, J.C.; Wolfe, D.B.; Paul, K.E.; Whitesides, G.M. Improved Pattern Transfer in Soft Lithography Using Composite Stamps *Langmuir* **2002**, *18*, 5314-5320.
143. Hedrick, J.L.; Brown, K.A.; Kluender, E.J.; Cabezas, M.D.; Chen, P.-C.; Mirkin, C.A. Hard Transparent Arrays for Polymer Pen Lithography *ACS Nano* **2016**, *10*, 3144-3148.
144. Bowden, N.; Brittain, S.; Evans, A.G.; Hutchinson, J.W.; Whitesides, G.M. Spontaneous formation of ordered structures in thin films of metals supported on an elastomeric polymer *Nature* **1998**, *393*, 146-149.
145. Genzer, J.; Groenewold, J. Soft matter with hard skin: From skin wrinkles to templating and material characterization *Soft Matter* **2006**, *2*, 310-323.
146. Imburgia, M.J.; Crosby, A.J. Rolling wrinkles on elastic substrates *Extreme Mechanics Letters* **2015** 23-30.
147. Ebata, Y.; Croll, A.B.; Crosby, A.J. Wrinkling and strain localizations in polymer thin films *Soft Matter* **2012**, *8*, 9086-9091.
148. Khang, D.-Y.; Rogers, J.A.; Lee, H.H. Mechanical Buckling: Mechanics, Metrology, and Stretchable Electronics *Advanced Functional Materials* **2009**, *19*, 1526-1536.
149. Nania, M.; Matar, O.K.; Cabral, J.T. Frontal vitrification of PDMS using air plasma and consequences for surface wrinkling *Soft Matter* **2015**, *11*, 3067-3075.
150. Liao, X.; Braunschweig, A.B.; Mirkin, C.A. "Force-feedback" leveling of massively parallel arrays in polymer pen lithography *Nano Lett* **2010**, *10*, 1335-1340.
151. Zheng, Z.; Daniel, W.L.; Giam, L.R.; Huo, F.; Senesi, A.J.; Zheng, G.; Mirkin, C.A. Multiplexed protein arrays enabled by polymer pen lithography: addressing the inking challenge *Angew Chem Int Ed Engl* **2009**, *48*, 7626-7629.
152. Basabe-Desmonts, L.; Reinhoudt, D.N.; Crego-Calama, M. Combinatorial Fabrication of Fluorescent Patterns with Metal Ions Using Soft Lithography *Advanced Materials* **2006**, *18*, 1028-1032.

153. Wang, Y.; Giam, L.R.; Park, M.; Lenhert, S.; Fuchs, H.; Mirkin, C.A. A self-correcting inking strategy for cantilever arrays addressed by an inkjet printer and used for dip-pen nanolithography *Small* **2008**, 4, 1666-1670.
154. Eichelsdoerfer, D.J.; Brown, K.A.; Mirkin, C.A. Capillary bridge rupture in dip-pen nanolithography *Soft Matter* **2014**, 10, 5603-5608.
155. Zhong, J.; Sun, G.; He, D. Classic, liquid, and matrix-assisted dip-pen nanolithography for materials research *Nanoscale* **2014**, 6, 12217-12228.
156. Chai, J.; Wong, L.S.; Giam, L.; Mirkin, C.A. Single-molecule protein arrays enabled by scanning probe block copolymer lithography *Proc Natl Acad Sci U S A* **2011**, 108, 19521-19525.
157. Nie, Z.; Kumacheva, E. Patterning surfaces with functional polymers *Nature Materials* **2008**, 7, 277-290.
158. Jang, J.; Hong, S.; Schatz, G.C.; Ratner, M.A. Self-assembly of ink molecules in dip-pen nanolithography: A diffusion model *The Journal of Chemical Physics* **2001**, 115, 2721-2729.
159. O'Connell, C.D.; Higgins, M.J.; Marusic, D.; Moulton, S.E.; Wallace, G.G. Liquid Ink Deposition from an Atomic Force Microscope Tip: Deposition Monitoring and Control of Feature Size *Langmuir* **2014**, 30, 2712-2721.
160. Thangawng, A.; Ruoff, R.; Swartz, M.; Glucksberg, M. An ultra-thin PDMS membrane as a bio/micro-nano interface: Fabrication and characterization *Biomedical microdevices* **2007**, 9, 587-595.
161. Lange, J.; Toll, S.; Månson, J.-A.E.; Hult, A. Residual stress build-up in thermoset films cured above their ultimate glass transition temperature *Polymer* **1995**, 36, 3135-3141.
162. Cooke, M.D.; Gibbs, M.R.J.; Pettifer, R.F. Sputter deposition of compositional gradient magnetostrictive FeCo based thin films *Journal of Magnetism and Magnetic Materials* **2001**, 237, 175-180.
163. Kafizas, A.; Parkin, I.P. Inorganic thin-film combinatorial studies for rapidly optimising functional properties *Chemical Society Reviews* **2012**, 41, 738-781.
164. Ludwig, A. Discovery of new materials using combinatorial synthesis and high-throughput characterization of thin-film materials libraries combined with computational methods *npj Computational Materials* **2019**, 5, 70, 1-7.
165. Kluender, E.J.; Hedrick, J.L.; Brown, K.A.; Rao, R.; Meckes, B.; Du, J.S.; Moreau, L.M.; Maruyama, B.; Mirkin, C.A. Catalyst discovery through megalibraries of nanomaterials *Proceedings of the National Academy of Sciences* **2019**, 116, 40-45.

166. Shimizu, T.; Kenndler, E. Capillary electrophoresis of small solutes in linear polymer solutions: Relation between ionic mobility, diffusion coefficient and viscosity *ELECTROPHORESIS* **1999**, 20, 3364-3372.
167. Su, G.; Guo, Q.; Palmer, R.E. Colloidal Lines and Strings *Langmuir* **2003**, 19, 9669-9671.
168. Fahrni, C.J. Biological applications of X-ray fluorescence microscopy: exploring the subcellular topography and speciation of transition metals *Curr. Opin. Chem. Biol.* **2007**, 11, 121-127.
169. Puri, S.; Chand, B.; Mehta, D.; Garg, M.L.; Singh, N.; Trehan, P.N. K and L Shell X-Ray Fluorescence Cross Sections *Atomic Data and Nuclear Data Tables* **1995**, 61, 289-311.
170. Jang, J.; Schatz, G.C.; Ratner, M.A. Capillary force on a nanoscale tip in dip-pen nanolithography *Phys. Rev. Lett.* **2003**, 90, 156104-156107.
171. Iijima, S. Helical microtubules of graphitic carbon *Nature* **1991**, 354, 56-58.
172. Zhang, R.; Zhang, Y.; Zhang, Q.; Xie, H.; Qian, W.; Wei, F. Growth of Half-Meter Long Carbon Nanotubes Based on Schulz-Flory Distribution *ACS Nano* **2013**, 7, 6156-6161.
173. Hamada, N.; Sawada, S.-i.; Oshiyama, A. New one-dimensional conductors: Graphitic microtubules *Physical Review Letters* **1992**, 68, 1579-1581.
174. Mintmire, J.W.; Dunlap, B.I.; White, C.T. Are fullerene tubules metallic? *Physical Review Letters* **1992**, 68, 631-634.
175. Tans, S.J.; Verschueren, A.R.M.; Dekker, C. Room-temperature transistor based on a single carbon nanotube *Nature* **1998**, 393, 49-52.
176. Bachtold, A.; Hadley, P.; Nakanishi, T.; Dekker, C. Logic Circuits with Carbon Nanotube Transistors *Science* **2001**, 294, 1317-1320.
177. Kumar, S.; Blanchet, G.B.; Hybertsen, M.S.; Murthy, J.Y.; Alam, M.A. Performance of carbon nanotube-dispersed thin-film transistors *Applied Physics Letters* **2006**, 89, 143501, 1-3.
178. Li, J.; Hu, L.; Wang, L.; Zhou, Y.; Grüner, G.; Marks, T.J. Organic Light-Emitting Diodes Having Carbon Nanotube Anodes *Nano Letters* **2006**, 6, 2472-2477.
179. Kymakis, E.; Alexandrou, I.; Amaratunga, G.A.J. High open-circuit voltage photovoltaic devices from carbon-nanotube-polymer composites *Journal of Applied Physics* **2003**, 93, 1764-1768.
180. Barnes, T.M.; Wu, X.; Zhou, J.; Duda, A.; van de Lagemaat, J.; Coutts, T.J.; Weeks, C.L.; Britz, D.A.; Glatkowski, P. Single-wall carbon nanotube networks as a transparent back contact in CdTe solar cells *Applied Physics Letters* **2007**, 90, 243503, 1-3.

181. Kong, J.; Franklin, N.R.; Zhou, C.; Chapline, M.G.; Peng, S.; Cho, K.; Dai, H. Nanotube Molecular Wires as Chemical Sensors *Science* **2000**, 287, 622-625.
182. Chen, R.J.; Bangsaruntip, S.; Drouvalakis, K.A.; Wong Shi Kam, N.; Shim, M.; Li, Y.; Kim, W.; Utz, P.J.; Dai, H. Noncovalent functionalization of carbon nanotubes for highly specific electronic biosensors *Proceedings of the National Academy of Sciences* **2003**, 100, 4984-4989.
183. T. Guo, P.N., A. Thess, D.T. Colbert, R.E. Smalley Catalytic growth of single-walled nanotubes by laser vaporization *Chemical Physics Letters* **1995**, 243, 49-54.
184. Bethune, D.S.; Klang, C.H.; de Vries, M.S.; Gorman, G.; Savoy, R.; Vazquez, J.; Beyers, R. Cobalt-catalysed growth of carbon nanotubes with single-atomic-layer walls *Nature* **1993**, 363, 605-607.
185. Thess, A.; Lee, R.; Nikolaev, P.; Dai, H.; Petit, P.; Robert, J.; Xu, C.; Lee, Y.H.; Kim, S.G.; Rinzler, A.G.; Colbert, D.T.; Scuseria, G.E.; Tománek, D.; Fischer, J.E.; Smalley, R.E. Crystalline Ropes of Metallic Carbon Nanotubes *Science* **1996**, 273, 483-487.
186. Endo, M.; Takeuchi, K.; Igarashi, S.; Kobori, K.; Shiraishi, M.; Kroto, H.W. The production and structure of pyrolytic carbon nanotubes (PCNTs) *Journal of Physics and Chemistry of Solids* **1993**, 54, 1841-1848.
187. Li, W.Z.; Xie, S.S.; Qian, L.X.; Chang, B.H.; Zou, B.S.; Zhou, W.Y.; Zhao, R.A.; Wang, G. Large-Scale Synthesis of Aligned Carbon Nanotubes *Science* **1996**, 274, 1701-1703.
188. Liu, B.; Ren, W.; Gao, L.; Li, S.; Liu, Q.; Jiang, C.; Cheng, H.-M. Manganese-Catalyzed Surface Growth of Single-Walled Carbon Nanotubes with High Efficiency *The Journal of Physical Chemistry C* **2008**, 112, 19231-19235.
189. Li, Y.; Cui, R.; Ding, L.; Liu, Y.; Zhou, W.; Zhang, Y.; Jin, Z.; Peng, F.; Liu, J. How catalysts affect the growth of single-walled carbon nanotubes on substrates *Adv Mater* **2010**, 22, 1508-1515.
190. Yuan, D.; Ding, L.; Chu, H.; Feng, Y.; McNicholas, T.P.; Liu, J. Horizontally Aligned Single-Walled Carbon Nanotube on Quartz from a Large Variety of Metal Catalysts *Nano Letters* **2008**, 8, 2576-2579.
191. Takagi, D.; Homma, Y.; Hibino, H.; Suzuki, S.; Kobayashi, Y. Single-Walled Carbon Nanotube Growth from Highly Activated Metal Nanoparticles *Nano Letters* **2006**, 6, 2642-2645.
192. Qian, Y.; Wang, C.; Ren, G.; Huang, B. Surface growth of single-walled carbon nanotubes from ruthenium nanoparticles *Applied Surface Science* **2010**, 256, 4038-4041.

193. Bhaviripudi, S.; Mile, E.; Steiner, S.A.; Zare, A.T.; Dresselhaus, M.S.; Belcher, A.M.; Kong, J. CVD Synthesis of Single-Walled Carbon Nanotubes from Gold Nanoparticle Catalysts *Journal of the American Chemical Society* **2007**, 129, 1516-1517.
194. Zhou, W.; Han, Z.; Wang, J.; Zhang, Y.; Jin, Z.; Sun, X.; Zhang, Y.; Yan, C.; Li, Y. Copper Catalyzing Growth of Single-Walled Carbon Nanotubes on Substrates *Nano Letters* **2006**, 6, 2987-2990.
195. Takagi, D.; Hibino, H.; Suzuki, S.; Kobayashi, Y.; Homma, Y. Carbon Nanotube Growth from Semiconductor Nanoparticles *Nano Letters* **2007**, 7, 2272-2275.
196. Swierczewska, M.; Rusakova, I.; Sitharaman, B. Gadolinium and europium catalyzed growth of single-walled carbon nanotubes *Carbon* **2009**, 47, 3139-3142.
197. Deck, C.P.; Vecchio, K. Prediction of carbon nanotube growth success by the analysis of carbon-catalyst binary phase diagrams *Carbon* **2006**, 44, 267-275.
198. Wagner, R.S.; Ellis, W.C. VAPOR - LIQUID - SOLID MECHANISM OF SINGLE CRYSTAL GROWTH *Applied Physics Letters* **1964**, 4, 89-90.
199. Ayre, G.N.; Uchino, T.; Mazumder, B.; Hector, A.L.; Hutchison, J.L.; Smith, D.C.; Ashburn, P.; Groot, C.H.d. On the mechanism of carbon nanotube formation: the role of the catalyst *Journal of Physics: Condensed Matter* **2011**, 23, 394201, 1-8.
200. Kong, J.; Cassell, A.M.; Dai, H. Chemical vapor deposition of methane for single-walled carbon nanotubes *Chemical Physics Letters* **1998**, 292, 567-574.
201. Maruyama, S.; Kojima, R.; Miyauchi, Y.; Chiashi, S.; Kohno, M. Low-temperature synthesis of high-purity single-walled carbon nanotubes from alcohol *Chemical physics letters* **2002**, 360, 229-234.
202. Tian, Y.; Hu, Z.; Yang, Y.; Wang, X.; Chen, X.; Xu, H.; Wu, Q.; Ji, W.; Chen, Y. In Situ TA-MS Study of the Six-Membered-Ring-Based Growth of Carbon Nanotubes with Benzene Precursor *Journal of the American Chemical Society* **2004**, 126, 1180-1183.
203. Sanchez-Valencia, J.R.; Dienel, T.; Groning, O.; Shorubalko, I.; Mueller, A.; Jansen, M.; Amsharov, K.; Ruffieux, P.; Fasel, R. Controlled synthesis of single-chirality carbon nanotubes *Nature* **2014**, 512, 61-64.
204. Ermakova, M.A.; Ermakov, D.Y.; Kuvshinov, G.G. Effective catalysts for direct cracking of methane to produce hydrogen and filamentous carbon *Applied Catalysis A: General* **2000**, 201, 61-70.
205. Li, Q.; Yan, H.; Zhang, J.; Liu, Z. Effect of hydrocarbons precursors on the formation of carbon nanotubes in chemical vapor deposition *Carbon* **2004**, 42, 829-835.

206. Picher, M.; Anglaret, E.; Arenal, R.; Jourdain, V. Self-Deactivation of Single-Walled Carbon Nanotube Growth Studied by in Situ Raman Measurements *Nano Letters* **2009**, 9, 542-547.
207. Nessim, G.D.; Hart, A.J.; Kim, J.S.; Acquaviva, D.; Oh, J.; Morgan, C.D.; Seita, M.; Leib, J.S.; Thompson, C.V. Tuning of Vertically-Aligned Carbon Nanotube Diameter and Areal Density through Catalyst Pre-Treatment *Nano Letters* **2008**, 8, 3587-3593.
208. Cantoro, M.; Hofmann, S.; Pisana, S.; Scardaci, V.; Parvez, A.; Ducati, C.; Ferrari, A.C.; Blackburn, A.M.; Wang, K.-Y.; Robertson, J. Catalytic Chemical Vapor Deposition of Single-Wall Carbon Nanotubes at Low Temperatures *Nano Letters* **2006**, 6, 1107-1112.
209. Hata, K.; Futaba, D.N.; Mizuno, K.; Namai, T.; Yumura, M.; Iijima, S. Water-Assisted Highly Efficient Synthesis of Impurity-Free Single-Walled Carbon Nanotubes *Science* **2004**, 306, 1362-1364.
210. Wang, H.; Yuan, Y.; Wei, L.; Goh, K.; Yu, D.; Chen, Y. Catalysts for chirality selective synthesis of single-walled carbon nanotubes *Carbon* **2015**, 81, 1-19.
211. Yu, X.; Zhang, J.; Choi, W.; Choi, J.-Y.; Kim, J.M.; Gan, L.; Liu, Z. Cap Formation Engineering: From Opened C60 to Single-Walled Carbon Nanotubes *Nano Letters* **2010**, 10, 3343-3349.
212. Omachi, H.; Segawa, Y.; Itami, K. Synthesis of Cycloparaphenylenes and Related Carbon Nanorings: A Step toward the Controlled Synthesis of Carbon Nanotubes *Accounts of Chemical Research* **2012**, 45, 1378-1389.
213. Matsui, K.; Fushimi, M.; Segawa, Y.; Itami, K. Synthesis, Structure, and Reactivity of a Cylinder-Shaped Cyclo[12]orthophenylene[6]ethynylene: Toward the Synthesis of Zigzag Carbon Nanobelts *Organic Letters* **2016**, 18, 5352-5355.
214. Liu, J.; Wang, C.; Tu, X.; Liu, B.; Chen, L.; Zheng, M.; Zhou, C. Chirality-controlled synthesis of single-wall carbon nanotubes using vapour-phase epitaxy *Nature Communications* **2012**, 3, 1-7.
215. Xiaomin, T.; Manohar, S.; Jagota, A.; Ming, Z. DNA sequence motifs for structure-specific recognition and separation of carbon nanotubes **2009**, 460, 250-253.
216. Arnold, M.S.; Green, A.A.; Hulvat, J.F.; Stupp, S.I.; Hersam, M.C. Sorting carbon nanotubes by electronic structure using density differentiation *Nat Nano* **2006**, 1, 60-65.
217. Liu, H.; Tanaka, T.; Urabe, Y.; Kataura, H. High-Efficiency Single-Chirality Separation of Carbon Nanotubes Using Temperature-Controlled Gel Chromatography *Nano Letters* **2013**, 13, 1996-2003.

218. Harutyunyan, A.R.; Chen, G.; Paronyan, T.M.; Pigos, E.M.; Kuznetsov, O.A.; Hewaparakrama, K.; Kim, S.M.; Zakharov, D.; Stach, E.A.; Sumanasekera, G.U. Preferential Growth of Single-Walled Carbon Nanotubes with Metallic Conductivity *Science* **2009**, 326, 116-120.
219. Li, Y.; Mann, D.; Rolandi, M.; Kim, W.; Ural, A.; Hung, S.; Javey, A.; Cao, J.; Wang, D.; Yenilmez, E.; Wang, Q.; Gibbons, J.F.; Nishi, Y.; Dai, H. Preferential Growth of Semiconducting Single-Walled Carbon Nanotubes by a Plasma Enhanced CVD Method *Nano Letters* **2004**, 4, 317-321.
220. Qu, L.; Du, F.; Dai, L. Preferential Syntheses of Semiconducting Vertically Aligned Single-Walled Carbon Nanotubes for Direct Use in FETs *Nano Letters* **2008**, 8, 2682-2687.
221. Keiji, S.; Hiroaki, T.; Kunihide, K.; Hirofumi, Y.; Nobuyuki, I.; Hiroshi, Y. Multi-Excitation-Laser Raman Analysis of Chirality-Controlled Single-Walled Carbon Nanotubes with Free Electron Laser Irradiation during Growth *Japanese Journal of Applied Physics* **2011**, 50, 01BJ13,1-5.
222. Kajiwara, K.; Suzuki, S.; Sato, H.; Hata, K. Chirality-selective synthesis of carbon nanotubes by catalytic-chemical vapor deposition using quasicrystal alloys as catalysts *Zeitschrift für Kristallographie - Crystalline Materials* **2009**, 224, 5-8.
223. Chiang, W.-H.; Mohan Sankaran, R. Linking catalyst composition to chirality distributions of as-grown single-walled carbon nanotubes by tuning  $\text{Ni}_x\text{Fe}_{1-x}$  nanoparticles *Nat Mater* **2009**, 8, 882-886.
224. Yang, F.; Wang, X.; Zhang, D.; Yang, J.; LuoDa; Xu, Z.; Wei, J.; Wang, J.-Q.; Xu, Z.; Peng, F.; Li, X.; Li, R.; Li, Y.; Li, M.; Bai, X.; Ding, F.; Li, Y. Chirality-specific growth of single-walled carbon nanotubes on solid alloy catalysts *Nature* **2014**, 510, 522-524.
225. An, H.; Kumamoto, A.; Takezaki, H.; Ohyama, S.; Qian, Y.; Inoue, T.; Ikuhara, Y.; Chiashi, S.; Xiang, R.; Maruyama, S. Chirality specific and spatially uniform synthesis of single-walled carbon nanotubes from a sputtered Co-W bimetallic catalyst *Nanoscale* **2016**, 8, 14523-14529.
226. Hamley, I.W. Nanotechnology with Soft Materials *Angewandte Chemie International Edition* **2003**, 42, 1692-1712.
227. Lu, J.; Yi, S.S.; Kopley, T.; Qian, C.; Liu, J.; Gulari, E. Fabrication of Ordered Catalytically Active Nanoparticles Derived from Block Copolymer Micelle Templates for Controllable Synthesis of Single-Walled Carbon Nanotubes *The Journal of Physical Chemistry B* **2006**, 110, 6655-6660.
228. Rao, R.; Liptak, D.; Cherukuri, T.; Yakobson, B.I.; Maruyama, B. In situ evidence for chirality-dependent growth rates of individual carbon nanotubes *Nat Mater* **2012**, 11, 213-216.

229. Rao, R.; Pierce, N.; Liptak, D.; Hooper, D.; Sargent, G.; Semiatin, S.L.; Curtarolo, S.; Harutyunyan, A.R.; Maruyama, B. Revealing the Impact of Catalyst Phase Transition on Carbon Nanotube Growth by in Situ Raman Spectroscopy *ACS Nano* **2013**, *7*, 1100-1107.
230. Mogab, C.J.; Adams, A.C.; Flamm, D.L. Plasma etching of Si and SiO<sub>2</sub>—The effect of oxygen additions to CF<sub>4</sub> plasmas *Journal of Applied Physics* **1978**, *49*, 3796-3803.
231. d'Agostino, R.; Flamm, D.L. Plasma etching of Si and SiO<sub>2</sub> in SF<sub>6</sub>-O<sub>2</sub> mixtures *Journal of Applied Physics* **1981**, *52*, 162-167.
232. Laermer, F.; Schilp, A., *Method of anisotropically etching silicon*. 1996, Google Patents.
233. Sivakumar, V.M.; Mohamed, A.R.; Abdullah, A.Z.; Chai, S.-P. Role of reaction and factors of carbon nanotubes growth in chemical Vapour decomposition process using methane: a highlight *J. Nanomaterials* **2010**, 2010, Article 11.
234. Guisbiers, G.; Mejia-Rosales, S.; Khanal, S.; Ruiz-Zepeda, F.; Whetten, R.L.; José-Yacaman, M. Gold-Copper Nano-Alloy, “Tumbaga”, in the Era of Nano: Phase Diagram and Segregation *Nano Letters* **2014**, *14*, 6718-6726.
235. Homma, Y.; Liu, H.; Takagi, D.; Kobayashi, Y. Single-walled carbon nanotube growth with non-iron-group “catalysts” by chemical vapor deposition *Nano Research* **2009**, *2*, 793-799.
236. Kim, D.; Resasco, J.; Yu, Y.; Asiri, A.M.; Yang, P. Synergistic geometric and electronic effects for electrochemical reduction of carbon dioxide using gold-copper bimetallic nanoparticles *Nat. Com.* **2014**, *5*, 4948, 1-8.
237. Motl, N.E.; Ewusi-Annan, E.; Sines, I.T.; Jensen, L.; Schaak, R.E. Au-Cu Alloy Nanoparticles with Tunable Compositions and Plasmonic Properties: Experimental Determination of Composition and Correlation with Theory *J. Phys. Chem. C* **2010**, *114*, 19263-19269.
238. Qiwu, W.; Jianlong, Y.; Jingfang, R.; Minming, H.; Chunhua, Y. Structure and catalytic properties of Cu-Ni bimetallic catalysts for hydrogenation *Catalysis Letters* **1990**, *4*, 63-74.
239. Fechete, I.; Wang, Y.; Védrine, J.C. The past, present and future of heterogeneous catalysis *Catalysis Today* **2012**, *189*, 2-27.
240. Keller, M.; Collière, V.; Reiser, O.; Caminade, A.-M.; Majoral, J.-P.; Ouali, A. Pyrene-Tagged Dendritic Catalysts Noncovalently Grafted onto Magnetic Co/C Nanoparticles: An Efficient and Recyclable System for Drug Synthesis *Angewandte Chemie International Edition* **2013**, *52*, 3626-3629.
241. Subramanian, N.D.; Balaji, G.; Kumar, C.S.S.R.; Spivey, J.J. Development of cobalt-copper nanoparticles as catalysts for higher alcohol synthesis from syngas *Catalysis Today* **2009**, *147*, 100-106.



242. Astruc, D. Introduction: Nanoparticles in Catalysis *Chemical Reviews* **2020**, 120, 461-463.
243. Zhang, L.; Zhou, M.; Wang, A.; Zhang, T. Selective Hydrogenation over Supported Metal Catalysts: From Nanoparticles to Single Atoms *Chemical Reviews* **2020**, 120, 683-733.
244. Huang, L.; Chen, P.-C.; Liu, M.; Fu, X.; Gordiichuk, P.; Yu, Y.; Wolverson, C.; Kang, Y.; Mirkin, C.A. Catalyst design by scanning probe block copolymer lithography *Proceedings of the National Academy of Sciences* **2018**, 115, 3764-3769.
245. Yan, Y.; Du, J.S.; Gilroy, K.D.; Yang, D.; Xia, Y.; Zhang, H. Intermetallic nanocrystals: Syntheses and catalytic applications *Advanced Materials* **2017**, 29, 1605997.
246. Orimoto, Y.; Toyota, A.; Furuya, T.; Nakamura, H.; Uehara, M.; Yamashita, K.; Maeda, H. Computational Method for Efficient Screening of Metal Precursors for Nanomaterial Syntheses *Industrial & Engineering Chemistry Research* **2009**, 48, 3389-3397.
247. Jenkins, G.M.; Kawamura, K. Structure of Glassy Carbon *Nature* **1971**, 231, 175-176.
248. Dai, X.; Wu, J.; Qian, Z.; Wang, H.; Jian, J.; Cao, Y.; Rummeli, M.H.; Yi, Q.; Liu, H.; Zou, G. Ultra-smooth glassy graphene thin films for flexible transparent circuits *Science Advances* **2016**, 2, e1601574.
249. Xiao, L.; Yeung, E.S. Optical Imaging of Individual Plasmonic Nanoparticles in Biological Samples *Annual Review of Analytical Chemistry* **2014**, 7, 89-111.
250. Fleischmann, M.; Hendra, P.; McQuillan, A. RAMAN SPECTRA OF PYRIDINE ADSORBED AT A SILVER ELECTRODE *Chemical physics letters* **1974**, 26, 163-166.
251. Huang, X.; El-Sayed, M.A. Plasmonic photo-thermal therapy (PPTT) *Alexandria journal of medicine* **2011**, 47, 1-9.
252. Gong, C.; Leite, M.S. Noble Metal Alloys for Plasmonics *ACS Photonics* **2016**, 3, 507-513.
253. Zhang, Y.; Cai, B.; Jia, B. Ultraviolet Plasmonic Aluminium Nanoparticles for Highly Efficient Light Incoupling on Silicon Solar Cells *Nanomaterials (Basel, Switzerland)* **2016**, 6, 95-104.
254. Cortie, M.B.; McDonagh, A.M. Synthesis and Optical Properties of Hybrid and Alloy Plasmonic Nanoparticles *Chemical Reviews* **2011**, 111, 3713-3735.
255. Ross, M.B.; Mirkin, C.A.; Schatz, G.C. Optical Properties of One-, Two-, and Three-Dimensional Arrays of Plasmonic Nanostructures *The Journal of Physical Chemistry C* **2016**, 120, 816-830.
256. Nam, J.-M.; Oh, J.-W.; Lee, H.; Suh, Y.D. Plasmonic Nanogap-Enhanced Raman Scattering with Nanoparticles *Accounts of Chemical Research* **2016**, 49, 2746-2755.

257. Baumberg, J.J.; Aizpurua, J.; Mikkelsen, M.H.; Smith, D.R. Extreme nanophotonics from ultrathin metallic gaps *Nature Materials* **2019**, 18, 668-678.
258. Benz, F.; Chikkaraddy, R.; Salmon, A.; Ohadi, H.; de Nijs, B.; Mertens, J.; Carnegie, C.; Bowman, R.W.; Baumberg, J.J. SERS of Individual Nanoparticles on a Mirror: Size Does Matter, but so Does Shape *The Journal of Physical Chemistry Letters* **2016**, 7, 2264-2269.
259. Kongsuwan, N.; Demetriadou, A.; Chikkaraddy, R.; Benz, F.; Turek, V.A.; Keyser, U.F.; Baumberg, J.J.; Hess, O. Suppressed Quenching and Strong-Coupling of Purcell-Enhanced Single-Molecule Emission in Plasmonic Nanocavities *ACS Photonics* **2018**, 5, 186-191.
260. Akselrod, G.M.; Argyropoulos, C.; Hoang, T.B.; Ciraci, C.; Fang, C.; Huang, J.; Smith, D.R.; Mikkelsen, M.H. Probing the mechanisms of large Purcell enhancement in plasmonic nanoantennas *Nature Photonics* **2014**, 8, 835-840.
261. Taylor, A.B.; Zijlstra, P. Single-Molecule Plasmon Sensing: Current Status and Future Prospects *ACS Sensors* **2017**, 2, 1103-1122.
262. Seferos, D.S.; Giljohann, D.A.; Hill, H.D.; Prigodich, A.E.; Mirkin, C.A. Nano-Flares: Probes for Transfection and mRNA Detection in Living Cells *Journal of the American Chemical Society* **2007**, 129, 15477-15479.
263. Etchegoin, P.G.; Le Ru, E. A perspective on single molecule SERS: current status and future challenges *Physical Chemistry Chemical Physics* **2008**, 10, 6079-6089.
264. Wu, Y.; Li, G.; Camden, J.P. Probing Nanoparticle Plasmons with Electron Energy Loss Spectroscopy *Chemical Reviews* **2018**, 118, 2994-3031.
265. Todeschini, M.; Bastos da Silva Fanta, A.; Jensen, F.; Wagner, J.B.; Han, A. Influence of Ti and Cr Adhesion Layers on Ultrathin Au Films *ACS Applied Materials & Interfaces* **2017**, 9, 37374-37385.
266. Lechevallier, L.; Richon, G.; Le Bas, J.; Bernole, M. Structure and ohmic behaviour of gold-chromium thin films obtained by controlled coevaporation *Vacuum* **1990**, 41, 1218-1220.
267. Martinez, W.E.; Gregori, G.; Mates, T. Titanium diffusion in gold thin films *Thin Solid Films* **2010**, 518, 2585-2591.
268. Li, L.; Hutter, T.; Steiner, U.; Mahajan, S. Single molecule SERS and detection of biomolecules with a single gold nanoparticle on a mirror junction *Analyst* **2013**, 138, 4574-4578.
269. Peng, J.; Jeong, H.-H.; Lin, Q.; Cormier, S.; Liang, H.-L.; De Volder, M.F.L.; Vignolini, S.; Baumberg, J.J. Scalable electrochromic nanopixels using plasmonics *Science Advances* **2019**, 5, eaaw2205.

270. Huang, Y.; Ma, L.; Li, J.; Zhang, Z. Nanoparticle-on-mirror cavity modes for huge and/or tunable plasmonic field enhancement *Nanotechnology* **2017**, 28, 105203, 1-6.
271. Duley, W. Refractive indices for amorphous carbon *The Astrophysical Journal* **1984**, 287, 694-696.
272. Jeon, H.B.; Tsalu, P.V.; Ha, J.W. Shape Effect on the Refractive Index Sensitivity at Localized Surface Plasmon Resonance Inflection Points of Single Gold Nanocubes with Vertices *Scientific Reports* **2019**, 9, 13635, 1-8.
273. Yee, K. Numerical solution of initial boundary value problems involving Maxwell's equations in isotropic media *IEEE Transactions on antennas and propagation* **1966**, 14, 302-307.
274. Johnson, P.B.; Christy, R.W. Optical Constants of the Noble Metals *Physical Review B* **1972**, 6, 4370-4379.
275. Rioux, D.; Vallières, S.; Besner, S.; Muñoz, P.; Mazur, E.; Meunier, M. An Analytic Model for the Dielectric Function of Au, Ag, and their Alloys *Advanced Optical Materials* **2014**, 2, 176-182.
276. Huang, L.; Lin, H.; Zheng, C.Y.; Kluender, E.J.; Golnabi, R.; Shen, B.; Mirkin, C.A. Multimetallic High-Index Faceted Heterostructured Nanoparticles *Journal of the American Chemical Society* **2020**, 142, 4570-4575.
277. Levin, S.; Fritzsche, J.; Nilsson, S.; Runemark, A.; Dhokale, B.; Ström, H.; Sundén, H.; Langhammer, C.; Westerlund, F. A nanofluidic device for parallel single nanoparticle catalysis in solution *Nature Communications* **2019**, 10, 4426, 1-8.

## CURRICULUM VITAE

**Edward J Kluender**  
ejkluender@gmail.com

### **Education**

---

**Northwestern University, Evanston, IL**, PhD Candidate (Expected July 2020)  
Materials Science and Engineering  
Advisor: Prof. Chad Mirkin

**Gustavus Adolphus College, St. Peter, MN**, B.A. 2014  
Majors: Physics, Chemistry  
Distinctions: President's Scholarship, Sigma Pi Sigma, Sigma Xi, *Cum Laude*

### **Research Experience**

---

#### **Northwestern University, Department of Materials Science and Engineering**

*Graduate Research Assistant with Prof. Chad Mirkin, November 2014-present*

- Developed platform for combinatorial screening of multimetallic nanoparticles. This enabled mapping of the entire nano-materials genome at a high throughput rate and lead to discovery of new materials for catalytic and physical applications
- My platform consists of fabricating cm-scale substrates, each containing millions of nanoparticles with size and composition spatially encoded, and subsequently analyzing particles for multiple chemical and physical properties
- I customized this platform for multiple collaborations with GlaxoSmithKline (heterogeneous catalysts), NU internal collaborations (E-Chem catalysts), Air Force Research Lab at Wright-Patterson AFB (SWNT catalysts, plasmonic structures)
- Conducted high-throughput catalyst screening research at Wright-Patterson Air Force Base after securing background checks and CAC card access

#### **Gustavus Adolphus College, Department of Physics**

*Undergraduate Research with Prof. Thomas Huber, 2013*

- Developed novel methods to measure vibrational resonances using non-contact confocal ultrasound transducers
- Wrote programs in Visual Basic, C++, and Matlab to generate excitation signal, and to collect and analyze data

#### **Purdue University, Department of Environmental and Ecological Engineering**

*REU Summer Research with Prof. John Sutherland and Prof. Fu Zhao, 2012*

- Calculated the water footprint of steel manufacturing through cradle-to-grave analysis
- Paper published in the Journal of Purdue Undergraduate Research (in top 10 read papers in JPUR)

### **Leadership Experience**

---

- Leader of Dip-Pen Nanolithography Subgroup *August 2018-present*
  - Lead grant writing and reporting (Contributed to >10 grants resulting in >\$5 million in funding, written and/or edited >20 grant reports)
  - Supervised and mentored ~15 graduate students and post docs
- Department of Materials Science and Engineering Graduate Curriculum Committee *Winter 2016-17*
  - Developed a new curriculum for the Northwestern MSE graduate program
- Two-sport athlete at Gustavus Adolphus College (Basketball and Track & Field)
- Teaching Assistant for the PEOPLE Program (UW-Madison Chemistry Department) *Summer 2011*
  - Science outreach for underprivileged middle and high school students

### **Selected Presentations**

---

- Kluender, Hedrick, Rao, Maruyama, Mirkin, “Expanding the Materials Genome Through Size” Materials Research Society Fall Meeting and Exhibit, Boston, MA, *November 2018*
- Kluender, Rao, Maruyama, Mirkin, “Expanding the Materials Genome Through Size” Invited Lecture at Wright Patterson Air Force Base, Dayton, OH, *May 2018*
- Kluender, Rao, Maruyama, Mirkin, “Screening Carbon Nanotube Catalyst Through Scanning Probe Block Copolymer Lithography” Invited Lecture at Wright Patterson Air Force Base, Dayton, OH, *July 2016*

### **Selected Publications**

---

- Huang, Lin, Zheng, **Kluender**, Golnabi, Shen Mirkin; “Multimetallic High-Index Faceted Heterostructured Nanoparticles” *JACS*, **2020**, *in press*, doi:10.1021/jacs.0C00045.
- **Kluender\***, Hedrick\*, Brown, Rao, Meckes, Du, Moreau, Maruyama, Mirkin; “Catalyst discovery through megalibraries of nanomaterials” *PNAS*, **2019**, 116 (1), 40-45.
- Highlighted in Science (doi.org/10.1126/science.aaw4511)
- Highlighted in Nature Chemical Reviews (doi.org/10.1038/s41570-019-0075-5)
- Du, Chen, Meckes, **Kluender**, Xie, Dravid, Mirkin; “Windowless Observation of Evaporation-Induced Coarsening of Au–Pt Nanoparticles in Polymer Nanoreactors” *JACS*, **2018**, 140 (23), 7213-7221
- Ashley, **Kluender**, Mirkin; “Fast Charge Extraction in Perovskite-Based Core-Shell Nanowires” *ACS Nano*, **2018**, 12 (7), 7206-7212 .
- Hedrick, Brown, **Kluender**, Cabezas, Chen, and Mirkin; “Hard Transparent Arrays for Polymer Pen Lithography” *ACS Nano*, **2016**, 10 (3), 3144-3148.

### **Scientific Laboratory Techniques**

---

- Atomic Force Microscopy (AFM)
- Scanning Electron Microscopy (SEM)
- Raman Spectroscopy
- X-Ray Photoelectron Spectroscopy (XPS)
- UV-Visible Spectroscopy (UV-Vis)
- Dark-Field Confocal Spectroscopy
- Photolithography
- Reactive Ion Etching
- E-beam Evaporation Deposition
- Chemical Vapor Deposition (CVD)
- Magnetron Sputtering Deposition
- 3D printing and CNC Drilling for prototyping combined with Autocad
- Coding in Matlab, Mathematica, Mathcad, Labview, Visual Basic, and C++